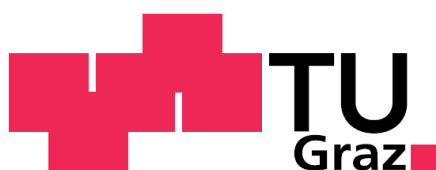


Dissertation submitted to the Graz University of Technology,  
Institute of Hydraulic Engineering and Water Resources Management, for the  
attainment of the degree of Doctor of Engineering Sciences (Dr. techn.)

## **Comparative Similarity Study on Local Losses of Hydraulic Model with Different Scale Factors**

**Umboro Lasminto**  
November 2012



Reviewed and examined by:

Ao.Univ.-Prof. Dipl.-Ing. Dr.techn. Roman Klasinc  
Institute of Hydraulic Engineering and Water Resources Management  
Graz University of Technology

Prof. Dipl. Ing. Dr. sc. Franci Steinman  
Department of Built Environment, Faculty for Civil and Geodetic Engineering  
University of Ljubljana

This page intentionally left blank

# Zusammenfassung

*Die Minimierung der hydraulischen Verluste ist ein wichtiger Aspekt bei der Auslegung von Rohrleitungssystemen in Wasserkraftwerken um die elektrische Energieproduktion zu optimieren. Die hydraulischen Verluste in Rohrleitungssystemen setzen sich zusammen aus Reibungsverlusten zwischen Flüssigkeit und Rohrwänden und aus Verlusten bedingt durch die Form der Sammler und Armaturen, also die lokalen Verluste. Hydraulische Verluste in turbulenter Strömung werden üblicherweise durch Strömungsuntersuchungen an einem physikalischen Modell abgeschätzt, die auf der Ähnlichkeit der Reynoldszahl basieren. Das Ergebnis wird anschließend auf den Prototypen übertragen. Dabei kann nun das Probleme auftreten, dass man im physikalischen Modell mitunter nicht in der Lage ist, die hohen Strömungsgeschwindigkeiten zu erreichen, welche zum Erzielen der selben Reynoldszahl wie beim Prototypen erforderlich wäre. Die Korrelation der Verlustkoeffizienten zwischen dem physikalischen Modell und dem Prototypen kann mit Hilfe eines Familienmodells ermittelt werden. Dafür sind jedoch aufwändige Untersuchungen erforderlich, die durch die Anwendung eines zusätzlichen numerischen Modells reduziert werden können.*

*In dieser Dissertation werden Ähnlichkeitsstudien ausgehend von Messdaten aus vorhergehenden Untersuchungen über Verlustkoeffizienten von Bögen und T-Stücken an diesen Komponenten mit unterschiedlichen Durchmessern durchgeführt. Ebenso wurde die Leistungsfähigkeit von numerischen Modellen zur Simulation von Strömungen in gegebenen Y-Stücken mit dem Ziel, den Verlustkoeffizienten abzuschätzen und das Ergebnis vom physikalischen Modell auf den Prototypen zu übertragen, durchgeführt.*

*Die Ähnlichkeitsstudie eines Familienmodells von industriellen Bögen und T-Stücken zeigt, dass für dieselbe Reynoldszahl die Verlustkoeffizienten dieser Bauteile um so ähnlicher werden, je proportionaler deren geometrische Abmessungen sind.*

*Die Ergebnisse aus dem numerischen Modell zeigen eine gute Übereinstimmung mit den Messungen aus dem physikalischen Modell. Bei der Simulation von Y-Stücken können auch für sehr hohe Reynoldszahlen verlässliche Ergebnisse erzielt werden. Die Anwendung des Modells auf Y-Stücke unterschiedlichen Durchmessers mit ähnlichen Reynoldszahlen und ähnlicher relativer Rauigkeit ergeben abnehmende Verlustkoeffizienten. Diese nähern sich jedoch für große Reynoldszahlen aneinander an. Das Modell wurde erfolgreich angewandt zur Abschätzung von Verlustkoeffizienten anderer Sammler und Armaturen bei hohen Reynoldszahlen.*

*Um die Ergebnisse dieser Arbeit zu bestätigen, werden zusätzliche Messungen an Physikalischen Modellen vorgeschlagen.*

## Abstract

*Minimizing hydraulic losses in the design of piping systems of hydropower plants is an important endeavor in order to achieve an optimum electrical power production. Hydraulic losses in piping systems arise from the friction between fluid and pipe walls, i.e. friction loss, as well as from the shape of manifolds/ fittings, i.e. local loss. Hydraulic losses in turbulent flow are usually estimated by using flow investigation in a physical model based on the similarity of the Reynolds number and the outcome of which is converted to its prototype. A problem can occur when transferring the results of the physical model to the prototype due to the fact that in the physical model it maybe not possible to reach sufficient high flow velocity to get the same Reynolds number as in the prototype. The correlation of the loss coefficient between physical model and prototype can be found by investigating a family model. However, physical family model require expensive investigation, which can be reduced by using an additional numerical model.*

*In this dissertation, based measurement data from previous research about loss coefficients, similarity studies of elbows and tees with different diameter had been conducted. The capability of numerical models to simulate the flow through certain Y-bifurcators with the aim of estimating the loss coefficient and transfer the result from the physical model to the prototype is also investigated.*

*The similarity study of a family model using manufactured elbows and tees shows that for the same Reynolds number, better proportional geometrical dimensions result in more similar loss coefficients.*

*The numerical model of Y-bifurcator showed a good agreement to the measurement from physical model. It also produces reliable results in simulating flow through Y-bifurcator with very high Reynolds numbers. Application of the numerical model to Y-bifurcator with different diameters but similar Reynolds number and similar relative roughness produce a decrease of the loss coefficient with increasing Reynolds number. The loss coefficients are getting close to each other. The model has been successfully applied for estimating the loss coefficient of other fittings in high Reynolds number flows.*

*To strengthen the results of this research, additional measurements with physical model are suggested as future research.*

# Acknowledgments

I am heartily thankful to my supervisor, Ao. Univ.-Prof. Dipl.-Ing. Dr.techn. Roman Klasinc, whose encouragement, guidance and support enabled me in the completion this research work. I owe my deepest gratitude to Prof. Dipl. Ing. Dr. sc. Franci Steinman for his review of this research.

I would like to acknowledge Head of Institute of Hydraulic Engineering and Water Resources Management-Graz University of Technology Univ.-Prof. Dipl.-Ing. Dr.techn. Gerald Zenz for his advise and all of the facility provided for my research. I am grateful to Ass. Prof. Dipl.-Ing. Dr.techn. Helmut Knoblauch, Dr.nat.techn. Josef Schneider and Dipl. –Ing. Dr. Techn. Alfred Hammer for their discussions and lectures on related topics.

I am also thankful to my colleagues Dr. Techn. Wolfgang Dobler, Dipl. Ing. Clements Dorfmann, Dipl. Ing. Simone Zechner, Dipl. Ing. Wolfgang Richter, Mag.rer.nat Cornelia Jobstl, Dipl.-Ing. Gabriele Harp, Dipl.-Ing. Rupert Feldbacher, Dipl.-Ing. Markus Goldgruber for many valuable discussion and friendship. I would like to thank to the Institute staff members Ing. Harald Breinhalter, Christine Vitas, Mag.phill, Amtsdirektor Ing. Friedrich Lazar, Dietmar Schafauer, and Ing. Julio Kuss.

Especially, I would give special thanks to my parents, my wife Ervina Triandari Septianingtyas and our sons Javier Aqila and Keyondre Athaullah for their prayers, love and patience.

I would like to thank to Indonesian friends in Graz, for their assistance and friendship that make our lives more easier and more enjoyable. I offer my regards and blessings to all of those who supported me in any respect during the completion this work.

Finally, I appreciate and convey many thanks to Direktorat Jendral Pendidikan Tinggi (DIKTI), Kementrian Pendidikan Nasional Republik Indonesia and Institut Teknologi Sepuluh Nopember Surabaya for the financial support of my study.

Graz, November 5, 2012

Umboro Lasminto

# Statutory declaration

I declare that I have authored this thesis independently, that I have not used other than the declared sources / resources, and that I have explicitly marked all materials, which have been quoted either literally or by content from the used sources.

November 5, 2012

-----

Date

-----

Signature

# Table of Contents

Zusammenfassung .....	iii
Abstract.....	iv
Acknowledgments .....	v
Statutory declaration.....	vi
1 Introduction .....	1
1.1 Background .....	1
1.2 Objectives .....	2
1.3 Dissertation layout .....	2
2 State of the Art Research .....	5
2.1 Physical model .....	5
2.1.1 Turbulent flow .....	5
2.1.2 Model law .....	5
2.1.3 Hydraulic losses .....	7
2.2 Numerical model of turbulent flow.....	10
2.2.1 Governing equations .....	10
2.2.2 Basic of numerical method .....	14
2.2.3 Numerical model tool .....	15
2.3 Measurement techniques.....	24
2.3.1 Pressure measurement.....	24
2.3.2 Flow measurement .....	27
3 Review of Past Investigation on Loss Coefficient of Manifolds .....	35
3.1. Study on loss coefficient of Alberschwende bifurcator .....	35
3.1.1. Physical model of Alberschwende bifurcator .....	35
3.1.2 Numerical model of bifurcator Alberschwende.....	41
3.2 Similarity study on loss coefficient of fittings .....	43
3.2.1 Steel pipe fittings diameter of 6, 8 and 10 inches .....	43
3.2.2 Pressure loss data for large pipe elbows and tees 12, 16, 20 and 24 inches .....	49
3.2.3 Pressure loss of PVC plastic pipe fittings .....	55
3.3 Conclusion .....	58
4 Study on Local Loss Coefficient of a Y-Bifurcator .....	59
4.1 Study on loss coefficient of a Y-bifurcator using a physical model .....	59

4.1.1	Past experiment on loss coefficient of bifurcator .....	59
4.1.2	Construction of a physical model .....	61
4.1.3	Data acquisition .....	62
4.1.4	Data analysis .....	63
4.1.5	The differential pressure head of the physical model .....	65
4.1.6	Loss coefficient of a physical model .....	66
4.2	Numerical Simulation of a Physical Model of Y- Bifurcator .....	76
4.2.1	General setup of the numerical model .....	77
4.2.2	Mesh size and boundary layer.....	77
4.2.3	Comparison of velocity profile .....	82
4.2.4	Comparison of differential pressure head .....	84
4.2.5	Loss coefficient of Y-bifurcator.....	88
4.2.6	Numerical Simulation of high Reynolds number inflow .....	94
4.2.7	Kinetic energy correction factor .....	99
4.3	Numerical Simulation of Pirris Y-Bifurcator with Different Scale Factor.....	105
4.3.1	Numerical model setup .....	105
4.3.2	Inflow of the models .....	106
4.3.3	Comparison of differential pressure head among models with different scale .....	107
4.3.4	Comparison of loss coefficient among models with different scale .....	109
4.3.5	Comparison of velocity among different scale of numerical models .....	110
4.3.6	Loss coefficient as function of velocity and pipe diameter .....	113
4.3.7	Influence of roughness .....	115
4.4	Conclusion .....	117
5	Application of numerical modeling in the investigation of hydraulic problems	119
5.1	Numerical model of long elbow with different scale.....	119
5.1.1	Introduction.....	119
5.1.2	Numerical model of flow through elbows .....	120
5.2	Hydraulic problems in the development of pumped storage hydro plant.....	125
5.2.1	PSP Kops II.....	126
5.2.2	PSP Limberg II .....	128
5.2.3	PSP Risseck II.....	129
5.2.4	PSP Atdorf-Schluchsewerk.....	130

5.3 Synthesis of the thesis result .....	131
5.4 Conclusion .....	132
6 Summary .....	133
References .....	137
List of tables .....	142
List of figures.....	143
List of symbols and abbreviations .....	150
Appendixes .....	153

This page intentionally left blank

# 1 Introduction

## 1.1 Background

Electrical energy is an important energy source in human life today. Continually, energy demand increases along with the increasing number of population and industry. This demand could be partly accomplished by generating environmentally friendly hydropower. Principally, hydropower can produce energy if water is able to rotate turbine. The amount of energy generated by hydropower depends on the flow, net head, and turbine efficiency. The net head is calculated from the total head subtracted by all losses in the system. The losses in the pipe system occur due to the friction between water and pipe wall and additional loss caused by fittings or manifolds for the changing of pipe in direction (bend), changing in dimensions (reducer or expansion), branching, mixing, entries or exits. The additional loss is called by minor or local losses. The shape, curvature or recirculation of a fitting or manifold induce secondary flows and generate additional energy dissipation.

Estimating hydraulic losses is usually done by investigating a scale model (physical model). The scale model is built based on similarity with the prototype. Besides, geometric similarity, Reynolds similarity must be fulfilled because the flow is turbulence. Using the same viscosity of water and Reynolds similarity between prototype and physical model, velocity of physical model is equal to the scale of model multiplied by the prototype velocity. In other words, flow velocity of the physical model is higher than that of the prototype. Differential pressure in the physical model is also higher than in the prototype. Some problems arise in the development of physical model with high velocity, such as leakage caused by high pressure and occurrence of cavitation. Simulation flow for high Reynolds number is very difficult to be realized in the laboratory. The investigation in the physical model can only be done until certain Reynolds number. It solely depends on the capabilities of existing resources in the laboratory. Some engineers predict that the energy losses in the range of prototype Reynolds numbers can be completed by extrapolating the results of the physical model. However, previous studies show that the extrapolation method is not universally applicable to various shape of manifold. The result of extrapolation also depends on trend and number of data used. Therefore, studies on the relationship between the prototype and the physical model particularly on the transferring of model results to prototype are needed.

Study on hydraulic behavior of two or more models with similar in geometry but different in size (family model) aims at understanding the correlation between the prototype and the physical model. By conducting an investigation on a family model, there is an expectation for an answer whether between a prototype and the physical

model with Reynolds similarity have a similarity in loss coefficient or not. However, investigation of physical family model is expensive. Therefore, along with the development of computer technology and programming, the numerical model can be used as a tool in investigation of energy loss of hydraulic structure with different scale. By knowing the relationship among models with different scale, good understanding in transferring the result of physical model to the prototype is expected. The numerical model is also expected to be a bridge between prototype and the physical model.

## 1.2 Objectives

The objective of this study is to find out the appropriate method for transferring local loss coefficient of manifolds resulted by physical model to the loss coefficient of prototype. More specifically, the objectives of this study are to:

- Estimate loss coefficient of manifolds using physical model investigation.
- Develop a 3-dimension numerical model and further understanding of numerical model in representing phenomena that are observed in the physical model. Examine the numerical model and compare the performance with the physical model.
- Study on correlation of flow parameters among several numerical models with different scale factor (family model) to understand the effect of scale. This study is expected to be a reference in transferring the result of a physical model to the prototype.
- Apply the method in determining loss coefficient to other manifolds and explore the possibility of using numerical model to solve problem in hydraulic structures.

## 1.3 Dissertation layout

### Chapter 1

The background, problem statement, objectives, and scope of the study are presented.

### Chapter 2

The state of the art of the research that consists of theoretical of physical and numerical modeling of turbulence flow and flow measurement method are described.

### Chapter 3

Past studies about loss coefficient is discussed in this chapter. The studies consist of investigation on loss coefficient of a Y-bifurcator using a physical model and numerical model and similarity study on the loss coefficient of fittings with different diameter.

**Chapter 4**

This chapter presents the result of investigation on flow through a Y-bifurcator using a physical model and numerical model. The physical model was simulated for several discharge inflow and several scenarios of outflow in the left and right branches. All cases investigated in the physical model were simulated in the numerical model. The results of numerical model were compared with the result of physical model. Numerical model is used to simulate large discharge to extend the discharge of physical model. The results of numerical simulation were compared to the result of extrapolation of physical model. Comparison of differential pressure head, differential energy head, velocity profile and loss coefficient resulted by several numerical models were also presented. Kinetic energy correction factor was calculated using the result of numerical model and it involved in the energy equation for calculation of loss coefficient. The loss coefficients calculated by involving kinetic energy correction factor were compared with the loss coefficient calculated with an assumption that the kinetic energy correction factor is equal to one. Numerical model was used to simulate flow through a Y-bifurcator with different scale factor. Differential pressures head, velocity and loss coefficient resulted by four different physical models were compared. The influence of relative roughness used in the numerical model to the result of loss coefficient was also studied.

**Chapter 5**

This chapter presents application of numerical modeling to estimate loss coefficient of long elbows with different diameter. Possibilities of numerical model to investigate some hydraulic problems in development of pumped storage hydro plant are also presented.

**Chapter 6**

The conclusions of individual chapter are summarized in this chapter.

This page intentionally left blank

## 2 State of the Art Research

### 2.1 Physical model

#### 2.1.1 Turbulent flow

Laminar flow is the flow where fluid moves in a pattern of layers. There is no mixing between the flows except for the diffusion of molecules from a layer to another. Contrary to the laminar flow, turbulent flow is not patterned by layers or parallel. In turbulent flow, the movements of fluid particles are highly uncertain because of mixing and rotation of particle between layers causing the exchange of momentum between parts of fluid with another. Fluid flow in the pipe will be a laminar flow at low velocity and change into turbulent flow with increasing velocity in certain viscosity. The dimensionless Reynolds number is used to distinguish between laminar flow and turbulent flow. The Reynolds number is ratio between inertia force and viscos force [1]. Test results showed that the fluid flow in the pipe is laminar when the Reynolds number is less than 2000 and turbulent when the Reynolds number higher than 4000. For conditions where the Reynolds number between 2000 and 4000, the fluid flow is transitional. The equation of Reynolds number (Re) for pipe flow is [2]:

$$\text{Re} = \frac{u \cdot D}{\vartheta} \quad (1)$$

where D is the pipe diameter (m), u is the average velocity (m/s), and  $\vartheta$  is the kinematic viscosity ( $\text{m}^2/\text{s}$ ).

#### 2.1.2 Model law

A hydraulic model should follow the principle of scaling, means rebuilding a problem in the nature (prototype) into a model in a smaller so that the hydraulic phenomena in the prototype and in the model are similar. There are three similarities, namely geometric, kinematic, and dynamic similarities. Geometric similarity occurs when prototype and model have the same shapes but different sizes. It means that the ratio of all length sizes between prototype and model are the same. There are two kinds of geometric similarity, i.e. distorted geometric similarity and undistorted geometric similarity. Distorted geometric similarity is a model where the length scales on horizontal and vertical direction are different. Conversely, undistorted geometric similarity is a model with the same length scale on horizontal and vertical directions. Kinematic similarity is fulfilled when prototype and model have a geometric similarity and have the same scale of velocity and acceleration. Dynamic similarity is fulfilled if there are geometric and kinematic similarities and the same ratio of forces acting between a prototype and the model. The forces are inertia, pressure, gravity, friction, elastic, and surface tension forces. The ratio of inertia forces to viscous forces

is essential because it is the dominant factor on pressurized pipe flow. Geometric scaling ratio between prototype and model:

$$\frac{L_p}{L_m} = \frac{D_p}{D_m} = \eta \quad (2)$$

where  $\eta$  is the length scale,  $L_p$  is the length of prototype,  $L_m$  is the length of model,  $D_p$  is the pipe diameter of prototype, and  $D_m$  is the pipe diameter of model. Using the equation (1), similarity of the Reynolds number between model and prototype is:

$$\frac{u_m D_m}{\nu} = \frac{u_p D_p}{\nu}$$

If the kinematic viscosity between prototype and model are the same, then the ratio of velocity between model and prototype is:

$$\frac{u_m}{u_p} = \frac{D_p}{D_m} = \eta \quad (3)$$

If velocity of the model is equal to scale of length multiplied by velocity of prototype then discharge ratio between model and prototype is:

$$\frac{Q_m}{Q_p} = \frac{0.25\pi D_m^2 u_m}{0.25\pi D_p^2 u_p} = \left(\frac{D_m}{D_p}\right)^2 \frac{u_m}{u_p}$$

$$\frac{Q_m}{Q_p} = \left(\frac{1}{\eta}\right)^2 \eta = \frac{1}{\eta} \quad (4)$$

Reynolds similarity between model and prototype is used when the inertia and friction forces plays an important role in the flow. However, if the forces that play an important role in the flow are inertia and gravitational forces, the Froude similarity should be used. Froude similarity use equation of Froude number. The Froude number equation is:

$$F_r = \frac{u}{\sqrt{gD}} \quad (5)$$

Using the equation (5), the Froude similarity between a model and the prototype:

$$\frac{u_m}{\sqrt{g \cdot D_m}} = \frac{u_p}{\sqrt{g \cdot D_p}}$$

The ratio of velocities between prototype and physical model is:

$$\frac{u_p}{u_m} = \frac{\sqrt{g \cdot D_p}}{\sqrt{g \cdot D_m}} = \sqrt{\frac{D_p}{D_m}}$$

$$\frac{u_p}{u_m} = \eta^{0.5} \quad (6)$$

The ratio of discharge between prototype and physical model is:

$$\frac{Q_p}{Q_m} = \frac{A_p \cdot u_p}{A_m \cdot u_m} = \eta^2 \eta^{0.5} = \eta^{2.5} \quad (7)$$

### 2.1.3 Hydraulic losses

Figure 1 shows a prismatic fluid particle with mass of  $dm = \rho \cdot dA \cdot ds$ , that moves along flow line in S direction. This figure is used to derive the energy equation.

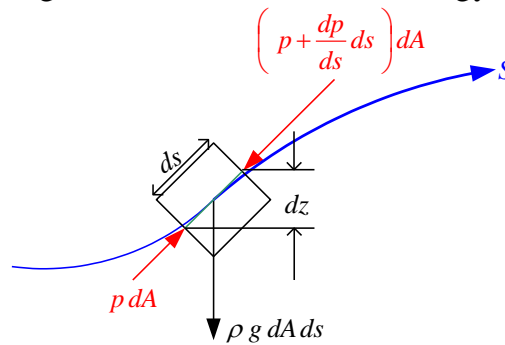


Figure 1: Components of the forces action on a fluid particle in the flow direction

Derivation of fluid motion equation can be simplified by taking an assumption that the fluid is not viscous, so that the action force is only the gravity. In Figure 1 also can be seen that the compressive forces act in positive S direction at the upstream and in negative S direction at the downstream faces. The forces action perpendicular to the S is not taken into account in the derivation of this equation.

The second Newton's law:

$$\sum F_s = dm a_s \quad (8)$$

Summary of force in S direction is:

$$p dA - \left( p + \frac{\partial p}{\partial s} ds \right) dA - \rho g dA ds \cos \theta = dm a_s \quad (9)$$

If  $dm$  is substituted by  $\rho dA ds$ , the equation (9) becomes:

$$p dA - \left( p + \frac{\partial p}{\partial s} ds \right) dA - \rho g dA ds \cos \theta = \rho dA ds a_s \quad (10)$$

Rearranging the equation (10) becomes:

$$-\frac{\partial p}{\partial s} ds dA - \rho g ds dA \cos \theta = \rho dA ds a_s \quad (11)$$

Equation (11) is divided by  $\rho dA ds$  becomes:

$$\frac{1}{\rho} \frac{\partial p}{\partial s} + g \cos \theta + a_s = 0 \quad (12)$$

If  $dz$  is different high of accent between downstream and upstream sections then:

$$\frac{dz}{ds} = \cos \theta = \frac{\partial Z}{\partial s} \quad (13)$$

The acceleration is derivative of velocity in time:

$$a_s = \frac{du}{dt} \quad (14)$$

Velocity is function of distance and time, =  $f(s, t)$  :

$$du = \frac{\partial u}{\partial s} ds + \frac{\partial u}{\partial t} dt \quad (15)$$

Equation (15) is divided by  $dt$ :

$$\frac{du}{dt} = \frac{\partial u}{\partial s} \frac{ds}{dt} + \frac{\partial u}{\partial t} \frac{dt}{dt} \quad (16)$$

$$\frac{du}{dt} = u \frac{\partial u}{\partial s} + \frac{\partial u}{\partial t} \quad (17)$$

Substituting equation 13, 14 and 17 into equation (12) will be obtained:

$$\frac{1}{\rho} \frac{\partial p}{\partial s} + g \frac{\partial Z}{\partial s} + u \frac{\partial u}{\partial s} + \frac{\partial u}{\partial t} = 0 \quad (18)$$

For steady flow where  $\frac{\partial u}{\partial t} = 0$  and because of flow parameter only change in S

direction, the equation can be written as:

$$\frac{dp}{\rho} + g dZ + u du = 0 \quad (19)$$

Equation (19) is known as Euler equation. By integrating the Euler equation, the Bernoulli equation is found as follow:

$$\frac{p}{\rho} + g Z + \frac{u^2}{2} = \text{constant} \quad (20)$$

Dividing equation (20) by gravity acceleration,  $g$  :

$$Z + \frac{p}{\rho g} + \frac{u^2}{2g} = H = \text{constant} \quad (21)$$

The first term in left side is position head (m), the second term is pressure head (m) and third term is velocity head (m). In right side, H is the energy head (m). Energy loss is also known as a pressure drop. Energy equation in one dimension can be obtained from Bernoulli's equation by taking into account energy loss. The pressure of flow in the pipe decreases if there is a component in the pipe that can change flow cross-section or height between the inlet and outlet. In addition, decrease in energy can also be caused by friction between fluid and pipe wall and heat transfer to and from surroundings. The energy loss of flow in the pipe caused by shape of component and friction can be explained using energy conservation that described in Figure 2. Energy conservation equation in one dimension between cross section 1 and 3 in horizontal condition can be written as:

$$\frac{u_{12}^2}{2g} + \frac{p_{12}}{\rho \cdot g} = \frac{u_{23}^2}{2g} + \frac{p_{23}}{\rho \cdot g} + \Delta h_{13} \quad (22)$$

Energy loss between section 1 and 3 can be calculated by rearranging equation (22) become:

$$\Delta h_{13} = \left( \frac{p_{12}}{\rho \cdot g} - \frac{p_{23}}{\rho \cdot g} \right) + \left( \frac{u_{12}^2}{2g} - \frac{u_{23}^2}{2g} \right) \quad (23)$$

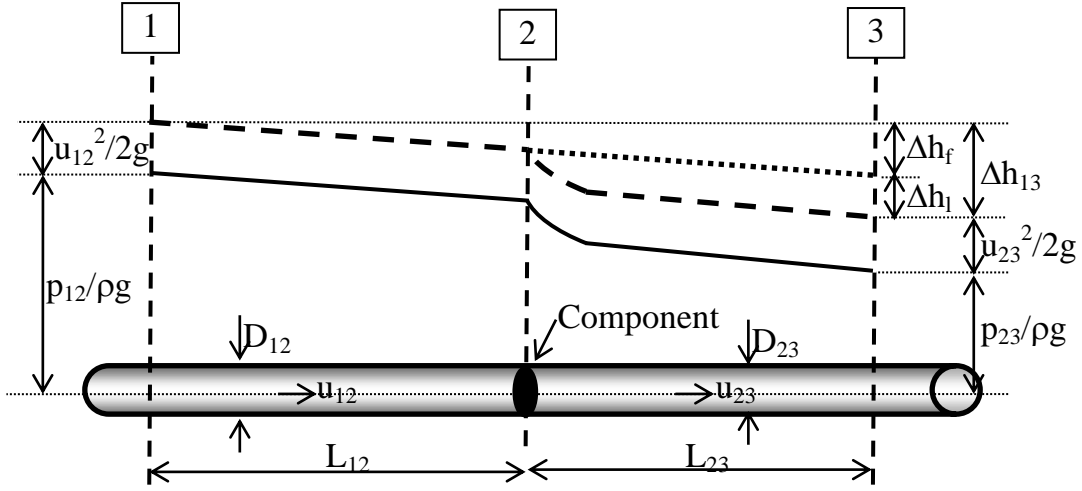


Figure 2: Energy Conservation

Total energy loss between section 1 to 3, which is caused by shape of component (local loss) and friction loss in the pipe section 1-2 and section 2-3, is written in equation:

$$\Delta h_{13} = \Delta h_l + (\Delta h_{f12} + \Delta h_{f23}) \quad (24)$$

Both local and friction losses can be defined as a kinetic energy in the inflow section multiplied by a coefficient, so that local loss is  $\Delta h_l = \zeta u^2/2g$  and friction loss is  $\Delta h_f = (\lambda L/D) u^2/2g$ . Substituting the local loss and friction loss equations to equation (24) becomes:

$$\Delta h_{13} = \zeta \frac{u_{12}^2}{2g} + \left( \lambda_{12} \frac{L_{12}}{D_{12}} \frac{u_{12}^2}{2g} + \lambda_{23} \frac{L_{23}}{D_{23}} \frac{u_{23}^2}{2g} \right) \quad (25)$$

The equation of coefficient of local loss ( $\zeta$ ) is found by arranging equation (25):

$$\zeta = \left( \Delta h_{13} - \left( \lambda_{12} \frac{L_{12}}{D_{12}} \frac{u_{12}^2}{2g} + \lambda_{23} \frac{L_{23}}{D_{23}} \frac{u_{23}^2}{2g} \right) \right) \frac{2g}{u_{12}^2} \quad (26)$$

Substituting equation (23) into equation (26) will result in equation local loss coefficient:

$$\zeta = \left( \left( \frac{p_{12}}{\rho g} - \frac{p_{23}}{\rho g} \right) + \left( \frac{u_{12}^2}{2g} - \frac{u_{23}^2}{2g} \right) \right) - \left( \lambda_{12} \frac{L_{12}}{D_{12}} \frac{u_{12}^2}{2g} + \lambda_{23} \frac{L_{23}}{D_{23}} \frac{u_{23}^2}{2g} \right) \frac{2g}{u_{12}^2} \quad (27)$$

where  $L$  is the length of pipe section (m),  $D$  is the hydraulic diameter (m),  $u$  is the flow velocity (m/s), and  $g$  is the acceleration of gravity ( $m/s^2$ ),  $\lambda$  is the friction factor and 1, 2 and 3 are location indexes. Equation (27) can also be applied for reverse flow from section 3 to section 1 where section 3 is defined as inflow and section 1 as outflow. Colebrook and White [3] proposed an equation to calculate friction factor in transition regime that use variables of Reynolds number and relative roughness  $k_s/D$ . General equation of friction factor ( $\lambda$ ) is:

$$\frac{1}{\sqrt{\lambda}} = -2.0 \cdot \log \left( \frac{2.51}{Re \cdot \sqrt{\lambda}} + \frac{k_s/D}{3.71} \right) \quad (28)$$

Friction factor of a flow depends on flow velocity, pipe diameter, fluid viscosity, and roughness of the pipe ( $k_s$ ). Moody [4] develops a diagram for presenting commercial pipe friction factor based on Colebrook-White equation (Figure 3). After Moody, several researchers like Wood [5], Swamee and Jain [6], Churchill [7], Chen [8], Round [9], Barr [10], Zigrang and Sylvester [11], Haaland [12], Manadilli [13] and Romeo et al [14] proposed empirical equations for calculating the friction factor.

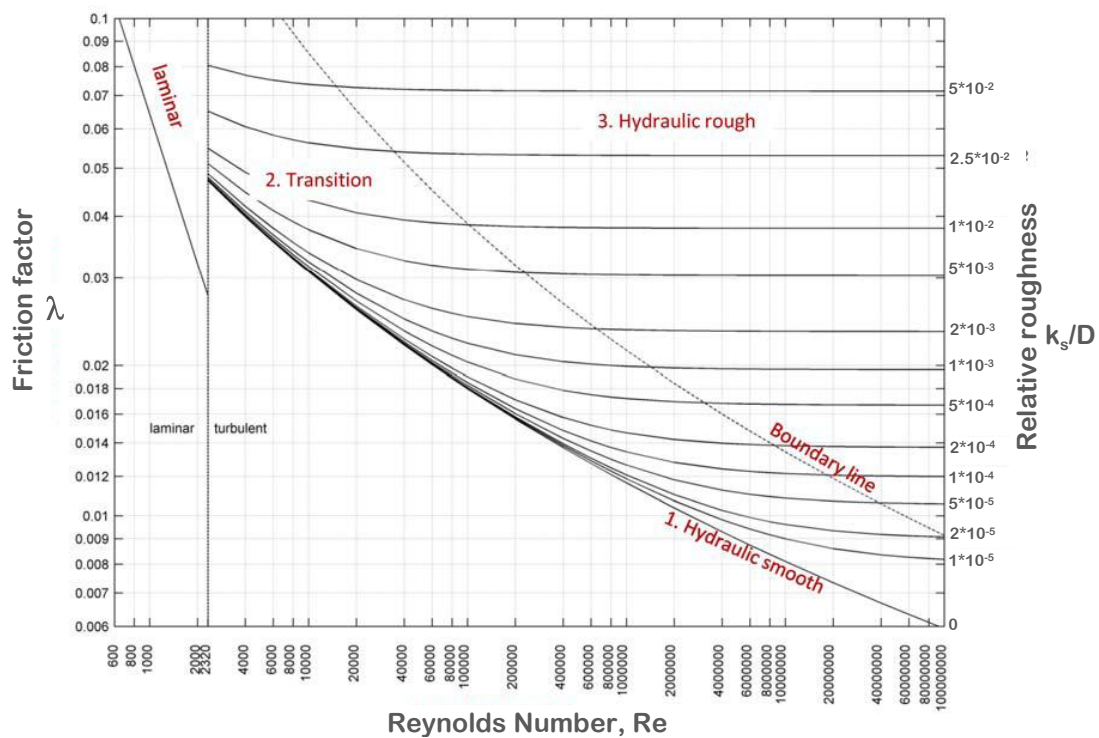


Figure 3: Moody diagram

## 2.2 Numerical model of turbulent flow

### 2.2.1 Governing equations

Navier-Stokes equations are differential equations that describe motion of the fluid. The equations consist of mass and momentum equations. Mass conservation in 2-

dimensions can be derived using mass balance that is described in Figure 4 as followed:

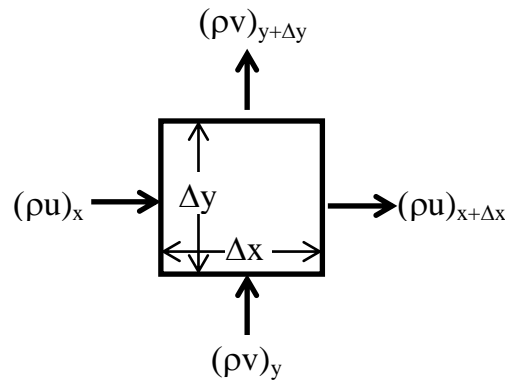


Figure 4: Mass balance

The principle of mass conservation can be expressed as the rate of mass accumulation within control volume. This is equal to the rate mass of flow into control volume minus the rate of mass flow out from control volume:

$$\frac{\partial(\rho\Delta x\Delta y)}{\partial t} = (\rho u)_x \Delta y + (\rho v)_y \Delta x - (\rho u)_{x+\Delta x} \Delta y - (\rho v)_{y+\Delta y} \Delta x \quad (29)$$

Equation (29) is divided by  $\Delta x \Delta y$ :

$$\frac{\partial \rho}{\partial t} = \frac{(\rho u)_x - (\rho u)_{x+\Delta x}}{\Delta x} + \frac{(\rho v)_y - (\rho v)_{y+\Delta y}}{\Delta y} \quad (30)$$

If the control volume is very small then the limit of  $\Delta x$  and  $\Delta y$  is close to zero. Using the Taylor series expansion of

$$(\rho u)_{x+\Delta x} \rightarrow (\rho u)_x + \Delta x \frac{\partial(\rho u)}{\partial x} \quad (31)$$

$$(\rho v)_{y+\Delta y} \rightarrow (\rho v)_y + \Delta y \frac{\partial(\rho v)}{\partial y} \quad (32)$$

and substituting the Taylor series expansion into equation (30) will be obtained:

$$\frac{\partial \rho}{\partial t} = - \frac{\partial(\rho u)}{\partial x} - \frac{\partial(\rho v)}{\partial y} \quad (33)$$

Rearranging equation (33) becomes:

$$\frac{\partial \rho}{\partial t} + \frac{\partial(\rho u)}{\partial x} + \frac{\partial(\rho v)}{\partial y} = 0 \quad (34)$$

In three-dimension flow, equation (34) can be extended becomes:

$$\frac{\partial \rho}{\partial t} + \frac{\partial(\rho u)}{\partial x} + \frac{\partial(\rho v)}{\partial y} + \frac{\partial(\rho w)}{\partial z} = 0 \quad (35)$$

where  $u, v, w$  is the velocity component in  $x, y$  and  $z$  direction respectively.

Momentum equation can be derived using momentum balance as described in Figure 5.

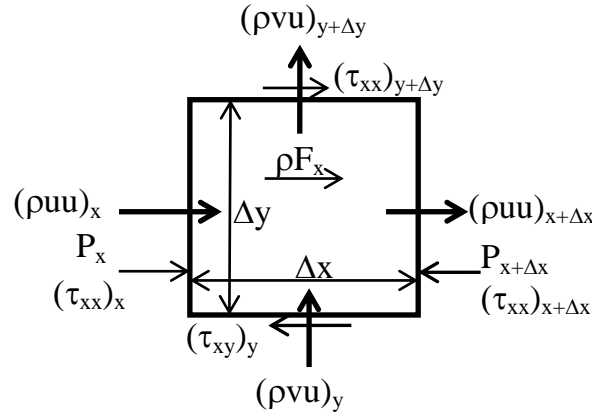


Figure 5: Momentum balance

Accumulation of momentum within control volume is equal to the difference of momentum flow rate between in and out of a control volume, plus force acting on control volume faces and body forces within control volume. This can be expressed in following equation:

$$\Delta x \Delta y \left[ \frac{\partial(\rho u)}{\partial t} \right] = [\Delta y(\rho u u)_x + \Delta x(\rho v u)_y] - [\Delta y(\rho u u)_{x+\Delta x} + \Delta x(\rho v u)_{y+\Delta y}] + \left[ ((P_x + \tau_{xx})_x - (P_x + \tau_{xx})_{x+\Delta x}) \Delta y + ((\tau_{xy})_y - (\tau_{xy})_{y+\Delta y}) \Delta x \right] + [\rho F_x \Delta x \Delta y] \quad (36)$$

Rearranging equation (36) becomes:

$$\Delta x \Delta y \left[ \frac{\partial(\rho u)}{\partial t} \right] = [(\rho u u)_x - (\rho u u)_{x+\Delta x}] \Delta y + [(\rho v u)_y - (\rho v u)_{y+\Delta y}] \Delta x + \left[ ((P_x + \tau_{xx})_x - (P_x + \tau_{xx})_{x+\Delta x}) \Delta y + ((\tau_{xy})_y - (\tau_{xy})_{y+\Delta y}) \Delta x \right] + [\rho F_x \Delta x \Delta y] \quad (37)$$

If equation (37) is divided by  $\Delta x \Delta y$  then will be obtained an equation:

$$\frac{\partial(\rho u)}{\partial t} = \frac{(\rho u u)_x - (\rho u u)_{x+\Delta x}}{\Delta x} + \frac{(\rho v u)_y - (\rho v u)_{y+\Delta y}}{\Delta y} + \frac{P_x - P_{x+\Delta x}}{\Delta x} + \frac{(\tau_{xx})_x - (\tau_{xx})_{x+\Delta x}}{\Delta x} + \frac{(\tau_{xy})_y - (\tau_{xy})_{y+\Delta y}}{\Delta y} + \rho F_x \quad (38)$$

For  $\Delta x, \Delta y \rightarrow 0$ , any quantity of:

$$\phi_{x+\Delta x} \rightarrow \phi_x + \Delta x \frac{\partial \phi}{\partial x} \text{ and } \phi_{y+\Delta y} \rightarrow \phi_y + \Delta y \frac{\partial \phi}{\partial y}$$

Applying to equation (38), equation of momentum balance in x direction:

$$\frac{\partial(\rho u)}{\partial t} = -\frac{\partial(\rho u u)}{\partial x} - \frac{\partial(\rho v u)}{\partial y} - \frac{\partial P}{\partial x} - \frac{\partial \tau_{xx}}{\partial x} - \frac{\partial \tau_{xy}}{\partial y} + \rho F_x \quad (39)$$

Rearranging equation (39) becomes:

$$\frac{\partial(\rho u)}{\partial t} + \frac{\partial(\rho u^2)}{\partial x} + \frac{\partial(\rho v u)}{\partial y} = -\frac{\partial P}{\partial x} - \frac{\partial \tau_{xx}}{\partial x} - \frac{\partial \tau_{xy}}{\partial y} + \rho F_x \quad (40)$$

Similarly, equation of momentum balance in y direction can be written:

$$\frac{\partial(\rho v)}{\partial t} + \frac{\partial(\rho uv)}{\partial x} + \frac{\partial(\rho v^2)}{\partial y} = -\frac{\partial P}{\partial y} - \frac{\partial \tau_{xy}}{\partial x} - \frac{\partial \tau_{yy}}{\partial y} + \rho F_y \quad (41)$$

For simple shear flow, using the Stokes law's state:

$$\tau_{xy} = -\mu \frac{\partial u}{\partial y} \quad (42)$$

Shear in 2-dimensions can be written as:

$$\tau_{xx} = -2\mu \frac{\partial u}{\partial x} \quad (43)$$

$$\tau_{yy} = -2\mu \frac{\partial v}{\partial y} \quad (44)$$

$$\tau_{xy} = -\mu \left( \frac{\partial u}{\partial y} + \frac{\partial v}{\partial x} \right) \quad (45)$$

Substitute equations (43) to (45) into equations (40) and (41) are obtained:

$$\frac{\partial(\rho u)}{\partial t} + \frac{\partial(\rho u^2)}{\partial x} + \frac{\partial(\rho uv)}{\partial y} = -\frac{\partial P}{\partial x} + \frac{\partial}{\partial x} \left[ 2\mu \frac{\partial u}{\partial x} \right] + \frac{\partial}{\partial y} \left[ \mu \left( \frac{\partial u}{\partial y} + \frac{\partial v}{\partial x} \right) \right] + \rho F_x \quad (46)$$

$$\frac{\partial(\rho v)}{\partial t} + \frac{\partial(\rho uv)}{\partial x} + \frac{\partial(\rho v^2)}{\partial y} = -\frac{\partial P}{\partial y} + \frac{\partial}{\partial x} \left[ \mu \left( \frac{\partial v}{\partial x} + \frac{\partial u}{\partial y} \right) \right] + \frac{\partial}{\partial y} \left[ 2\mu \frac{\partial v}{\partial y} \right] + \rho F_y \quad (47)$$

Equations (46) and (47) are Navier-Stokes equations of momentum in 2-dimension in x and y direction. Meanwhile, Navier-Stokes equations in 3-dimensions can be written as continuity and momentum equations as follow:

The continuity equation:

$$\frac{\partial \rho}{\partial t} + \frac{\partial(\rho u)}{\partial x} + \frac{\partial(\rho v)}{\partial y} + \frac{\partial(\rho w)}{\partial z} = 0 \quad (48)$$

The momentum equation in x direction:

$$\frac{\partial(\rho u)}{\partial t} + \frac{\partial(\rho u^2)}{\partial x} + \frac{\partial(\rho uv)}{\partial y} + \frac{\partial(\rho wu)}{\partial z} = -\frac{\partial P}{\partial x} + 2 \frac{\partial}{\partial x} \left[ \mu \frac{\partial u}{\partial x} \right] + \frac{\partial}{\partial y} \left[ \mu \left( \frac{\partial u}{\partial y} + \frac{\partial v}{\partial x} \right) \right] + \frac{\partial}{\partial z} \left[ \mu \left( \frac{\partial u}{\partial z} + \frac{\partial w}{\partial x} \right) \right] + \rho F_x \quad (49)$$

The momentum equation in y direction:

$$\frac{\partial(\rho v)}{\partial t} + \frac{\partial(\rho uv)}{\partial x} + \frac{\partial(\rho v^2)}{\partial y} + \frac{\partial(\rho vw)}{\partial z} = -\frac{\partial P}{\partial y} + \frac{\partial}{\partial x} \left[ \mu \left( \frac{\partial v}{\partial x} + \frac{\partial u}{\partial y} \right) \right] + 2 \frac{\partial}{\partial y} \left[ \mu \frac{\partial v}{\partial y} \right] + \frac{\partial}{\partial z} \left[ \mu \left( \frac{\partial v}{\partial z} + \frac{\partial w}{\partial y} \right) \right] + \rho F_y \quad (50)$$

The momentum equation in z direction:

$$\frac{\partial(\rho w)}{\partial t} + \frac{\partial(\rho uw)}{\partial x} + \frac{\partial(\rho vw)}{\partial y} + \frac{\partial(\rho w^2)}{\partial z} = -\frac{\partial P}{\partial z} + \frac{\partial}{\partial x} \left[ \mu \left( \frac{\partial w}{\partial x} + \frac{\partial u}{\partial z} \right) \right] + \frac{\partial}{\partial y} \left[ \mu \left( \frac{\partial w}{\partial y} + \frac{\partial v}{\partial z} \right) \right] + 2 \frac{\partial}{\partial z} \left[ \mu \frac{\partial w}{\partial z} \right] + \rho F_z \quad (51)$$

where u, v, and w are the velocity component in x, y and z directions; x, y and z are the coordinate directions;  $\mu$  is the kinematic viscosity;  $\rho$  is the density; p is the pressure; t is the time; and F is the force. To simulate turbulent flow, Navier-Stokes equations can be solved only by converting differential equation into numerical equation and then performed calculation using a computer program.

## 2.2.2 Basic of numerical method

Turbulent flow is a three dimension, time-dependent, eddying motion with many scales and causing continuous mixing of fluid. Navier-Stokes equations are derived based on equilibrium of force on a small volume of water in laminar flow. The equations can also be written in form [15]:

$$\frac{\partial U_i}{\partial t} + U_j \frac{\partial U_i}{\partial x_j} = \frac{1}{\rho} \frac{\partial}{\partial x_j} \left( -P \delta_{ij} + \rho \vartheta_t \left( \frac{\partial U_i}{\partial x_j} + \frac{\partial U_j}{\partial x_i} \right) \right) \quad (52)$$

Reynolds average is used in turbulent flow and the equation is written as:

$$\frac{\partial U_i}{\partial t} + U_j \frac{\partial U_i}{\partial x_j} = \frac{1}{\rho} \frac{\partial}{\partial x_j} \left( -P \delta_{ij} + \rho \overline{u_i u_j} \right) \quad (53)$$

$\delta_{ij}$  is the Kronecker delta (if  $i=j$ ,  $\delta_{ij}$  is equal to 1 and otherwise  $\delta_{ij}$  is equal to 0). Reynolds stress term can be solved using Bousinesq approximation:

$$\rho \overline{u_i u_j} = \rho \vartheta_t \left( \frac{\partial U_i}{\partial x_j} + \frac{\partial U_j}{\partial x_i} \right) - \frac{2}{3} \rho k \delta_{ij} \quad (54)$$

where  $k$  is the turbulence kinetic energy. The last equation is found by substituting equation (54) into equation (53):

$$\frac{\partial U_i}{\partial t} + U_j \frac{\partial U_i}{\partial x_j} = \frac{1}{\rho} \frac{\partial}{\partial x_j} \left[ - \left( P + \frac{2}{3} k \right) \delta_{ij} + \vartheta_t \frac{\partial U_i}{\partial x_j} + \vartheta_t \frac{\partial U_j}{\partial x_i} \right] \quad (55)$$

The first term in the left side is transient term and the second term is convective term. In the right side, the first term is pressure/kinetic term, the second term is diffusive term, and the last term is stress term. In control volume approach, the pressure term can be solved using Semi Implicit Method for Pressure-Linked Equation (SIMPLE). Other solvers are the improvement of SIMPLE solver such as SIMPLEC (SIMPLE Consistent), PISO (Pressure Implicit with Splitting of Operators) and Couple. Differential equations of fluid motion that have been converted to numerical equations are written using a programming language so that they become user-friendly software of Computational Fluid Dynamic (CFD).

Simulation process using CFD in general can be divided into three steps, namely pre-processing, solving, and post-processing. Pre-processing step consists of building the model geometry, meshing, determining fluid properties, determining boundaries condition, and providing an initial condition. In the solving step, CFD software will perform calculations using equations that have been selected and boundaries condition set in the pre-processing step. Post-processing step is interpretation of CFD result that is visualized in a form of report data, images, graphics, or animations.

## 2.2.3 Numerical model tool

CFD software is a very important tool that is widely used to predict flow behavior and hydraulic equipment in the world of design and engineering industry. Mainly, CFD software is developed by using Navier-Stokes equations. These equations describe pressure and velocity fields in water. The equations are constructed not only for laminar flow but also can be used for turbulent flow using Reynolds averaging and turbulent models. For  $\nabla \cdot \mathbf{v} = 0$  and viscosity is constant (incompressible flow), the Navier-Stokes equation is written in the vector form as:

$$\rho \left( \frac{\partial \mathbf{v}}{\partial t} + \mathbf{v} \cdot \nabla \mathbf{v} \right) = -\nabla p + \mu \nabla^2 \mathbf{v} + F \quad (56)$$

where  $\mu$  is the viscosity,  $\nabla$  is the del operator and  $F$  represent other forces such as gravity or centrifugal forces. First and second terms in the left hand side are unsteady acceleration and convective acceleration terms. While in the right hand side are pressure gradient, viscosity and other force terms respectively. With increasing computing speed and intensive development capability of numerical methods, the optimization of hydraulic computation becomes possible at this time. Some researchers also revealed about using CFD as a useful device to obtain optimal solution in the hydraulic field. Usage of CFD gives advantages in cost and time saving especially in machinery design optimization.

Currently, some CFD software developed for both commercial and open sources. One of the commercial software that is widely used to simulate turbulent flow is FLUENT. FLUENT is a CFD developed using finite volume method and the code is written using C language. This software has three formulation solvers, namely segregated, coupled implicit and coupled explicit. Each solver mentioned above can produce accurate solution for certain cases. Segregated and coupled solvers have different ways in solving equations that are used. The segregated solver will solve equation separately while the coupled solver will solve all equations simultaneously. Some cases that can be solved by using a segregated solver are cavitation, porous media, multiphase, combustion (premixed and non-premixed), Probability Density Function (PDF) transport, formation of soot and NO<sub>x</sub>, radiation of Roseland, melting or freezing, and periodic flow. Whereas other cases must be resolved with the coupled solver such as conduction on the tube, cases that use a variety of operating pressure, model real gas, and non-reflecting boundary condition [79]. FLUENT software has several kinds of models and basic equations that can be selected depend on condition of the case (Figure 6). The viscous model in the FLUENT provides several model options for simulating turbulent flow, such as k- $\epsilon$  model, k- $\omega$  model, Large Eddy Simulation (LES) and Reynolds Stress Model (RSM).

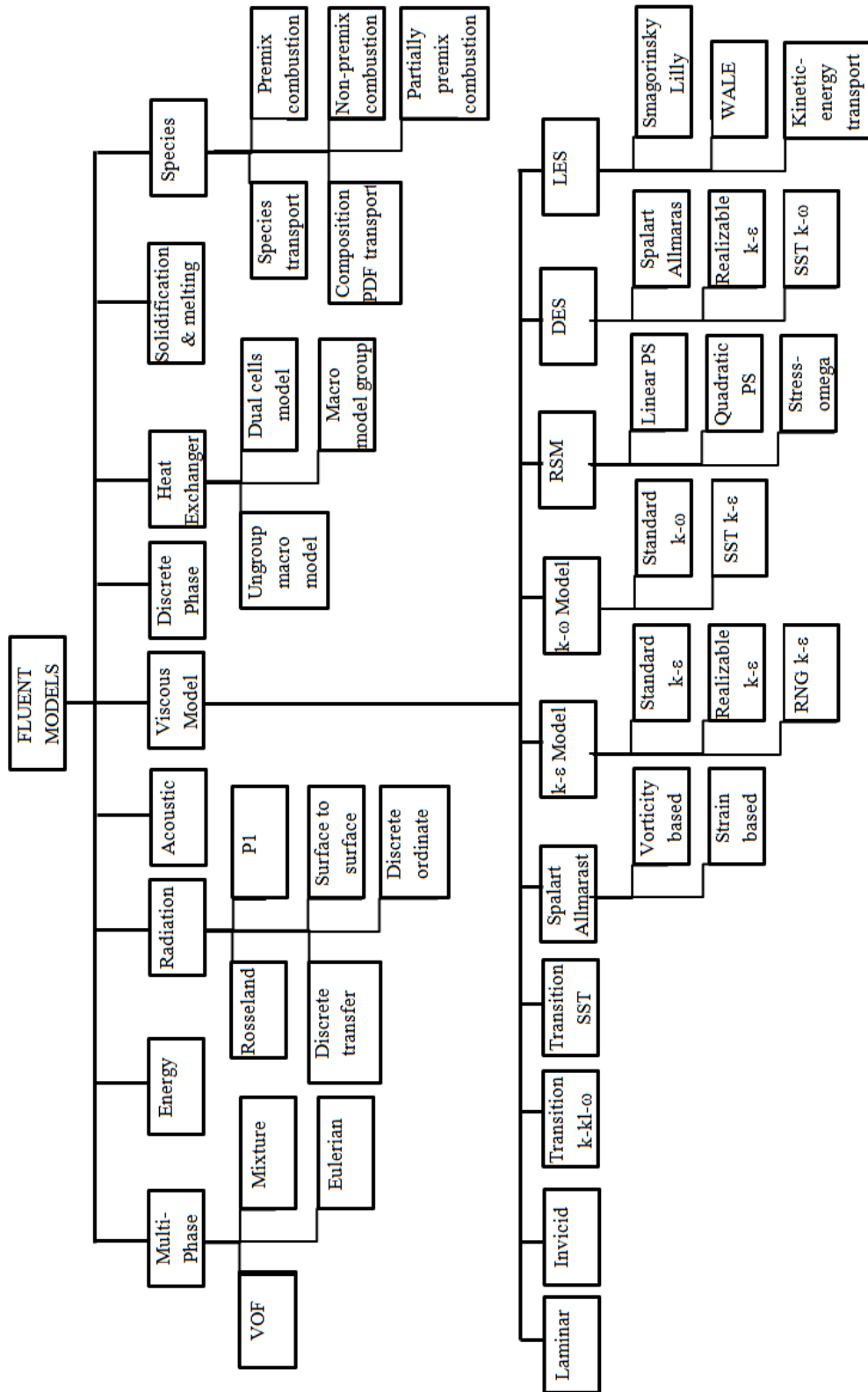


Figure 6: Turbulent model in FLUENT [21]

### 2.2.3.1 k-ε model

Turbulent k-ε model proposed by Launder and Spalding [16] is characterized by two transport equations, namely turbulence kinetic energy, k and rate dissipation of turbulence kinetic energy, ε. Kinetic energy and dissipation rate equations for standard k-ε are obtained from the following transport equations:

$$\frac{\partial}{\partial t}(\rho k) + \frac{\partial}{\partial x_i}(\rho k u_i) = \frac{\partial}{\partial x_j} \left[ \left( \mu + \frac{\mu_t}{\sigma_k} \right) \frac{\partial k}{\partial x_j} \right] + G_k + G_b - \rho \varepsilon - Y_M + S_k \quad (57)$$

$$\begin{aligned} \frac{\partial}{\partial t}(\rho \varepsilon) + \frac{\partial}{\partial x_i}(\rho \varepsilon u_i) &= \frac{\partial}{\partial x_j} \left[ \left( \mu + \frac{\mu_t}{\sigma_\varepsilon} \right) \frac{\partial \varepsilon}{\partial x_j} \right] + C_{1\varepsilon} \frac{\varepsilon}{k} (G_k + C_{3\varepsilon} G_b) \\ &- C_{2\varepsilon} \rho \frac{\varepsilon^2}{k} + S_\varepsilon \end{aligned} \quad (58)$$

where  $G_k$  is the generation of turbulence kinetic energy due to the mean velocity gradient and calculated by:

$$G_k = -\rho \overline{u'_i u'_j} \frac{\partial u_j}{\partial x_i} \quad (59)$$

and  $G_b$  is the generation of turbulence kinetic energy due to buoyancy and calculated by :

$$G_b = \beta g_i \frac{\mu_t}{Pr_t} \frac{\partial T}{\partial x_i} \quad (60)$$

$Pr_t$  is the turbulent Prandtl number for energy and  $g_i$  is component of the gravitational vector in the  $i^{\text{th}}$  direction.  $\beta$  is calculated using equation:

$$\beta = -\frac{1}{\rho} \left( \frac{\partial \rho}{\partial T} \right)_p \quad (61)$$

$Y_M$  is the contribution of fluctuating dilatation in the compressible turbulence to the overall dissipation rate, and can be calculated using equation:

$$Y_M = 2\rho \varepsilon M_t^2 \quad (62)$$

$$M_t = \sqrt{\frac{k}{a^2}} \quad (63)$$

$$a = \sqrt{\gamma RT} \quad (64)$$

$C_{1\varepsilon}$ ,  $C_{2\varepsilon}$  and  $C_{3\varepsilon}$  are constant values.  $\sigma_k$  is the turbulent Prandtl number for kinetic energy and  $\sigma_\varepsilon$  is the turbulent Prandtl number for dissipation rate.  $S_k$  and  $S_\varepsilon$  are the user defined sources term. Meanwhile,  $\mu_t$  is the turbulent viscosity and it is computed by equation:

$$\mu_t = \rho C_\mu \frac{k^2}{\varepsilon} \quad (65)$$

The constant values for standard k-ε model are  $C_\mu = 0.09$ ,  $C_{1\varepsilon} = 1.44$ ,  $C_{2\varepsilon} = 1.92$  and  $C_{3\varepsilon} = 1.3$ .

New models resulted by improvement of standard k- $\varepsilon$  models are Re-Normalization Group (RNG) k- $\varepsilon$  and realizable k- $\varepsilon$ . The equations of RNG k- $\varepsilon$  model are derived by rigorous a statistical method that is called by theory renormalizes group. This model uses equation of standard k- $\varepsilon$  with additional parameters on the dissipation rate of  $\varepsilon$  that can improve the accuracy of the model with the flow suddenly blocked. This model is able to simulate the effect of rotation on the turbulence to improve the accuracy of swirl flow modeling. In addition, RNG model also provides an analytical formula for turbulent Prandtl numbers and formula for low Reynolds number. The kinetic energy and dissipation rate equations for RNG k- $\varepsilon$  are obtained from the following transport equations:

$$\frac{\partial}{\partial t}(\rho k) + \frac{\partial}{\partial x_i}(\rho k u_i) = \frac{\partial}{\partial x_j} \left( \alpha_k \mu_{\text{eff}} \frac{\partial k}{\partial x_j} \right) + G_k + G_b - \rho \varepsilon - Y_M + S_k \quad (66)$$

$$\begin{aligned} \frac{\partial}{\partial t}(\rho \varepsilon) + \frac{\partial}{\partial x_i}(\rho \varepsilon u_i) &= \frac{\partial}{\partial x_j} \left( \alpha_\varepsilon \mu_{\text{eff}} \frac{\partial \varepsilon}{\partial x_j} \right) + C_{1\varepsilon} \frac{\varepsilon}{k} (G_k + C_{3\varepsilon} G_b) \\ &- C_{2\varepsilon} \rho \frac{\varepsilon^2}{k} - R_\varepsilon + S_\varepsilon \end{aligned} \quad (67)$$

Differential equation for turbulent viscosity is resulted from elimination procedure in the RNG theory as follow:

$$d \left( \frac{\rho^2 k}{\sqrt{\varepsilon \mu}} \right) = 1.72 \frac{\hat{v}}{\sqrt{\hat{v}^3 - 1 + C_v}} d\hat{v} \quad (68)$$

where  $\hat{v} = \mu_{\text{eff}}/\mu$  and  $C_v \approx 100$ . Equation (68) can be integrated towards in order to describe accurately how the turbulent effective transport varies with Reynolds number. This method allows the model to solve the condition of flow with low Reynolds number and proximity to the wall. For high Reynolds number, equation (68) becomes similar to equation (65) with  $C_\mu = 0.0845$ . To calculate the effect of swirl or rotation, the RNG model in FLUENT makes a modification:

$$\mu_t = \mu_{t0} f \left( \alpha_s, \Omega, \frac{k}{\varepsilon} \right) \quad (69)$$

where  $\mu_{t0}$  is the value of turbulent viscosity calculated without swirl modification using either Equation(65) or (68),  $\Omega$  is a characteristic swirl number evaluated within FLUENT,  $\alpha_s$  is swirl constant that assumes different values depend on swirl flow, whether dominated or only partly dominated,  $\alpha_k$  and  $\alpha_\varepsilon$  are computed using equation derived analytically by RNG theory:

$$\left| \frac{\alpha - 1.3929}{\alpha_0 - 1.3929} \right|^{0.6321} \left| \frac{\alpha + 2.3929}{\alpha_0 + 2.3929} \right|^{0.3679} = \frac{\mu_{\text{mol}}}{\mu_{\text{eff}}} \quad (70)$$

In the high Reynolds number limit ( $\mu_{\text{mol}}/\mu_{\text{eff}} \leq 1$ ) where  $\alpha_0 = 1.0$  it is obtained that  $\alpha_k = \alpha_\varepsilon = 1.3929$ . The term  $R_\varepsilon$  is calculated using equation:

$$R_\varepsilon = \frac{C_\mu \rho \eta^3 (1 - \eta/\eta_0) \varepsilon^2}{1 + \beta \eta^3} k \quad (71)$$

where  $\eta \equiv S k/\varepsilon$ ,  $\eta_0 = 4.38$  and  $b = 0.012$ . Substituting equation (71) into equation (67) will be obtained:

$$\frac{\partial}{\partial t}(\rho\varepsilon) + \frac{\partial}{\partial x_i}(\rho\varepsilon u_i) = \frac{\partial}{\partial x_j} \left( \alpha_\varepsilon \mu_{\text{eff}} \frac{\partial \varepsilon}{\partial x_j} \right) + C_{1\varepsilon} \frac{\varepsilon}{k} (G_k + C_{3\varepsilon} G_b) - C_{2\varepsilon}^* \rho \frac{\varepsilon^2}{k} \quad (72)$$

where  $C_{2\varepsilon}^* = C_{2\varepsilon} + \frac{C_\mu \rho \eta^3 (1 - \eta/\eta_0)}{1 + \beta \eta^3}$ ,  $C_{1\varepsilon} = 1.42$  and  $C_{2\varepsilon} = 1.68$ .

The realizable k- $\varepsilon$  model was introduced by Shih et al [17]. The model has a new formulation in the modeling of turbulent viscosity. The equation is derived from the standard k- $\varepsilon$  equation for calculating average vortices fluctuations. One of the advantages of this model is the ability to predict spread rate of the fluid from the jet or nozzle more accurately. This model also produces good performance in modeling the flow involving rotation, boundary layers which have a large pressure gradients, separation, and recirculation. In the realizable k- $\varepsilon$ , the kinetic energy and dissipation rate equations for are calculated using the following transport equations:

$$\frac{\partial}{\partial t}(\rho k) + \frac{\partial}{\partial x_i}(\rho k u_i) = \frac{\partial}{\partial x_j} \left[ \left( \mu + \frac{\mu_t}{\sigma_k} \right) \frac{\partial k}{\partial x_j} \right] + G_k + G_b - \rho \varepsilon - Y_M + S_k \quad (73)$$

$$\begin{aligned} \frac{\partial}{\partial t}(\rho\varepsilon) + \frac{\partial}{\partial x_i}(\rho\varepsilon u_i) &= \frac{\partial}{\partial x_j} \left[ \left( \mu + \frac{\mu_t}{\sigma_\varepsilon} \right) \frac{\partial \varepsilon}{\partial x_j} \right] + \rho C_1 S_\varepsilon \\ -\rho C_{2\varepsilon} \frac{\varepsilon^2}{k + \sqrt{\nu \varepsilon}} + C_{1\varepsilon} \frac{\varepsilon}{k} C_{3\varepsilon} G_b + S_\varepsilon & \end{aligned} \quad (74)$$

where  $C_1 = \max \left[ 0.43, \frac{\eta_a}{\eta_a + 5} \right]$  and  $\eta_a = S \frac{k}{\varepsilon}$ . The eddy viscosity is computed using equation (65) but the  $C_\mu$  is not constant value and it is computed using equation:

$$C_\mu = \frac{1}{A_0 + A_s \frac{k U^*}{\varepsilon}} \quad (75)$$

where  $U^* = \sqrt{S_{ij} S_{ij} + \widehat{\Omega}_{ij} \widehat{\Omega}_{ij}}$ ,  $\widehat{\Omega}_{ij} = \Omega_{ij} - 2\epsilon_{ijk} \omega_k$ ,  $A_0 = 4.04$ ,  $A_s = \sqrt{6} \cos \phi$ ,  $\phi = \frac{1}{3} \cos^{-1}(\sqrt{6}W)$ ,  $W = \frac{S_{ij} S_{jk} S_{ki}}{\widehat{S}}$ ,  $\widehat{S} = \sqrt{S_{ij} S_{ij}}$ , and  $S_{ij} = \frac{1}{2} \left( \frac{\partial u_j}{\partial x_i} + \frac{\partial u_i}{\partial x_j} \right)$

The default constant parameters of realizable k- $\varepsilon$  are  $C_{1\varepsilon} = 1.44$ ,  $C_2 = 1.9$ ,  $\sigma_k = 1.0$  and  $\sigma_\varepsilon = 1.20$ .

### 2.2.3.2 k - $\omega$ model

FLUENT has a standard k- $\omega$  model. The model is developed based on the Wilcox [18] k- $\omega$  model that has been modified to be able to calculate the flow at low Reynolds number, compressibility and shear flow distribution. Shear Stress Transport (SST) k- $\omega$  model is also available in FLUENT besides the standard k- $\omega$  model. The last model was developed by Menter [19] by combining the advantages equation of k- $\omega$  and k- $\varepsilon$ .

The equation of standard  $k-\omega$  has advantages in accuracy and stability for the flow near the wall, while the equation  $k-\epsilon$  model has an advantage in free-stream flow. When simulate flow that involves adverse pressure gradient flows, airfoils, and transonic shock waves using SST  $k-\omega$ , then will be obtained better result. The two-equations of standard  $k-\omega$  model are:

$$\frac{\partial}{\partial t}(\rho k) + \frac{\partial}{\partial x_i}(\rho k u_i) = \frac{\partial}{\partial x_j} \left( \Gamma_k \frac{\partial k}{\partial x_j} \right) + G_k - Y_k + S_k \quad (76)$$

$$\frac{\partial}{\partial t}(\rho \omega) + \frac{\partial}{\partial x_i}(\rho \omega u_i) = \frac{\partial}{\partial x_j} \left( \Gamma_\omega \frac{\partial \omega}{\partial x_j} \right) + G_\omega - Y_\omega + S_\omega \quad (77)$$

where  $G_\omega$  is the generation  $\omega$ .  $Y_\omega$  and  $Y_k$  are the dissipation of  $\omega$  and  $k$  due to turbulence.  $\Gamma_\omega$  and  $\Gamma_k$  are the effective diffusivity of  $\omega$  and  $k$ .  $S_\omega$  and  $S_k$  are the sources terms that can be defined by user.

### 2.2.3.3 Reynolds Stress Model (RSM)

Reynolds Stress Model [20] solves transport and dissipation rate equations simultaneously using the approach of the Navier-Stokes equations (Reynolds-average). This model requires four additional transport equations for 2-dimensional model and seven additional equations for 3-dimensional model. Because the number of equations used is more, then this model is expected to be the most accurate turbulence model in FLUENT but the impact is longer computation time and larger computer memory required. Reynolds Stress transport equation is written as follow:

$$\begin{aligned} \frac{\partial}{\partial t}(\rho \overline{u'_i u'_j}) + \frac{\partial}{\partial x_k}(\rho u_k \overline{u'_i u'_j}) = & - \frac{\partial}{\partial x_k} \left[ \rho \overline{u'_i u'_j u'_k} + p(\delta_{kj} \overline{u'_i} + \delta_{ik} \overline{u'_j}) \right] + \\ \frac{\partial}{\partial x_k} \left[ \mu \frac{\partial}{\partial x_k} (\overline{u'_i u'_j}) \right] - \rho \left( \overline{u'_i u'_k} \frac{\partial u_j}{\partial x_k} + \overline{u'_j u'_k} \frac{\partial u_i}{\partial x_k} \right) - \rho \beta (g_i \overline{u'_j \theta} + g_j \overline{u'_i \theta}) + p \left( \frac{\partial u'_i}{\partial x_j} + \frac{\partial u'_j}{\partial x_i} \right) - \\ 2\mu \frac{\partial u'_i}{\partial x_k} \frac{\partial u'_j}{\partial x_k} - 2\rho \Omega_k (\overline{u'_j u'_m} \epsilon_{ikm} + \overline{u'_i u'_m} \epsilon_{jkm}) + S \end{aligned} \quad (78)$$

The first term in the left side is local time derivative term and the second term is convective term. While in the right side, the terms are turbulence diffusion, molecular diffusion, stress production, buoyancy production, pressure strain, dissipation, production by system rotation and user defined sources term respectively.

### 2.2.3.4 Large Eddy Simulation (LES) model

Reynolds Average Navier-Stokes (RANS) equation is an equation for time average of the flow motion. This equation describes turbulent flow. Large Eddy Simulation only models small eddies, while the large eddy is resolved directly.

Filtered Navier-Stokes equations used in LES [21] are:

$$\frac{\partial \rho}{\partial t} + \frac{\partial}{\partial x_i} (\rho \bar{u}_i) = 0 \quad (79)$$

$$\frac{\partial}{\partial t_i} (\rho \bar{u}_i) + \frac{\partial}{\partial x_i} (\rho \bar{u}_i \bar{u}_{ij}) = \frac{\partial}{\partial x_i} \left( \mu \frac{\partial \sigma_{ij}}{\partial x_j} - \frac{\partial \bar{p}}{\partial x_i} - \frac{\partial \tau_{ij}}{\partial x_j} \right) \quad (80)$$

where the stress tensor,  $\sigma_{ij}$  due to molecular viscosity is calculated using equation:

$$\sigma_{ij} = \left[ \mu \left( \frac{\partial \bar{u}_i}{\partial x_j} + \frac{\partial \bar{u}_j}{\partial x_i} \right) \right] - \frac{2}{3} \mu \frac{\partial \bar{u}_i}{\partial x_i} \delta_{ij} \quad (81)$$

where  $\tau_{ij}$  is the sub grid-scale stress and calculated by  $\tau_{ij} \equiv \rho \overline{u_i u_j} - \rho \bar{u}_i \bar{u}_j$ .

### 2.2.3.5 Wall function and Near-wall treatment

Flow in the near wall is influenced by the roughness of wall. Therefore, near wall region is divided into three sub layers as seen in Figure 7 [21]. The closest layer to the wall called viscous sub layer. In this sub layer, the flow is usually laminar, so the viscosity plays important role. The outer sub layer is fully turbulent region or log-law region. In this sub layer, the flow is turbulent so turbulence plays an important role. Buffer layer is a region between viscous and fully turbulent. In this sub layer, effect of viscosity and turbulence together play an important role.

There are two approaches used in the completion of bounded turbulent flow (Figure 8). The first approach is using semi-empirical formulas called wall function to link the turbulent flow and the wall region. In this case, viscosity that affects viscous sub-layer and buffer layer are not resolved. The second approach is called Near-wall model. Enhanced wall treatment is a method for modeling near wall. The method combines a two layers model with enhanced wall function. In the two layer model, near wall region is divided into a viscous affected region and a fully turbulence region. In the fully turbulence region, k- $\epsilon$  model is employed. While in the viscous affected region, one equation model of Wolfstein [22] is employed. Boundary between two regions is determined by a wall distance based on criteria of turbulent Reynolds number.

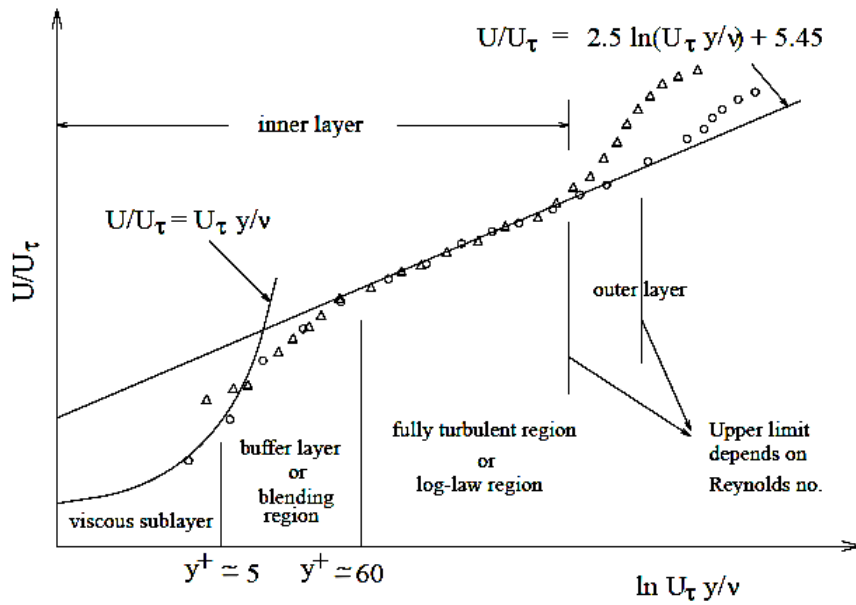


Figure 7: Sub-division of near wall region [21]

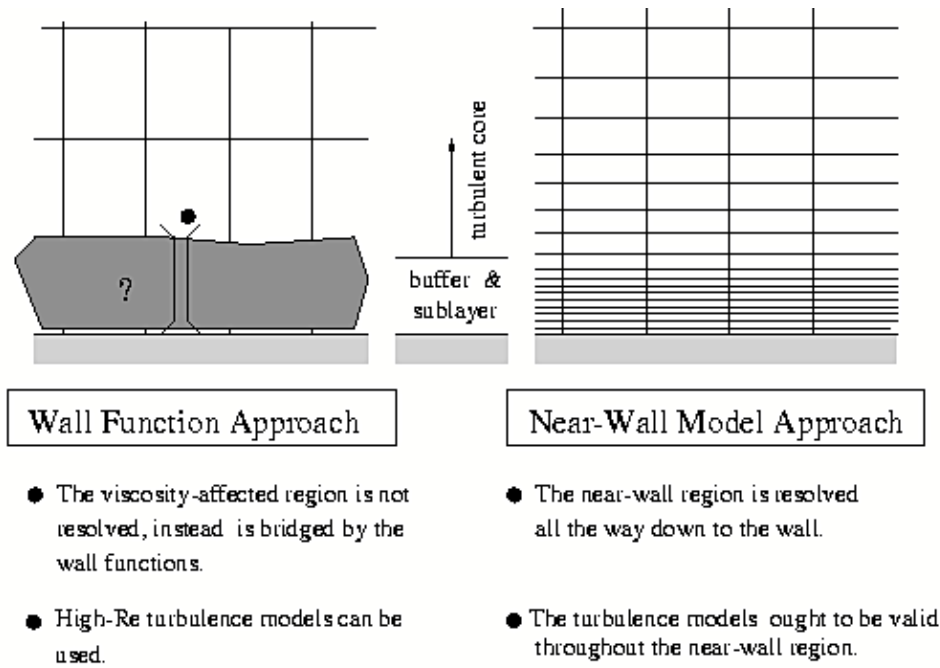


Figure 8: Near Wall treatment in FLUENT [21]

**a. Standard Wall Function**

The law of wall functions for mean velocity yields [23]:

$$U^* = \frac{1}{\kappa} \ln(E y^*) \tag{82}$$

$$U^* = \frac{U_p C_\mu^{1/4} k_p^{1/2}}{\tau_w / \rho} \quad (83)$$

$$y^* = \frac{\rho C_\mu^{1/4} k_p^{1/4} y_p}{\mu} \quad (84)$$

where  $\kappa$  is the Von Karman constant ( $=0.42$ ),  $E$  represents the empirical constant ( $=9.793$ ),  $U_p$  is the average velocity of fluid at point P,  $k_p$  is the turbulence kinetic energy at point P,  $y_p$  is the distance from point P to the wall and  $\mu$  is the dynamic viscosity of fluid. Logarithmic law for mean velocity is known to be valid for  $y^* >$  about 30 to 300. Log-law is implemented in FLUENT when  $y^* > 11.225$ . For  $y^* < 11.225$ , FLUENT applies laminar stress-strain relationship that expresses  $U^*=y^*$ .

### b. Non-Equilibrium Wall Function

The method of Non-equilibrium wall function was introduced by Kim and Choudhury [24]. In this method, the log-law from Launder and Spalding for mean velocity is sensitized to pressure gradient effect.

$$\frac{\bar{U} C_\mu^{1/4} k^{1/2}}{\tau_w / \rho} = \frac{1}{\kappa} \ln \left( E \frac{\rho C_\mu^{1/4} k^{1/2} y}{\mu} \right) \quad (85)$$

$$\bar{U} = U - \frac{1}{2} \frac{dp}{dx} \left[ \frac{y_v}{\rho \kappa \sqrt{k}} \ln \left( \frac{y}{y_v} \right) + \frac{y - y_v}{\rho \kappa \sqrt{k}} + \frac{y_v^2}{\mu} \right] \quad (86)$$

$$y_v = \frac{\mu y_v^*}{\rho C_\mu^{1/4} k_p^{1/2}} \quad (87)$$

Two-layer-based concept is adopted to compute the budget of turbulence kinetic energy ( $\overline{G_k}, \bar{\varepsilon}$ ) in the wall-neighboring cells.

$$\overline{G_k} = \frac{1}{y_n} \int_0^{y_n} \tau_t \frac{\partial U}{\partial y} dy = \frac{1}{\kappa y_n} \frac{\tau_w^2}{\rho C_\mu^{1/4} k_p^{1/2}} \ln \left( \frac{y_n}{y_v} \right) \quad (88)$$

$$\bar{\varepsilon} = \frac{1}{y_n} \int_0^{y_n} \varepsilon dy = \frac{1}{y_n} \left[ \frac{2\nu}{y_v} + \frac{k_p^{1/2}}{\kappa C_\mu^{-3/4}} \ln \left( \frac{y_n}{y_v} \right) \right] k_p \quad (89)$$

### c. Enhanced wall treatment

Enhanced wall treatment is a method for modeling near wall region. This method combines the two-layer model with enhanced wall function. The near wall region is divided into a viscous affected region and a fully turbulence region. The boundary between two regions is determined by a wall distance based on the criteria of turbulent Reynolds number:

$$Re_y = \frac{\rho y \sqrt{\kappa}}{\mu} \quad (90)$$

where  $y$  is the normal distance from the wall to the cell centers.  $K$ - $\varepsilon$  model is used for fully turbulent region i.e. the  $Re_y > Re_y^*$  where  $Re_y^* = 200$ . While one-equation of Wolfstein [22] is used for viscous affected region. The difference between one-equation and  $k$ - $\varepsilon$  models is the method to compute the turbulent viscosity. One-equation model use equation:

$$\mu_{t,2layer} = \rho C_\mu l_\mu \sqrt{\kappa} \quad (91)$$

where  $l_\mu$  is the length scale and computed using equation :

$$l_\mu = y c_1 (1 - e^{-Re_y/A_\mu}) \quad (92)$$

The two layers viscosity for enhanced wall treatment is calculated using formula:

$$\mu_{t,enh} = \lambda_\varepsilon \mu_t + (1 - \varepsilon) \mu_{t,2layer} \quad (93)$$

The blending function is:

$$\lambda_\varepsilon = \frac{1}{2} \left[ 1 + \tanh \left( \frac{Re_y - Re_y^*}{A_y} \right) \right] \quad (94)$$

where  $A_y$  is a width of blending function:

$$A_y = \frac{|\Delta Re_y|}{\tanh(0.98)} \quad (95)$$

In the condition of  $Re_y < 200$ ,  $\varepsilon$  is not obtained from the transport equation but from calculation using equation:

$$\varepsilon = \frac{\kappa^{3/2}}{l_\varepsilon} \quad (96)$$

where  $l_\varepsilon$  is the length scale :

$$l_\varepsilon = y c_1 (1 - e^{-Re_y/A_\varepsilon}) \quad (97)$$

where  $c_1 = \kappa C_\mu^{3/4}$ , and the constant values are  $A_\mu = 70$  and  $A_\varepsilon = 2c_1$ .

## 2.3 Measurement techniques

### 2.3.1 Pressure measurement

Pressure is caused by a force acts on an area of the fields. There are some important terms relate to the pressure, such as absolute pressure, relative pressure, vacuum

pressure and differential pressure. Absolute pressure is pressure that stated and measured using reference of zero pressure. Relative pressure is pressure that stated and measured using reference of atmosphere pressure. Relative pressure is equal to difference between absolute and atmosphere pressures. Vacuum pressure is a pressure that is lower than atmosphere pressure. Differential pressure is difference in pressure between two-measurement points. Pressure can be measured using a pressure gauge. Pressure gauge can be grouped into several types, such as Liquid column, Bourdon tube, Diaphragm pressure gage, Bellows element and Mcleod gages.

U-tube manometer is an example instrument for measuring pressure using liquid column. A U-tube manometer is filled by a high mass density liquid and connected into the pipe to measure pressure in the pipe. Water pressure in the pipe pushes the liquid in the tube so that there is a difference level of liquid surface. Pressure in the pipe is equal to difference level of liquid surface in the tube multiplied by specific gravity of the liquid. Bourdon tube is a non-liquid pressure gauge. Pressure is guided into the tube causing change of tube length due to the differential pressure between inside and outside of the tube. The change of tube length is converted into scale pointer movement. There are three type of Bourdon tube, i.e. C-type, spiral and helical. Diaphragm pressure gage use a principle of change in the form of an elastic diaphragm to measure an unknown pressure refers to a reference pressure. Bellows element is an elastic element that is flexible in axial direction. This element is used to make linear correlation between pressures and changes in volume. Mcleod gauge is an instrument gauge to measure low pressure using principle of height of liquid column. Mcleod gauge will compress known volume of low-pressure gas become higher pressure. The results of compressed volume and pressure are measured and the initial unknown pressure can be calculated using Boyle's Law equation.

Investigation of water pressure in the hydraulic model of internal flow is usually done using pressure transducer. The transducer converts a pressure into an analog electric signal. The analog signal is transferred to the data acquisition system. Computer controlled recording data permits efficient storage and processes large quantity data. There are several technologies used by pressure transducer, such as piezo-resistive strain gauge, capacitive, electromagnetic, piezoelectric, optical, and potentiometric. Pressure sensor is designed and installed in the hydraulic model to acquire dynamic and static pressure data from various measurement points. To obtain average pressure over cross section, the pipe walls were bored for several points and all points are connected to the pressure transducer (see Figure 10). The tube between measured boring and the pressure transducer must be made as short as possible to obtain high frequency response [25].

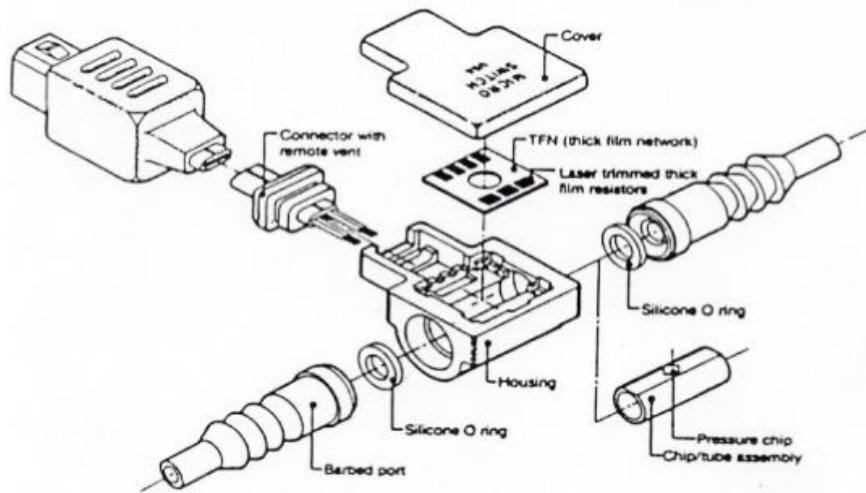


Figure 9: 3-D drawing of pressure sensor [25]



Figure 10: Control section and the pressure hole, Top: example of pressure hole, Bottom: picture of the ring line [26]

Measurement of differential pressure in a hydraulic model can use a differential pressure piezo-resistive transmitter, e.g. PD-23. This transmitter is designed to measure pressure of liquid in range of 0.2 to 1000 bars. The maximum uncertainty of the PD-23 pressure sensor is 0.5 % of the full range. If the maximum measurement in the hydraulic model tests is 5 m, an uncertainty of head level occurs of 2.5 cm. An uncertainty of 0.1 cm occurs in the smallest head level of 0.2 m. Before the piezometer difference measurement can be started, a calibration is needed. This can be done by determining a certain hydrostatic head level in the calibration tube and scale the pressure sensor to that height [26].



Figure 11: Pressure head calibration tool [26]

### 2.3.2 Flow measurement

Flow in principle is calculated by multiplying flow velocity with the cross section area. The cross section area of the developed pipe flow is constant, so flow rate in the pipe just depends on the velocity. Measurement of flow in the pipe can be done using some techniques with measuring: differential pressure, positive displacement measurement, mass, and velocity.

Measuring differential pressure is essentially applying the Bernoulli equation that expresses the relation between pressure and velocity of fluid flow. Some measurement tools that use a principle of differential pressure are Orifice, Venturi tube, Flow nozzle, Pitot tube, Target, Anubar, Elbow flow meter, Wedge, V-cone, Dall Tube and Rotameter. The working principle of each tool will be further explained. Flow through an orifice with a constriction will decrease the pressure. The pressure change is measured and used to calculate the average velocity in the pipe. When the average flow velocity is known, the flow rate can be calculated. Pressure

loss in the orifice is relatively high. Venturi tube is designed by reducing the cross section area to generate differential pressure. This design causes the pressure loss in the Venturi tube is smaller than that in the orifice and flow nozzle. Velocity can be obtained by measuring differential pressure between two points in the Venturi. The idea of Flow Nozzle is to minimize energy loss in Orifice. Similar to Orifice and Venturi, velocity in the nozzle can be obtained by measuring differential pressure between two points. Elbow flow meter uses a principle of flow through a bend. Flow in a bend is influenced by centrifugal force. This force causes a different pressure between inside and outside of the bend. The different pressure between inside and outside of the bend is measured and used to calculate flow velocity. Characteristic of Anubar tube is similar to the Pitot tube, but Anubar tube has better accuracy than Pitot tube. Wedge flow meter uses a wedge to change the cross section area of the pipe that will cause pressure drop. The difference pressure between upstream and downstream wedge is measured. V-cone flow meter uses a cone that placed in the center of flow to generate different pressure. Dall tube is a flow measurement tool that combines Orifice and Venturi tube.

Principle of flow measurement using method of positive displacement is measuring the volume of fluid flow. A mechanical rotating unit is installed in the chamber. Fluid flow is directed into a chamber that has a certain volume and it will drive the rotating unit. Volume of fluid flow through a chamber can be obtained by calculating the rounds number of rotating unit. Flow rate is determined by rotation rate of the rotating unit. There are several types of flow measurement tools using positive displacement such as Nutating disc, Rotating valve, Single piston reciprocating, Oscillating, Piston, Oval gear, Rotating Lobe (Roots), and Rotating impeller.

Flow measurement tools that use method of mass flow measurement are Thermal mass flow meter and Coriolis flow meter. Thermal mass flow meter measures heat absorption from the sensor due to fluid flow. Mass flow rate is determined by amount of heat absorbed. The flow meter uses a technology relatively new compared to other flow meters. Coriolis principle states that if a particle in rotating motion move toward or away from the center of rotation, the particle will generate internal force acting on the particle. The flow meter measure mass flow directly and it has high in accuracy and range ability. The principle of this method is measuring flow velocity in the pipe directly. Flow is obtained by multiplying flow velocity with the cross section area.

Flow measurement tools that use method of measuring velocity are Turbine, Vortex, Ultrasonic, Time flight ultrasonic and Magnetic. Turbine flow meter measures rate of turbine spin caused by fluid movement. Vortex flow meter uses a non-streamline obstacle to generate vortices in the pipe flow. The number of vortices depends on the flow magnitude. The measurement performed uses heat thermistor where the cooling head thermistor depends on flow direction according to the vortex form. Frequency of returning signal will increase when the fluid move toward a transducer and it will

decrease when fluid move away from a transducer. The fluid flow speed can be calculated using the frequency difference.

Some new techniques in measurement of velocity and flow rate that usually used in the hydraulic experiment have been developed such as Magnetic-inductive Flow Measurement, Ultrasonic Flow Meter (UFM), Laser Doppler Anemometer (LDA), and Particle Image Velocimetry (PIV). Each basic principle of the measurement will be discussed as follows:

### Magnetic-inductive Flow Measurement

Flow measurement using magnetic-inductive is based on Faraday's Law of magnetic induction. Moving a conductor through a magnetic field will induce a voltage proportionally to the flow. The measuring principle is based on electromagnetic induction where an electromagnetic field  $B$  is used to measure the velocity and the discharge rate  $Q$  in the pipe. When an electro-conductive fluid (e.g. water) in the pipe crosses the electromagnetic field that is generated by an electromagnet, a voltage  $U$  is measured between two electrodes.  $U$  is proportional to the velocity in the pipe. The sample rate of the flow meter in the laboratory is 1 kHz. If an internal damping of two seconds in the flow meter itself is determined, then the flow meter calculates continuously mean values in the range of two seconds [26].

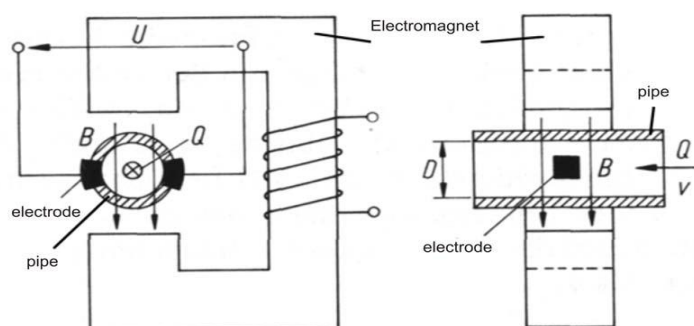


Figure 12: Principle of inductive flow measurement [26]

### Ultrasonic Flow Meter

UFM measures the time transit of high-frequency sound pulses across a pipe flow to determine flow velocity. Transit time is the time used by the sound pulse to transverse the pipeline in two directions, first is in the same direction with flow, and second is in the opposite direction with flow. Transit time required by acoustic pulse to cross a pipe diagonally in the same direction with flow can be calculated [27]:

$$t_{A \rightarrow B} = \frac{L}{(c + V \cos \theta)} \quad (98)$$

While the transit time required for the opposite direction to the flow is:

$$t_{B \rightarrow A} = \frac{L}{(c - V \cos \theta)} \quad (99)$$

From both equations can be known that the time needed by acoustic pulse to cross a pipe diagonally in the same direction of flow smaller than that in opposite direction of flow. The difference between both times is proportional to average flow velocity.

$$V = \frac{L}{2 \cos \theta} \frac{(t_{B \rightarrow A} - t_{A \rightarrow B})}{(t_{B \rightarrow A} * t_{A \rightarrow B})} \quad (100)$$

Where L is the length of acoustic pulse trajectory, c is the speed of sound in the liquid,  $\theta$  is the angle between the trajectory of pulse and the pipe axis, and V is the average velocity of fluid flow in the pipe.

Figure 13 shows the working principle of Ultrasonic flow meter. Signal Processing Unit (SPU) sends an electronic signal to the Transducer A. transducer A generates an acoustic pulse that propagates in the liquid touches the receiver of Transducer B on the other side of pipe and produces an electronic signal. The reverse process, Transducer B sends acoustic pulse to Transducer A. Receiver circuit in the SPU receives electronic signals from the receiver transducer for further processing. SPU calculates the average velocity using data of time travel of acoustic pulse from transduce A to B and from transducer B to A.

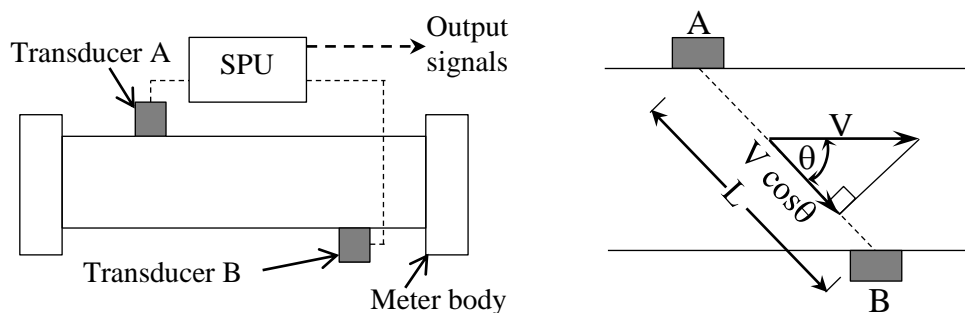


Figure 13: Basic principle of ultrasonic flow meter

Knoblauch et al. [28] investigated flow velocity in the pipe using ultrasound-pulse-Doppler. The investigation performed in the physical model of inverted syphon of Düker Oitenbach. The velocity profile of flow in the pipe is obtained by moving the transducer around the pipe into four angles. Wang et al. [29] investigated accuracy of ultrasonic flow meter to measure flow in the hydro turbine intake penstock of Three Georges Power station. The flow meter produces good accuracy of below 1% and it is sufficiently accurate for the turbine performance testing.

## Laser Doppler Anemometry

Laser Doppler Anemometry (LDA) is a measurement tool that can be used to measure velocity of fluid without disturbing the flow. Yeh and Cummins [30] developed this technique to measure laminar water flow in 1964. LDA also known as Laser Doppler Velocimetry (LDV), is an optical technique ideal for non-intrusive 1D, 2D and 3D point measurement of velocity and turbulence distribution in both free flows and internal flows [31]. The LDA uses a working principle of sending a monochromatic laser beam towards the target and collects the reflected radiation. The wave length of the reflected laser light is obtained by superimpose the original and reflected signals and it is used to calculate the velocity of the object.

Figure 14 shows basic principle of velocity measurement using LDA. The basic configuration of an LDA consist of : a continuous wave laser; transmitting optic including a beam splitter and a focusing lens; receiving optics comprising a focusing lens, an interference filter; and a photo detector and a signal conditioner and signal processor.

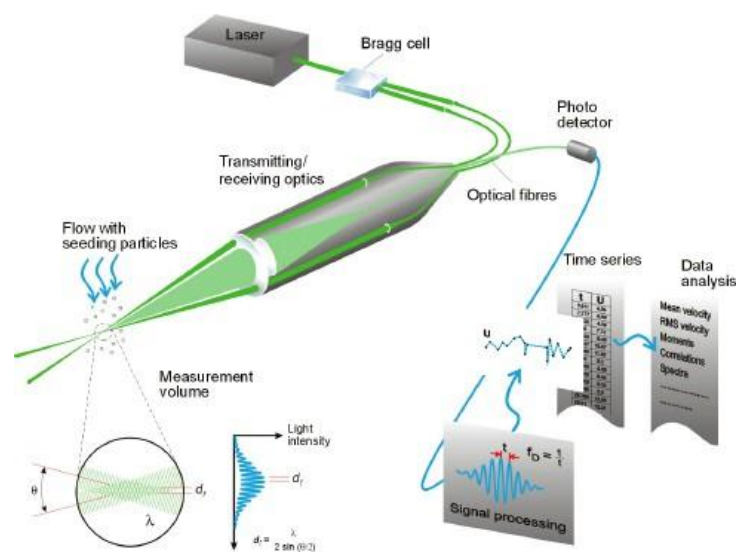


Figure 14: Basic principle of the Laser Doppler Anemometry [31]

A Bragg cell is used to split single beam sent by laser becomes two beams with equal intensity but different frequency. Both beams focused into optical fiber and brought them to a probe. The parallel exit beams from the fibers are focused by a lens to intersect in the probe volume. The light intensity is modulated due to interference between the laser beams [31]. This produces parallel planes of high light intensity, so it called fringe. The fringe distance  $d_f$  is defined by the wave length of the laser light and the angle between the beams:

$$d_f = \frac{\lambda}{2 \sin(\theta/2)} \quad (101)$$

The particles in the water that can be used in measurement are in the range between 1  $\mu\text{m}$  and 10  $\mu\text{m}$ . The light scattered by seeding particles carried in the fluid contains a Doppler shift, the Doppler frequency  $f_D$  and brings information about flow velocity. Flow velocity is expressed in the equation:

$$V = d_f \cdot f_D \quad (102)$$

Three-velocity components can be measured by using two separate probes, different wave length for each component and three photo-detectors with appropriate interference filters.

### Particle Image Velocimetry

Measuring instantaneous velocity of flow can be done using technique called Particle Image Velocimetry (PIV). The basic principle of velocity measurement using PIV technique is shown in Figure 15. The technique uses a principle stating that velocity is equal to distance divided by time, which actually measures the distance-traveled particle in the flow at specified interval time. The measurement is done by adding particle to the flow and by seeding those particles by light seed of laser. A high-speed camera is used to capture the images in two different times. Both images, which are divided into several small rectangular regions is called interrogation areas (IA). The interrogation areas from each image frame are cross-correlated pixel by pixel with each other. The common particle displacement  $\Delta\vec{X}$  can be determined by identifying a peak signal produced in cross correlation. The velocity is obtained by dividing the distance with the time between two images captured.

$$\bar{V} = \frac{\Delta\vec{X}}{\Delta t} \quad (103)$$

The cross-correlation for each interrogation area over the two image frames captured by the camera is repeated to produce a velocity vector map over the whole target area. Particle that follows the flow satisfactorily and scatters enough light to be captured by the camera can be used for seeding material. Material size in the range 5  $\mu\text{m}$  to 100  $\mu\text{m}$  usually can be used for application of water [31]. The number of particle in the flow should be enough to obtain good peak signal in the cross-correlation.

The measurement volume can be defined when the size of the interrogation area, the magnification of the imaging and the light-sheet thickness are known. The side length of the interrogation area,  $d_{IA}$ , and the image magnification,  $s'/s$  should be balanced with the size of the flow structures to be measured. One method to realize this condition is to minimize velocity gradient within the interrogation area:

$$\frac{S'}{S} \cdot \frac{|V_{max} - V_{min}|_{IA} \cdot \Delta t}{d_{IA}} < 5\% \quad (104)$$

To avoid the loss of velocity information due to the particles travelling further than the size of the interrogation area within the time,  $\Delta t$  should be determined by equation:

$$\frac{S'}{S} \cdot \frac{V \cdot \Delta t}{d_{IA}} < 25\% \quad (105)$$

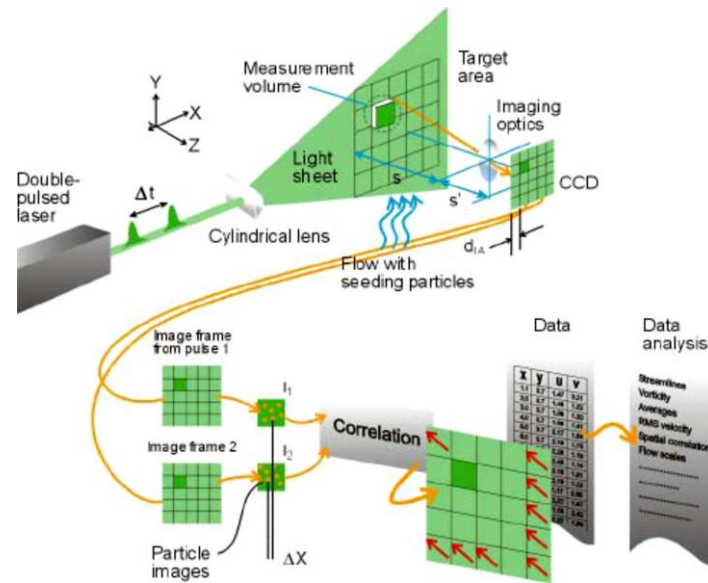


Figure 15: Basic principle of the PIV technique [31]

Schluter and Merkirch [32] have used PIV to measure time-average velocity of flow conditioners in a pipeline. Hammad et.al [33] used real time digital PIV to investigate experimentally the laminar flow through an asymmetric sudden expansion. Nikolaidis and Mathioulakis [34] have investigated experimentally axial and secondary flow in a  $90^\circ$  bifurcation of square tubes, under pulsating conditions and equal branch flow rates using PIV. Pan and Peng [35] used PIV to investigate turbulence mixing in a Tee mixer. Woisetschlager et. al. [36] used PIV to clarify the vortex shedding process in investigation of the vortex street of a turbine blade profile. Zang and Hugo [37] used stereo PIV to study a vortex generated via tangential injection of water. Ozturk et. al. [38] used PIV to investigate the flow past a confined circular cylinder built into a narrow rectangular duct with a Reynolds number range of 1,500 to 6,150.

This page intentionally left blank

## 3 Review of Past Investigation on Loss Coefficient of Manifolds

### 3.1. Study on loss coefficient of Alberschwende bifurcator

Bifurcator Alberschwende is a Y-bifurcator with branches angle of  $38^\circ$ . The main pipe diameter is 3.7 meter and each branch pipe diameter is 1.65 meter, so that the diameter ratio between the branch and the main pipes is 0.45. The bifurcator was designed to flow the water discharge of  $38 \text{ m}^3/\text{s}$  into both branches with the same flow rate (symmetrical flow) and the water discharge of  $19 \text{ m}^3/\text{s}$  only into one branch (asymmetrical flow). The objective of the study was to determine the loss coefficient of bifurcator for symmetrical and asymmetrical flow. Study on physical model of Alberschwende bifurcator is done using data from the internal report of *Hydraulisch Modellversuch Verteilrohrleitung* in 1990 by Institute of Hydraulic Engineering and Water Resources Management [40]. Study on physical model of Alberschwende bifurcator is done using data from dissertation report of *Dissipationsvorgänge in Rohrleitungssystemen*, TU Graz by Knoblauch [42].

#### 3.1.1. Physical model of Alberschwende bifurcator

To achieve the objectives of the study, a physical model of 1:12.85 using Plexiglas was constructed in the laboratory (Figure 16). The physical model has dimension of 0.288 m and 0.128 m for the main pipe and branch pipe respectively. The inductive pressure transducers measured the differential pressure between two sections. The pressure transducers were installed in six sections at upstream and four sections at downstream of bifurcator (see Figure 17). Each measurement cross section consists of four drills that distributed over the circumference of the pipe and connected by a ring line [39]. The flow was measured by the magneto-inductive flow meters at the end of each branch. The flow was controlled by the Howell-Bunger valves to ensure the accurate of flow adjustment. The measuring time is 40 second with frequency of 50 Hz.



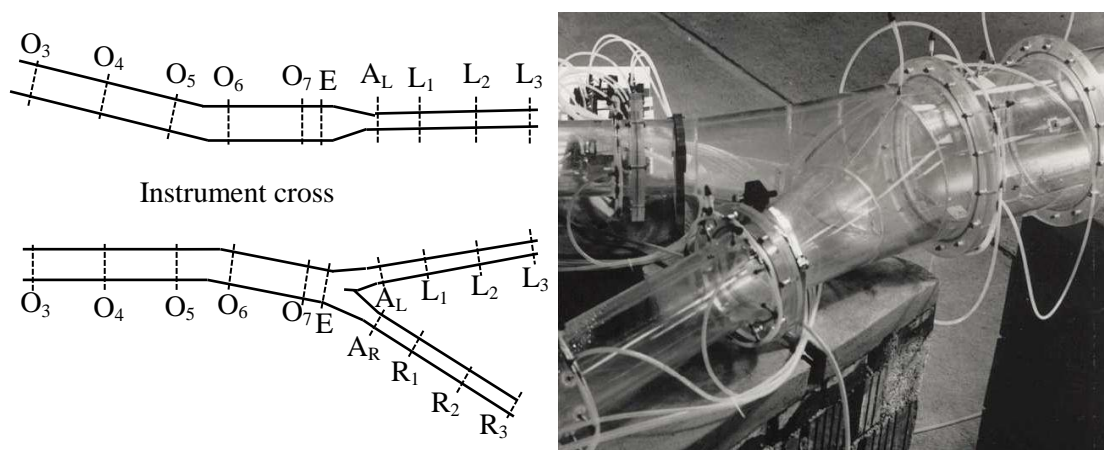
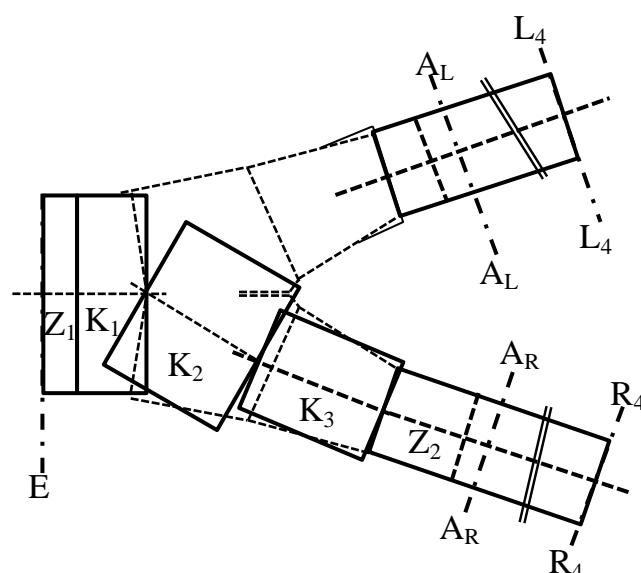


Figure 17: Location installation of pressure transducer [39]



	SECTION					
	Z1	K1	K2	K3	Z2	Z3
Diameter (m)	0.288	0.296	0.245	0.158	0.128	0.128
Length (m)	0.039	0.100	0.168	0.198	0.161	0.114

Figure 18: Idealized pipe sections for calculation friction loss [42]

The physical model was simulated in condition of asymmetrical and symmetrical flows [40]. Asymmetrical flow means that water only flows into one branch and symmetrical flow means that the water flows from the main pipe into both branches with the same flow rate. Four experiments were done in the symmetrical flow. Each experiment measured differential pressure between main pipe and branch pipe. For the experiment using left branch, the pressure was measured in the section E and  $A_L$ . For the experiment using right branch, the pressure was measured in the section E and  $A_R$ . The net differential pressure is the pressure change that caused only by shape of Y-

bifurcator. The net differential pressure is obtained by subtracting the measured differential pressure between sections E and A with friction loss between those sections. Figure 19 to 21 show the result of flow simulation in symmetrical condition, while the result of asymmetrical condition is shown in Figure 22 to 24. Figures in the left side are the result of calculation between two sections in the main pipe and left branch. Figures in the right side are the result of calculation between two sections in the main pipe and right branch. For high Reynolds number, the average loss coefficient of symmetrical flow that calculated using left and right branches are 0.15 and 0.1 respectively. Asymmetrical flow produce higher loss coefficient. The average loss coefficient in high Reynolds number asymmetrical flow using left and right branches pipe is 1.7. The right branch test gives the result with smaller deviation compared to the result of left branch. Figure 19 shows the net differential pressure head between sections E and A resulted by four tests for several discharges. Both of left and right figures that showed the net differential pressure head resulted by four tests are close to each other. The loss coefficient was calculated by inputting the net differential pressure head and differential velocity head into energy equation.

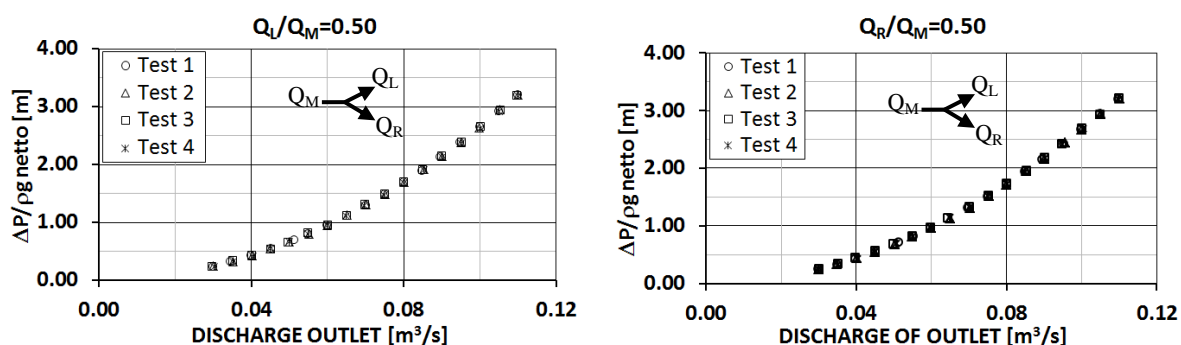


Figure 19: Comparison of net differential pressure head among several tests on physical model of bifurcator for symmetrical flow [40].

Normalized loss coefficients resulted by four tests is showed in Figure 20. The left and right figures show loss coefficients for symmetrical flow resulted by measurement using left and right branch. Loss coefficient calculated in the left branch is smaller than that in the right branch. The net pressure differences showed in Figure 19 were extrapolated over Reynolds number to predict loss coefficient for high Reynolds number. Extrapolation of different pressure was done only for three high Reynolds number.

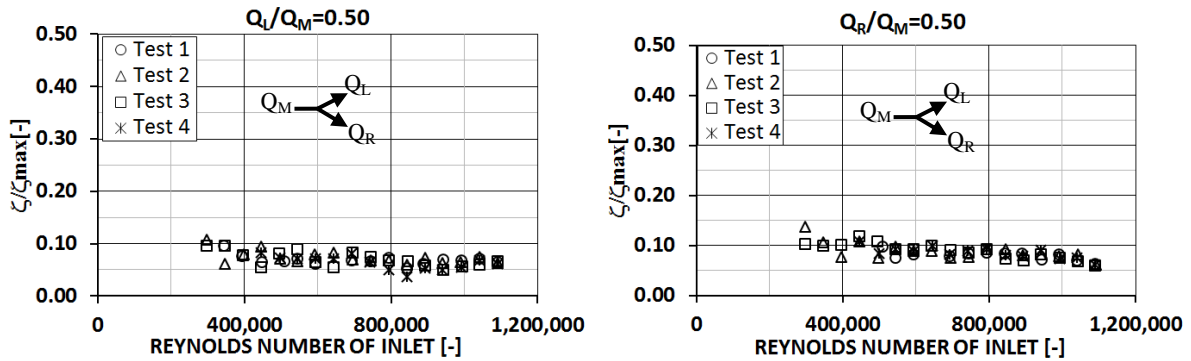


Figure 20: Normalized loss coefficient of physical model of bifurcator symmetrical flow.

Figure 21 shows normalized loss coefficients resulted by extrapolation of the net differential pressure head that measured in left and right branches. Loss coefficient resulted by extrapolation method depends on the trend of the data used. The net differential pressure head measured by left branch has a trend to increase steeper than that measured by right branch. Extrapolated loss coefficients of left branch are higher than that of right branch.  $Q_M$ ,  $Q_L$ , and  $Q_R$  are discharges measured in the main pipe, left branch and right branch respectively.

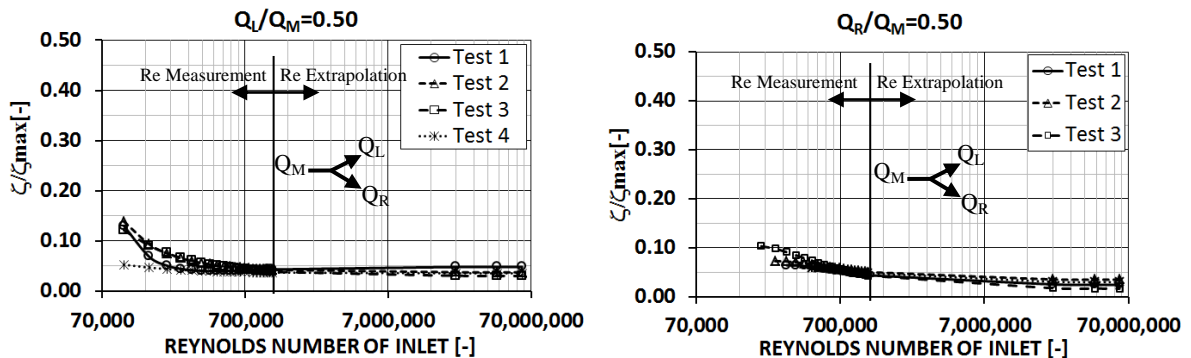


Figure 21: Normalized loss coefficients of physical model of bifurcator for symmetrical flow resulted by extrapolation of differential pressure head

Using similar method, the net differential pressures head of asymmetrical flow were calculated and the results were presented in Figure 22. The left figure presents the results of net differential pressures head measured in the left branch. The right figure presents the results of measured right branch. The normalized loss coefficients for asymmetrical flow were calculated and presented in Figure 23. Like the result of experiment in symmetrical flow, loss coefficient of asymmetrical flow calculated using left branch is lower than that using right branch. However, loss coefficient for high Reynolds number resulted by extrapolation of net differential pressure head in the left branch is higher than that in right branch. The average loss coefficient in high Reynolds number resulted by both branches do not show a significant difference.

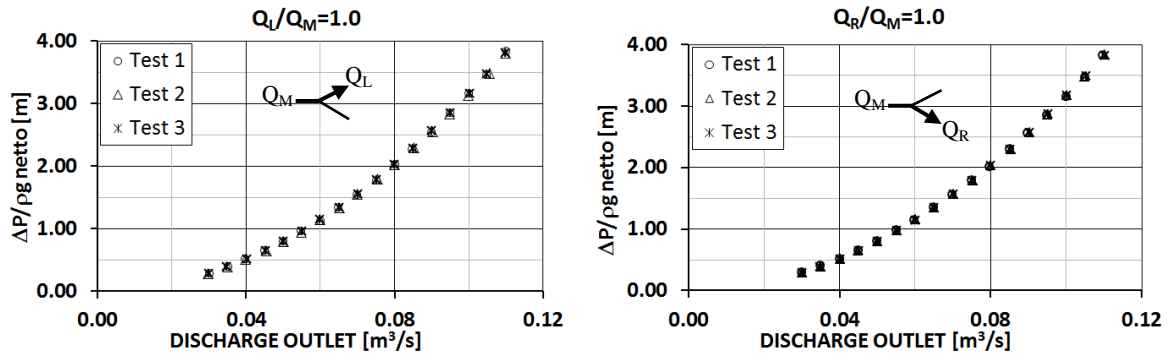


Figure 22: Comparison of net differential pressure head among several tests on physical model of bifurcator for asymmetrical flow [40]

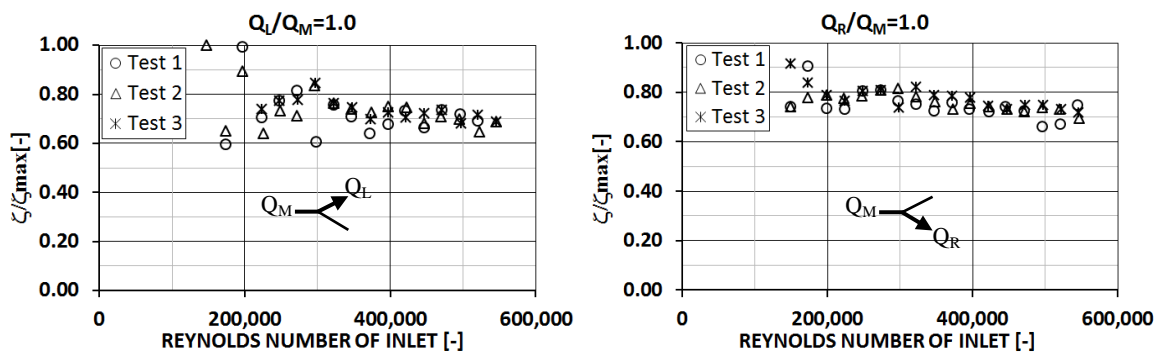


Figure 23: Normalized loss coefficients of physical model of bifurcator for asymmetrical flow

Figure 24 shows comparison of normalized loss coefficients among three test resulted by calculation using extrapolation equation of differential pressure head from measurement in scale model. In the study, the loss coefficient in the extrapolation area only calculated for three-selected Reynolds number; because of the study consider predicting loss coefficient for very high Reynolds number. From the figures can be seen that loss coefficient resulted by extrapolation method is determined by the trend of measurement data.

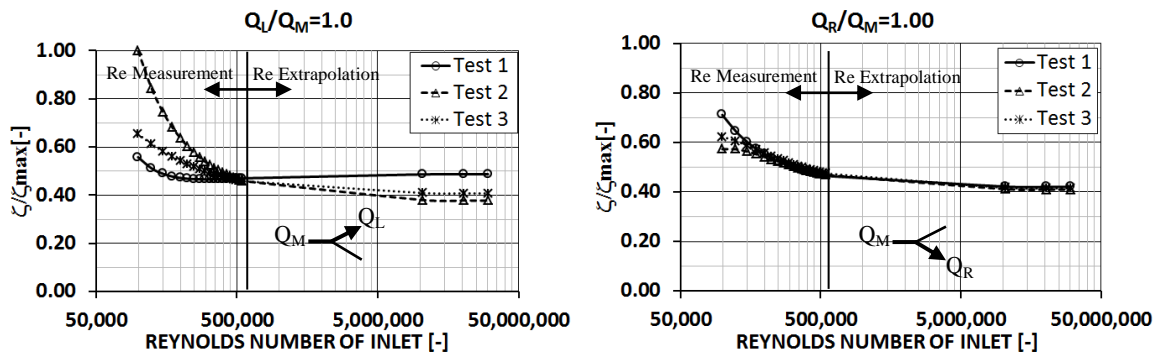


Figure 24: Normalized loss coefficients of physical model of bifurcator for asymmetrical flow resulted by extrapolation of differential pressure head

Figure 21 and Figure 24 show normalized loss coefficients resulted by several tests in the end of Reynolds number measurement are close each other. However, the trend of decreasing loss coefficient of each test from low to high Reynolds number is different. Therefore, loss coefficient of each test for very high Reynolds number produced by extrapolation of differential pressure head is also different.

### 3.1.2 Numerical model of bifurcator Alberschwende

For numerical model simulation, model domain was determined by developing the geometry of Y-bifurcator and discretized by the finite volume mesh [41] (about 30000 elements, Figure 25). The inlet opening at the beginning of main pipe was decided as inflow boundary condition, the outlet opening at the end of both branches is outflow boundary conditions, and the wall of geometry is wall boundary condition. A roughness value of 0.015 mm was used for the Plexiglas wall. Standard k- $\epsilon$  model in Flow In Reciprocating Engine (FIRE, AVL) software package was used for numerical simulation [42] [43]. Two geometries with different size were prepared for the simulation. The first is geometry with size of physical model and the second one is geometry with size of nature (the geometry of nature 12.85 times larger than geometry of physical model). The Reynolds similarity was applied to physical model and nature.

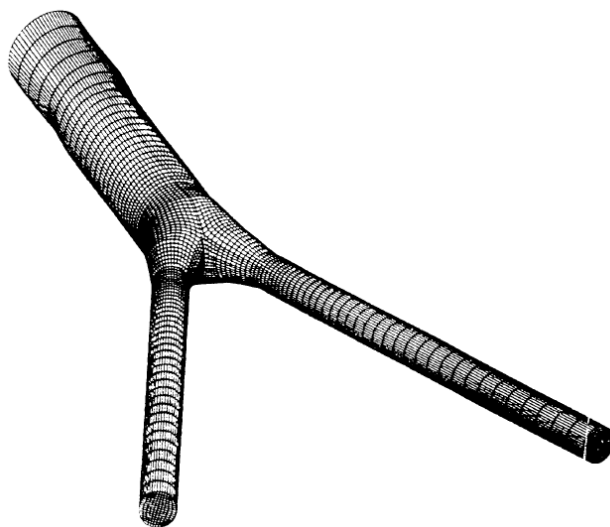


Figure 25: Geometry and generated mesh for numerical model [42]

Figure 26 shows the comparison of loss coefficients between the result of numerical and physical models. Numerical model with nature size was simulated using Reynolds number of the maximum value of physical model as beginning until the value of nature. For the same Reynolds number, loss coefficient resulted by numerical model with nature size is higher than that resulted by numerical model with physical model size. In the high Reynolds number, loss coefficient of numerical model with nature size decreases close to the loss coefficient of numerical model with physical model size.

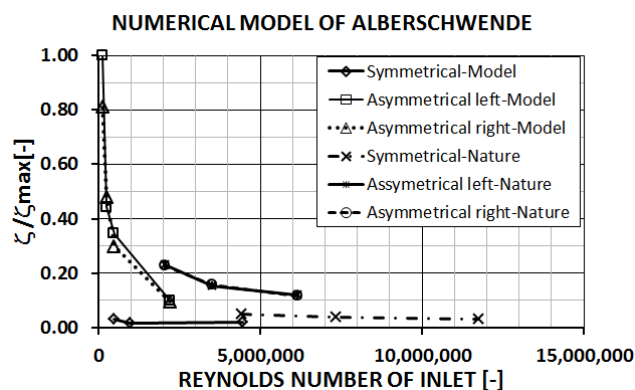


Figure 26: Normalized loss coefficients resulted by numerical model of bifurcator Alberschwende in physical model and nature sizes.

Figure 27 shows comparison of normalized loss coefficients of symmetrical flow between the result of physical model extrapolation and the result of numerical model. Numerical model with physical model size generates loss coefficients, which are closer to the result of extrapolation compared to numerical model with nature size. Numerical model of nature size produce loss coefficient higher than that produced by extrapolation method.

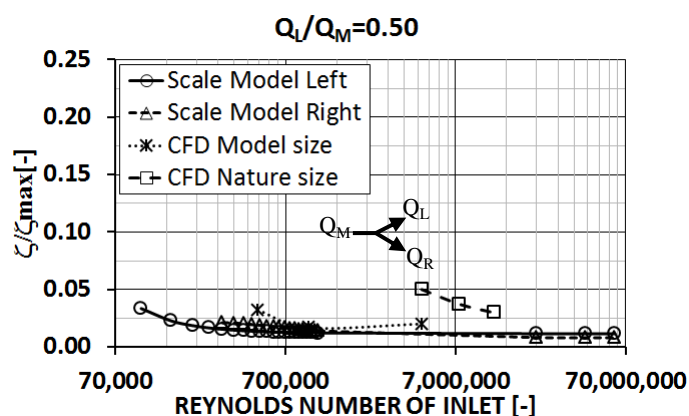


Figure 27: Comparison of normalized loss coefficients between results of physical model and numerical model for symmetrical flow.

Figure 28 shows the comparison of normalized loss coefficients of asymmetrical flow between the result of extrapolation and numerical model. Normalized loss coefficients of scale model are calculated using data from scale model investigation of Alberschwende bifurcator [40]. While normalized loss coefficients of numerical model with physical model and nature sizes are calculated from the result of another study using the same bifurcator [42]. Numerical model for nature size was simulated in the range of Reynolds number extrapolation. Contrast to the results of symmetrical flow, in asymmetrical flow, numerical model with nature size generates loss coefficients, which are closer to the result of extrapolation than numerical model with physical model size.

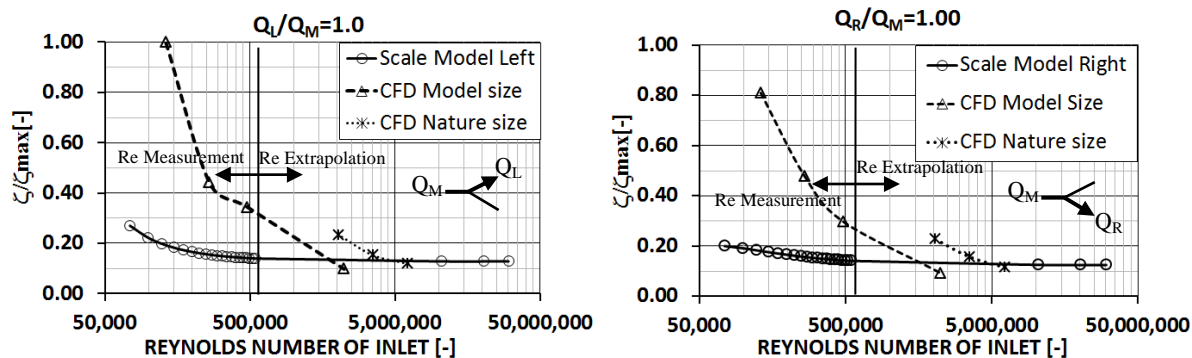


Figure 28: Comparison of normalized loss coefficient between results of physical model and numerical model for asymmetrical flow.

Numerical model of model scale size produce loss coefficient for asymmetrical flow much higher than produced by scale model in low Reynolds number. Numerical model has low accuracy in simulating low Reynolds number flow. In the high Reynolds number, loss coefficient produced by numerical and scale model are close. However, loss coefficient produces by numerical model of scale model and size of nature is different for the same Reynolds number.

## 3.2 Similarity study on loss coefficient of fittings

This sub chapter will review and discuss the investigation of energy loss that caused by flow through a fitting. The fittings data that used for similarity study are long elbows and tees from several researches.

### 3.2.1 Steel pipe fittings diameter of 6, 8 and 10 inches

This study was done using partial data of Project Report number 461 with title Pressure Loss Coefficients of 6, 8 and 10-inch Steel Pipe Fittings by Chengwei (Alex) Ding, Luke Carlson, Christopher Ellis and Omid Mohseni from St. Anthony Falls Laboratory University of Minnesota [44]. The research carried out testing of butt-welded steel fittings size 6, 8 and 10 inches to determine the value of minor loss coefficients. The fittings consist of 90° long elbows, reducing elbow, expansions elbow, tees, reducing tees, concentric reducers, and expansions. Each test was carried out by measuring the differential pressure between sections at the point before and after fitting. The primary flow rate was measured at the SAFL weight tanks, which has been calibrated with NIST traceable standards so it can measure flow accurately up to 453 liter/s. In additions, the discharge measurements were taken at each observation point using an orifice. The orifice was designed to produce differential pressure of 90'' at maximum discharge. The discharge range for test are 8.5- 85 liter/s 6 inch fittings, 20 – 200 liter/s for fittings 8 inch and 31 – 310 liter/s for fittings 10 inch. The differential pressure between two observation points before and after fitting were measured using Validyne Model DP15 transducers with accuracy of 0.25%. During

the experiment, the average temperature of water is 71.6° F (22° C), the average kinematic viscosity is  $1.02 \cdot 10^{-6} \text{ m}^2/\text{s}$ . The coefficient of minor losses (K) is calculated using equation:

$$K = \frac{h_m}{u_1^2/2g} \quad (106)$$

where  $h_m$  is the minor loss that caused by fitting and  $u$  is the average velocity at inlet. The minor loss is calculated using Bernoulli equation:

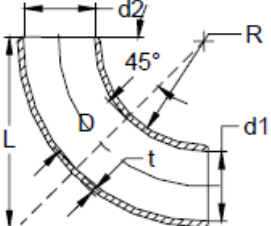
$$h_m = \frac{P_1 - P_2}{\gamma} + \frac{u_1^2 - u_2^2}{2g} - \sum_i \frac{f_i L_i}{D_i} \frac{u_i^2}{2g} \quad (107)$$

Subscribe 1 in the equation is location of pressure measurement at the upstream of fitting and subscribe 2 is location of pressure measurement at the downstream of fitting. The first term in right side is obtained from the differential pressure between point 1 and 2 that measured by pressure transducer. The  $u_1$  and  $u_2$  are average velocities that obtained by measuring discharge and cross section area at point 1 and 2. The last term is the total friction loss that caused by friction between water and the pipe wall. The friction at pipe section between point 1 and fitting inlet and between fitting outlet and point 2 were calculated. According to the geometric similarity, only long elbow and tees tests can be used for the study of family model. The other fittings are far from the geometric similarity.

### 3.2.1.1 Long elbow 6, 8 and 10 inches

Two elbows have geometric similarity if between both elbows have the same shape and ratio of each size variables. The geometric similarity between an elbow with another is evaluated and shown in Table 1. The ratios of size variables between elbow 6 and 8 inches vary from 0.749 to 0.762, between elbow 6 and 10 inches vary from 0.586 to 0.607, and between elbow 8 and 10 inches vary from 0.782 to 0.799. It means that among three elbows are not fully similar in geometry. This happens because the elbows are commercial product and they are not designed for the purpose of model similarity. However, because the variation of size ratio is quite small, the result of this experiment is used for study the relationship between the size of model and loss coefficient.

Table 1: Variable size ratios of long elbow diameter 6, 8 and 10 inches [44]

	RATIO OF DIAMETER	RATIO OF VARIABLES SIZE (-)			
		d1	d2	R	D
	D6"/D8"	0.762	0.759	0.749	0.759
	D6"/D10"	0.603	0.605	0.586	0.607
	D8"/D10"	0.792	0.798	0.782	0.799

In the project report number 461 [44], the authors recommended the minor loss coefficients of 6", 8", and 10" long elbow as function of flow velocity. Figure 29 shows the normalized loss coefficients for long elbows over flow velocity. The error bars in the graph denote the standard deviation of measured loss coefficient.

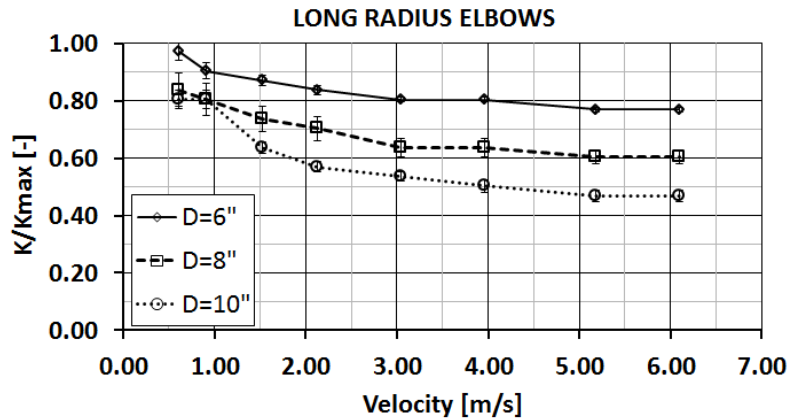


Figure 29: Normalized minor loss coefficients of long radius elbow 6, 8 and 10 inches

The minor loss coefficients have a decreasing trend with increasing flow velocity. For different size of fitting, the loss coefficients also decrease with increasing size of fitting. The minor loss of fitting is caused by the shape of fitting and the friction between water and the fitting wall. Loss coefficient ( $K$ ) is calculated without reducing the energy loss due to the friction inside of the fitting. Therefore, to obtain the local loss coefficient ( $\zeta$ ) that is only caused by the shape of the fitting, the minor loss should be subtracted by friction loss in the fitting.

Using Reynolds similarity, the local loss coefficients ( $\zeta$ ) are calculated and are performed in Figure 30. Local loss coefficient decreases with increasing Reynolds number. The highest local loss coefficient is produced by the smallest elbow (6 inches). Similar with the Reynolds similarity, Froude similarity gives the results of loss coefficient that will decrease with the increasing Reynolds number. The highest local loss coefficient is produced by the smallest elbow (6 inches).

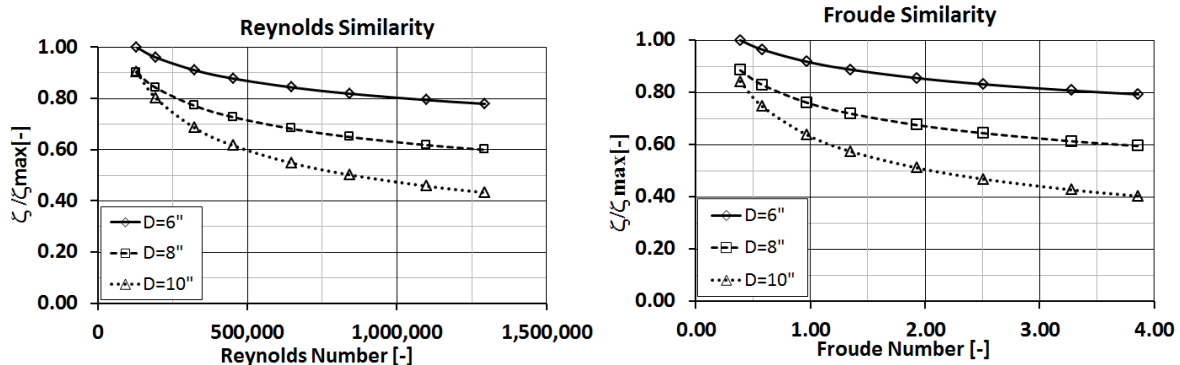


Figure 30: Normalized local loss coefficients of long elbow 6, 8 and 10 inches using Reynolds similarity (left) and Froude similarity (right)

Figure 31 left shows the relationship between normalized local loss coefficient and elbow diameter for several Reynolds numbers. For high Reynolds number, correlation between loss coefficient and elbow diameter is also close to linear. Figure 31 right shows the relationship between normalized loss coefficient and elbow diameter for several Froude numbers. Similar in the high Reynolds number, for high Froude number, the correlation between loss coefficient and elbow diameter is close to linear.

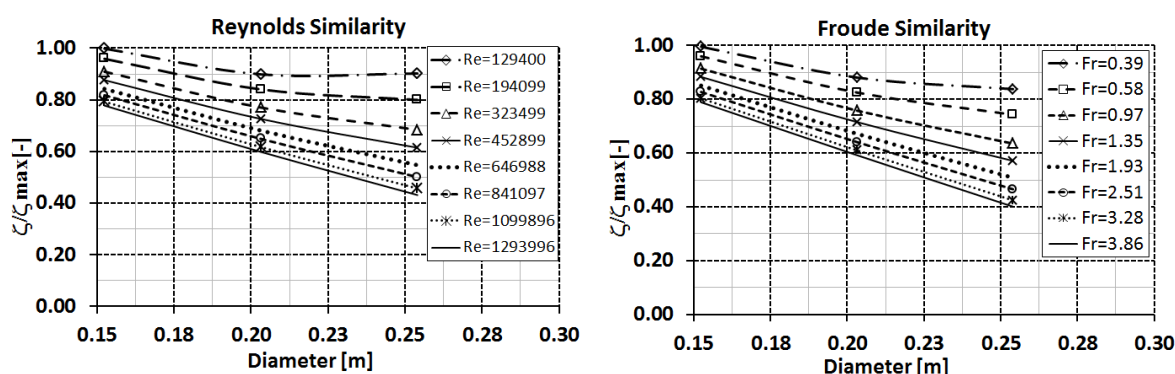


Figure 31: Normalized local loss coefficients of long elbow as function of diameter for several Reynolds number (left) and Froude number (right)

### 3.2.1.2 Tees 6, 8 and 10 inches

Tees with diameter 6, 8 and 10 inches produced by 4 vendors were tested to investigate the pressure loss. About 448 numbers of tests were done for branching and mixing flow. Loss coefficients for branching flow were calculated using equations:

$$Q_1 = Q_2 + Q_3 \quad (108)$$

$$h_{m1-2} = \frac{P_1 - P_2}{\gamma} + \frac{1}{2g} \left( \frac{Q_1^2}{A_1^2} - \frac{Q_2^2}{A_2^2} \right) - \left( \lambda_1 \frac{L_1}{D_1} \frac{u_1^2}{2g} + \lambda_2 \frac{L_2}{D_2} \frac{u_2^2}{2g} \right) \quad (109)$$

$$K_{12} = \frac{h_{m1-2}}{u_1^2/2g} \quad (110)$$

K is minor loss coefficient of fitting caused by the shape of fitting and by friction between water and fitting wall. Meanwhile,  $\zeta$  is local loss coefficient only caused by the shape of fitting.

$$h_{m1-3} = \frac{P_1 - P_3}{\gamma} + \frac{1}{2g} \left( \frac{Q_1^2}{A_1^2} - \frac{Q_3^2}{A_3^2} \right) - \left( \lambda_1 \frac{L_1}{D_1} \frac{u_1^2}{2g} + \lambda_3 \frac{L_3}{D_3} \frac{u_3^2}{2g} \right) \quad (111)$$

$$K_{13} = \frac{h_{m1-3}}{u_1^2/2g} \quad (112)$$

Loss coefficient for mixing flow is calculated using equations:

$$Q_1 + Q_3 = Q_2 \quad (113)$$

$$h_{m1-2} = \frac{P_1 - P_2}{\gamma} + \frac{1}{2g} \left( \frac{Q_1^2}{A_1^2} - \frac{Q_2^2}{A_2^2} \right) - \left( \lambda_1 \frac{L_1}{D_1} \frac{u_1^2}{2g} + \lambda_2 \frac{L_2}{D_2} \frac{u_2^2}{2g} \right) \quad (114)$$

$$K_{12} = \frac{h_{m1-2}}{u_1^2/2g} \tag{115}$$

$$h_{m3-2} = \frac{P_3 - P_2}{\gamma} + \frac{1}{2g} \left( \frac{Q_3^2}{A_3^2} - \frac{Q_2^2}{A_2^2} \right) - \left( \lambda_3 \frac{L_3}{D_3} \frac{u_3^2}{2g} + \lambda_2 \frac{L_2}{D_2} \frac{u_2^2}{2g} \right) \tag{116}$$

$$K_{32} = \frac{h_{m3-2}}{u_3^2/2g} \tag{117}$$

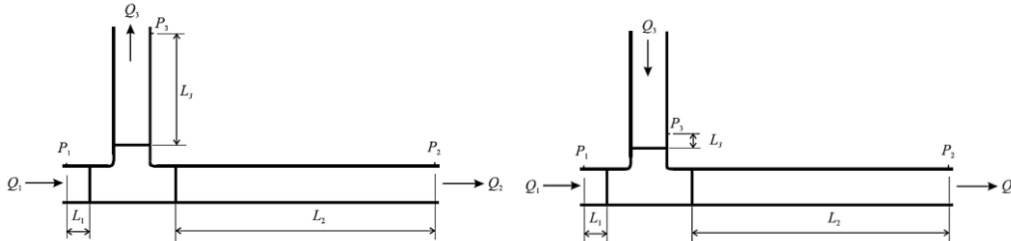


Figure 32: Schematic of flow for branching (left) and mixing tees (right) [44]

Ratio of size variables between two tees is presented in Table 2. The ratio of size variables between tees of 6 and 8 inches are in the range of 0.667 to 0.836, between tees of 6 and 10 inches are in the range of 0.5 to 0.723, and between tees 8 and 10 inches are in the range of 0.75 to 0.864.

Table 2: Ratio of size variables of tees 6, 8 and 10 inches [44]

	RATIO OF DIAMETER	RATIO OF SIZE VARIABLES (-)						
		d1	d2	d3	R	Ld	Lt	D
	D6"/D8"	0.758	0.759	0.755	0.836	0.667	0.802	0.746
	D6"/D10"	0.600	0.599	0.605	0.723	0.500	0.660	0.577
	D8"/D10"	0.791	0.790	0.801	0.864	0.750	0.823	0.774

Figure 33 left and right show the normalized loss coefficients of inline and perpendicular flows of branching tees as a function of discharge percentage. Lowest loss coefficient is found in the inline flow ( $K_{1-2}$ ) for discharge ratios of 50% and 75%.

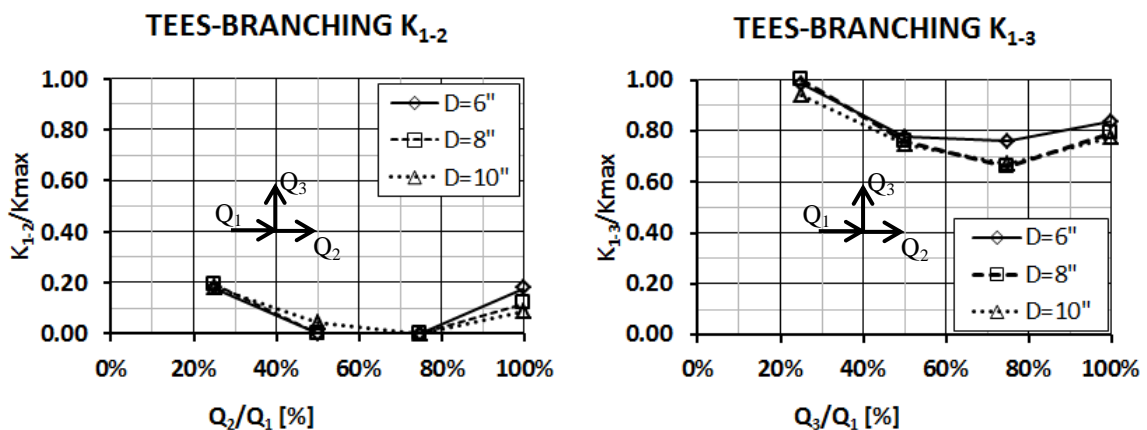


Figure 33: Normalized loss coefficient of branching tees for several discharge ratios

Negative value of loss coefficient is obtained in the perpendicular ( $K_{3-2}$ ) mixing flow with low discharge ratio of 25% (Figure 34). Negative value come from the pressure in the section 2 that higher compared with the pressure in section 3 because of the inflow discharge from section 3 is small.

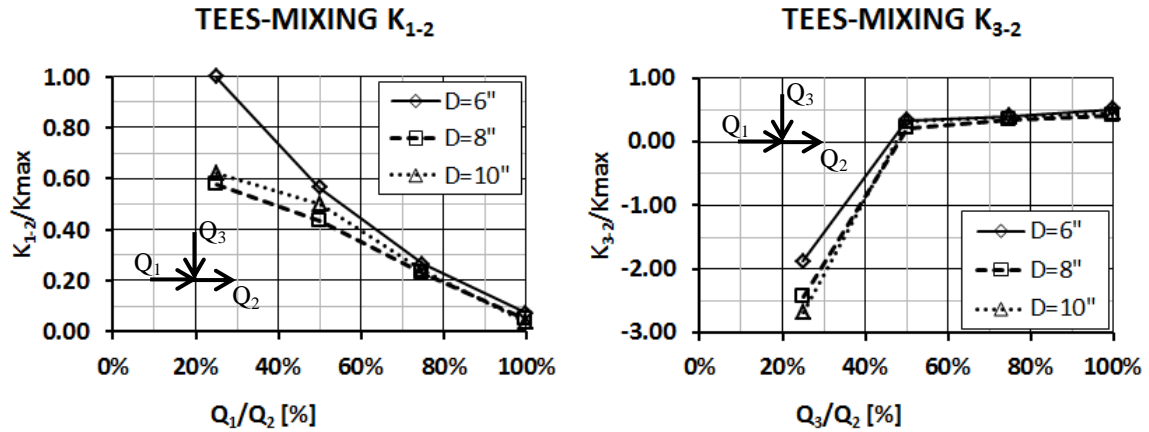


Figure 34: Normalized loss coefficients of mixing tees for several discharge ratios

With the Reynolds similarity, the third tees producing the loss of coefficient that closes enough to each other. Figure 35 left and right shows the normalized loss coefficients of inline and perpendicular flows of branching tees that presented as a function of Reynolds number. Loss coefficient of branching tee decreases with the increasing Reynolds number. The three different sizes of tees have similar value of loss coefficient in low and high Reynolds number.

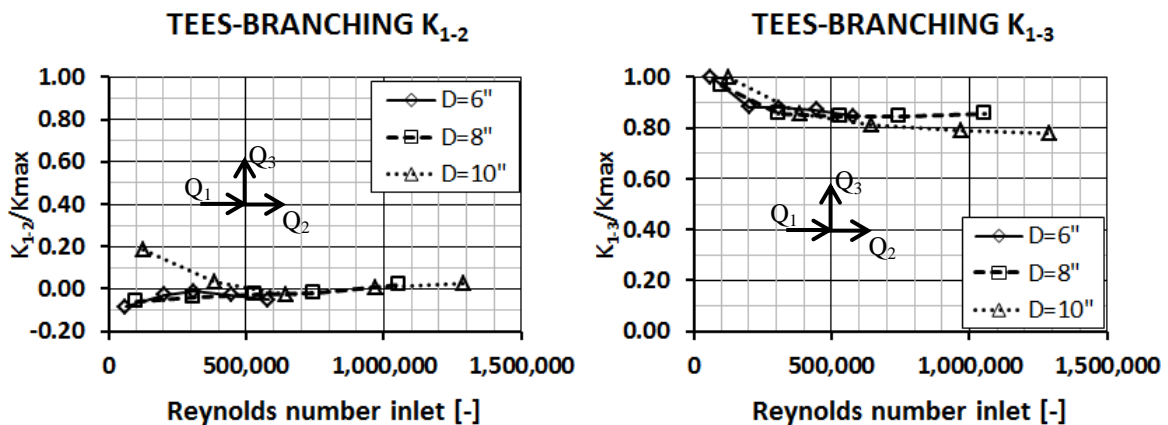


Figure 35: Normalized loss coefficients of branching tees over Reynolds number

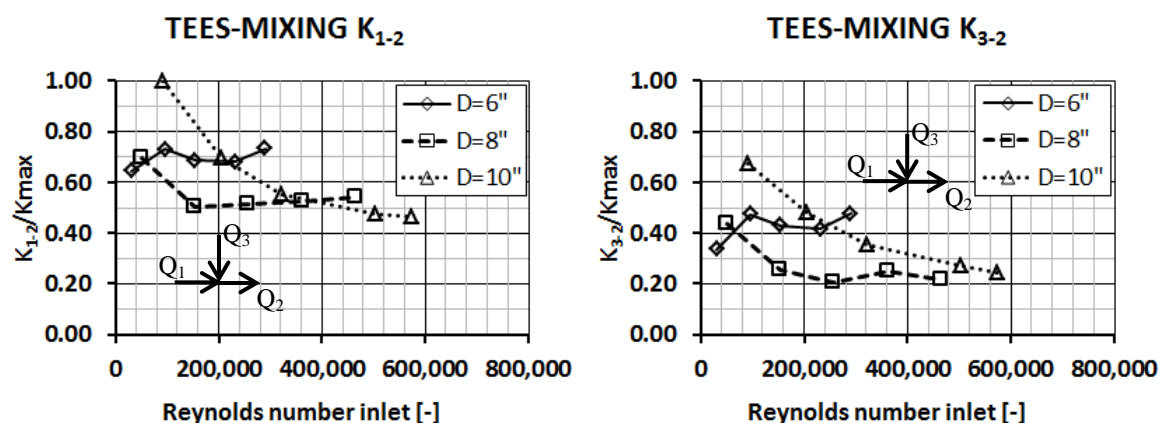


Figure 36: Normalized loss coefficients of mixing tees over Reynolds number

Figure 36 shows the normalized loss coefficients of inline (left) and perpendicular (right) flow of mixing tees that presented as a function of Reynolds number. Loss coefficient of tees in mixing flow varies with Reynolds number and tee diameter.

### 3.2.2 Pressure loss data for large pipe elbows and tees 12, 16, 20 and 24 inches

This study uses data from the research on pressure loss of large pipe elbow, reducer, and expansions [45], [46], [47] and for large pipe tees [48]. One of the research objectives is to determine loss coefficients for the large diameter fittings. The tests for forged steel weld fittings with diameter between 12 to 24 inches were conducted in the hydraulic laboratory at Utah State University. Each elbow, reducer, and expansion was tested over 10 different flows with velocity ranges of 0.6 – 6.1 m/s. The flow rates were measured using four different types of flow measurements; volumetric type tanks, weight tanks, orifice plates and venturi flow meters. Flow measurement using weight and time yields the accuracy of 0.5% and using venturi meter produces the accuracy of 1%. The water temperature during test is 55°F (12.8°C). The pressure tabs to measure differential pressure were installed at upstream and downstream of fitting where the flows are uniform and fully developed, as seen in Figure 37.

#### 3.2.2.1 Large Elbows diameter of 12, 16, 20 and 24 inches

The configuration of large elbow test is shown in Figure 37. Two pressure tabs were installed at the upstream and downstream of elbow to measure the differential pressure. Discharge flow through the elbow was controlled by upstream and downstream control valves.

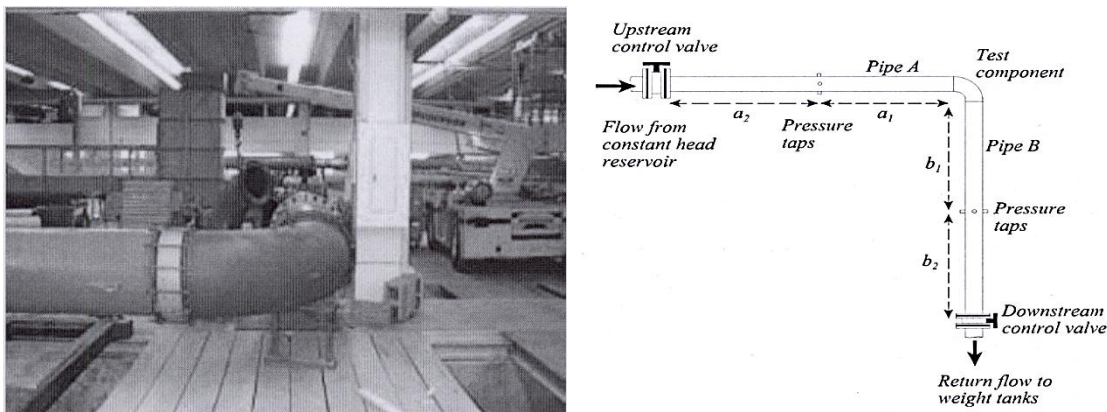
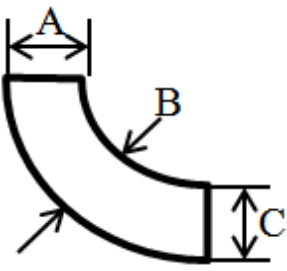


Figure 37: Configuration of test elbow [48]

Calculation of ratio of size variable between two elbows was done and presented in Table 3 to check the geometric similarity among elbows. From the table can be seen that the deviation of dimensions ratio is relatively small, so that four elbows have geometry in good similarity.

Table 3: Ratios of size among long elbow 12, 16, 20 and 24 inches [48]

	RATIO OF DIAMETER	RATIO OF SIZE VARIABLES (-)		
		A	B	C
	D12"/D16"	0.785	0.785	0.787
	D12"/D20"	0.622	0.622	0.622
	D12"/D24"	0.514	0.514	0.515
	D16"/D20"	0.792	0.792	0.791
	D16"/D24"	0.654	0.655	0.655
	D20"/D24"	0.826	0.827	0.828

In the report, calculation of loss coefficients ( $K$ ) was done by dividing minor losses ( $h_m$ ) with velocity head ( $u^2/2g$ ). The minor loss is loss that caused by the shape and friction in the elbow and calculated using equation 107. Figure 38 shows the normalized loss coefficients of elbow from four vendors (W, X, Y, and Z) with diameter of 12, 16, 20, and 24 inches. Each diameter shows comparison of loss coefficient among elbows from four vendors, which is relatively close. Using this result, average loss coefficients for each diameter is calculated.

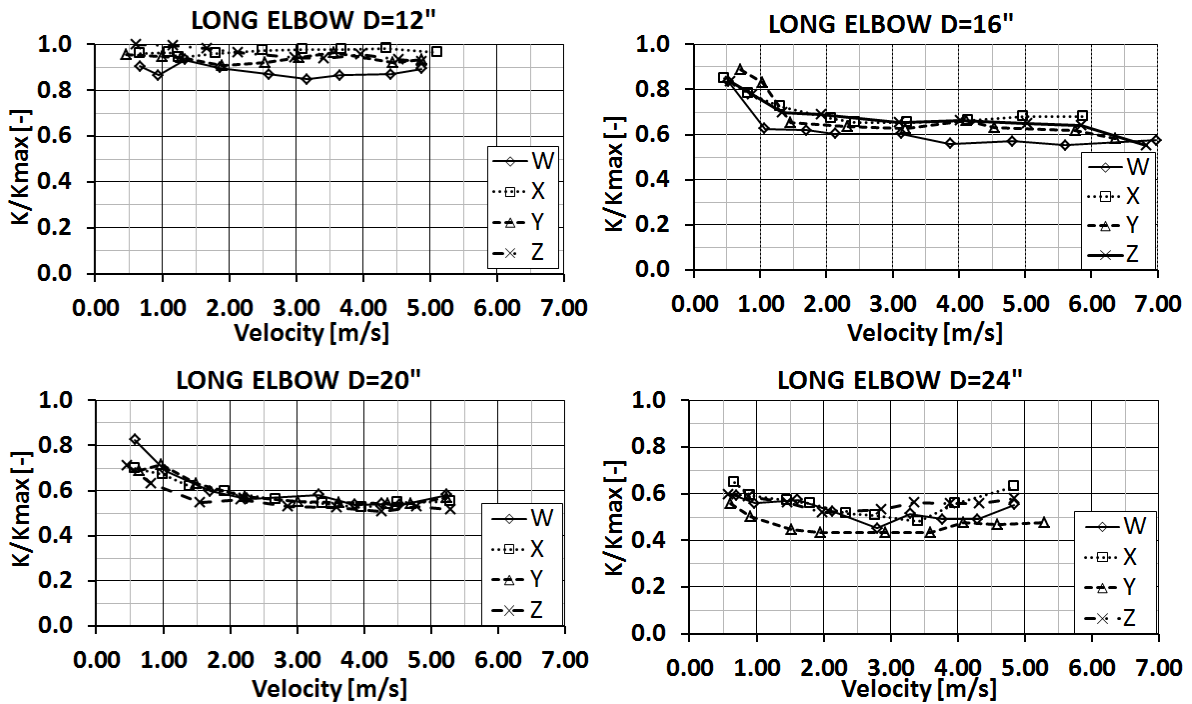


Figure 38: Normalized loss coefficients of long elbow 12, 16, 20 and 24 inches from four vendors [48]

Note: W, X, Y, and Z are replacement name of the fitting vendors.

Using Reynolds similarity, normalized local loss coefficients caused only by the elbow shape ( $\zeta$ ) for each elbow over Reynolds number are plotted together in Figure 39. The loss coefficients have decreasing trend with increasing elbow diameter. The loss coefficients also decrease with increasing Reynolds number. Among four elbows, loss coefficient of elbow 12 inches is much higher and it has different trend compared to the other elbows.

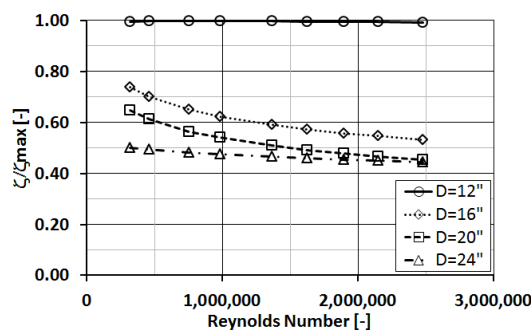


Figure 39: Normalized loss coefficients of long elbows with similarity of Reynolds

### 3.2.2.2 Tees 12 and 16 inches

The investigation on pressure loss through tees was done only using tees with diameter of 12 and 16 inches. Tees were tested in condition of branching and mixing

flow with configuration as described in Figure 40. Eight size variable ratios of tees 12 and 16 inches are compared in Table 4. The standard deviation of size ratio is 1.5%.

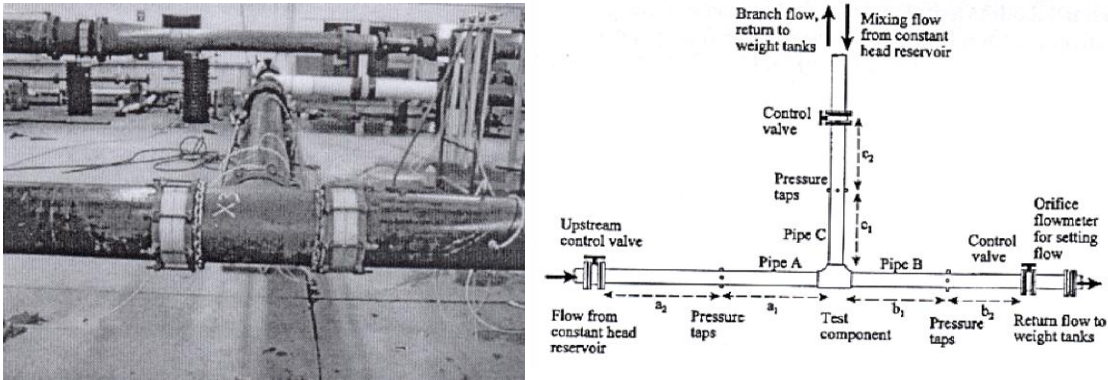


Figure 40: Pipe configuration for branching and mixing tees [48]

Table 4: Ratio of size variables between tees 12 and 16 inches [48]

	D12"/D16"	RATIO OF SIZE VARIABLES (-)			
		A	B	C	D
	D12"/D16"	RATIO OF SIZE VARIABLES (-)			
		E	F	G	H
		0.777	0.784	0.781	0.803
		0.794	0.810	0.798	0.796

Calculation of loss coefficients on tees of 12 and 16 inches were done using similar method with tees of 6, 8, and 10 inches. Normalized loss coefficients of branching tee are presented in Figure 41 left and the mixing tees in figure right. Loss coefficients of branching tees in perpendicular flow are higher than that in inline flow. Tees with size of 12 and 16 inches have almost the same value of loss coefficient both in perpendicular and inline flow. In the inline flow of mixing tees, loss coefficient decreases if the water flows into the outlet increases. In the perpendicular flow of mixing tees, loss coefficient increases if the water flows into the outlet increases. Negative value of loss coefficient is found in the perpendicular flow of mixing tee with discharge ratio of 25%. Loss coefficients of tees with diameter of 12 inches are close to loss coefficient of tee 16 inches in both branching and mixing flow.

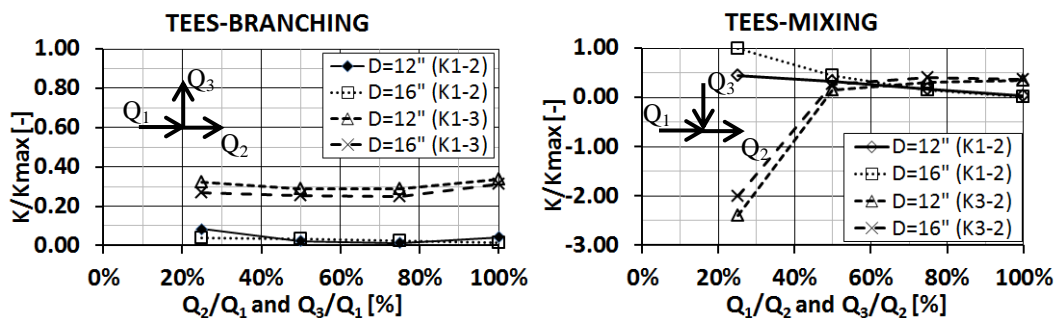


Figure 41: Normalized loss coefficients of branching tee over discharge ratio

Similarity study of tees is done by comparing of loss coefficient between tees of 12 and 16 inches for branching and mixing flow with the same Reynolds number. Figure 42 to 45 present comparison of normalized loss coefficients between tees of 12 and 16 inches.

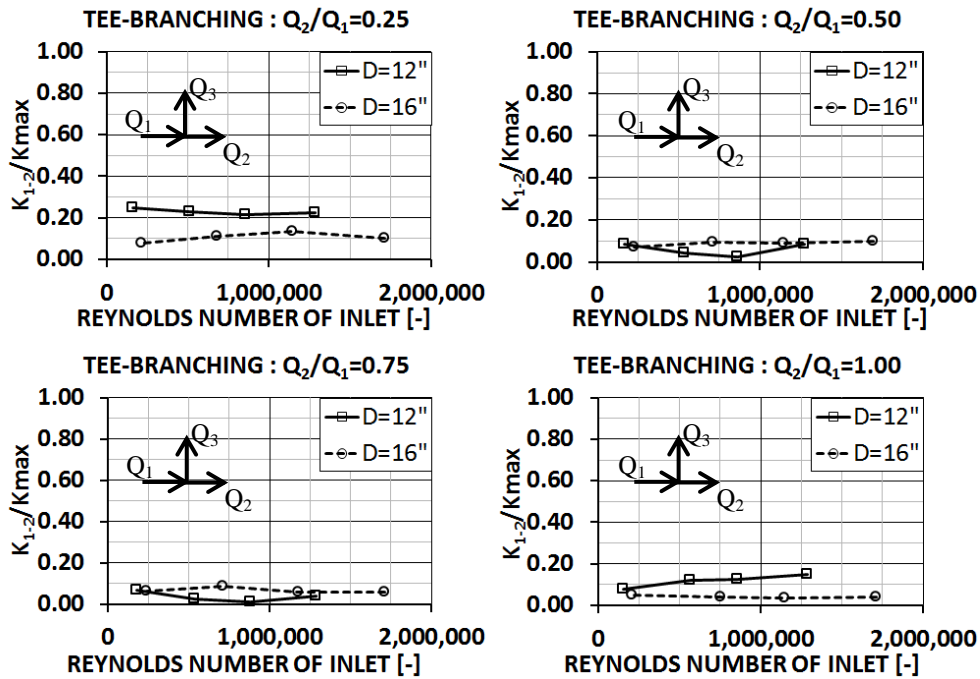


Figure 42: Normalized loss coefficients of inline flow branching tee

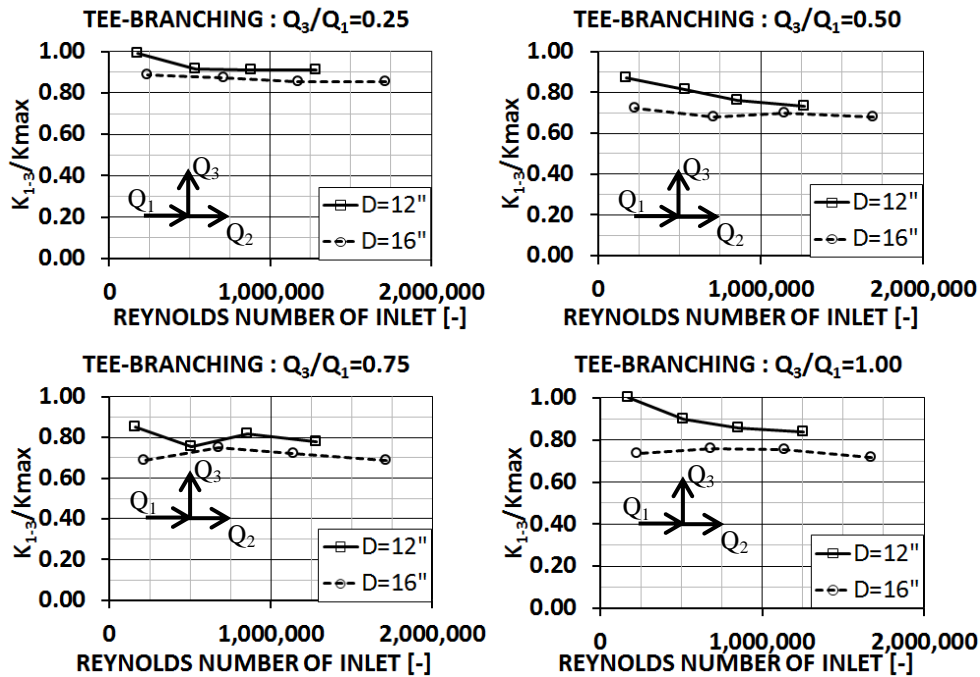


Figure 43: Normalized loss coefficients of perpendicular flow of branching tees

Figure 42 and Figure 43 show comparison of normalized loss coefficients between tees of 12 and 16 inches in inline and perpendicular branching flow, which come to the higher loss coefficient in perpendicular flow than in inline flow. In the figure, it also can be seen that loss coefficients of tee of 12 inches are close to loss coefficient 16 inches tee for the same Reynolds number.

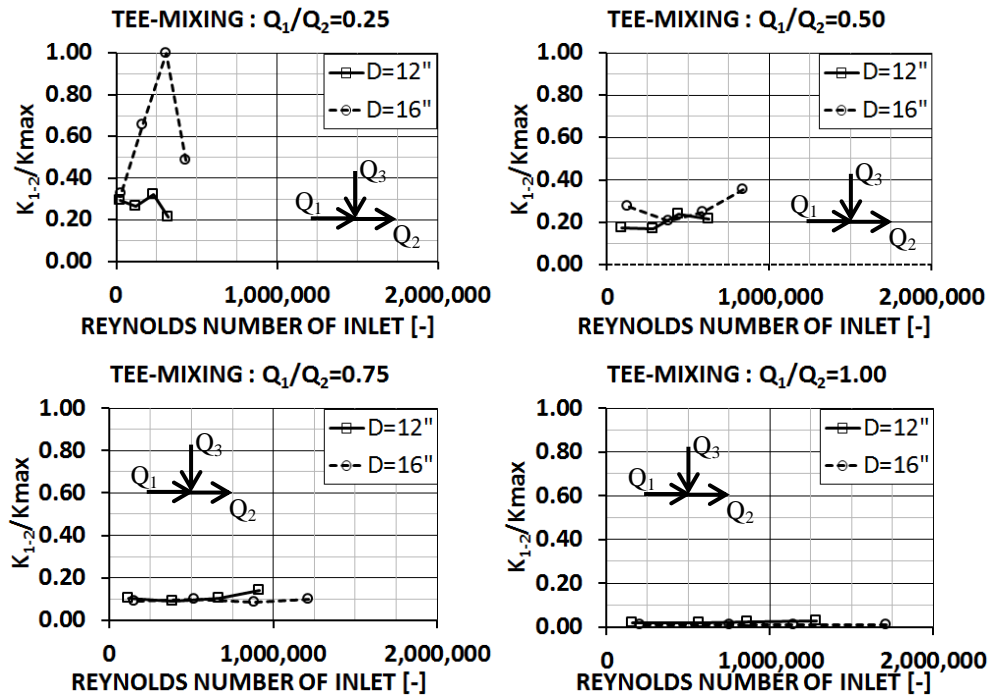


Figure 44: Normalized loss coefficients of inline flow of mixing tees

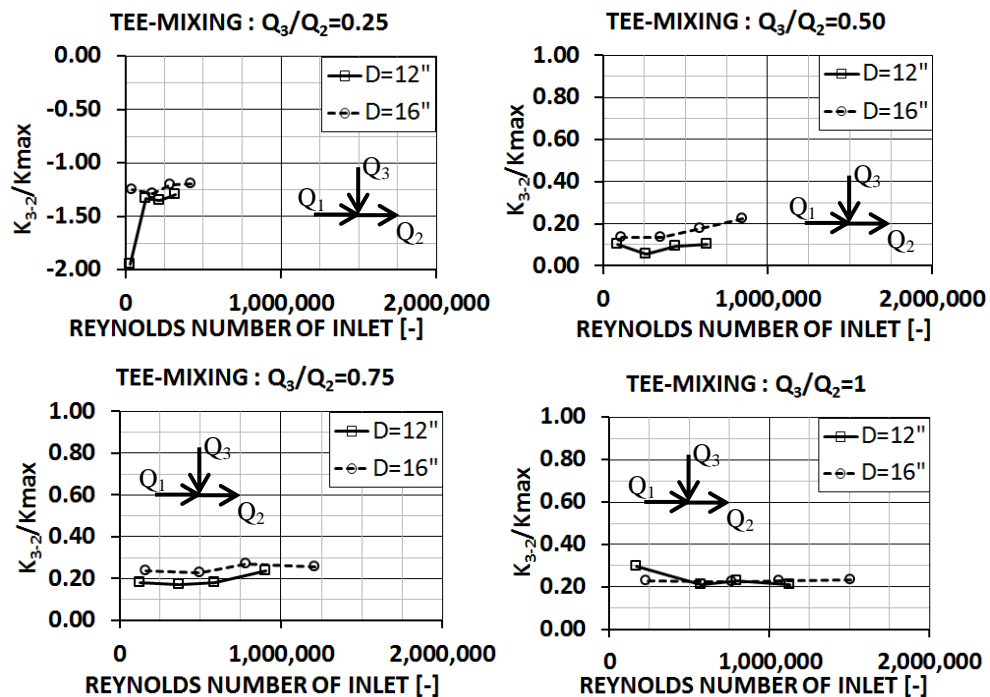


Figure 45: Normalized loss coefficients of perpendicular flow mixing tees

Figure 44 and Figure 45 show comparison of normalized loss coefficients between tees of 12 and 16 inches in inline and perpendicular mixing flow. Most of loss coefficients of tees of 12 and 16 inches in mixing flow are closer each other than that in branching flow. The difference of loss coefficients resulted by 12 and 16 inches tees is relatively small.

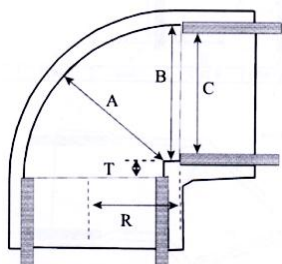
### 3.2.3 Pressure loss of PVC plastic pipe fittings

This study was done using data from the investigation of PVC plastic fitting pressure loss presented by Utah Water Research Laboratory, Utah State University [49]. The fittings investigated consist of elbows, reducers, expansions, and tees. The reducers and expansions fittings have non-comparable sizes, therefore the study of similarity only uses elbow and tee.

#### 3.2.3.1 PVC elbows 2, 4, 6 and 8 inches

The molded 90-degree elbows are made from PVC plastic. Ratio of size variables between an elbow and other elbows is calculated to know their similarities. The size ratios between elbow diameter of 2 and 4 inches, 2 and 6 inches, 2 and 8 inches, 4 and 6 inches, 4 and 8 inches and 6 and 8 inches are presented in Table 5. The standard deviation of size ratio are 25%, 40%, 49%, 26%, 31% and 13% respectively. The smallest deviation is the size ratio between elbows 6 and 8 inches and the highest deviation is the size ratio between elbows 2 and 8 inches.

Table 5: Size ratio of PVC Elbows diameter 2, 4, 6, and 8 inches [49]

	RATIO of D	RATIO OF SIZE VARIABLES (-)					
		A	B	C	T	R	R/C
	D2"/D4"	0.514	0.515	0.511	0.753	0.346	0.676
	D2"/D6"	0.376	0.367	0.337	0.330	0.231	0.687
	D2"/D8"	0.278	0.274	0.259	0.322	0.161	0.623
	D4"/D6"	0.730	0.712	0.658	0.439	0.669	1.015
	D4"/D8"	0.541	0.531	0.506	0.428	0.466	0.921
	D6"/D8"	0.740	0.745	0.768	0.975	0.697	0.907

Comparison of normalized loss coefficients among four elbows are presented in Figure 46. The biggest diameter of elbow has the lowest loss coefficient. Increasing the flow velocity in an elbow will decrease the loss coefficient. Using similarity of Reynolds number, the normalized loss coefficient for each elbow was calculated and presented. The elbows with diameter of 2 and 4 inches have similar trend over the Reynolds number. The elbows of 2, 4, and 6 inches have similar value of loss coefficient in the high Reynolds number, whereas elbow of 8 inch have lowest loss

coefficient. Figure 46 also shows correlation between normalized loss coefficient and elbow diameter that is close to linear. Increasing elbow diameter will decrease loss coefficient. The different of loss coefficients between elbow of 2 and 8 inches are high because the deviation of size ratio between both elbows is high.

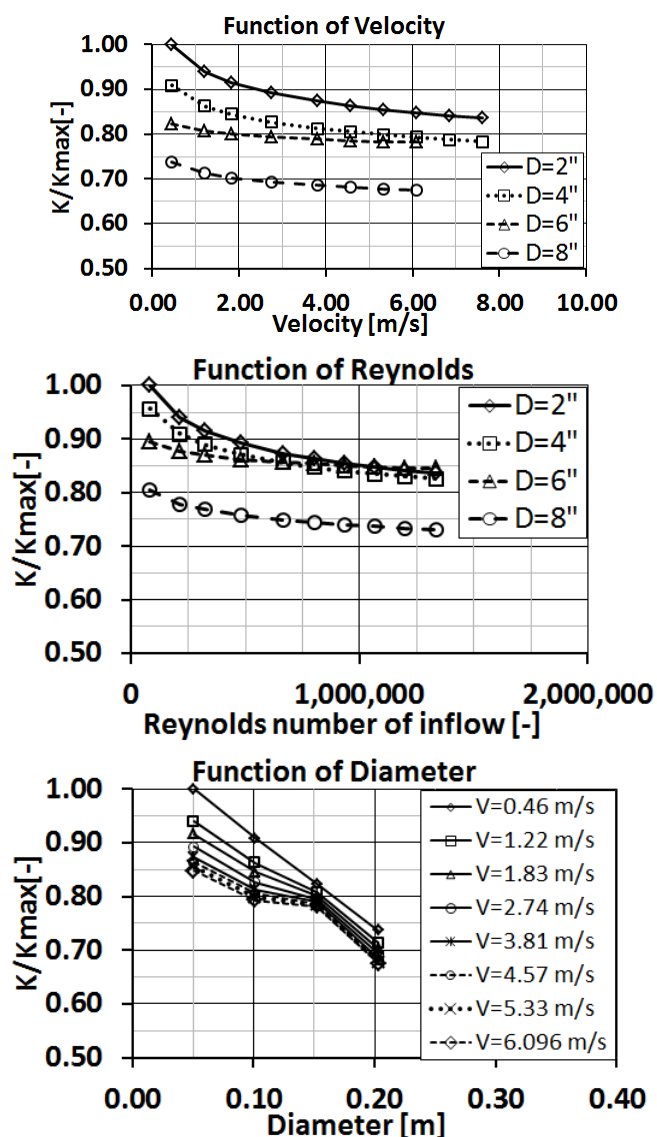


Figure 46: Normalized loss coefficients of PVC elbows as function of velocity, Reynolds number, and pipe diameter

### 3.2.3.2 PVC Tees 2, 4, 6 and 8 inches

Similar to PVC elbow, ratio of size variables ratios between tees diameter of 2 and 4 inches, 2 and 6 inches, 2 and 8 inches, 4 and 6 inches, 4 and 8 inches and 6 and 8 inches were also calculated and presented in Table 6. The standard deviation of size ratios are 48%, 47%, 49%, 2.3%, 1.8% and 1.8% respectively. The high standard deviations of size ratios are caused by variable L of tee 2 inch.

Table 6: Size ratios among PVC Tees diameter of 2, 4, 6 and 8 inches [49]

RATIO of D	RATIO OF SIZE VARIABLES			
	A	B	C	L
D2"/D4"	0.511	0.525	0.526	1.183
D2"/D6"	0.337	0.362	0.360	0.782
D2"/D8"	0.259	0.276	0.276	0.620
D4"/D6"	0.658	0.688	0.685	0.661
D4"/D8"	0.506	0.525	0.525	0.524
D6"/D8"	0.768	0.764	0.767	0.794

Normalized loss coefficients of flow through PVC tees in the inline and perpendicular branching flow is presented in Figure 47. These results are similar with the result of steel tees with diameter of 6 to 10 inches. Loss coefficients of branching and mixing tees in perpendicular flow are higher than that in inline flow. PVC tees with different sizes show loss coefficients close to each other. In the mixing flow, loss coefficients of perpendicular flow with 25% discharge ratio are positive and they are different with previous steel tees where the loss coefficient is negative.

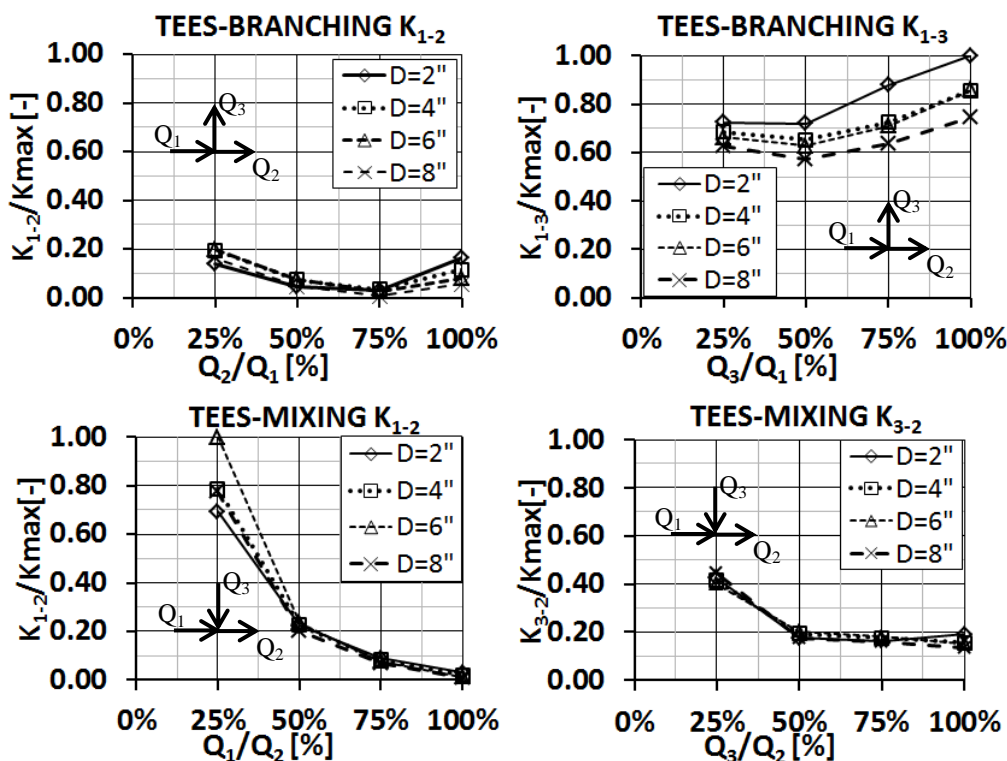


Figure 47: Normalized loss coefficients of tees for several discharge ratios in branching flow (top) and mixing flow (bottom)

### 3.3 Conclusion

Conclusions of study on loss coefficient of manifolds/fittings using data from past investigations are:

- Loss coefficient of flow through Y-bifurcator Alberschwende decreased with the increasing Reynolds number. Each test in the scale model produce different trend of decreasing loss coefficient, but in high Reynolds number, loss coefficient produced by all tests are almost the same.
- Loss coefficients of flow through Y-bifurcator Alberschwende with very high Reynolds number generated by extrapolating the differential pressure head of several tests are different. Extrapolation method does not provide satisfactory results for estimating loss coefficient of flow with prototype Reynolds number.
- Loss coefficients of Y-bifurcator Alberschwende in asymmetrical flows are higher than that in symmetrical flow.
- Physical model and numerical model of Y-bifurcator Alberschwende showed relatively good agreement in estimating loss coefficients, especially for the high Reynolds number flow.
- Loss coefficient produced by a numerical model of Y-bifurcator with prototype geometry is different with that produced by a numerical model with physical model geometry for the same Reynolds number.
- The use of numerical model can be regarded as an important and valuable supplement to the studies on a physical model.
- Loss coefficient of manufactured elbows decreased with the increasing Reynolds number and the increasing elbow diameter.
- Loss coefficients of manufactured tees in perpendicular flow higher than those in inline flow. The loss coefficients of tees with different diameters are closer to each other than that of elbows.
- The difference of loss coefficients between two manufactured elbows or tees with the same Reynolds number is contributed by dissimilarity of the geometry and low accuracy of some differential pressure measurement.

## **4 Study on Local Loss Coefficient of a Y-Bifurcator**

### **4.1 Study on loss coefficient of a Y-bifurcator using a physical model**

In this sub chapter, estimation of Y-bifurcator loss coefficient through an investigation on a hydraulic model test will be presented and discussed. The hydraulic model test used is a physical model of Pirris hydropower Y-bifurcator with scale 1:8.13 that was built in the Laboratory of Institute of Hydraulic Engineering and Water Resources Management, Graz University of Technology. Pirris hydropower itself is constructed in the southern part of San Jose province, Costa Rica to generate electricity about 140 MW. The bifurcator will divide flow from penstock to the both Pelton turbines to generate electricity. This hydro power plant is designed to contribute in the grid stabilization and meets the future electricity demand in Costa Rica.

#### **4.1.1 Past experiment on loss coefficient of bifurcator**

Several researches on investigation of loss coefficient especially for dividing and combining flow will be presented here. Vogel [50] has investigated loss coefficients of T-bifurcator with angle of  $90^\circ$ , Peterman [51] has investigated loss coefficient for separating flow in junctions of  $45^\circ$  and  $135^\circ$  and Kinne [52] has investigated of loss coefficient for separating flow in junctions of  $60^\circ$ ,  $90^\circ$  and  $120^\circ$ . Investigating loss coefficient of pipe junction also done by Blaisdell et al [53] [54], Al Naib [55] and Nichols [56]. Wood [57] has investigated pipe junction and stated that the differential pressure between section before and after junction is determined by the geometry of junction and the rate, as well as the direction of flow in several of legs in the junction.

Gardel [58], [59] formulated empirical expression to calculate pressure loss coefficient of T-junction. Ito and Imai [60] studied loss coefficient of T-junction with lateral branch angle of  $90^\circ$  and presented empirical equations for loss coefficient for Tees. Serre [61] performed a chart for loss coefficient for several discharge and area ratios. Oka [62] has investigated loss coefficient for tees with branch angle of  $45^\circ$ ,  $60^\circ$ ,  $90^\circ$ ,  $120^\circ$  and  $135^\circ$  and performed empirical equation for loss coefficient of tees with large area ratios. The equation was developed from the continuity, momentum, and energy equations.

Bingham and Blair [63] and Bassett et al [64] have performed tests on several tree-pipe junctions and formulated expression for separating flow case. Flamang [65] has developed analytical expression to calculate loss coefficient of a junction for dividing

and combining flow. Bassett [66] developed simple expression to calculate loss coefficient for tree-junction using variable of branch angle and discharge ratio.

Idelchik [67] shows diagram for loss coefficient of manifolds for diverging and merging flow. Loss coefficient was found as function of branching angle, cross section area ratio, and discharge ratio between branch and main pipes. Miller [68] also shows chart for determining loss coefficient of Y dividing and combining flow using variable of relative area ( $A_1/A_3$ ), discharge ratio ( $Q_1/Q_3$ ) and angle between the branches. Data set of dividing and combining flow for T and Y junction for several branch angle and area ratios were provided by ESDU [69], [70].

The bifurcator of Lucendro Power Station [71] has diameter of 1.10 meter and 0.80 meter for main pipe and branch respectively. Transition of the branch uses conical rounded transition, and the angle between both branches is  $55^\circ$ . The result of the study showed a good agreement between model test and field measurement, but the model test tended to produce loss coefficients higher than produced by field measurement. Salvesen [72] measured a dividing flow on plastic wye model in 1961-1962. The model has diameter of 2.78 m for main pipe and 1.80 m for the branches ( $D_{\text{branch}} = 0.65 D_{\text{main}}$ ). Six internal ribs were tested and the hydraulic loss was found very small for all cases.

Study on the hydraulic model of Causey Dam with scale 1:11 was reported by King [73]. This model consists of Y branching, high-pressure slide gate, sloping chute, stilling basin and stream channel. The discharge through the model was measured using volumetrically calibrated Venturi meter. Loss pressure in Y branch was measured using piezometer that was installed at a point before and after Y branch. This study produces a graph of loss coefficient based on the percentage of ratio between the discharge of branch and main pipe.

Russ [74] investigated the energy loss of flow through wye and manifold. The investigation was done using model scales and was conducted several tests. The model scales consists of three conical wyes with bifurcator angle of  $60^\circ$ ,  $45^\circ$  and  $90^\circ$ . The loss coefficients are calculated from total loss divided by velocity head in the main pipe. The total loss is loss caused by friction and shape of wye or manifold. The correlation between Reynolds number and loss coefficient for several types of wye and manifold were published. The result of the study can be summarized that in the symmetrical flow, the wye and manifold head loss can be minimized by decreasing angle of the bifurcation. Head loss is less than 10 % of the main pipe velocity head in the symmetrical flow bifurcator with angle less than  $60^\circ$ . Head loss of the prototype is likely different from those in the physical model.

Lee et al [75] investigated loss coefficient of Y branch of pumped storage Muju located in southern portion of the Keum River basin Republic of Korea. The pumped

storage has capacity of 600 MW generated by two turbines. A Y branch steel penstock that located in a vertical bend was used to divide flow to the turbines. The diameter of main pipe is 4.0 meter and diameter of each branch was 2.8 meter. In order to know the influence of designed Y-branch to the flow and pump turbine operation, a 1:13.7 physical model made from clear acrylic pipes was constructed. Loss coefficient was calculated from energy loss divided by velocity head in the operated branch. Loss coefficient for symmetrical generating or pumping operation was found in range of 0.2 to 0.3 and in range of 0.3 to 0.4 for asymmetrical operation. The number of sickle plates did not give a significant difference in loss coefficient.

A physical model of Y-bifurcator Alberschwende [76] with scale 1:12.85 was built using Plexiglas. To investigate loss coefficient of bifurcator, the flow was measured by magneto-inductive precision flow meters and at both branches controlled by Howell-Bunger valves. Pressures at six cross sections at point before junction and four cross sections at point after junction were measured by pressure transducer. This model has been discussed in the previous chapter.

Hydraulic investigation on a physical model of Pirris Y-bifurcator also has been done by Dobler et al [77], [78]. The investigation consist of pressure losses measurements along the penstock for certain flow distribution and velocity measurement using Particle Image Velocimetry (PIV) to know the velocity profile at certain control section. Investigation data from this scale model measurement are used by author for further study.

### **4.1.2 Construction of a physical model**

A physical model of Pirris Y-bifurcator with scale 1:8.13 was made using Plexiglas with diameters of 0.246 m for the main pipe and 0.123 m for each branch. The branch angle was  $40^\circ$ . Transition from diverging point to the branch used pipes diameter of 0.185 and 0.172 mm. Installation of the physical model in the laboratory can be seen in the Figure 52. Total length of model scale was 70 meter, 50 meter for the upstream and 20 meter for the downstream of bifurcator. A bend in the main pipe and a confusor in each branch that exist in the prototype design were also involved in the physical model. A flow conditioner located at the beginning of the model was used to smoothing inflow to avoid the secondary flow.

Pressure sensors used to measure differential pressure head between two sections at upstream and downstream of bifurcator. Pressure sensors were calibrated using pressure head calibration tool. The calibration was done by adjusting pressure head that read by pressure sensor to become the same with the hydrostatic head level in the calibration tool.



Figure 48: Installation of physical model Y-bifurcator in the laboratory [26]

### 4.1.3 Data acquisition

Discharges were measured using flow meter in the main pipe, left and right branches. The sample rate frequency of flow meter was 1 kHz and the time length for each measurement is 60 seconds. Therefore, the number of discharge rates and differential pressure for one measurement are 60,000 data points. Principle of the flow meter in measuring velocity and discharge in the pipe is based on the electromagnetic induction. In the measurement of high discharge, flow meter can achieve accuracy of 0.5 to 1 % of the measured discharge rate. The discharge rate flows in the branches are controlled by two automatic dispersion valves.

Differential pressures were measured using PD-23 pressure sensor at seven sections in the main branch and six sections in each left and right branches (Figure 49). At each section, the pipe was drilled to make eight holes with a diameter of 1 mm and all holes were connected together to obtain average value of pressure in the pipe. The maximum uncertainty of the pressure probe was 0.5% of the full range [78]. Similar to the discharge measurement, sample rate frequency of pressure sensor was also 1 kHz and the time length of each measurement was 60 seconds. Section on the main pipe, left and right branches were marked by M, L and R respectively and its index number.

Discharge flow to the left and right branches is regulated by operating the valve at both branches in the physical model. Experiment carried out six simulations case that are distinguished by the weighted factor of discharges flowing in the left and right branches, as shown in Table 7. There are six cases, case 1 to 4 are experiments in turbine mode where the water flows from the main pipe to the branch. Case 5 and 6 are experiments in pumping mode, where the water flow reverses from the branch to the main pipe. For each case in turbine mode, there are four experiment groups (RUN) is done. Each experiment group is distinguished by ratio between discharge flow to the left or right branch and the main discharge. Experiment RUN2 is a repetition of experiment RUN1, while experiment RUN4 is also a repetition of experiment RUN3. Experiment RUN3 and RUN4 are the inverse discharge ratio of experiment RUN1 and RUN2. The pumping mode experiments are only done for two groups for each case.

Every group is performed nine simulations with discharge range from  $0.010\text{m}^3/\text{s}$  to  $0.210\text{m}^3/\text{s}$ . The discharges are measured at the main and branches pipes for each experiment. The differential pressure head between section M1 and certain section at the main pipe (M2 to M6) or branches (L1 to L6 and R1 to R6) are also measured.

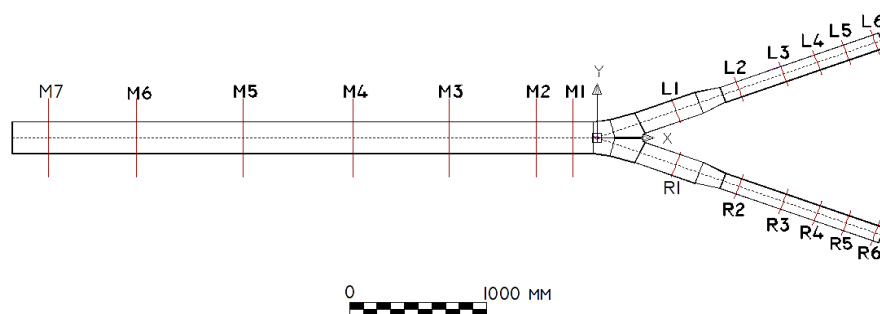


Figure 49: Measurement sections of differential pressure head [26]

Table 7: Scenario of discharge weighted factor for physical model simulation

CASES	RUN	Weighted factors of discharge		MODE
		LEFT	RIGHT	
1	1	1	0	Turbine
	2	1	0	
	3	0	1	
	4	0	1	
2	1	1	0.5	Turbine
	2	1	0.5	
	3	0.5	1	
	4	0.5	1	
3	1	1	0.75	Turbine
	2	1	0.75	
	3	0.75	1	
	4	0.75	1	
4	1	1	1	Turbine
	2	1	1	
	3	1	1	
	4	1	1	
5	1	1	0	Pumping
	2	0	1	
6	1	1	1	Pumping
	2	1	1	

Note: 1 = fully opened and 0 = fully closed.

#### 4.1.4 Data analysis

Each measurement is addressed to obtain 60,000 data sets consisting of the time series of discharges and differential pressures. With these data, it is feasible to calculate the average value and the standard deviation. The result of data analysis shows that the percentage of standard deviation obtained in the simulation on low discharge is quite high, but it decreases with increasing discharge. This appears on the results of discharge measurement in both of the main and branches pipes as shown in Figure 50.

The discharge deviation percentage measured in the main pipe is started with value of 3.2% for first simulation (inflow=0.0123 m<sup>3</sup>/s) and decreases until the last simulation (inflow=0.1083 m<sup>3</sup>/s) reaches the value of 0.5%. The discharge deviation percentage in branch pipe is smaller than that in the main. The first simulation shows that the discharge deviation percentage in branch pipe is 0.72 % and decreases to become 0.25% at the last simulation (highest inflow discharge).

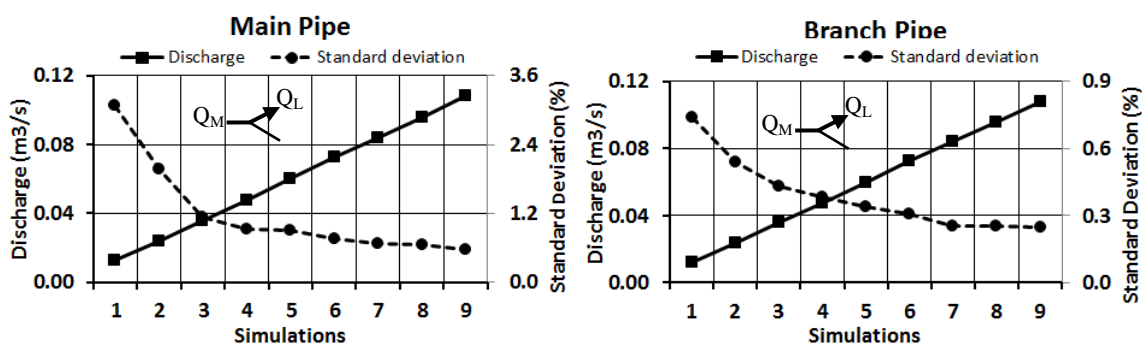


Figure 50: Discharge measurement and standard deviation of the main pipe (left) and the branch pipe (right).

Differential pressure head between section M1 and sections in left branch (L1 to L6) is shown in Figure 51-top. Figure 51-bottom shows standard deviation of differential pressure. The highest percentage of differential pressure deviation occurs at measurement of M1-L1. Section L1 is located between the bifurcator and the confusor, so the existence of both structures causes secondary flow that strongly affects in the way that the pressure changes in time. Pressure measured in the section L1 is high uncertainty and it will not be used for further calculation. Like discharge measurement, differential pressure also shows high percentage of standard deviation in low discharge simulation and it decreases with increasing flow rate. The measurement accuracy of differential pressure between sections in the main pipe and in the downstream of branch confusor is almost the same. The accuracy increases if the discharge increases.

Y-bifurcator and confusor are designed to flow water from main pipe with diameter of 246 mm to branches pipe with diameter of 123 mm. Bifurcator and confusor connected by transition pipe with diameter 185 mm in bifurcator side and diameter of 172 in confusor side. In Figure 51 top can be seen that differential pressure head increase steeply from section L1 to section L2. In this section, the confusor is located to connect pipe with diameter of 172 mm and pipe with diameter of 123 mm. The differential pressure head is not only caused by friction but also by contraction flow in the confusor. At downstream confusor (between section L3 and L6), differential pressure head increases gradually where it mainly caused by friction between water and pipe wall.

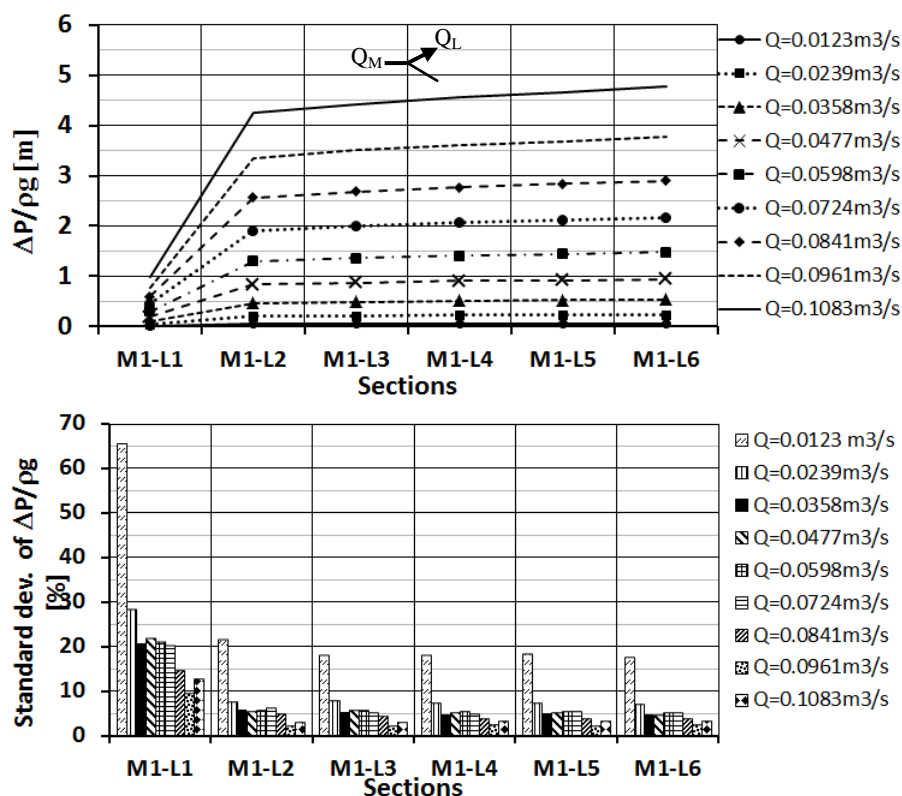


Figure 51: Differential pressure head (top) and the standard deviation (bottom)

#### 4.1.5 The differential pressure head of the physical model

Pressure head can be defined as an internal energy of a fluid due to the pressure exert on its container. The pressure head (m) is calculated from the fluid pressure ( $N/m^2$ ) divided by specific weight of the fluid ( $N/m^3$ ). The differential pressure head (differential pressure) between each measurement section and section M1 is plotted in the Figure 52. The top figure shows the differential pressure head for different inflow discharge in condition of asymmetrical flow (water only flow to the left branch because the right branch is closed). The bottom figure shows the differential pressure head for different inflow discharge in condition of symmetrical flow (water flow to the both branches with the same magnitude).

Pressure drop on the main pipe from section M6 to M1 is mostly caused by friction between water and the pipe wall. After section M1, pressure drop is caused by friction and shape of the bifurcator. Therefore, the pressure decreases sharply in the section L1. Meanwhile, decreasing pressure in section L2 is caused by combination of the friction, the shape of bifurcator and the confusor. In the figure can be seen that pressure drop caused by bifurcator is smaller than that caused by confusor. In the section L1, the flow is influenced by bifurcator and confusor that they can cause secondary flow, so the pressure measured in this section is very fluctuate (pressure has high standard deviation as seen in See Figure 51) and has low accuracy. Pressure drop

in section L3 to L6 is caused by friction and small influence of confusor. The pressure in this section decrease gradually and the decreasing is nearly linear. Because of the confusor is part of bifurcator, loss coefficient should be calculated by using different pressure measured in between upstream of bifurcator and downstream of confusor.

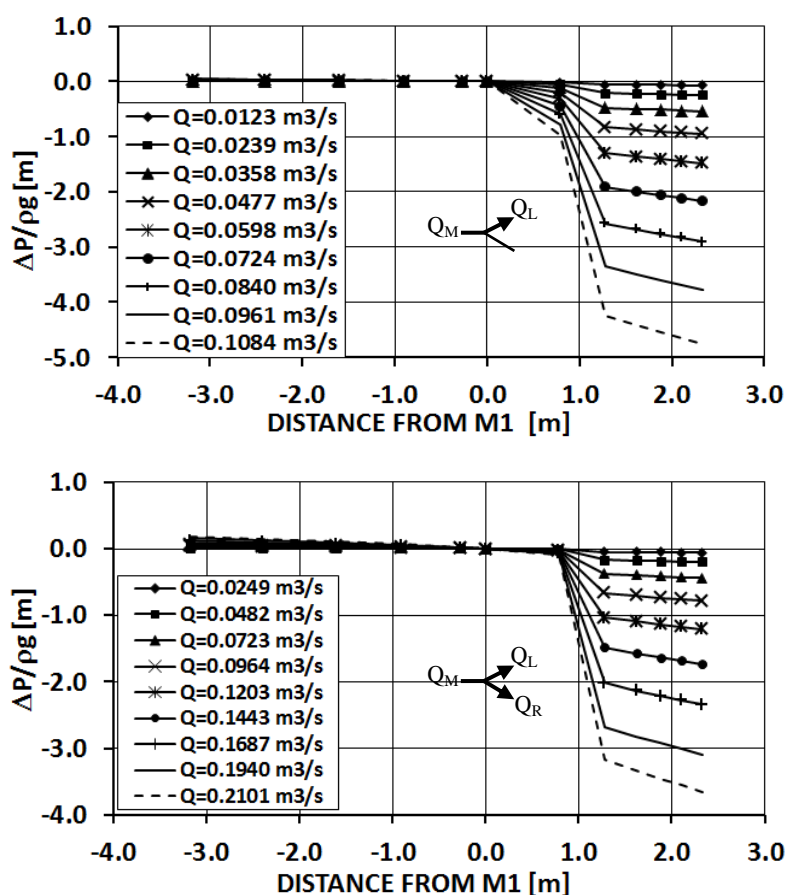


Figure 52: Differential pressure head of asymmetrical (top) and symmetrical flows (bottom)

#### 4.1.6 Loss coefficient of a physical model

Differential pressure head and differential velocity head between section in the main and branch pipe are used for calculation of loss coefficient. The total loss is calculated by applying the energy equation to the sections at upstream (M) and downstream (L/R) of bifurcator. The local loss is obtained by subtracting total loss with friction loss. Actually, separating friction loss from the total loss is very difficult because there is an interaction between friction and shape. Nevertheless, to calculate friction loss, an approach can be done by calculating friction loss over an equivalent length straight pipe with assumption that the flow in the pipe is a fully developed. For this purpose, the bifurcation is idealized into 15 cylinders with different length and diameter to enable this calculation, as shown in Figure 53.

Calculation of friction loss in a straight pipe for certain inflow is used to determine the friction of each cylinder. The total friction loss is the sum of cylinders friction loss between two sections, before and after bifurcator, is reviewed. The friction loss calculation uses Darcy-Weisbach and Colebrook-White equations.

The loss coefficients are calculated from the local loss divided by velocity head in the inflow section. To calculate loss coefficient, two measurement data at the point before and after bifurcation are needed, e.g. loss coefficient of M6-L2 means that the loss coefficient is obtained from the calculation using data at section M6 for the upstream and section L2 for the downstream. The inflow discharge ( $Q_{in}$ ) is discharge, which is measured in the main pipe. The inflow velocity ( $u_{in}$ ) is calculated from the inflow discharge  $Q_{in}$  divided by cross section area of M2. The outflow discharge ( $Q_{out}$ ) is discharge, which is measured in the branch pipe. The outflow velocity ( $u_{out}$ ) is calculated from the outflow discharge  $Q_{out}$  divided by cross section area of L6. Using both velocities, the differential velocity head ( $\Delta u^2/2g$ ) between main and branch pipes can be calculated. The equation of Darcy-Weisbach is used to calculate the friction loss ( $\Delta h_f$ ) of idealized pipe between section M2 and L6 (pipe sections S6 to S15 in Figure 53). The differential pressure head ( $\Delta h_p$ ) is obtained from measurement of differential pressure head between section M2 and L6. Referring to energy equation, the local loss was calculated by adding differential pressure head with differential velocity head and subtracting with friction loss. Finally, the loss coefficient M6-L2 is calculated by dividing the local loss with the velocity head in the main pipe (M2).

The Reynolds number was calculated to perform the loss coefficients in a graph. Calculation of loss coefficients were also done for others two different sections, that are sections M6-L2, M6-L3, M6-L4, M6-L5, M6-L6, M5-L2, M5-L3, M5-L4, M5-L5, M5-L6, M4-L2, M4-L3, M4-L4, M4-L5, M4-L6, M3-L2, M3-L3, M3-L4, M3-L5, M3-L6, M2-L2, M3-L3, M2-L4, M2-L5, and M2-L6. With these results, average value of loss coefficient for each Reynolds number was obtained. Regarding to the confidentiality of data, real loss coefficient values were normalized by value of maximum loss coefficient.

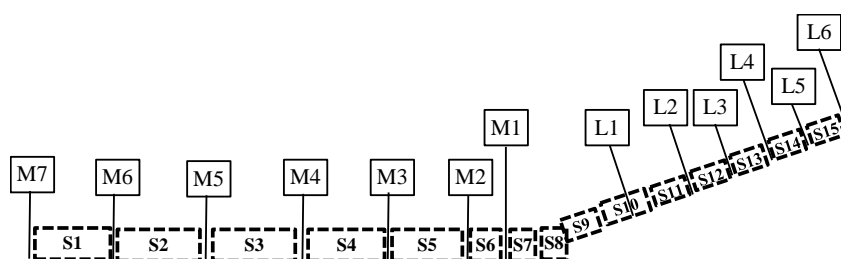
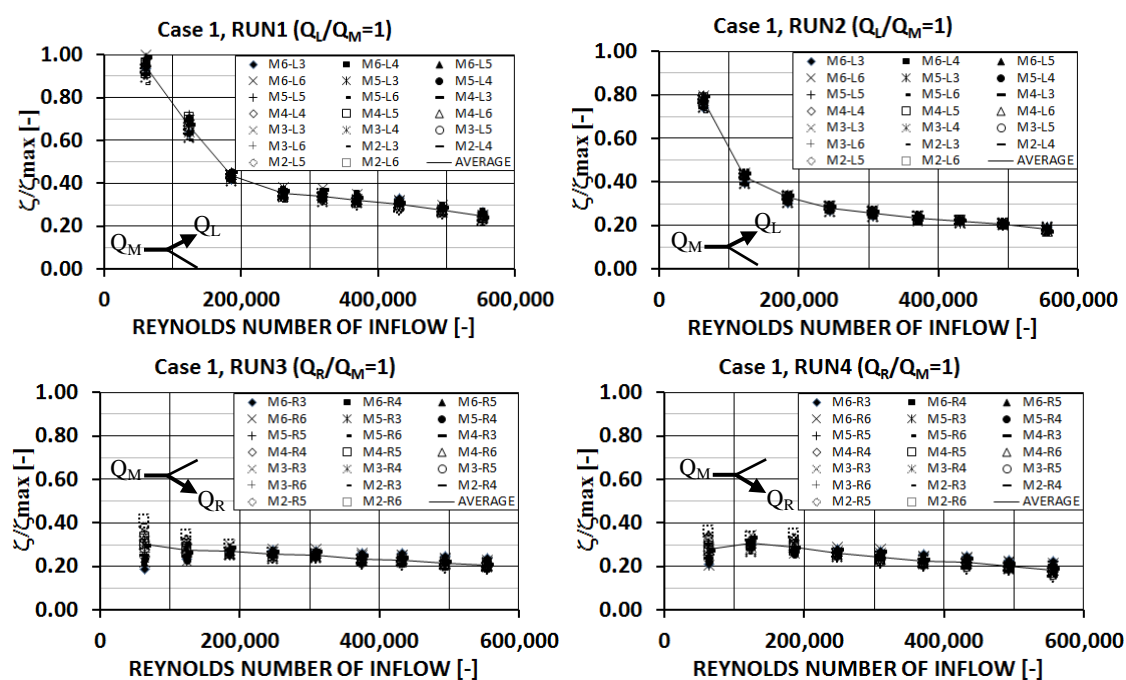


Figure 53: Idealized pipe sections of Pirris Y-bifurcator [26]

Table 8: List of diameter and length of idealized pipe

No	Sections	Diameter (m)	Length (m)
1	S1	0.246	0.637
2	S2	0.246	0.782
3	S3	0.246	0.800
4	S4	0.246	0.695
5	S5	0.246	0.637
6	S6	0.246	0.268
7	S7	0.246	0.147
8	S8	0.262	0.140
9	S9	0.185	0.234
10	S10	0.172	0.543
11	S11	0.123	0.163
12	S12	0.123	0.345
13	S13	0.123	0.262
14	S14	0.123	0.225
15	S15	0.123	0.225

Figure 54 shows the normalized loss coefficients for Case 1, RUN1 to RUN4 that calculated from several sections.

Figure 54: Normalized loss coefficients of Case 1, RUN1 to RUN4,  $Q_{out}/Q_{in}=1$ 

The four graphs show similar trend that loss coefficient decreases with the increasing Reynolds number. Reynolds number has significant influence to the loss coefficient in low flow. Effect of Reynolds number on loss coefficients decreases with increasing flow. Loss coefficients that are calculated in different sections in the low Reynolds number region give greater variation than those in high Reynolds number region. The friction loss is calculated using approximation of friction of a straight pipe and the friction factor calculated by Colebrook-White equation. In the low Reynolds number region of Moody diagram, friction factor decreases rapidly with increasing Reynolds

number, but in the high Reynolds number region, it decreases gradually. RUN1 and RUN2 have similar trend where the loss coefficient declines rapidly at Reynolds number below 200,000 and then declines gradually. Loss coefficient of RUN3 and RUN4 decreases gradually from low to high Reynolds number.

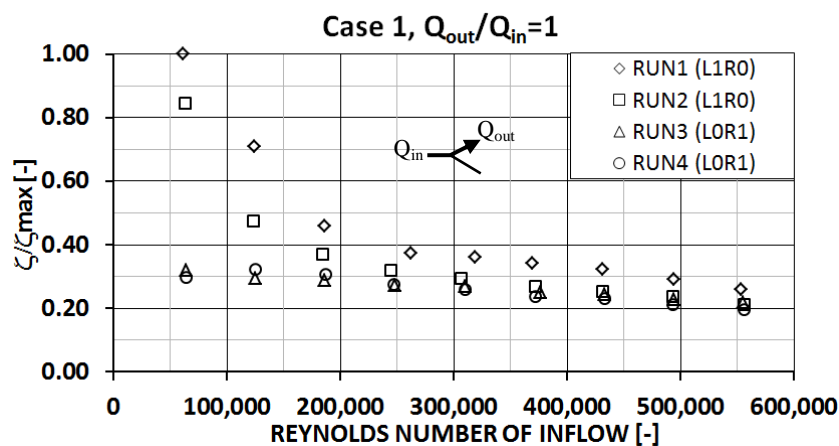


Figure 55: Normalized loss coefficients (average value) of Case 1

The differences of loss coefficient between experiment left and right branches are identified by comparison of normalized loss coefficient in Figure 55. In the low Reynolds number, simulations using left and right branches give different result. Normalized loss coefficients (average values) produced by RUN1 in high Reynolds number are about 25% higher than produced by others. Loss coefficient of low Reynolds number is much higher than that of high Reynolds number. The loss coefficient of Case 1 in high Reynolds numbers varies from 20% to 27% of the maximum loss coefficient.

In the experiment of Case 2, water from the main pipe is divided to be 67% flow to one branch and the rest flow to another branch. Differential pressure head between main pipe and branch in Case 2 is lower than that in Case 1 caused by the decrease in discharge flowing into the branch. Figure 56 shows the normalized loss coefficients calculated from the experiment of Case 2 where 67% water flows to a branch. In RUN1 and RUN2, 67% of water from the main pipe is supplied to the left branch and 33% to the right branch. RUN3 and RUN4 are the inverses of RUN1 and RUN2 where 67% of water flows to the right branch and 33% to the left branch. The four graphs show considerable variation of loss coefficient values in the all range of Reynolds numbers.

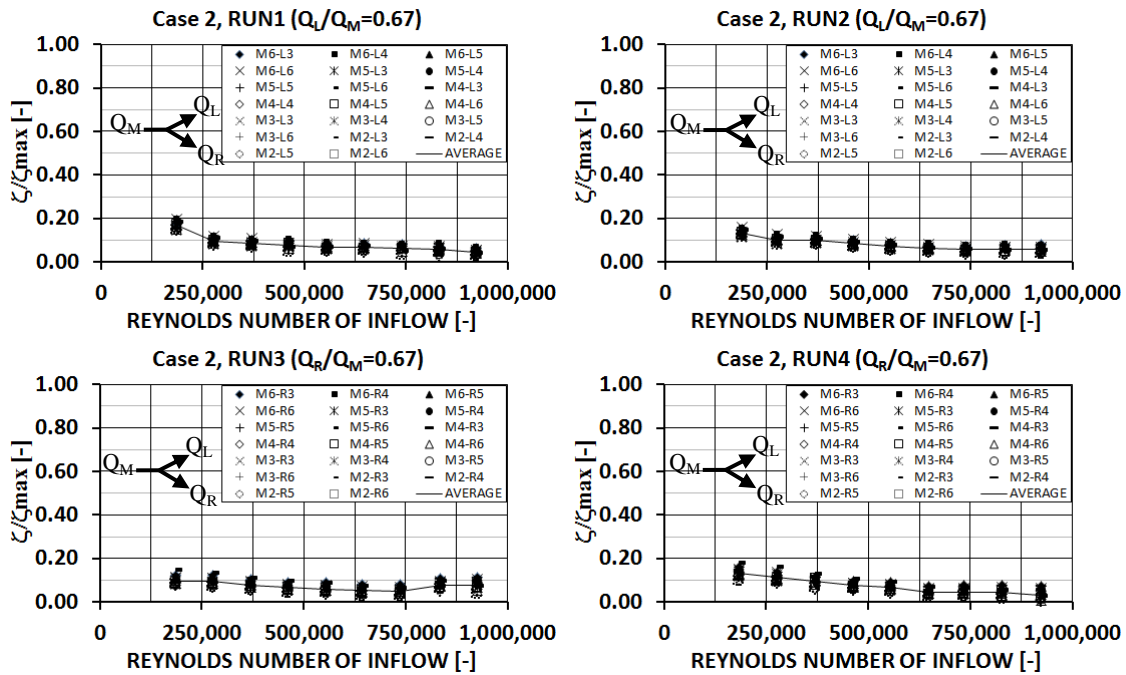


Figure 56: Normalized loss coefficients of Case 2, RUN1 to RUN4,  $Q_{out}/Q_{in}=0.67$

Figure 57 shows the result of experiment in Case 2 where 33% water flows to a branch. From the previous result of Case 2 with  $Q_{out}/Q_{in}=0.67$ , the loss coefficient which is computed on each pair of inflow and outflow sections in these experiments varies in small range for both low and high Reynolds numbers. The difference of loss coefficient between low and high Reynolds number region is small.

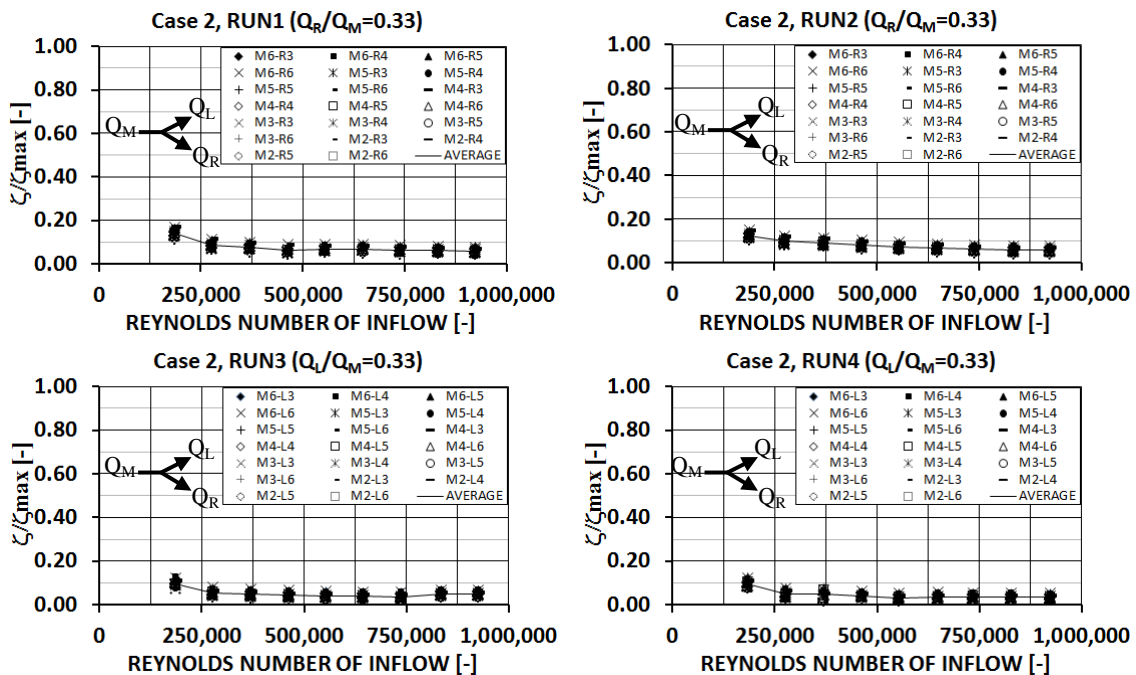


Figure 57: Normalized loss coefficients of Case 2, RUN1 to RUN4,  $Q_{out}/Q_{in}=0.33$

Figure 58 shows the normalized loss coefficient (average value) produced by four experiments of Case 2 with 67% discharge flow to one branch. The normalized loss coefficients of all experiments are close each other with the increasing discharge, except the result of RUN3. RUN3 generate loss coefficient increases in the high Reynolds number. The graph of normalized loss coefficient of Y-bifurcator  $Q_{out}/Q_{in}=0.67$  declines with the increasing Reynolds number. In high flow, the Reynolds number gives small influence to the loss coefficient. The loss coefficient of the highest Reynolds numbers in Case 2 with  $Q_{out}/Q_{in}=0.67$  varies from 5 % to 8 % of the maximum loss coefficient. There is a small difference between average loss coefficient produced by experiments using the left and right branches. The experiments using left branch gives loss coefficient a little higher than those using right branch. The two experiments using the same branch give loss coefficient close to each other. In RUN3 with  $Q_{out}/Q_{in}=0.33$ , loss coefficients in high Reynolds region increase, as occur in the experiment of  $Q_{out}/Q_{in}=0.67$ . The loss coefficient of experiment on high Reynolds number varies from 4 % to 8% of maximum loss coefficient.

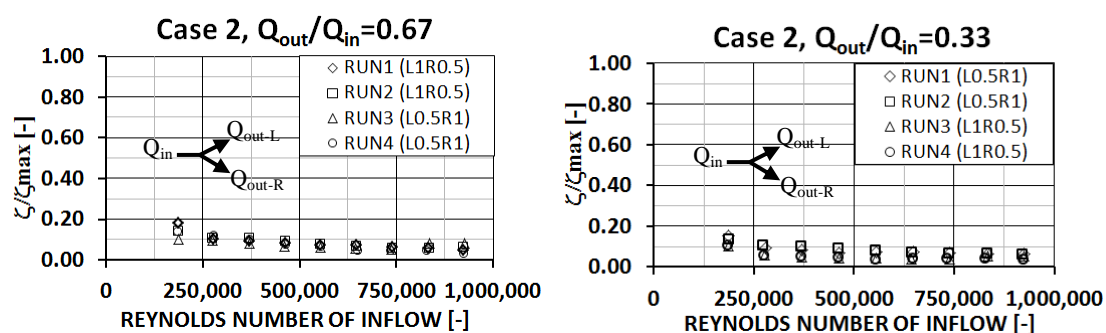


Figure 58: Normalized loss coefficients (average value) of Case 2,  $Q_{out}/Q_{in}=0.67$  (left) and  $Q_{out}/Q_{in}=0.33$  (right)

In experiment of Case 3, water flows from the main pipe are 57% to one branch and the rest to another branch. Comparison among calculation results of normalized loss coefficients for experiment in Case 3 with ratio of outflow and inflow discharge of 0.57 are shown in Figure 59. Variations of loss coefficients produced by several pressure measurements in different section in upstream and downstream of bifurcator are small. Loss coefficient decreases with the increasing Reynolds number. The difference of loss coefficient between low and high Reynolds number is also small.

Normalized loss coefficients of flow through bifurcator with discharge ratio 43% produced by four experiments are presented in Figure 60. Similar to other cases, loss coefficient in this case also decreases with the increasing Reynolds number. Variations of loss coefficient calculated by several sections in upstream and downstream of bifurcator for all experiments are small except the result of RUN3. The result of loss coefficient calculation of Case 3 with  $Q_{out}/Q_{in}=0.43$  has similar trend to

the result of Case 2 with  $Q_{out}/Q_{in}=0.33$  compared with the result of Case 3 with  $Q_{out}/Q_{in}=0.57$ .

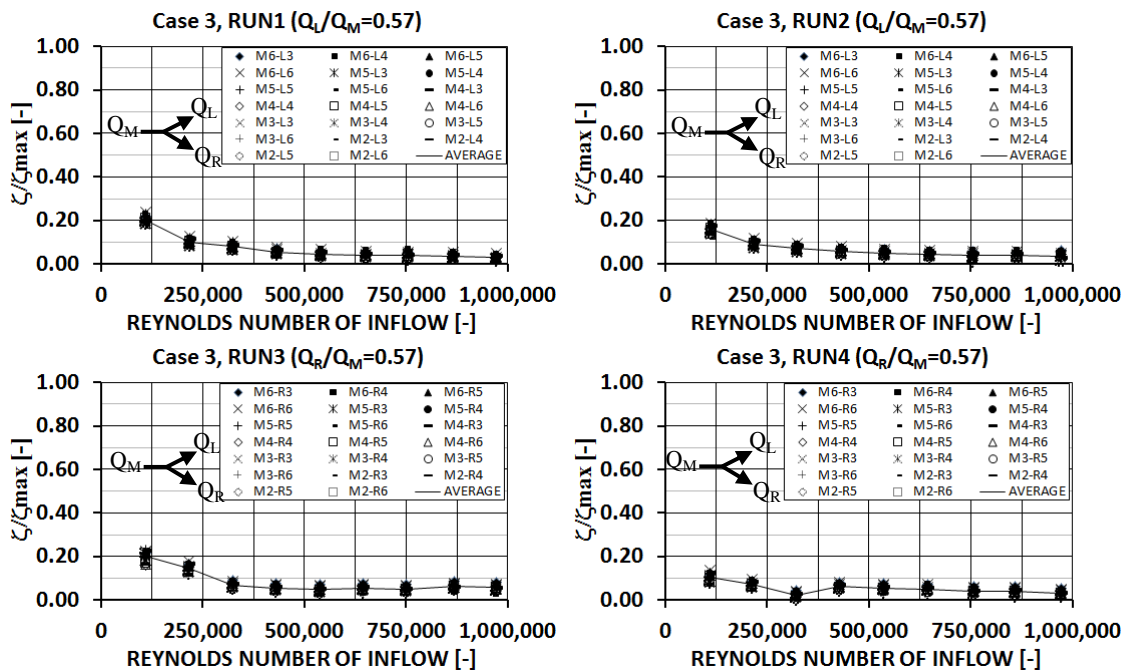


Figure 59: Normalized loss coefficients of Case 3, RUN1 to RUN4,  $Q_{out}/Q_{in}=0.57$

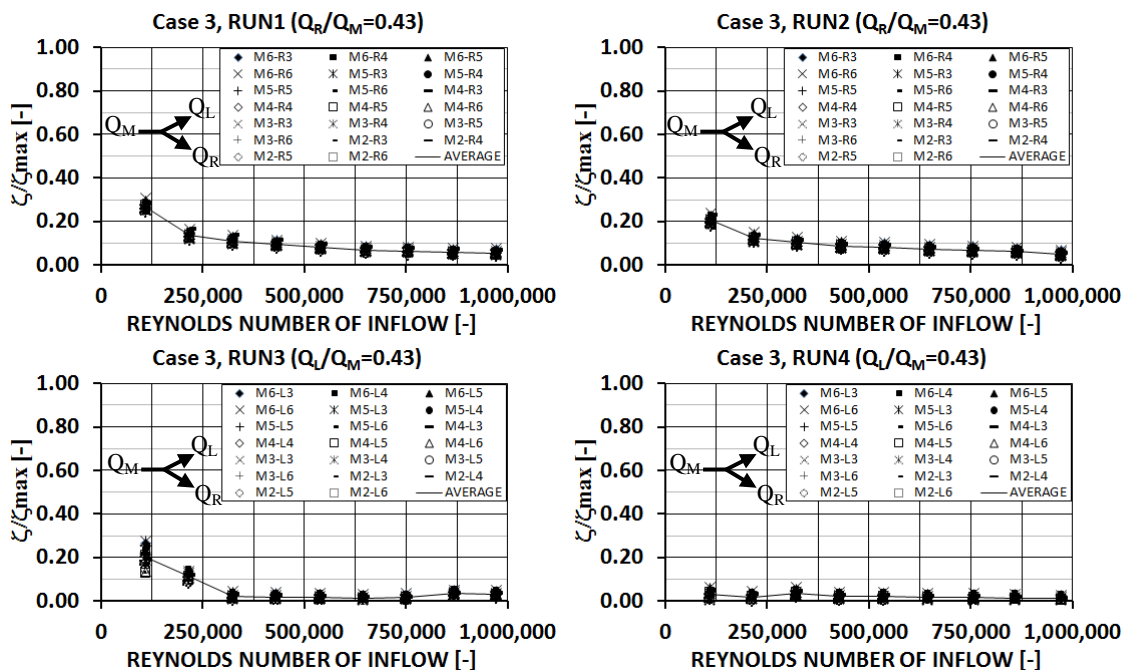


Figure 60: Normalized loss coefficients of Case 3, RUN1 to RUN4,  $Q_{out}/Q_{in}=0.43$

The normalized loss coefficients (average value) for Case 3 with  $Q_{out}/Q_{in}=0.57$  are performed in Figure 61 (left). In the low Reynolds region, loss coefficients that are calculated from the left branch measurements (RUN1 and RUN2) are almost the same. Different result obtained from right branch measurement where loss coefficient

of RUN3 is two times higher than that of RUN4. Loss coefficients that are calculated by all experiment in this case in high Reynolds number region are close to each other except the result of RUN3. The results of experiment RUN1 and RUN2 (left branch) are closer each other compared with the result of experiment RUN3 and RUN4 (right branch) for low and high Reynolds number region. The normalized loss coefficients (average value) in the high Reynolds number vary from 3% to 7% of the maximum. Figure 61 (right) shows the comparison of normalized loss coefficients (average value) among four experiments of Case 3 with  $Q_{out}/Q_{in}=0.43$ . The left branch experiment produces loss coefficient higher than the right branch. Left branch experiment also gives better and more consistent result than right branch. Loss coefficient for higher Reynolds number varies from 1% to 7% of maximum loss coefficient.

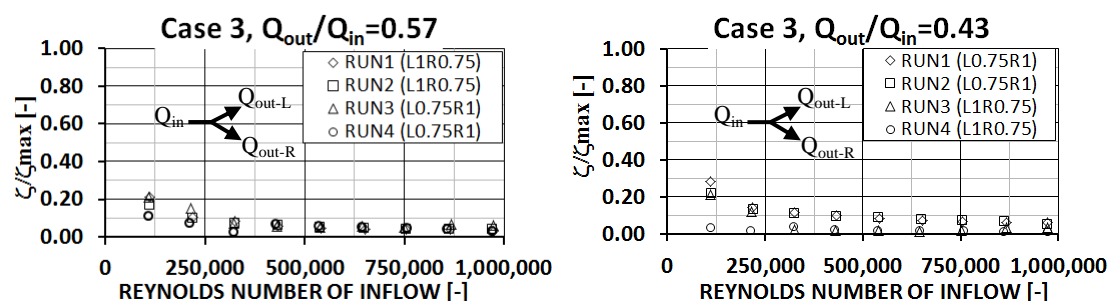


Figure 61: Normalized loss coefficients (average value) of Case 3,  $Q_{out}/Q_{in}=0.57$  (left) and  $Q_{out}/Q_{in}=0.43$  (right)

The last case for the experiment on the turbine mode is Case 4. Experiments Case 4 simulates symmetrical flow condition. The discharge flows from the main pipe to the both branches with the same magnitude. The first experiment group is controlled by operation of the left branch valve in order to flow 50% of the water (Figure 62). The second group is controlled by the right branch valve (Figure 63).

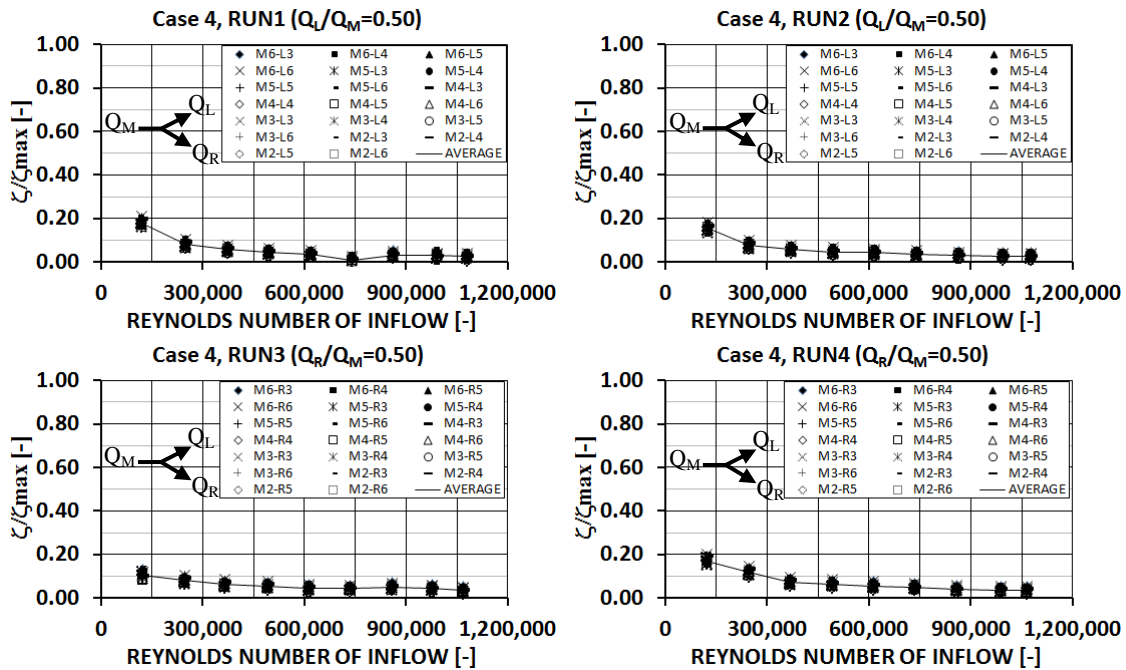


Figure 62: Normalized loss coefficients of Case 4-L, RUN1 to RUN4,  $Q_{out}/Q_{in}=0.5$

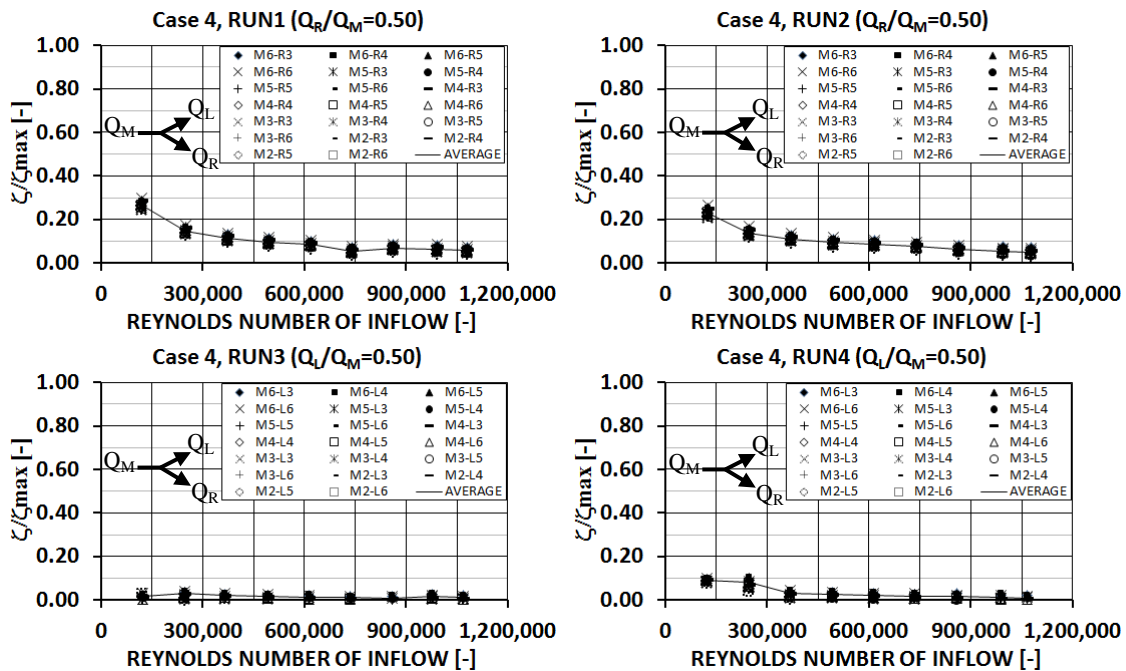


Figure 63: Normalized loss coefficients of Case 4-R, RUN1 to RUN4,  $Q_{out}/Q_{in}=0.5$

The loss coefficient in the symmetrical flow experiment is smaller than that in the asymmetrical flow. The trend of loss coefficient decreases with the increasing Reynold number. When the flow is controlled by left valve, the loss coefficient resulted by left and right branch are similar. But when flow is controlled by right valve, the loss coefficient resulted by left branch are smaller than that resulted by right branch. Similar with previous experiments, the loss coefficients that are found from four group experiments using left branch are closer to each other compared with the

result of experiment using right branch (see Figure 64). The left branch experiments are more consistent compared to the right branch experiments.

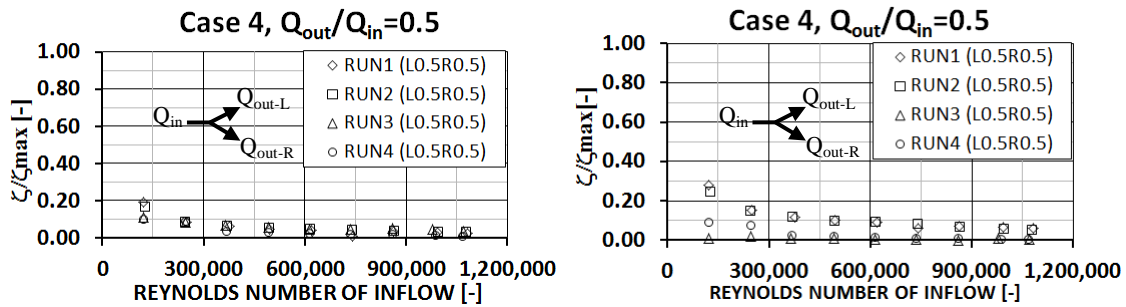


Figure 64: Normalized loss coefficients (average value) of Case 4,  $Q_{out}/Q_{in}=0.5$  using left branch (left) and right branch (right)

Reverse to the turbine mode, in the pumping mode, the water is pumped from one or two branches into the main pipe. The loss coefficient of pumping mode is calculated by dividing local loss with the velocity head of inflow (branch pipe). Because the diameter of branch pipe is small, the velocity is high, so the value of velocity head is also high. High velocity head will cause loss coefficient in pumping mode becomes smaller compared with the loss coefficient of turbine mode. When water only flows from a branch to the main pipe while another branch is closed, this simulation is called asymmetrical flow pumping mode. Case 5 is simulation in asymmetrical flow pumping mode. Figure 65 illustrates normalized loss coefficients in several Reynolds number as the result of experiment in asymmetrical pumping mode. The variation of loss coefficient to the Reynolds number and different section is small.

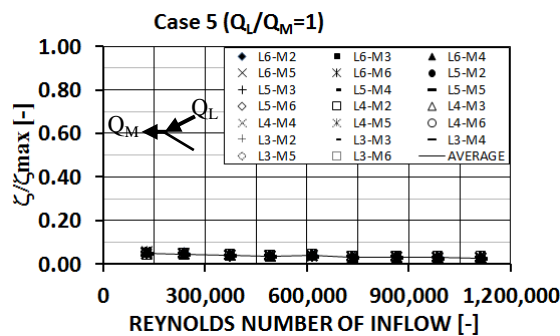


Figure 65: Normalized loss coefficients of Case 5 ( $Q_L/Q_M=1.0$ ) pumping mode

Case 6 is a simulation of flow through a bifurcator from both branches with the same flow rate to the main pipe. There are two group experiments in the Case 6. First group is the flow controlled by left valve and the second group is the flow controlled by right valve. Similar to the result of asymmetrical flow, the loss coefficient calculated from the result of measurement in symmetrical pumping mode is presented in Figure 66. Pumping mode simulations produce smaller variation of loss coefficient in Reynolds number and different sections compared to those in the turbine mode simulation.

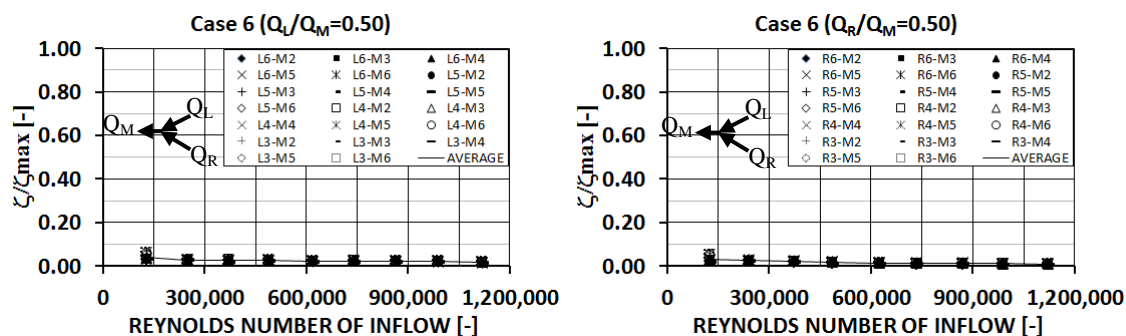


Figure 66: Normalized loss coefficients of Case 6,  $Q_L/Q_M=0.50$  (left) and  $Q_L/Q_M=0.50$  (right) in pumping mode

## 4.2 Numerical Simulation of a Physical Model of Y-Bifurcator

Computational Fluid Dynamic (CFD) is a branch of science that studies the fluid flow, heat transfer, chemical reaction and other phenomena associated with fluid motion by using an approach of solving mathematical equations [79]. The advantages using CFD are widely understanding of model flow behavior and give possibility to look virtually deeply into parts of the model that are difficult to be seen in the prototype. The other advantage is that CFD can be used to predict the phenomenon caused by changes in the model geometry and boundary conditions. Economic benefit of using CFD is saving time and cost in the design or problem-solving process, so it enables to analyze various alternatives or conditions to obtain the optimal solution.

Several researchers have used numerical model and compared the result with investigation results on a physical model and field measurements. Unsteady modeling of flow through a manifold was done by Benson [80]. Basset et al. [81], [82] have modeled the propagation of shock waves through junctions using steady flow losses. Investigation on loss coefficient using CFD was done by Kuo et al [83] [84], Klell et al. [85], Dimitriadis et al. [86] and Flamang and Sierens [87]. Zmrhal and Schwarzer [88] have used CFD to estimate the loss coefficient of elbows and bends. The simulation results give good agreement with the published measurement data. Klasinc and Bilus [89] have obtained reasonable agreement between experimental and numerical investigation on flow through a nozzle of pipe-junction for different geometric scales. Klasinc et al. have also conducted some experimental and numerical studies to observe head loss in the manifold of pump storage system [39], pressure loss of a penstock bifurcator [41], and pressure loss of a manifold in the hydropower scheme [43]. The result of numerical model shows good agreement with the measurement on the physical model.

This sub chapter will discuss numerical simulations of a physical model of Pirris Y-bifurcator. The objective is to gain a good understanding in the numerical modeling and to know the capability of numerical model in simulating turbulence flow through

a Y-bifurcator. The numerical model results were compared to measurements in the physical model. Numerical model will be used to predict loss coefficient of flow with high Reynolds number and to investigate correlation of loss coefficient among numerical model with different geometry size.

### 4.2.1 General setup of the numerical model

Numerical model geometry of Y-bifurcator was built based on the geometry of a physical model, including sloping pipe, horizontal pipe, bend, bifurcator, and confusor. The geometry mesh was generated by Gambit software using grid interval of 10, 12, and 14 mm. Mesh with interval of 10 mm consist of 1,468,487 cells, 3,862,813 faces, and 931,684 nodes (Figure 67). Numerical model simulations were done using commercial software of ANSYS FLUENT 12.1. The pressured-based was chosen as a solver and use absolute for velocity formulation. To simulate turbulent flow, the viscous model of realizable k- $\epsilon$  was used with the default constant of C2- $\epsilon$ , TKE Prandtl number and TDR Prandtl number are equal to 1.9, 1.0 and 1.2 respectively. The model used standard wall functions for near wall treatment. Water with constant density of 1000 kg/m<sup>3</sup>, constant specific head of 4182 J/kg.k, and constant viscosity of 0.00101kg/m.s was used for fluid material type. Numerical model was simulated flow through a Y-bifucator in 3-dimension steady and unsteady. The inflow boundary condition is mass flow rate using turbulence specification method of intensity and hydraulic diameter. The mass flow rates are the measurement discharges at the main pipe of physical model multiplied by water density. The outflow boundary conditions are the weighted factor of discharge flow to the left and right branches. The weighted factor of outflow was determined in accordance with outflow discharge measured in both branches in physical model. The wall boundary condition used was static wall with the roughness height for Plexiglas of 0.0187 mm according to the research of Dobler [78]. The equations of flow and turbulence are used for solution control. A SIMPLE model was used as pressure velocity coupling. The discretization of momentum, turbulence kinetic energy, and turbulence dissipation rate used second order upwind. The value of thermal conductivity used 0.6 W/m.k. The Reynolds numbers of inflow were in range of  $6,3 \cdot 10^3$  to  $1,077 \cdot 10^6$  according to the physical model. The area weighted average pressure and discharge were calculated in seven cross sections at the main pipe and six cross sections at the each branch. The cross section locations for monitoring pressure of numerical model are the same with the physical model (see Figure 49).

### 4.2.2 Mesh size and boundary layer

Flow is continuous in the nature, whereas the numerical model is only able to use a discrete approach. The smaller mesh interval used by numerical model, closer result to analytical solution is expected. Therefore, three meshes with interval of 10, 12, and 14 mm were built and simulated to evaluate mesh size to the result of numerical model.

Figure 67 shows geometry and mesh of numerical model of Y-bifurcator. The loss coefficients of each numerical model were calculated and compared with the physical model. Figure 68 shows comparison of normalized loss coefficient resulted by numerical models with different mesh interval for asymmetrical flow in turbine mode. The finest mesh (smallest interval) produces loss coefficient closest to the physical model. The mesh size of 10mm is good enough to simulate flow through a bifurcator. Mesh with interval less than 10 mm was not used because it requires a large memory and high-speed computer processor for simulation.

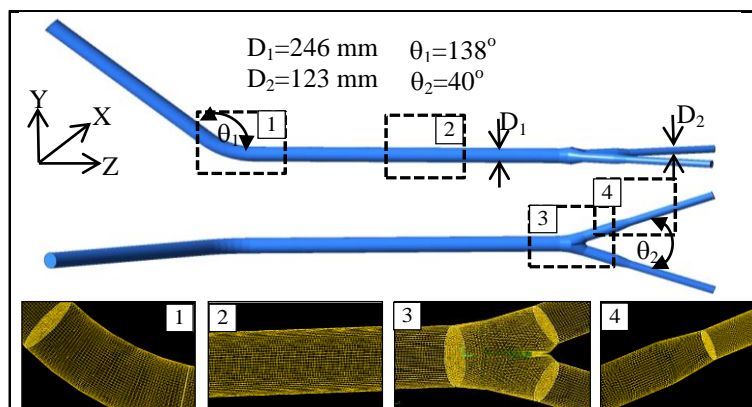


Figure 67: Geometry and mesh of Y bifurcator

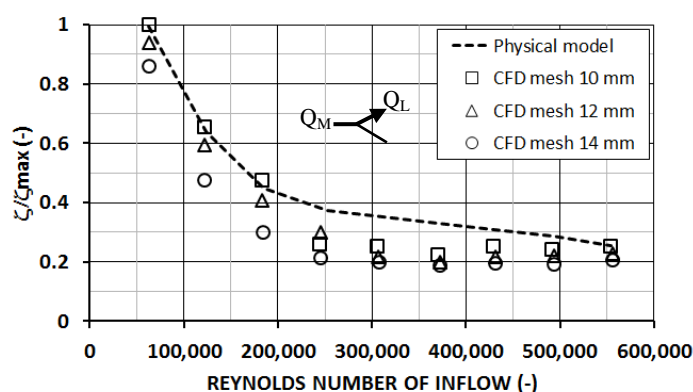


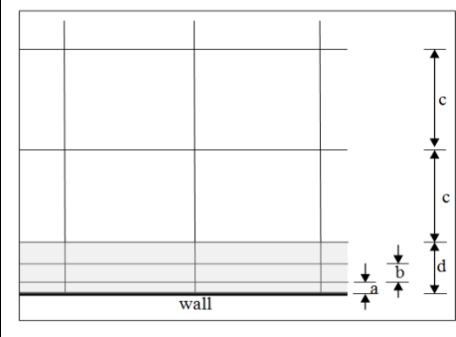
Figure 68: Normalized loss coefficients of numerical models Y-bifurcator with different mesh interval

Turbulent flow is characterized by high velocity in the fully turbulence region and there will be large gradient due to the existence of wall boundary in the near wall region. Very fine mesh is needed to resolve the large gradient of flow variable in the near wall. The use of very fine mesh will have an impact on requirement of computer memory and computational time. There are no rule exist to define boundary mesh size of a turbulent model with complex geometry like a bifurcator. The boundary mesh size is studied by comparing several different boundary sizes. Five different boundary layer mesh size models were created and simulated to study its influence to the flow

variable (Table 9). The use of standard wall function was applied in the model and compared with the results of measurement on the physical model.

Table 9: Mesh size of the boundary layer (in mm)

Variables	Models				
	1	2	3	4	5
A	0.05	0.075	0.1	0.2	0.5
b/a	1.6	1.5	1.5	1.1	1.1
C	10				
D	0.79	0.99	0.81	0.93	1.66
Rows	5	5	4	4	3



Five numerical models with different boundary layer mesh have been simulated in the asymmetrical turbine mode condition. Some of the selected models are also simulated in the symmetrical turbine mode condition. The pumping mode simulations are only performed for asymmetrical flow conditions. Differential pressure head between two sections is obtained by dividing the static differential pressure with the specific weight of water ( $\Delta P/\rho g$ ). Calculation of differential pressure head, differential velocity head, and loss coefficient due to the flow through a Y-bifurcator was done by extracting the result of numerical simulation on the selected sections.

Table 10 and Figure 69-top show differential pressure head between sections M2 and L6 resulted by the numerical models  $(\Delta P/\rho g)_{CFD}$  compared with the measurement results of a scale model  $(\Delta P/\rho g)_{SM}$ . The percentage of differential pressure head deviation between the result of the numerical models and measurement can be seen in the figure using the right ordinate scale. In the low Reynolds number, the deviation of differential pressure head between the numerical models and measurement is less than 10%, and continues to be smaller with the increasing Reynolds number. The last six simulations of model 3 have deviation of differential pressure head less than 1%. The differential pressure head between two sections at the point before and after bifurcator (M2 and L6) resulted by numerical models number 1, 3 and 4 in symmetrical flow are presented in Table 11. As well as the result of asymmetrical flow, the differential pressure head between sections M2 and L6 for symmetrical flow in turbine mode resulted by third numerical models give deviation less than 10% to the measurement. The highest percentage of deviation occurs in the simulation of low discharge, but the deviation percentage decreases with the increasing discharge. This can be more clearly seen in Figure 69-bottom. Deviation of differential pressure head between physical model and numerical model 3 in last six simulations are also less than 1% and smaller compared with the other numerical models.

Table 10: Absolut deviation of differential pressure head between section M2 and L6 for asymmetrical turbine flow

No	Reynolds number	$(\Delta P/\rho g)_{SM}$ (m)	$ (\Delta P/\rho g)_{SM} - (\Delta P/\rho g)_{CFD}  / (\Delta P/\rho g)_{SM} * 100$ (%)				
			CFD 1	CFD 2	CFD 3	CFD 4	CFD 5
1	63261	0.069	6.380	7.038	4.180	0.988	5.046
2	122659	0.246	7.654	6.378	3.772	0.765	1.512
3	183720	0.543	5.806	4.351	2.005	2.106	0.264
4	244562	0.952	4.413	2.468	0.688	1.808	0.147
5	306579	1.487	3.142	1.018	0.702	1.587	0.393
6	371423	2.171	2.049	0.049	0.996	1.349	0.659
7	430790	2.907	1.655	0.540	0.449	0.935	0.936
8	492704	3.787	0.596	0.078	0.179	0.819	1.177
9	555708	4.771	1.133	1.321	0.877	0.212	1.708

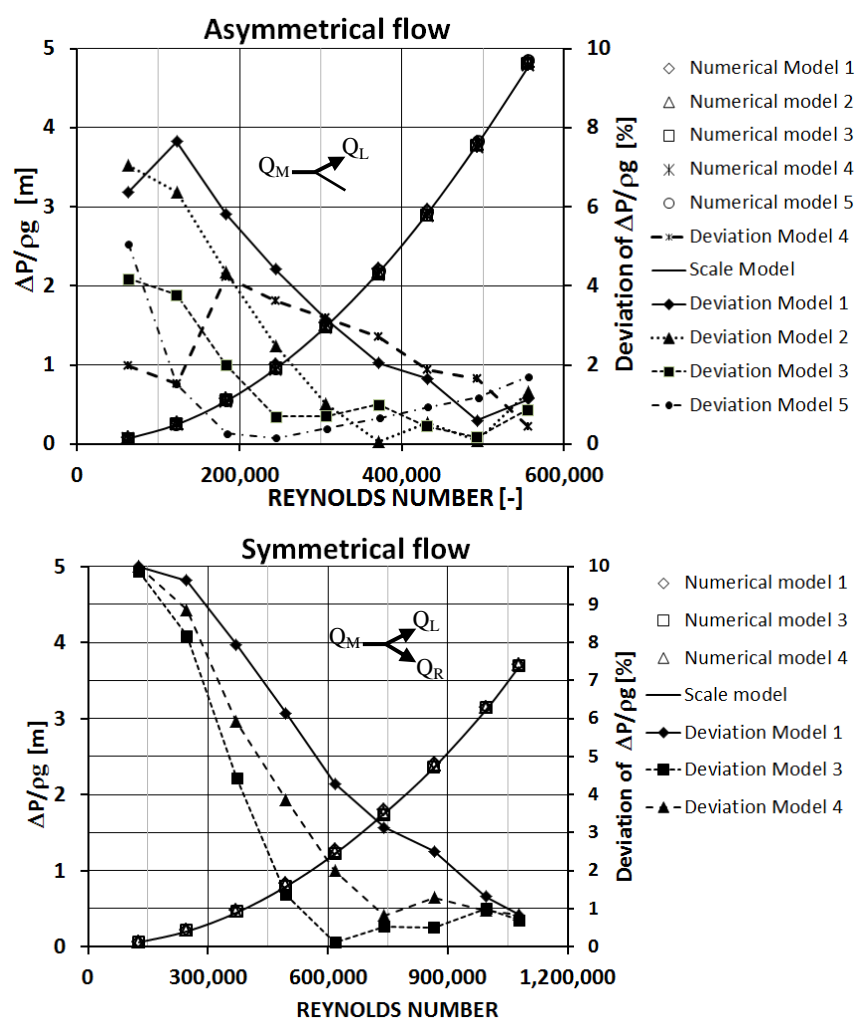


Figure 69: Comparison of differential pressure head (M2 to L6) between measurement and numerical models in asymmetrical (top) and symmetrical (bottom) flow

Table 11: Absolut deviation of differential pressure head between physical and numerical models for symmetrical turbine flow

No	Reynolds number	$(\Delta P/\rho g)_{SM}$ (m)	$ (\Delta P/\rho g)_{SM} - (\Delta P/\rho g)_{CFD}  / (\Delta P/\rho g)_{SM} * 100$ (%)		
			CFD 1	CFD 3	CFD 4
1	127397	0.058	9.999	9.864	9.990
2	246898	0.201	9.635	8.176	8.859
3	370668	0.446	7.945	4.443	5.914
4	494156	0.788	6.135	1.364	3.870
5	616975	1.220	4.286	0.114	1.998
6	740059	1.746	3.133	0.529	0.818
7	864823	2.353	2.507	0.507	1.288
8	994708	3.110	1.321	1.003	0.956
9	1077355	3.675	0.830	0.700	0.852

Table 12 and Figure 70-left show the comparison of normalized loss coefficients between the result of the numerical models 1 to 5 and the result of physical model. The high deviation of loss coefficient between models and measurement is resulted in low Reynolds number region. Otherwise, in the high Reynolds number region, the loss coefficient resulted by all models becomes closer to the physical model. Among the five models, the Model 3 gives the closest result of loss coefficient to the physical model. Figure 70-right shows the result of numerical simulation for symmetrical flow in the turbine mode that has similar trend with the asymmetrical flow. Loss coefficients produced by numerical models are compared with the result of physical model. The high difference of loss coefficient between the result of numerical models and physical model occurs in the low Reynolds number region. In high Reynolds number region, all numerical models show loss coefficient close to the result of physical model. Model 3 also produces a better result compared to the other models.

Table 12: Comparison of normalized loss coefficient between physical and numerical models for asymmetrical turbine flow

No	Reynolds number	$\zeta/\zeta_{max}$ of Physical model (-)	$\zeta/\zeta_{max}$ of Numerical models (-)				
			1	2	3	4	5
1	63261	0.70	0.96	1.00	0.88	0.61	0.26
2	122659	0.38	0.76	0.68	0.57	0.25	0.24
3	183720	0.30	0.59	0.50	0.40	0.12	0.21
4	244562	0.26	0.47	0.36	0.25	0.10	0.20
5	306579	0.24	0.38	0.26	0.17	0.10	0.20
6	371423	0.21	0.29	0.18	0.14	0.10	0.20
7	430790	0.20	0.26	0.13	0.17	0.11	0.20
8	492704	0.18	0.18	0.14	0.16	0.10	0.19
9	555708	0.15	0.16	0.17	0.18	0.11	0.20

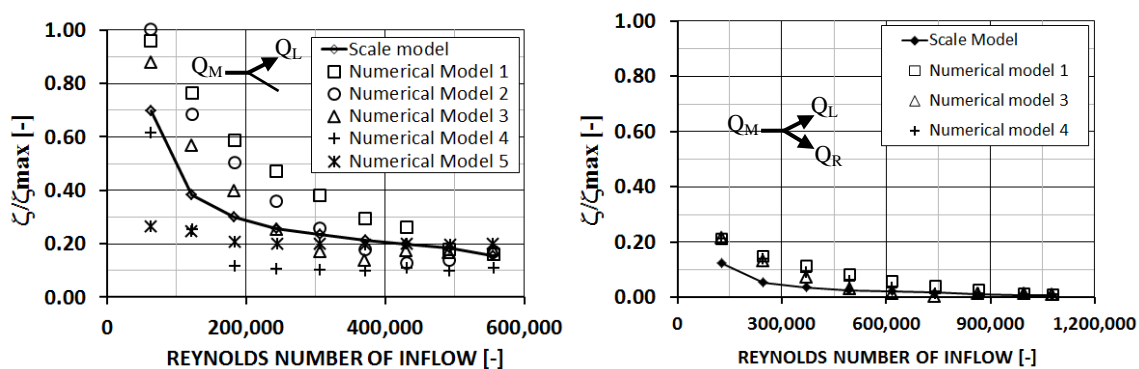


Figure 70: Comparison of normalized loss coefficients between scale and numerical models for asymmetrical (left) and symmetrical (right) turbine mode

### 4.2.3 Comparison of velocity profile

Flow velocity measurement using Particle Image Velocimetry (PIV) on the main and the branch pipe are done for asymmetrical flow with inlet discharge of  $0.080 \text{ m}^3/\text{s}$  and symmetrical flow with inlet discharge of  $0.160 \text{ m}^3/\text{s}$ . The velocity was measured in three different sections in the main pipe at downstream of bend (box B200), in the main pipe before Y-bifurcator (box B201) and in the left branch pipe (box B202L) [77]. For each section, the velocity was measured in four planes: horizontal, diagonal left, diagonal right and vertical.

Comparison of normalized velocity profile between the result of PIV measurement and the result of realizable  $k-\epsilon$  numerical model in asymmetrical flow simulation is shown in Figure 71. The left column of the figure is the result of PIV measurement, while the right is the result of numerical model. First row in the figure is horizontal plane, second row is diagonal left plane, third row is diagonal right plane, and the last row is vertical plane. In the horizontal plane, velocity profile of numerical model has similar shape with the PIV measurement, but the velocity magnitudes of numerical model are slightly higher. In the diagonal left, diagonal right and vertical planes, velocity profile, and magnitude of numerical model are closer to the PIV measurement compared with that in the horizontal plane. There are some errors in the result of PIV measurement in diagonal left plane, so that part of plane was not measured correctly. More errors occur in the PIV measurement in location of box B201 and box B202. In general, velocity profile resulted by numerical model and PIV measurement has similar magnitude and direction.

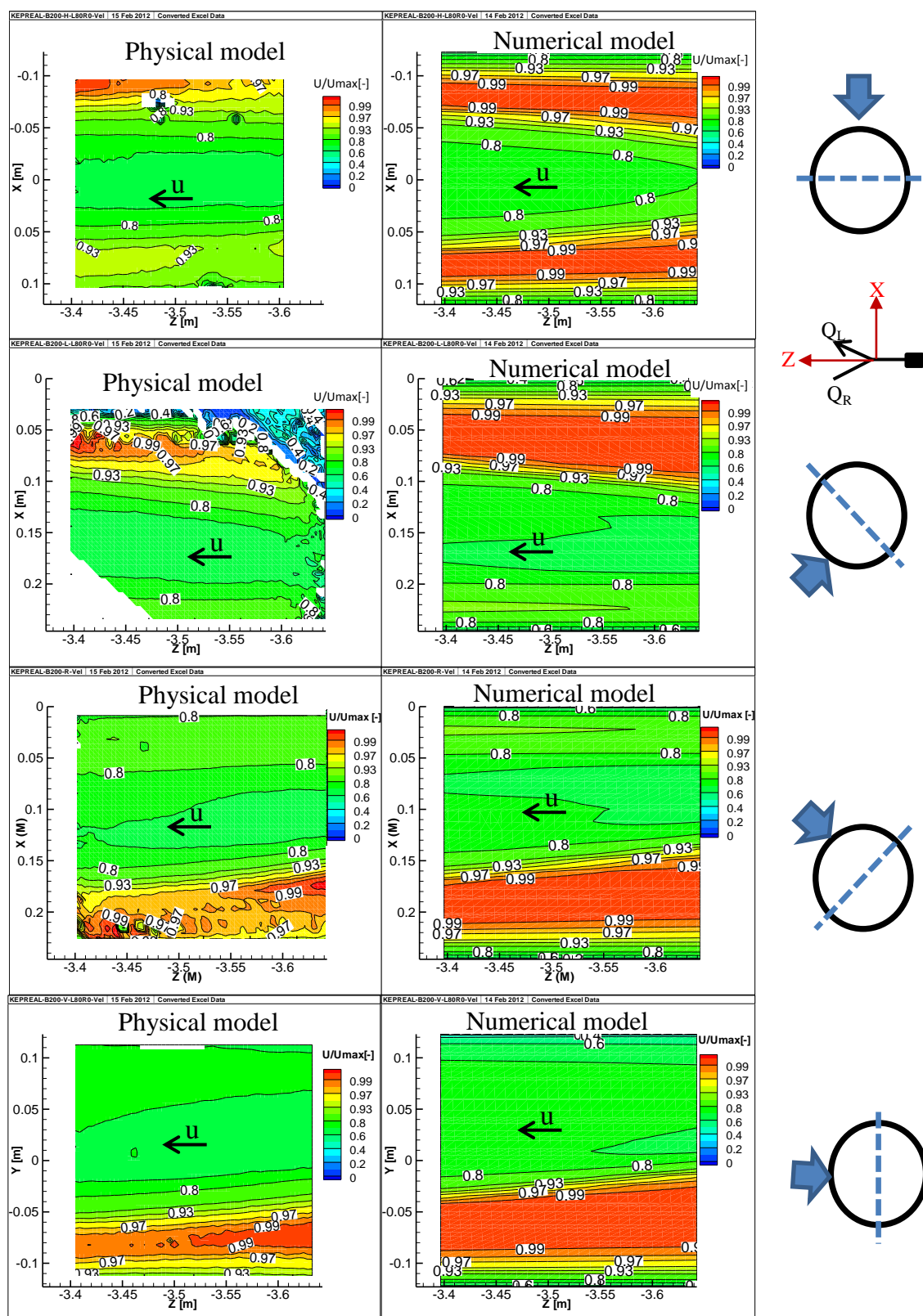


Figure 71: Comparison of normalized velocity contour between result of PIV measurement (left) and Realizable k-ε (right).

Velocity distributions resulted by measurement in the physical model are compared with results of some numerical models. One example of comparison of velocity profile for asymmetrical flow among PIV Measurement (a) [78], realizable  $k-\varepsilon$  (b), Reynolds Stress Model, (c) and SST  $k-\omega$  model (d) are shown in Figure 72. Velocity in this location is influenced by bend so the maximum velocity is not concentrated in the center of pipe. Among three numerical models, the realizable  $k-\varepsilon$  model produces velocity profile with the closest value to the PIV measurement. Measurement of velocity profile in location near bifurcator (box B201) and branch pipe (box B202) has lower accuracy compared with measurement in location box B200.

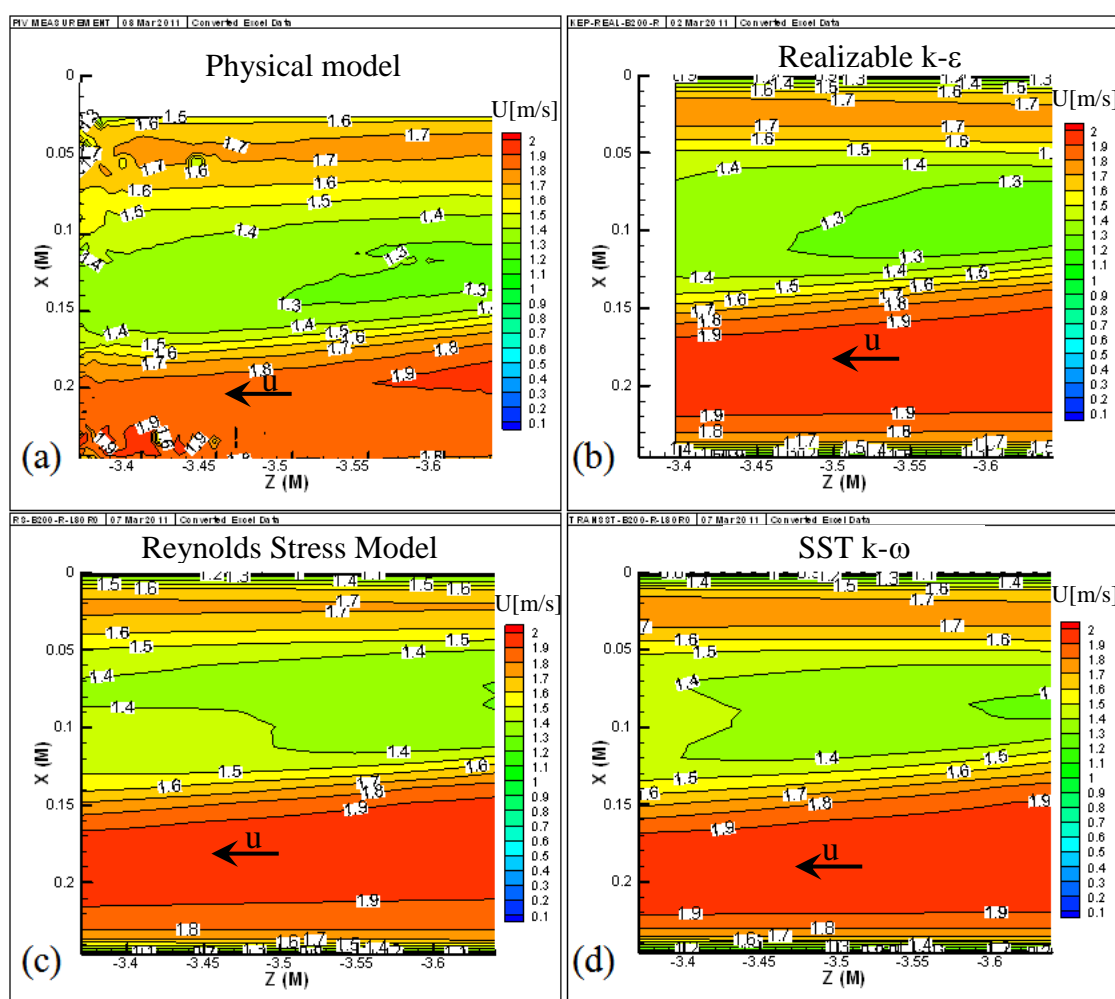


Figure 72: Comparison of velocity (m/s) between result of physical model and numerical models of asymmetrical flow in diagonal right plane

#### 4.2.4 Comparison of differential pressure head

To compare the result of numerical model with the measurement in a physical model, the numerical model simulations are carried out in six different cases such as in the

physical model. Figure 73 shows the comparison of differential pressure head of section M2 to section L6 or R6 between the result of measurements on physical model and numerical model simulations. In the figure, it can be seen that the value of differential pressure head resulted by numerical model is very close to the measurement. Increasing the ratio of discharge at the branch and the main pipe leads to increasing differential pressure head. Similarly, increasing discharge inflow on the main pipe causes increasing differential pressure head.

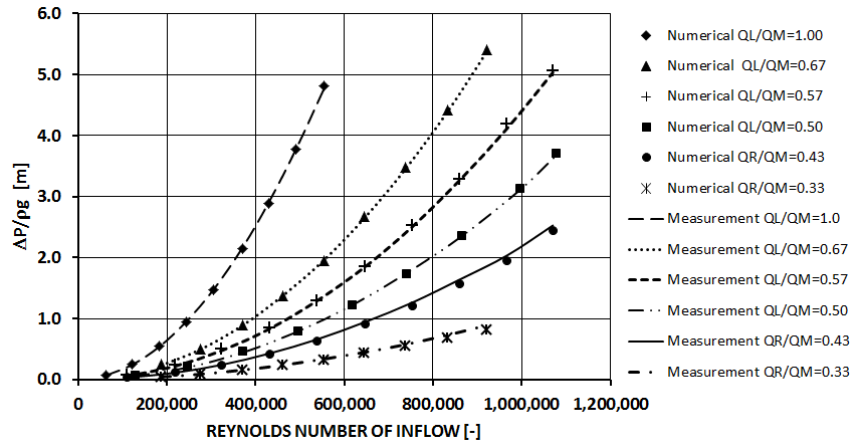


Figure 73 : Comparison of differential pressure head (section M2 and L6/R6) between physical and numerical models for various ratios of discharge.

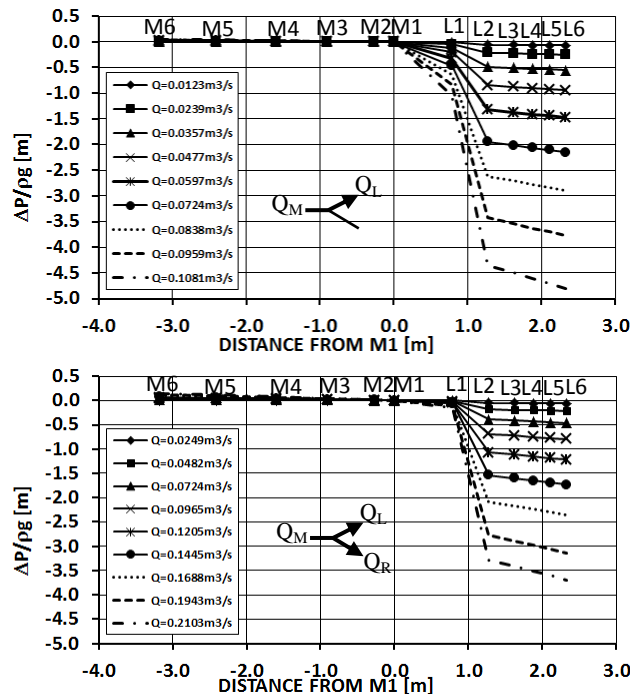


Figure 74: Differential pressure head for asymmetrical flow (top) and symmetrical flow (bottom) for several discharges

The differential pressure head for various flow rates were resulted by simulations of realizable  $k-\varepsilon$  model. In Figure 74, it can be seen that the pressure gradually decreases near to linear from section M6 to M1 due to the friction between water and pipe wall. In the section between M1 and L2, the pressure decreases drastically due to the friction and the shape of bifurcator and confusor. While in the section between L2 and L6, the pressure decreases linearly due to the friction loss in the pipe. Pressure drop increases if the inflow discharge increases. Simulation in asymmetrical flow through a Y-bifurcator produces differential pressure head higher than that in symmetrical flow. For the same discharge inflow, the pressure drop in the asymmetrical flow is fourfold higher than that in symmetrical flow.

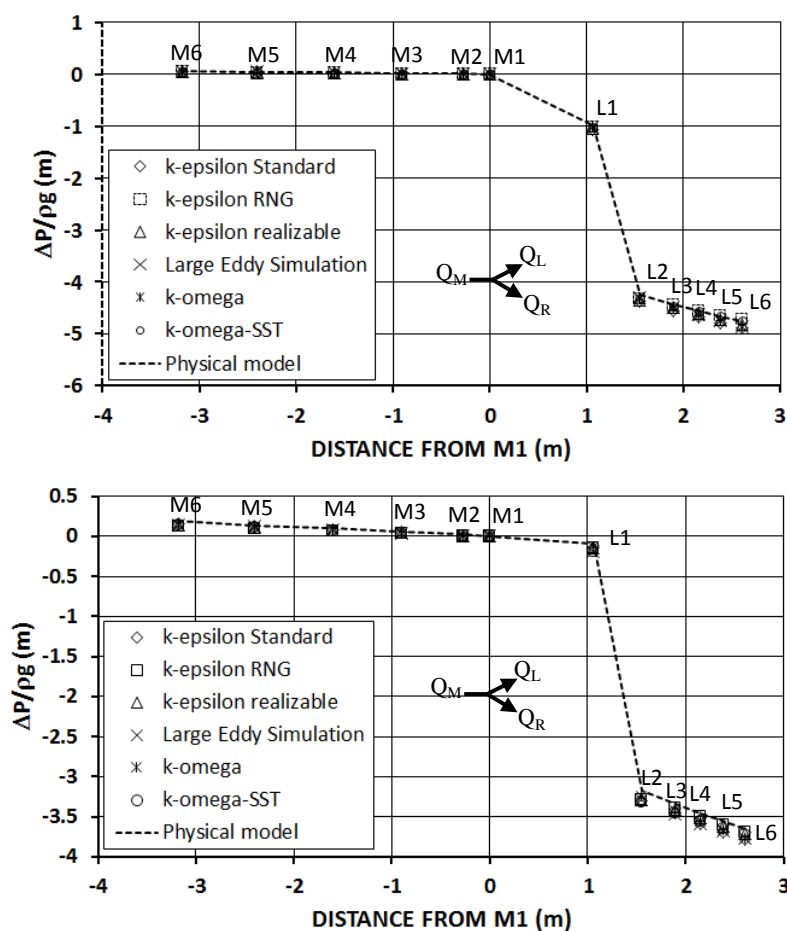


Figure 75: Differential pressure head (refer to M1) for asymmetrical flow (top) and symmetrical flow (bottom)

To compare several turbulent models in simulating flow through a bifurcator, model geometry was simulated with inflow of  $0.108\text{m}^3/\text{s}$  in asymmetrical turbine mode using  $k-\varepsilon$ ,  $k-\omega$ , Reynolds Stress and Large Eddy Simulation. Comparison of differential pressure head ( $\Delta P/\rho g$ ) among results of measurement in physical model and several numerical models are shown in Figure 75. In the asymmetrical flow simulation, the

results show that the closest differential pressure head to the measurement are SST  $k-\omega$ , RNG  $k-\varepsilon$ , LES and realizable  $k-\varepsilon$  respectively. While the closest differential pressure head to the physical model in symmetrical flow simulation is the result of RNG  $k-\varepsilon$ , realizable  $k-\varepsilon$  and standard  $k-\omega$ . However, if the comparison is conducted under differential energy head ( $\Delta P/\rho g + \Delta u^2/2g$ ), then the closest differential energy head are SST  $k-\omega$ , RNG  $k-\varepsilon$ , and realizable  $k-\varepsilon$  for asymmetrical flow and realizable  $k-\varepsilon$ , SST  $k-\omega$  and RNG  $k-\varepsilon$  for symmetrical flow (Figure 76).

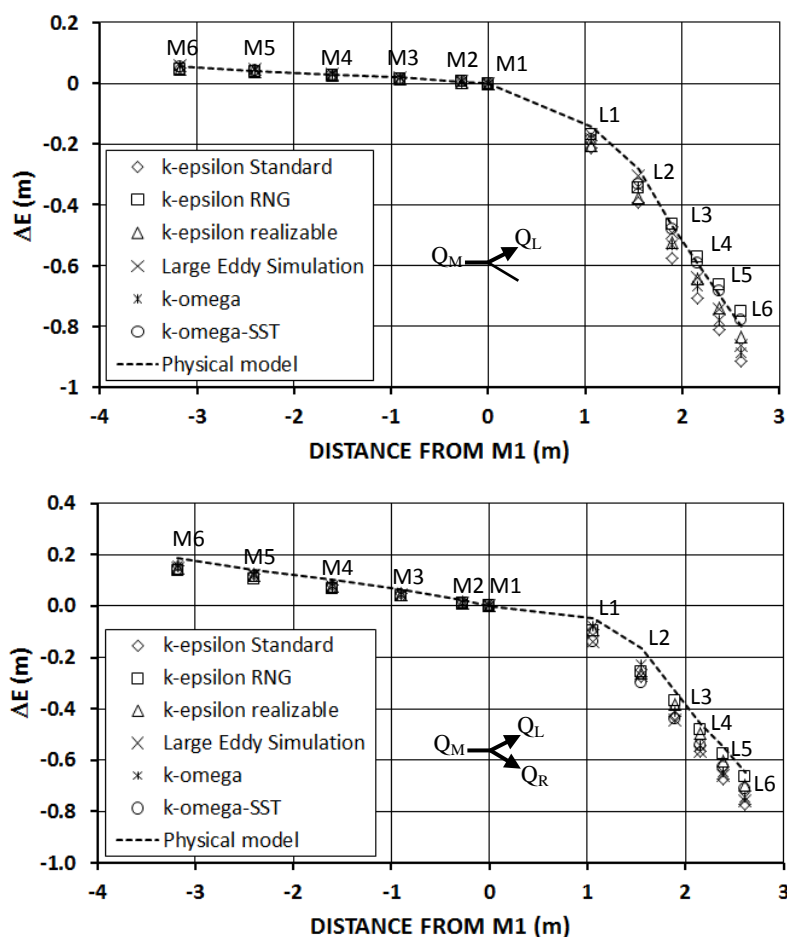


Figure 76: Differential energy head (refer to M1) for asymmetrical flow (top) and symmetrical flow (bottom)

In the Figure 75 and Figure 76 (section L2 to L6) can be seen that the deviation of differential energy head between measurement of physical model and result of numerical model are higher than deviation of differential pressure head. The difference of velocity between measurement of physical model and result of numerical model contribute to the deviation of differential energy head.

Root Mean Square Deviation (RMSD) of differential pressure head and energy head between measurements in the physical model and numerical model simulations are shown in Table 13. Additionally, in that table, it also can be seen that the lowest

number of iterations needed to reach convergence (convergence value=0.001) are standard k- $\omega$ , SST k- $\omega$ , realizable k- $\epsilon$ , standard k- $\epsilon$ , Reynolds Stress, RNG k- $\epsilon$  and Large Eddy Simulation. From the results above, the realizable k- $\epsilon$  generates differential pressure head and differential energy head, which is close enough to the measurement, both in symmetrical and asymmetrical flow conditions. The realizable k- $\epsilon$  model also needs the number of small iterations; this means that the computation time required is short.

Table 13: Number of iteration and Root Mean Square Deviation

No	Numerical Models	Asymmetrical Flow			Symmetrical Flow		
		Number of Iteration	RMSD of Diff. Pressure	RMSD of Diff. Energy	Number of Iteration	RMSD of Diff. Pressure	RMSD of Diff. Energy
1	k- $\epsilon$ Standard	792	0.083	0.077	792	0.087	0.038
2	k- $\epsilon$ RNG	1625	0.028	0.026	1625	0.051	0.031
3	k- $\epsilon$ Realizable	750	0.050	0.043	750	0.055	0.021
4	k- $\omega$ Standard	475	0.057	0.050	475	0.069	0.025
5	k- $\omega$ SST	682	0.026	0.021	682	0.079	0.035
6	LES	1650	0.050	0.030	1650	0.087	0.039
7	Reynolds Stress	988	0.065	0.057	988	0.074	0.071

## 4.2.5 Loss coefficient of Y-bifurcator

Three-dimension numerical model produces several variables of flow in each center or node of the cells, such as flow, pressure, velocity and others. After performing numerical simulation, some derivatives variables can be defined by user defined function from the result of model. For calculating loss coefficient, needs to compute the area weighted average of pressure, velocity magnitude and flow rate over each investigated cross section. Pressure head is calculated by dividing the static pressure with specific weight of the water. Differential pressure, differential velocity, and friction loss are applied into energy equation to calculate loss coefficient.

### 4.2.5.1. Comparison of loss coefficient among several turbulent model

Loss coefficients of several numerical models for asymmetrical flow were calculated. Figure 77 and 78 shows comparison of normalized loss coefficient between result of physical model and result of several numerical models of k- $\epsilon$ , k- $\omega$ , LES and RSM. Normalized loss coefficients resulted by standard k- $\epsilon$  is higher compared with the result of realizable k- $\epsilon$ . It can be seen that the closest to the result of physical model in both asymmetrical and symmetrical flow is loss coefficient resulted by the realizable k- $\epsilon$  model. Variation of loss coefficient resulted by several sections of realizable k- $\epsilon$  is smaller than that of standard k- $\epsilon$ . Loss coefficient of RSM model has different trend with the LES model. LES produces decrease loss coefficients continually with the

increasing Reynolds number. Variation of loss coefficient resulted by several sections of LES is smaller than that of RSM model. In the low Reynolds number, both standard and SST k- $\omega$  did not produce highest loss coefficients like other models. The highest loss coefficient is produced by the middle of Reynolds number.

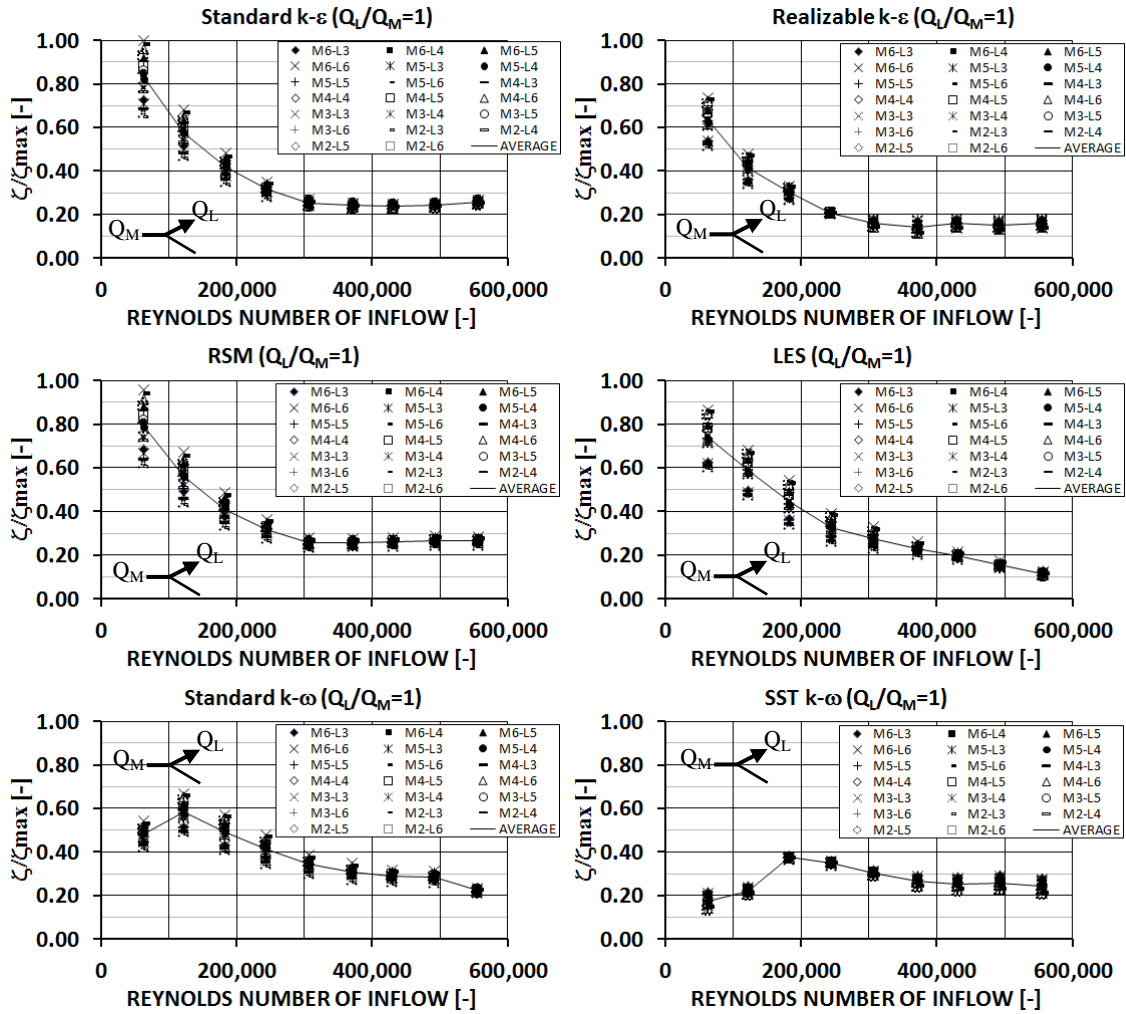


Figure 77: Comparison of normalized loss coefficients among several turbulent models in asymmetrical flow in turbine mode.

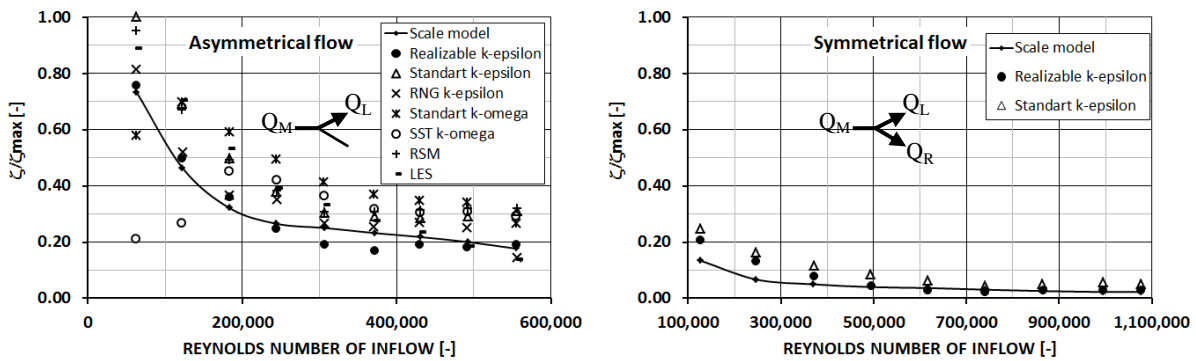


Figure 78: Comparison of normalized loss coefficient between measurement and numerical models for asymmetrical (left) and symmetrical (right) flow

#### 4.2.5.2 Loss coefficient a Y-bifurcator for several cases

The normalized loss coefficients calculated in several section of numerical simulation in turbine mode are performed in Figure 79. Loss coefficients are decrease with the increasing Reynolds number.

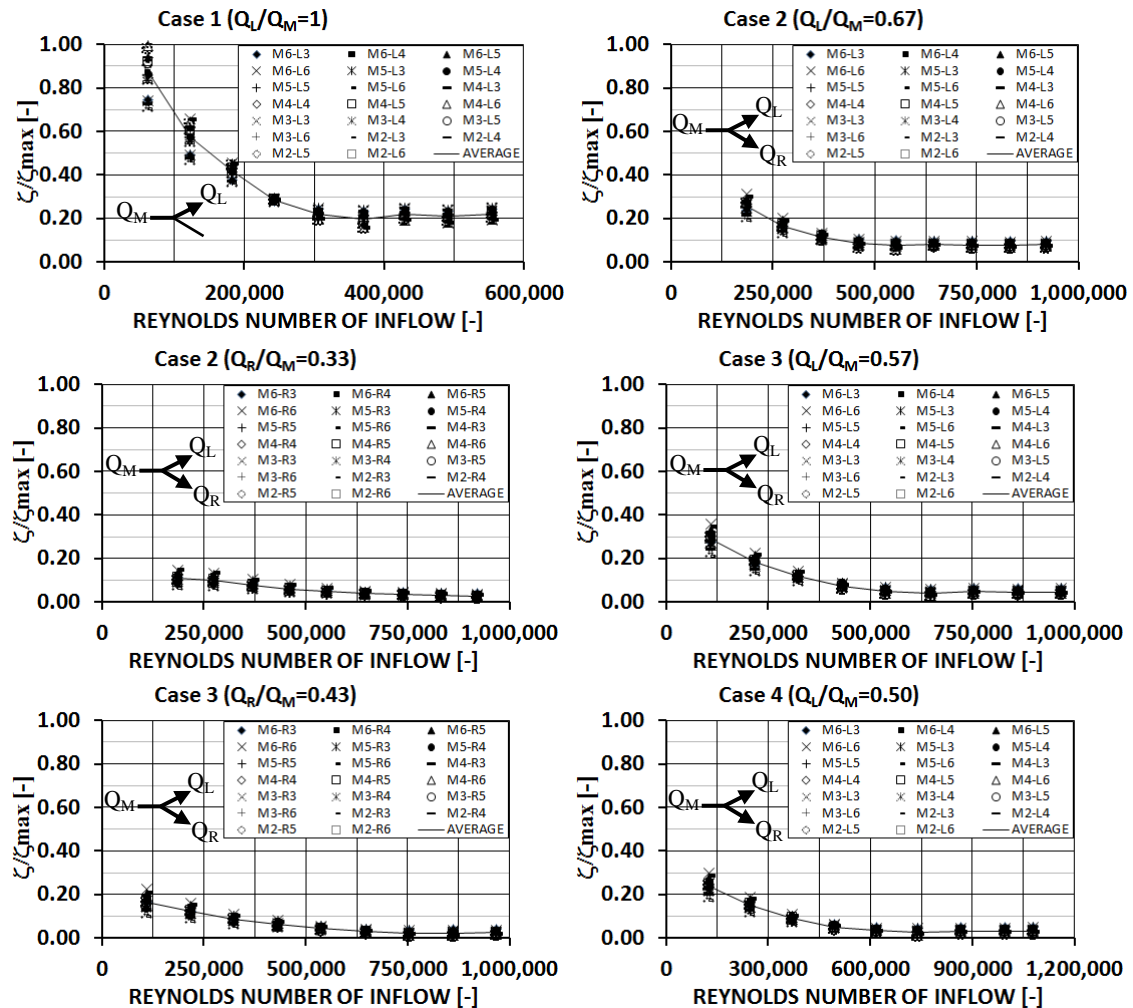


Figure 79: Normalized loss coefficients of realizable k- $\epsilon$  numerical model for Case 1 to Case 4 (turbine mode)

Case 1 is water flow from main pipe only to one branch and the other branch is closed. Case 2 separates 67% of water flow to one branch and the rest to the other branch. Case 3 divides 57% of water flow to one branch and the rest to the other branch. Case 4 divides water in the same rate to both branches. The normalized loss coefficients resulted by simulation in pumping mode are performed in Figure 80. Case 5 is asymmetrical pumping simulation and Case 6 is symmetrical pumping mode simulation with discharge ratio between inflow and outflow of 0.50 in both branches. The loss coefficients that calculated from two different sections in the upstream and downstream of bifurcator come to the high difference values for low flow (low

Reynolds number). Meanwhile, the differences of loss coefficient become smaller for the high flow.

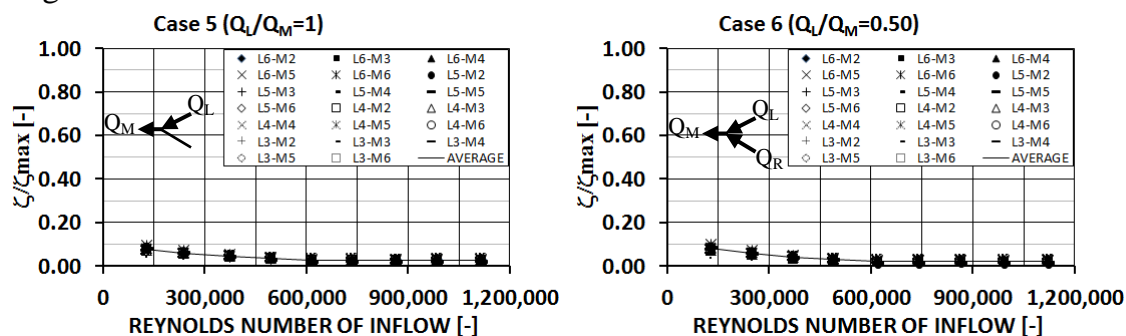


Figure 80: Normalized loss coefficients of realizable  $k$ - $\varepsilon$  numerical model for Case 5 and Case 6 (pumping mode)

#### 4.2.5.3 Comparison of loss coefficient between physical and numerical models

This section will compare the average loss coefficient resulted by physical and numerical models. The comparison of normalized loss coefficients (average value) between physical model and realizable  $k$ - $\varepsilon$  numerical model for Case 1 to Case 4 are performed in Figure 81. Loss coefficient decreases if Reynolds number increases. In low Reynolds region, loss coefficient resulted by numerical model in Case 1 to Case 4 is higher than that of physical model. In the high Reynolds region, loss coefficients of numerical model are closer to physical model. The symmetrical flow produces loss coefficient smaller compared with asymmetrical flow. Numerical model has a good agreement with the physical model in term of loss coefficient calculation.

Figure 82 shows comparison of normalized loss coefficients (average value) between physical model and numerical model in the pumping mode (Case 5 and Case 6). Similar to the result of turbine mode, in the pumping mode, the loss coefficient of numerical model is slightly higher than that of the physical model in the low Reynolds number and it is closer in the high Reynolds number. The difference of loss coefficient in the pumping mode between asymmetrical and symmetrical flow is small.

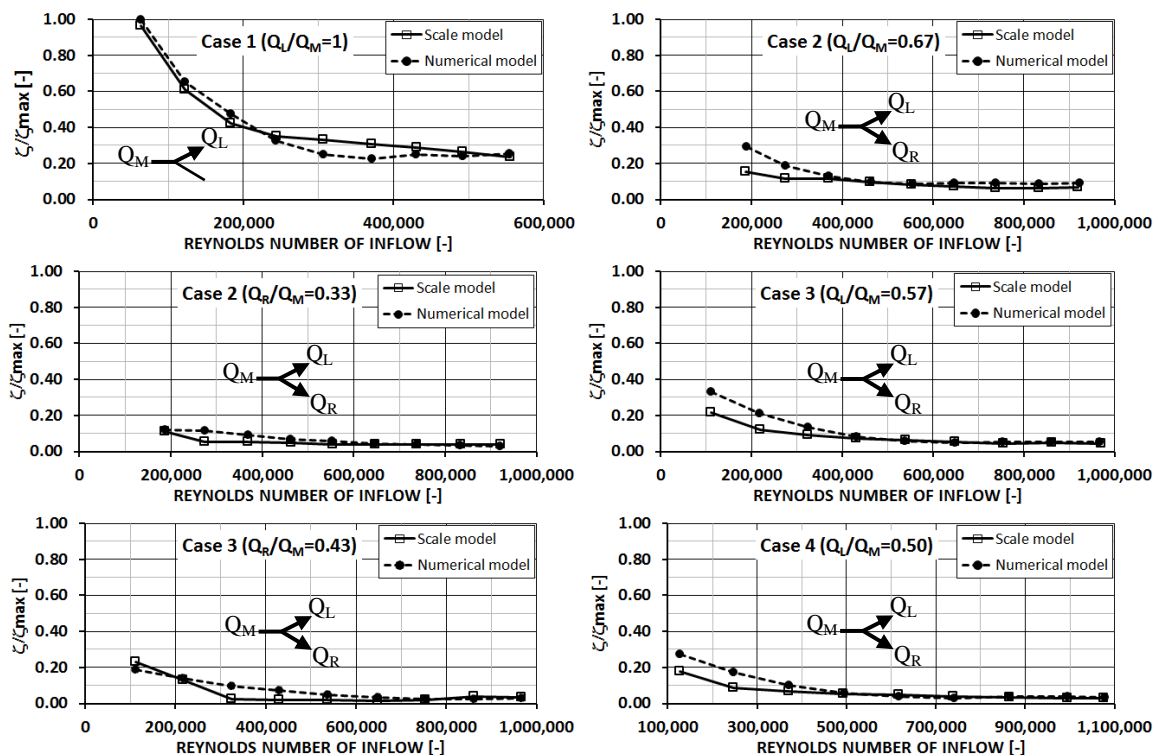


Figure 81: Comparison of normalized coefficient loss for Case 1 to 4

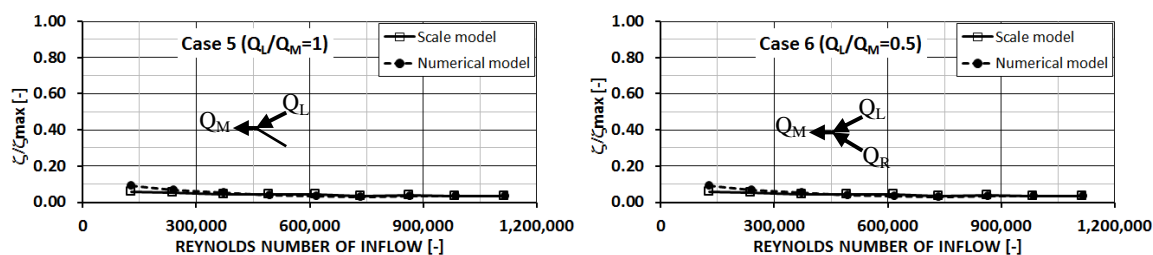


Figure 82: Comparison of normalized loss coefficient for Case 5 and 6

#### 4.2.5.4 Comparison of loss coefficient between steady and unsteady simulations

FLUENT can be used to simulate flow in steady and unsteady conditions. The steady flow solver is designed to perform a time-averaged flow solution. The unsteady flow solver can be used for a dynamic simulation; it means that the result varies with time. Steady simulation uses steady state equation, upwind method, and program written using relaxation method. Unsteady simulation uses transient equation, central difference method, and program written using explicit method. The steady and unsteady simulations were done using the same geometry, mesh and boundaries condition. Figure 83 shows comparisons of normalized loss coefficients resulted by steady simulation (left) and unsteady simulation (right). The difference of loss coefficient between the result of steady and unsteady simulations is small. The unsteady simulation needs longer time to reach the convergence compared to the steady state simulation.

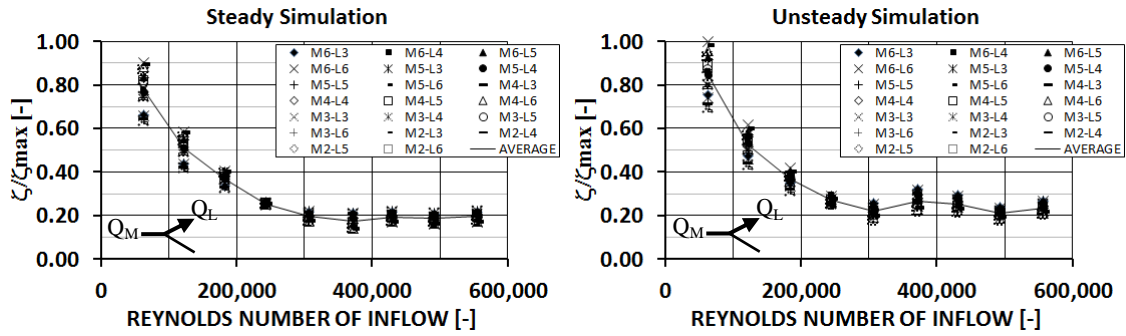


Figure 83: Normalized loss coefficient of steady and unsteady simulation

#### 4.2.5.5 Comparison of losses coefficient with the previous researches

Studies on the loss coefficient of flow through a divider were done by Lucendro [71], Salvesen [72], Causey [73], Russ [74], Escher Wyss [90], and Munich [75]. The studies used dividers with different shape, size and branching angle. Therefore the result obtained also varies. The normalized loss coefficients resulted by previous study compared with the result of Y-bifurcator of Pirris is plotted in Figure 84.  $U_M$  is velocity in the main pipe at the upstream of bifurcator section.  $U_L$  and  $U_R$  are velocity in the left and right branches at the downstream of bifurcator section. Pirris bifurcator which has diameter of main pipe is twice the diameter of branch pipe. The cross section area of main pipe is four times as much as the cross section area of branch pipe. In the asymmetrical flow, discharge in the branch is the same as in the main pipe; the velocity in the branch is four times as much as velocity in the main pipe. In the symmetrical flow, discharge flow in the branch is the half of the discharge in the main pipe; the velocity in the branch is twice the velocity in the main pipe. By comparing the result of several researches, it can be seen that the loss coefficient of a flow divider is determined by the shape, diameter ratio, branching angle and the ratio of outflow and inflow. In the Figure 84 can be seen that the numerical model of Pirris Y-bifurcator produce normalized loss coefficient smaller compared with the others.

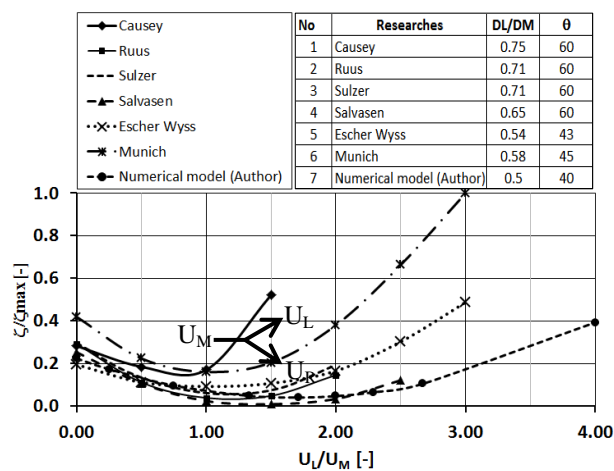


Figure 84: Comparison of normalized losses coefficient among several bifurcator with different shape, size and angle

## 4.2.6 Numerical Simulation of high Reynolds number inflow

It has been explained earlier that the physical model of Pirris Y-bifurcator can only do simulation with maximum inflow of  $0.108\text{m}^3/\text{s}$  in asymmetrical flow and  $0.210\text{m}^3/\text{s}$  in symmetrical flow. The both flows have Reynolds number of  $5,5.10^5$  and  $1,08.10^6$  respectively. Referring to the prototype, the design inflow for asymmetrical flow is  $9\text{m}^3/\text{s}$  and symmetrical flow is  $18\text{m}^3/\text{s}$ . Therefore, the Reynolds numbers that occur are  $5,68.10^6$  and  $1,138.10^7$ . Physical model was made based on Reynolds similarity to the prototype. Therefore, loss coefficient of Y-bifurcator caused by high flow will be studied using numerical model. Numerical model will be simulated by increasing inflow gradually so that the Reynolds number increases until it reaches the Reynolds number of prototype. The numerical model inflows for asymmetrical and symmetrical simulation are presented in Table 14.

Table 14: Discharge and velocity inflow for turbine mode simulation

Asymmetrical flow			Symmetrical flow		
Reynolds	Q (m <sup>3</sup> /s)	u (m/s)	Reynolds	Q (m <sup>3</sup> /s)	u (m/s)
1,283,096	0.250	5.268	1,284,615	0.250	5.269
2,161,275	0.421	8.874	2,798,359	0.545	11.477
3,193,173	0.623	13.110	4,312,335	0.840	17.686
4,020,691	0.784	16.508	5,826,250	1.134	23.896
5,055,345	0.986	20.756	7,340,123	1.429	30.106
5,681,736	1.107	23.327	8,844,907	1.724	36.314
			10,366,787	2.019	42.523
			11,376,380	2.215	46.663

### 4.2.6.1 Differential pressure head of high Reynolds number

The differential pressures head between sections M2 and L6 resulted by simulation of asymmetrical and symmetrical flows are performed in logarithmic scale in Figure 85. The differential pressure head increases with the increasing Reynolds number of inflow. The differential pressure head of high Reynolds number flow follows the trend of differential pressure head of low Reynolds number flow. For the same Reynolds number of inflow, the differential pressure head of asymmetrical flow is four times as high as that of symmetrical flow. This value is obtained from the square of discharge ratio between symmetrical and asymmetrical flow.

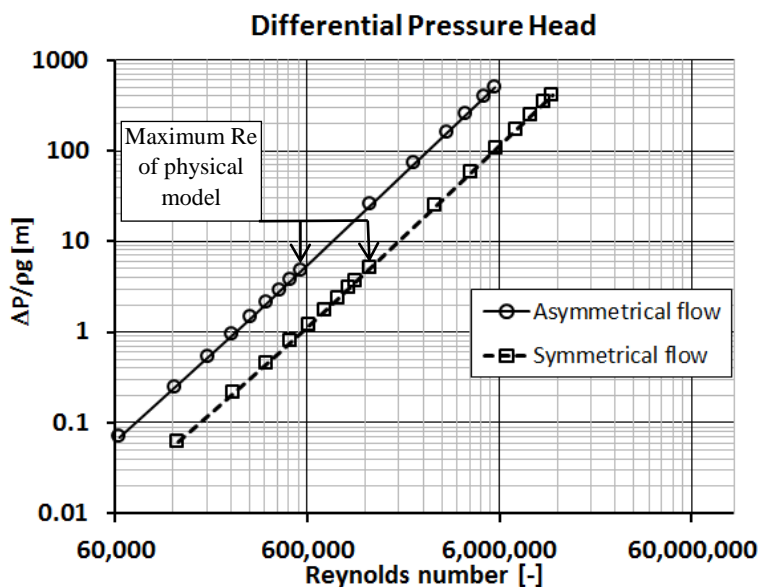


Figure 85: Differential pressure head of asymmetrical and symmetrical turbine mode

Differential pressures head resulted by numerical model were compared to the extrapolation of physical model result. Klasinc et. al. approximated differential pressure head of high Reynolds number using second order, third order, and four-order polynomials. Comparison of different polynomials shows that the higher order functions gave no reasonable results [89]. In this study, the differential pressures head of physical model Y-bifurcator are extrapolated using polynomial second and third orders. The second order polynomial regression of asymmetrical flow produces equations:

$$\Delta P/\rho g = 1.5 \cdot 10^{-11} \cdot Re^2 + 2.8115 \cdot 10^{-7} \cdot Re - 1.4527 \cdot 10^{-2}$$

The third order polynomial regression produces an equation:

$$\Delta P/\rho g = -1.76 \cdot 10^{-13} \cdot Re^3 + 1.6165 \cdot 10^{-11} \cdot Re^2 - 1.451 \cdot 10^{-7} Re + 1.3271 \cdot 10^{-2}$$

By eliminating the cube component of third order polynomial equation:

$$\Delta P/\rho g = 1.6165 \cdot 10^{-11} \cdot Re^2 - 1.451 \cdot 10^{-7} Re + 1.3271 \cdot 10^{-2}$$

For symmetrical flow, the second order polynomial regression produces an equation:

$$\Delta P/\rho g = 3.04 \cdot 10^{-12} \cdot Re^2 + 3.6046 \cdot 10^{-8} \cdot Re - 2.8585 \cdot 10^{-3}$$

The third order polynomial regression produces an equation:

$$\Delta P/\rho g = 1.7817 \cdot 10^{-19} \cdot Re^3 + 2.7168 \cdot 10^{-12} \cdot Re^2 + 2.0018 \cdot 10^{-7} Re - 1.809 \cdot 10^{-2}$$

The second order also obtained from the third order polynomial by eliminating the cube component:

$$\Delta P/\rho g = 2.7168 \cdot 10^{-12} \cdot Re^2 + 2.0018 \cdot 10^{-7} Re - 1.809 \cdot 10^{-2}$$

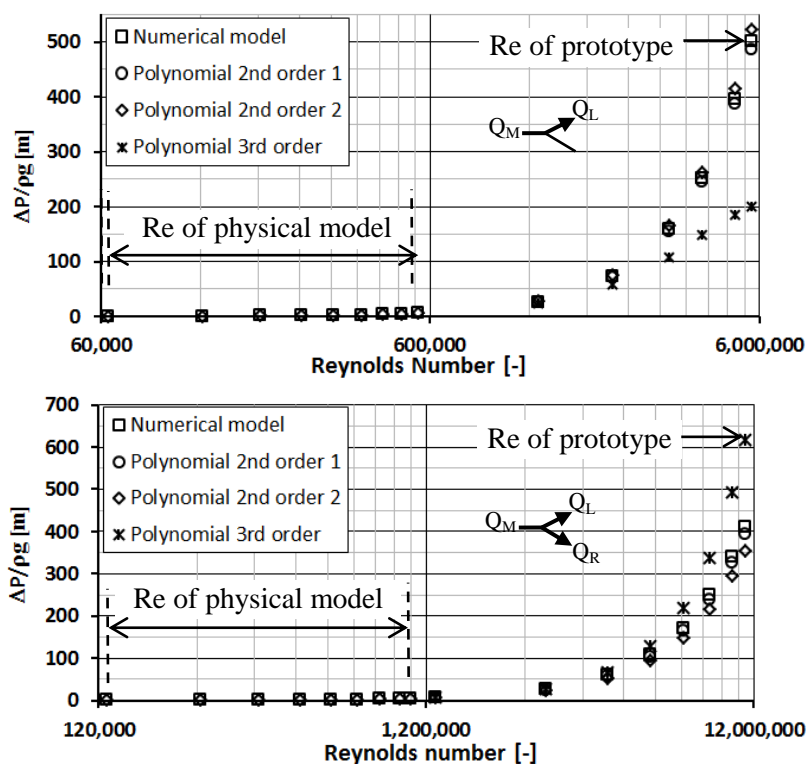


Figure 86: Comparison differential pressure head between numerical model and extrapolation of physical model in turbine mode.

The comparison of differential pressure head between the result of numerical model and extrapolation of physical model for asymmetrical flow is performed in Figure 86 (top). Differential pressures head resulted by third order extrapolations of physical model are lower than those resulted by numerical model. The second order polynomial extrapolation is closer to the numerical model compare to the third order. Figure 86 (bottom) shows the comparison of differential pressure head of symmetrical flow between the result of numerical model and result of extrapolation of physical model. In symmetrical flow, differential pressures head resulted by third order extrapolations of physical model are higher than those resulted by numerical model.

#### 4.2.6.2 Loss Coefficient of high Reynolds number

Loss coefficients that are calculated from the result of numerical simulation using different couple of sections in turbine mode are performed in Figure 87. Figure 87-top shows the normalized loss coefficient for the asymmetrical flow and the bottom shows the loss coefficient for the symmetrical flow. In the figure, it can be seen that the loss coefficient increases after the maximum of Reynolds number of physical model for both asymmetrical and symmetrical flow. Calculation using two different sections in the upstream and downstream of bifurcator produces varies of loss coefficient. Figure 88 shows the normalized loss coefficient that is calculated from the result of numerical simulation using different couple of sections in pumping mode. Variation of

loss coefficient calculated from different sections in low Reynolds number is large and it decreases with increasing the Reynolds number.

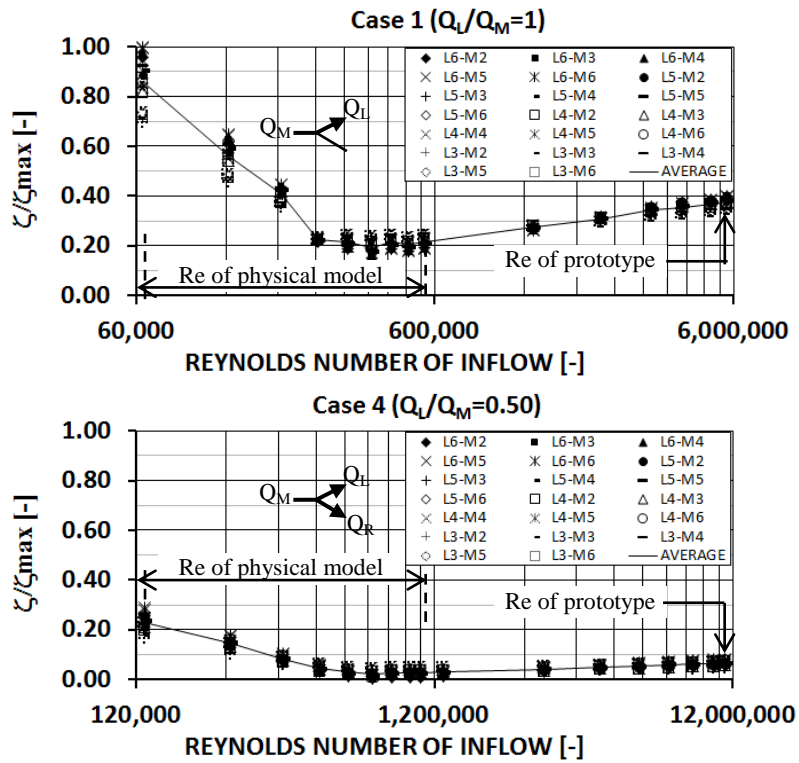


Figure 87: Normalized loss coefficient of asymmetrical (top) and symmetrical (bottom) flow turbine mode

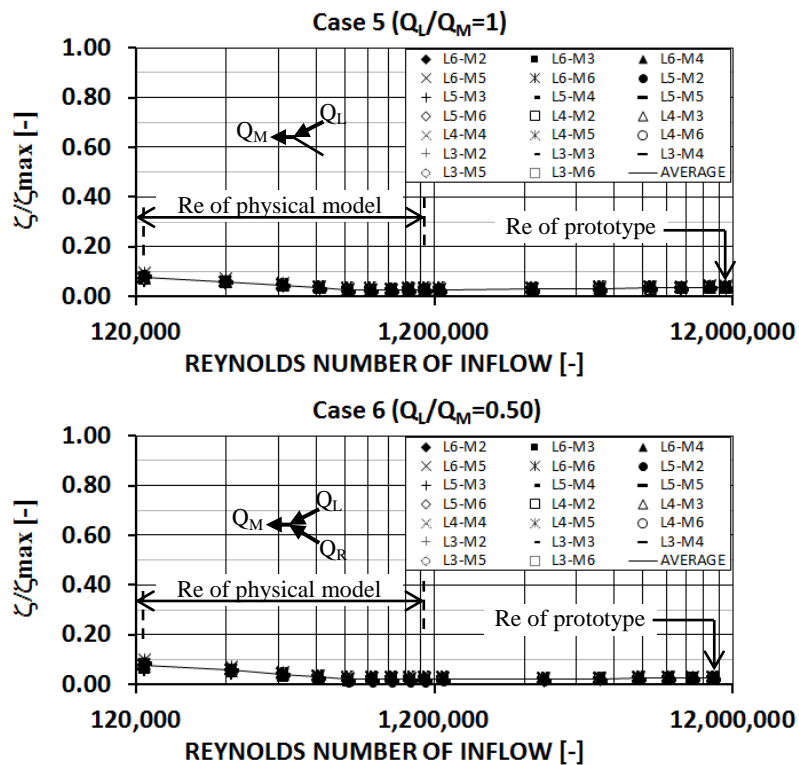


Figure 88: Normalized loss coefficient of asymmetrical (top) & symmetrical (bottom) flow in pumping mode

### 4.2.6.3 Comparison of loss coefficient between numerical model and extrapolation of physical model

Comparison between average normalized loss coefficients resulted by numerical model and normalized loss coefficients resulted by physical model and its extrapolation are performed in the Figure 89. The difference between the result of numerical model and the extrapolation is explained as follows. In the figure, it can be seen that the loss coefficients between results of numerical model are higher than the one resulted by second order extrapolation. Friction loss and differential velocity head normalized by differential pressure head are performed in the Figure 90. The friction loss decreases with increasing Reynolds number, but the differential velocity heads increase with approaching the Reynolds number to physical model and then decrease again with increasing Reynolds number. Therefore loss coefficient resulted by numerical model in high flow is higher than resulted by physical model. The method used for calculating loss coefficient also gives contribution to the loss coefficient of numerical model.

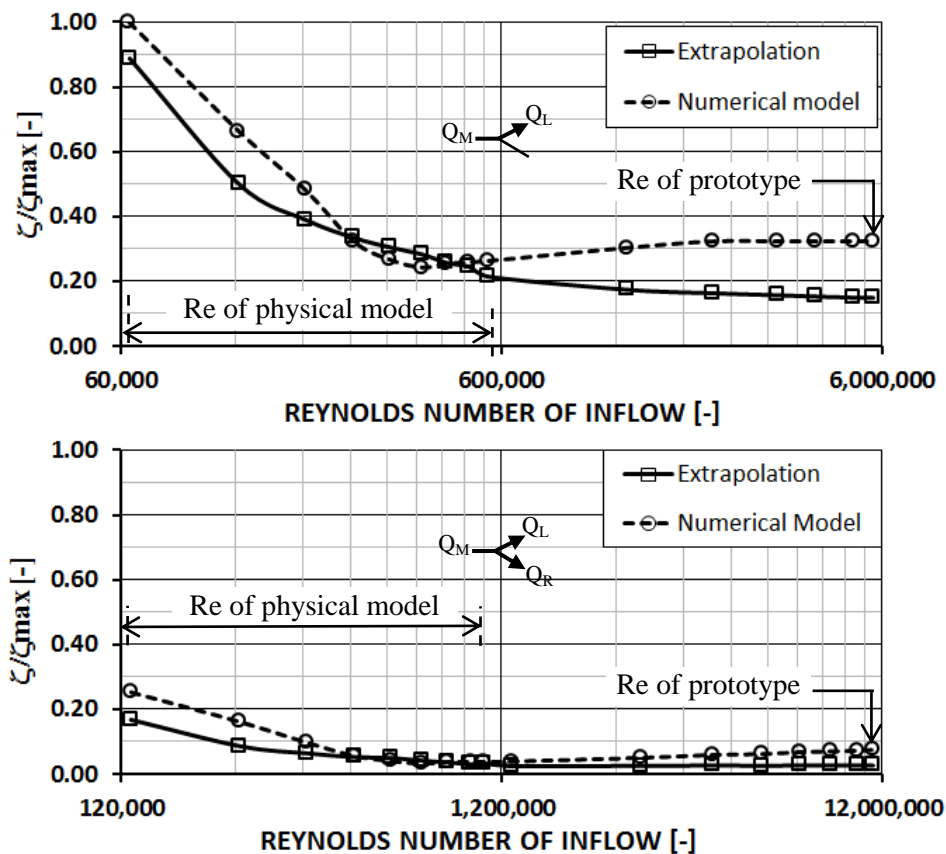


Figure 89: Comparison of normalized loss coefficient between numerical model and extrapolation of physical model.

Top: asymmetrical and Bottom: symmetrical flow

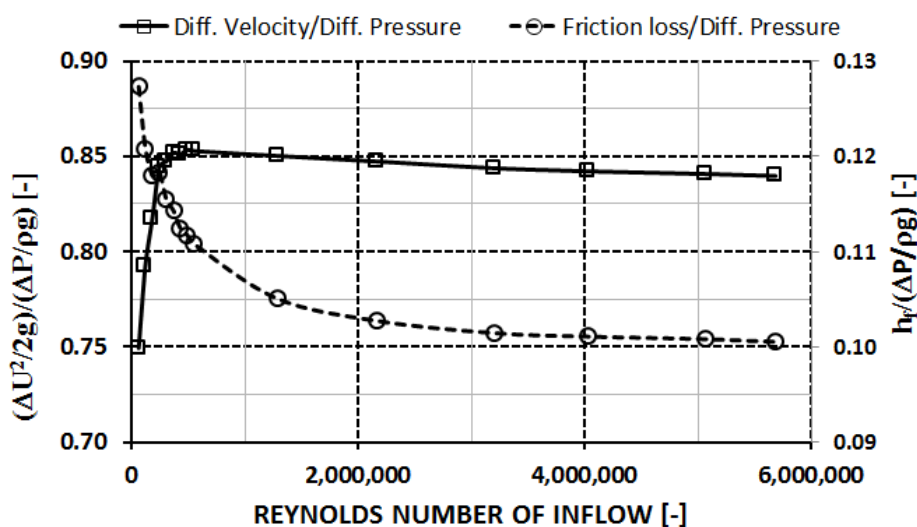


Figure 90: Friction loss and differential velocity head normalized by differential pressure head

## 4.2.7 Kinetic energy correction factor

Energy equation used in flow is assumed that the flow is one dimension. In this case, the flow is considered as a large current pipe with average velocity  $\bar{u}$  at each cross section. However, it is important to keep in mind that the magnitude of the kinetic energy per unit weight or the velocity head that obtained from value of  $\bar{u}^2/2g$  is not equal to average value of  $u^2/2g$  that obtained from the entire cross section area. It is explained with the figure and the following equation:

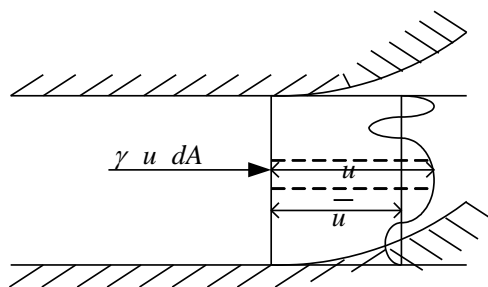


Figure 91: Illustration of velocity and average velocity of flow in the pipe

Figure 91 shows a cross-sectional distribution of velocity in a flow, where  $u$  is the velocity in each point and  $\bar{u}$  is the average velocity. The amount kinetic energy through section of flow per unit time is:

$$E_k = \gamma \frac{1}{A} \int_A \frac{u^2}{2g} u dA \quad (118)$$

where  $\gamma u dA$  is the fluid weight per unit time that flows through section with area of  $dA$ , and  $u^2/2g$  is the kinetic energy per unit weight. If equation (118) is equal to the total kinetic energy through a section in form of  $\gamma \bar{u} A \alpha \bar{u}^2/2g$ , it will be obtained a relation:

$$\alpha \frac{\bar{u}^2}{2g} \gamma \bar{u} A = \gamma \int_A \frac{u^2}{2g} u dA \quad (119)$$

Rearranging equation 119 becomes:

$$\alpha = \frac{1}{A} \int_A \left( \frac{u}{\bar{u}} \right)^3 dA \quad (120)$$

The value of  $\alpha$  is always larger than one. In practice,  $\alpha = 2$  is usually used for laminar pipe flow, while value between 1,01 and 1,10 are commonly used for turbulence pipe flow except for detail calculation. By involving  $\alpha$ , the energy equation can be written as :

$$z_1 + \frac{p_1}{\rho g} + \alpha_1 \frac{\bar{u}_1^2}{2g} = z_2 + \frac{p_2}{\rho g} + \alpha_2 \frac{\bar{u}_2^2}{2g} + \Delta h \quad (121)$$

#### 4.2.7.1 Calculation of kinetic energy correction factor

FLUENT is software developed using Finite Volume method. The model domain is divided into many small volumes that is expressed the mathematical equations. Therefore, in each volume, the flow variables such as pressure, velocity, etc. are calculated. In the pipe cross section, the velocity distribution is not uniform. This is caused by the friction between water and pipe wall. Therefore, without the influence of secondary flow, the velocity becomes smaller as the flow approaches the pipe wall. The average velocity is used in the calculation of kinetic energy. Thus, in the energy equation, a factor is added to correct the kinetic energy. Calculation of kinetic energy correction factor from the result of numerical model is explained below.

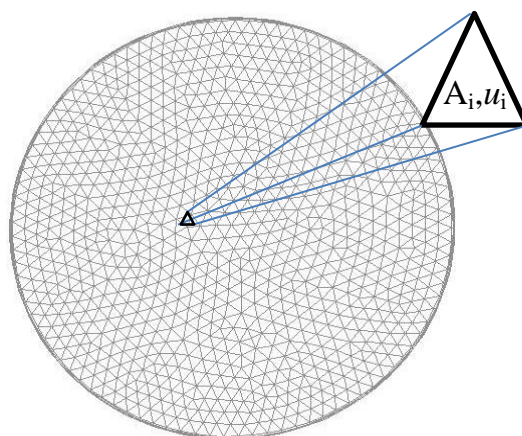


Figure 92: Mesh of pipe cross section.

The equation (120) can be written in the form of:

$$\alpha = \frac{1}{A \bar{u}^3} \sum_{i=1}^n A_i u_i^3 \quad (122)$$

The area weighting average of velocity  $u_a$  can be calculated in the FLUENT using the equation:

$$u_a = \frac{1}{A} \sum_{i=1}^n A_i u_i^3 \quad (123)$$

Then the kinetic energy correction factor can be calculated by:

$$\alpha = \frac{u_a}{\bar{u}^3} \quad (124)$$

Figure 93 shows normalized velocity profile in the main pipe cross sections, which is from the result of the numerical simulation of asymmetrical flow in turbine model with inflow discharge of  $0.108\text{m}^3/\text{s}$ .

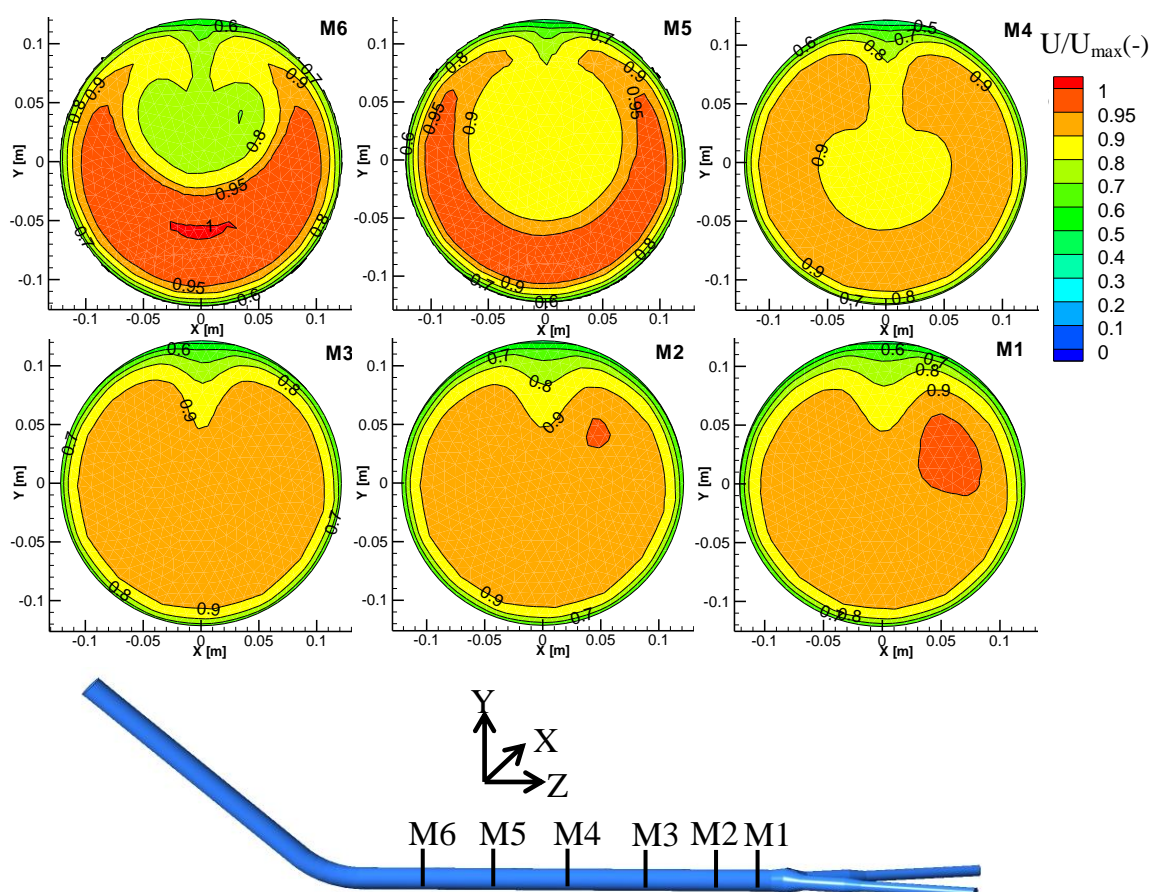


Figure 93: Velocity profile in the main pipe cross sections of asymmetrical flow-turbine mode

It is clearly seen that velocity profile in the section of M6 and M5 are influenced by the bend, where the maximum velocities concentrated in the bottom part and smaller velocity in the upper part of pipe cross-section. In the downstream direction, the influence of the bend to the velocity profile in the pipe decreases, as shown in sections M1 and M2. Section M1 shows the influence of Y-bifurcator, where the maximum velocity is concentrated on the positive X-axis because water flows to the left branch only (asymmetrical flow).

Figure 94 shows the normalized velocity profile in the left branch cross sections. Velocity profile in the section L1 is influenced by separating flow after the bifurcator. By closing the right branch, the water can only flow into the left branch. Branching angles of bifurcator causes maximum velocity in the branch pipe is not in the center but shifted into the outside of the branching in positive X-axis (see Figure 94-L1). Velocity in inner side of the branch is smaller than that in outer side. Contraction effect occurs in the section L2 that make maximum velocity occur in this section. The existence of confusor also influences to the velocity profile in sections between L3 and L6. Velocity profile in the section L6 receives smallest influence of contraction flow from confusor because of the location farthest from confusor.

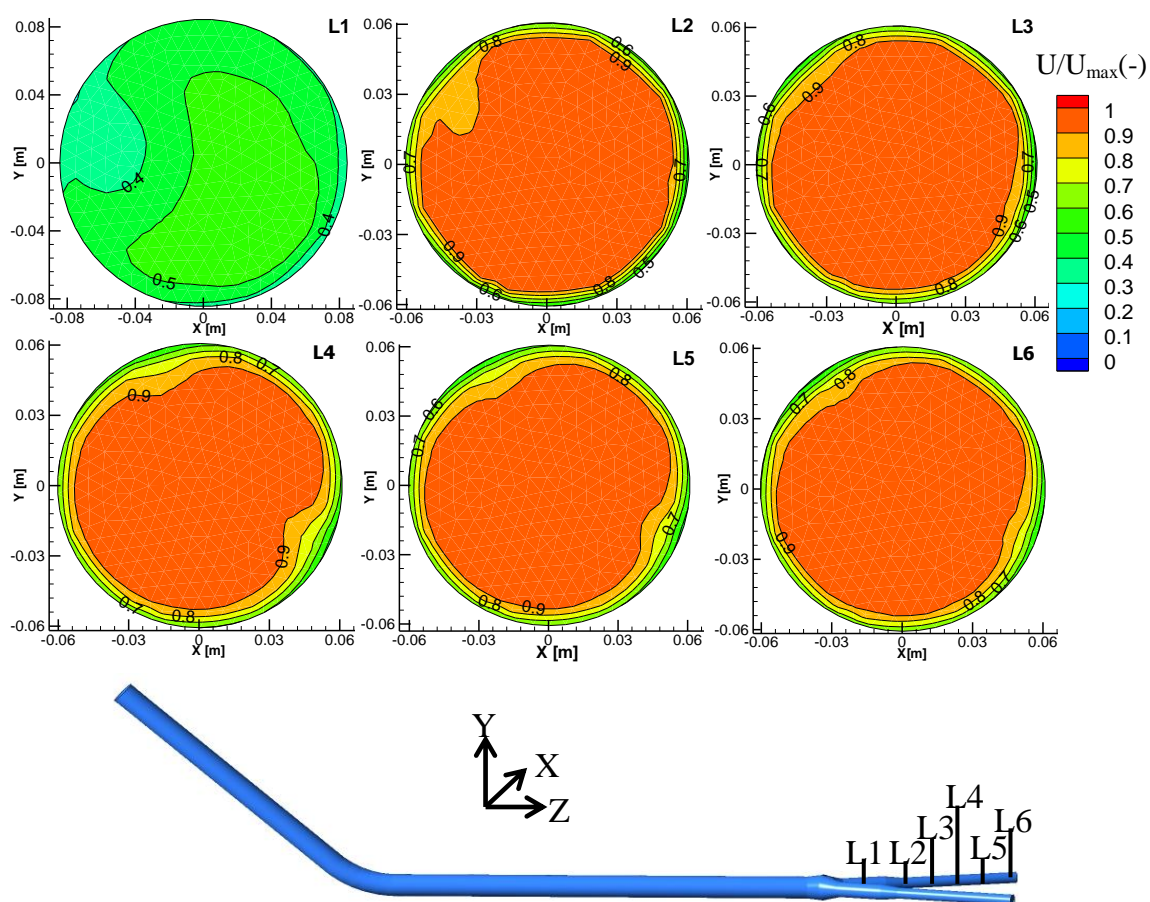


Figure 94: Velocity profile in the left branch cross sections of asymmetrical flow-turbine mode

Figure 95 shows the energy correction factor calculated by realizable k- $\epsilon$  model in the several sections for asymmetrical flow (top) and symmetrical flow (bottom). In the main pipe, the  $\alpha$  values decreases from the upstream section (M6) to the downstream section (M1) but in the branch section (L2 to L6), the value of  $\alpha$  is relative the same. By increasing the inflow, the Reynolds number also increases and the flow is more turbulent, so that the value of  $\alpha$  decreases approaching to one.

The kinetic energy correction factors in the several sections that are produced by several numerical models are also calculated. The standard k- $\epsilon$  produces the highest energy correction factor in section M2. The RSM and LES produce the highest energy correction factor in section M1. The lowest kinetic energy correction factor is produced by the third model occurs in the section L6. Kinetic energy correction factors of LES model are higher than that of two other models. Kinetic energy correction factors of LES in the main pipe are also higher than that in the branch pipe. The existence of bifurcator affects significantly to the velocity distribution in the LES model.

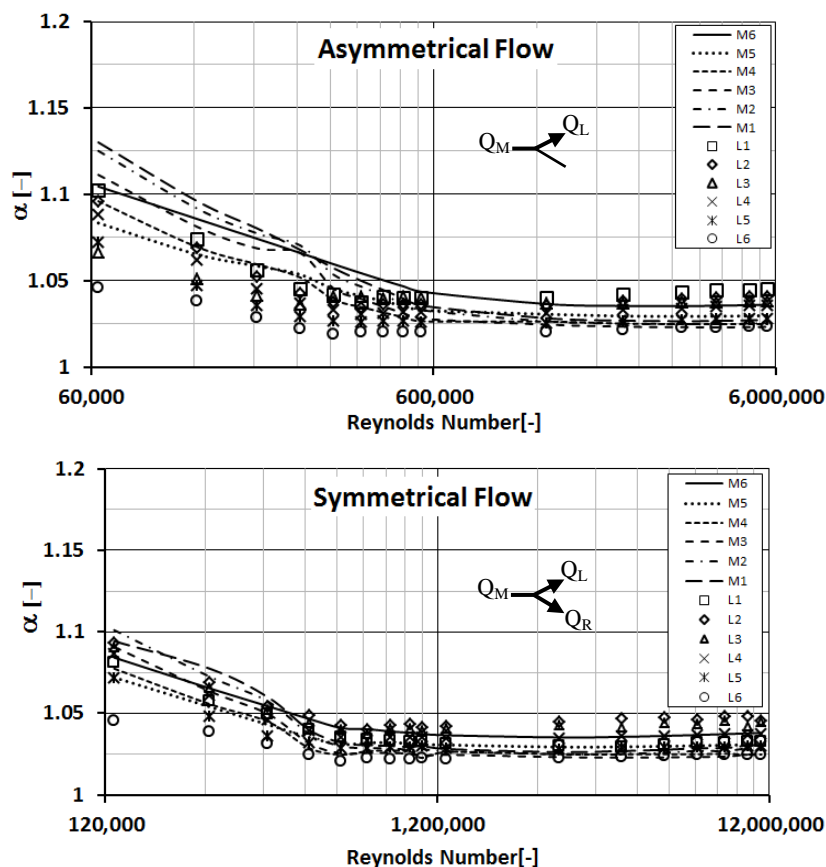


Figure 95: Kinetic energy correction factor for each section  
Top: asymmetrical flow and Bottom: symmetrical flow

### 4.2.7.2 Calculation of loss coefficient with involving kinetic energy correction factor

The loss coefficients were calculated by including the kinetic energy correction factors in energy equation that are shown in Figure 95. Those loss coefficients were compared with the loss coefficient calculated without kinetic energy correction factor. Figure 96 presents that by involving calculated  $\alpha$  in the energy equation, the loss coefficient of asymmetrical flow in turbine simulation is smaller than that without involving energy correction factor. This is caused by diameter of branch pipe, which is the half of diameter of the main pipe. Therefore, in the asymmetrical flow, the velocity in the branch is four times of velocity in the main pipe. In the energy equation,  $\alpha$  is a multiplier factor of kinetic energy (square of velocity), thus the influence of  $\alpha$  in the branch pipe is sixteen times larger than that in the main pipe. Because the velocity in the branch pipe is much higher than the velocity in the main pipe, coefficient  $\alpha$  will increase the kinetic energy in the branch pipe leading to much higher than that in the main pipe. This cause decreases local loss of calculated  $\alpha$  compared to the calculation using  $\alpha=1$ . The loss coefficients calculated using energy equation with assuming  $\alpha =1$  is much larger than that involving  $\alpha$  calculated using equation 124.

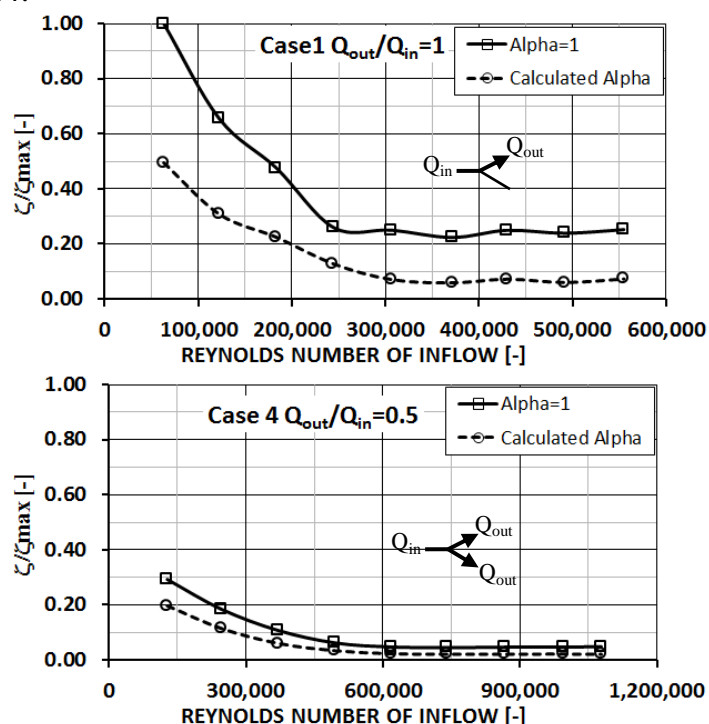


Figure 96: Comparison normalized loss coefficient resulted by realizable k- $\epsilon$  between calculated  $\alpha$  and  $\alpha=1$  in the energy equation

Loss coefficient of standard k- $\epsilon$  model and RSM with an assumption of  $\alpha=1$  and involving calculated energy correction factor are also compared. By involving calculated  $\alpha$  in the energy equation, the loss coefficients that are resulted by all different models are lower than those models using  $\alpha=1$ . Loss coefficient produced

using  $\alpha=1$  is about twice much higher than that using calculated  $\alpha$ . In the asymmetrical flow, the velocity in branch pipe is four times larger than that in the main pipe. Therefore, the kinetic energy in the branch pipe is sixteen times larger than that in main pipe. The influence of kinetic energy correction factor in branch pipe is also sixteen times larger than that in main pipe.

### 4.3 Numerical Simulation of Pirris Y-Bifurcator with Different Scale Factor

#### 4.3.1 Numerical model setup

To study the relationship among models with different scales, four model with scales of 1:1 (prototype size), 1:2 (half of prototype size), 1:8.13 (physical model size) and 1:16.26 (half of physical model size) were developed. Mesh of model scale 1:8.13 is used to build mesh of three other models by scaling with the ratio of length scale. For example, mesh of physical model 1:1 is obtained from the mesh 1:8.13 scaled by 8.13. All four models have the same shape or geometry, type and number of mesh but with different mesh sizes. The size and property of four models are shown in Table 15. Similarity of relative roughness ( $k_s/D$ ) is used so that the friction factors for certain Reynolds number calculated using Colebrook equation are the same for all four models. Thus, the influence of inaccuracy in friction loss calculation can be minimized.

Table 15: Property of Y-bifurcator for numerical modeling with different scales

	Scale			
	1:1	1:2	1:8.13	1:16.26
D main [m]	2.00	1.00	0.246	0.123
D branch [m]	1.00	0.50	0.123	0.065
$k_s$ [m]	0.000152	0.000076	0.0000187	0.000009
$k_s/D_{\text{main}}$	0.000076			
Viscosity [ $\text{m}^2/\text{s}$ ]	0.00000101			

The four 3-dimension steady state numerical model simulations were done using commercial software of ANSYS FLUENT 12.1. The pressured-based was chosen as a solver and the absolute was used for velocity formulation. The viscous model of realizable  $k-\varepsilon$  with standard wall functions was used. Density and viscosity of water was  $1000 \text{ kg/m}^3$  and  $0.00101 \text{ kg/m.s}$  respectively. The inflow boundary condition was mass flow rate using turbulence specification method of intensity and hydraulic diameter. The mass flow rates were obtained from the inflow discharge in Table 16 and Table 17 multiplied by the water density. The outflow boundary conditions were the weighted factor of discharge flow to the left and right branches. The weight factors

of left and right in the asymmetrical flow were 1 and 0; and weight factors of 0.5 for each left and right branches in the symmetrical flow. The wall boundary condition was static wall with the roughness height as shown in Table 15. The equations of flow and turbulence were used for solution control. A SIMPLE model was used as pressure velocity coupling. The discretization of momentum, turbulence kinetic energy, and turbulence dissipation rate used second order upwind.

### 4.3.2 Inflow of the models

Inflow of the four numerical models were calculated based on Reynolds similarity and shown in Table 16 for asymmetrical and Table 17 for symmetrical flow. The Reynolds numbers used in the simulation are taken from the Reynolds number of physical model and extended to achieve the Reynolds number of prototype. Using the Reynolds number equation and the same kinematic viscosity for all scales, inflow velocity (U) of each scale are calculated. The discharge inflows (Q) for each model are calculated by multiplying the velocity with the cross section area at each inflow point of model.

Table 16: Discharge and velocity inflow of models in asymmetrical flow

Reynolds number	Scale							
	1:1		1:2		1:8.13		1:16.26	
	U [m/s]	Q [m <sup>3</sup> /s]						
63,003	0.032	0.100	0.064	0.050	1.036	0.012	0.517	0.006
122,369	0.062	0.194	0.124	0.097	2.012	0.024	1.005	0.012
183,352	0.093	0.291	0.185	0.145	3.014	0.036	1.506	0.018
244,822	0.124	0.388	0.247	0.194	4.024	0.048	2.010	0.024
306,493	0.155	0.486	0.310	0.243	5.038	0.060	2.517	0.030
371,201	0.187	0.589	0.375	0.294	6.102	0.072	3.048	0.036
429,979	0.217	0.682	0.434	0.341	7.067	0.084	3.531	0.042
491,899	0.248	0.780	0.497	0.390	8.086	0.096	4.039	0.048
554,812	0.280	0.880	0.560	0.440	9.119	0.108	4.556	0.054
1,283,096	0.648	2.035	1.296	1.017	5.268	0.250	10.536	0.125
2,161,275	1.091	3.427	2.183	1.714	8.874	0.421	17.747	0.211
3,193,173	1.613	5.063	3.225	2.532	13.110	0.623	26.220	0.311
4,020,691	2.030	6.376	4.061	3.188	16.508	0.784	33.015	0.392
5,055,345	2.553	8.016	5.106	4.008	20.756	0.986	41.511	0.493
5,681,736	2.869	9.009	5.739	4.505	23.327	1.107	46.655	0.554

Table 17: Discharge and velocity inflow of models in symmetrical flow

Reynolds number	Scale							
	1 : 1		1 : 2		1 : 8.13		1 : 16.26	
	U [m/s]	Q [m <sup>3</sup> /s]						
127,441	0.064	0.202	0.129	0.101	0.524	0.025	1.047	0.012
246,894	0.125	0.391	0.250	0.196	1.015	0.048	2.029	0.024
371,053	0.187	0.588	0.375	0.294	1.526	0.072	3.046	0.036
494,242	0.250	0.783	0.500	0.392	2.032	0.096	4.063	0.048
617,203	0.312	0.978	0.624	0.489	2.538	0.120	5.073	0.060
739,715	0.374	1.172	0.748	0.587	3.042	0.144	6.084	0.072
864,587	0.437	1.370	0.874	0.686	3.555	0.169	7.110	0.084
995,046	0.503	1.577	1.006	0.789	4.091	0.194	8.178	0.097
1,076,784	0.544	1.706	1.089	0.855	4.428	0.210	8.857	0.105
1,284,615	0.649	2.036	1.298	1.018	5.269	0.250	10.552	0.125
2,798,359	1.413	4.435	2.825	2.216	11.477	0.545	22.985	0.273
4,312,335	2.178	6.834	4.353	3.415	17.686	0.840	35.419	0.420
5,826,250	2.942	9.233	5.881	4.614	23.896	1.134	47.855	0.568
7,340,123	3.707	11.632	7.409	5.813	30.106	1.429	60.295	0.716
8,844,907	4.467	14.016	8.937	7.011	36.314	1.724	72.728	0.863
10,366,787	5.235	16.428	10.472	8.215	42.523	2.019	85.162	1.011
11,376,380	5.745	18.028	11.488	9.012	46.663	2.215	93.452	1.109

### 4.3.3 Comparison of differential pressure head among models with different scale

The differential pressure head ( $\Delta P/\rho g$ ) resulted by four models with different scales are presented in the Table 18 for the asymmetrical flow and Table 19 for the symmetrical flow. The differential pressures are calculated using the area weighted average pressure in the section M3 subtracted by the area weighted average pressure in the section L6. Correlations of differential pressures among model with different scale are plotted in the Figure 97-top for asymmetrical flow and Figure 97-bottom for symmetrical flow. In the logarithmic graph can be seen a good correlation between Reynolds number and differential pressure resulted by four different scale of numerical models. Table 19 shows the differential pressure head of each model is normalized by its square of geometric scale factor ( $(\Delta P/\rho g)/\eta^2$ ). If the differential pressure of one model divided by differential pressure of another model, the result is equal to the square of length scale ratio of both models. In other words, ratio of differential pressure head between two models is equal to square of length scale ratios. For the same Reynolds number, differential pressure resulted by model with scale of 8.13 is equal to the 66.10 ( $8.13^2$ ) multiplied the differential pressure that resulted by model with scale of 1:1. Using Reynolds number similarity, the normalized

differential pressure head of four models are almost the same. The numerical models applied Reynolds similarity in the calculation of pressure.

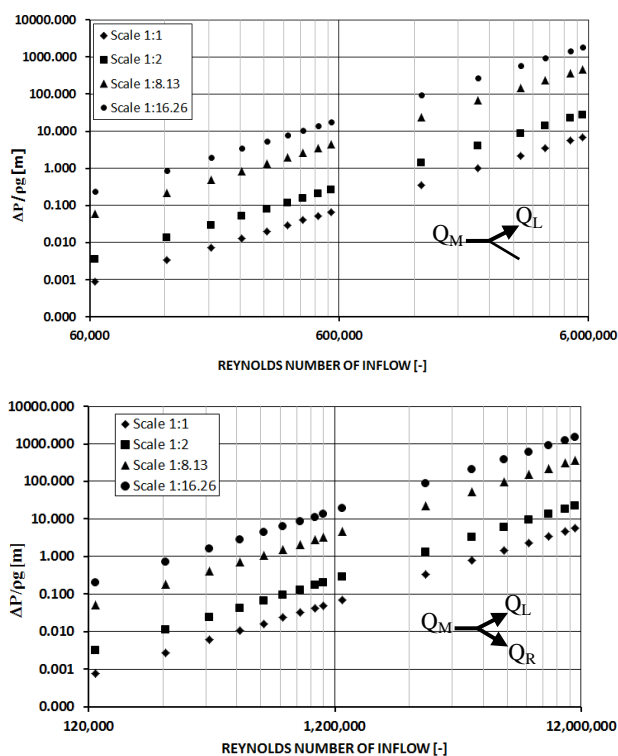


Figure 97: Comparison of differential pressure head among different scales models  
Top: asymmetrical and bottom: symmetrical flows in turbine mode

Table 18: Differential pressure head of models in asymmetrical flow

Reynolds number	$(\Delta P/\rho g)$ [m]			
	1:1	1:2	1:8.13	1:16.26
63,130	0.001	0.004	0.060	0.238
122,604	0.003	0.013	0.219	0.882
183,746	0.007	0.029	0.486	1.943
244,119	0.013	0.052	0.847	3.418
307,143	0.020	0.081	1.332	5.335
371,994	0.030	0.119	1.958	7.840
430,610	0.040	0.159	2.625	10.515
492,620	0.052	0.209	3.432	13.769
555,621	0.066	0.265	4.366	17.512
1,284,306	0.354	1.417	23.409	93.692
2,163,808	1.009	4.029	66.536	266.466
3,197,069	2.199	8.849	145.851	585.300
4,023,777	3.495	14.020	231.452	926.752
5,060,359	5.518	22.198	366.116	1467.941
5,688,469	6.994	27.992	461.864	1850.791

Table 19: Differential pressure head of models in symmetrical flow

Reynolds	$(\Delta P/\rho g)$ [m]				$(\Delta P/\rho g)/\eta^2$ [m]			
	1 : 1	1 : 2	1 : 8.13	1 : 16.26	1 : 1	1 : 2	1 : 8.13	1 : 16.26
127,441	0.001	0.003	0.051	0.205	0.0008	0.0008	0.0008	0.0008
246,894	0.003	0.011	0.183	0.728	0.0027	0.0028	0.0028	0.0028
371,053	0.006	0.024	0.401	1.593	0.0060	0.0060	0.0061	0.0060
494,242	0.011	0.042	0.701	2.801	0.0106	0.0106	0.0106	0.0106
617,203	0.016	0.066	1.085	4.338	0.0164	0.0164	0.0164	0.0164
739,715	0.024	0.095	1.562	6.243	0.0235	0.0236	0.0236	0.0236
864,587	0.032	0.128	2.114	8.456	0.0319	0.0320	0.0320	0.0320
995,046	0.042	0.170	2.809	11.222	0.0424	0.0425	0.0425	0.0424
1,076,784	0.050	0.201	3.319	13.271	0.0500	0.0502	0.0502	0.0502
1,284,615	0.071	0.284	4.675	18.829	0.0709	0.0709	0.0707	0.0712
2,798,359	0.337	1.346	22.217	89.451	0.3367	0.3365	0.3361	0.3383
4,312,335	0.802	3.204	52.834	213.121	0.8022	0.8010	0.7993	0.8061
5,826,250	1.464	5.861	96.532	388.867	1.4642	1.4652	1.4605	1.4708
7,340,123	2.326	9.316	153.419	617.911	2.3256	2.3290	2.3211	2.3371
8,844,907	3.380	13.567	223.393	900.465	3.3795	3.3917	3.3798	3.4059
10,366,787	4.651	18.639	306.784	1234.868	4.6508	4.6598	4.6414	4.6707
11,376,380	5.601	22.439	369.610	1489.255	5.6012	5.6099	5.5919	5.6328

#### 4.3.4 Comparison of loss coefficient among models with different scale

Normalized loss coefficients of Y-bifurcator with different scales for asymmetrical and symmetrical flow in turbine mode are calculated and presented in Figure 98. Four numerical models with different scales produce not only similar trend of loss coefficient over Reynolds number but also almost the same average values. In the figure can be seen that the normalized loss coefficients of Y-bifurcator for four different physical models are fit to each other. The Reynolds similarity in the numerical model produces loss coefficient that is small influenced by the length scale of model. Normalized loss coefficients of different scales Y-bifurcator for asymmetrical and symmetrical flow in pumping mode are presented in Figure 99. Similar in the turbine mode, loss coefficient in the pumping mode produced by numerical models with different scale are almost the same, so that the loss coefficients are also small influenced by the length scale of model.

Using similarity of Reynolds number and relative roughness, four different scales of numerical models of Y-bifurcator produce similar value of loss coefficient. They are both for asymmetrical and symmetrical flows (Figure 98 and 99).

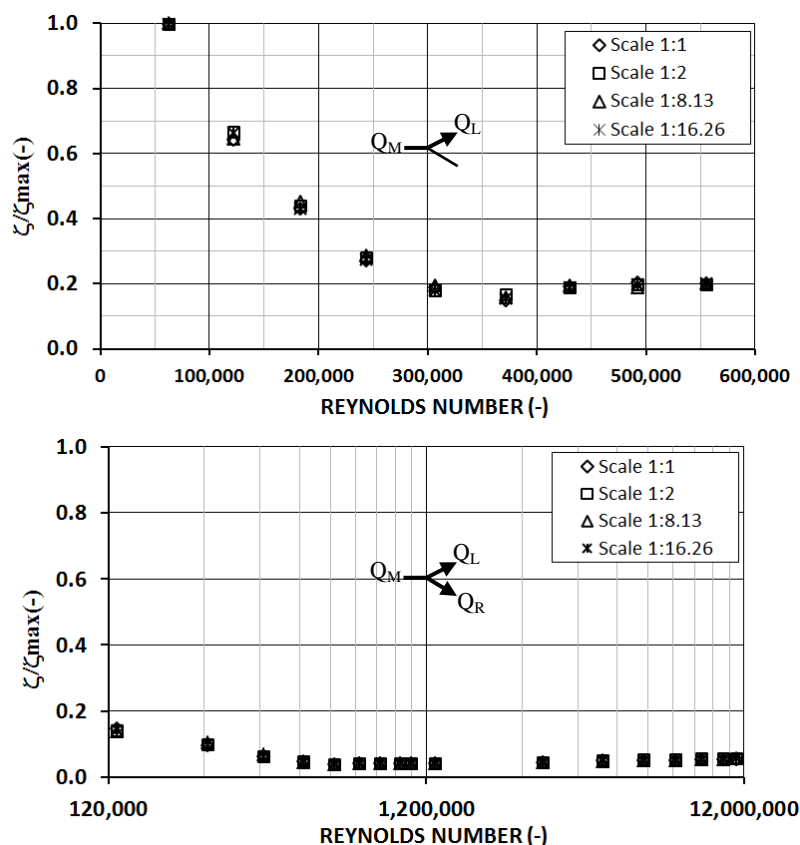


Figure 98: Comparison of normalized loss coefficients among four different models  
 Top: asymmetrical flow and bottom: symmetrical flow in turbine simulation

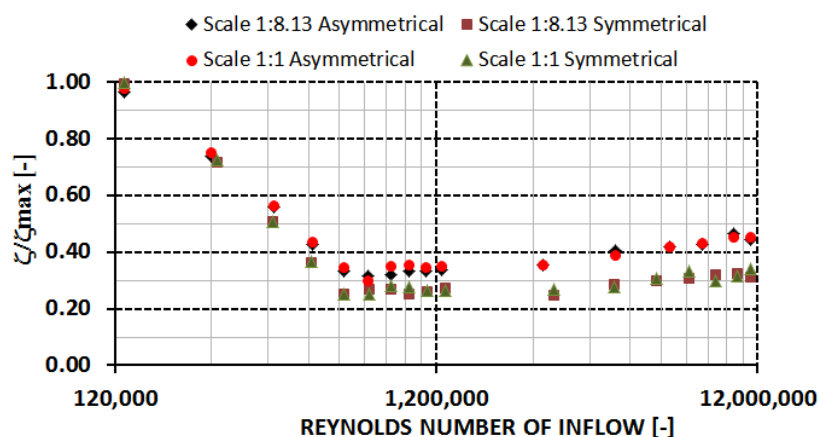


Figure 99: Comparison of normalized loss coefficients between two different scale models for symmetrical flow in pumping mode simulation

### 4.3.5 Comparison of velocity among different scale of numerical models

Four numerical models with scale 1:1, 1:2, 1:8.15, and 1:16.26 are simulated to compare the velocity profile. The numerical models with different sizes were simulated for asymmetrical flow in the inflow Reynolds number of 554,812. Using

Reynolds number similarity, the inflow of four numerical models are  $0.054 \text{ m}^3/\text{s}$ ,  $0.108 \text{ m}^3/\text{s}$ ,  $0.440 \text{ m}^3/\text{s}$ , and  $0.880 \text{ m}^3/\text{s}$  respectively. The four numerical models use the same configuration.

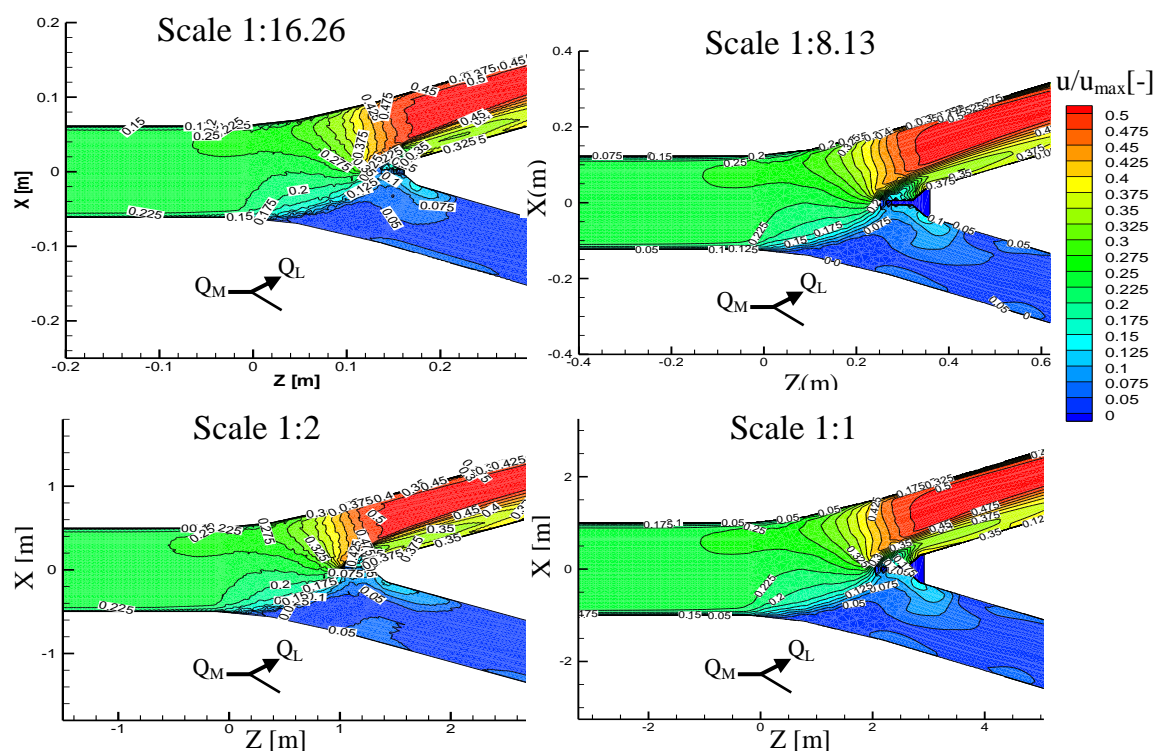


Figure 100: Normalized velocity contour in the center of pipe in asymmetrical flow

Correlation of velocity between two models with different scales is explained as follows. The maximum velocities that are obtained by numerical models with scale of 1:8.13 and of 1:1 are  $9.89 \text{ m/s}$  and  $1.216 \text{ m/s}$  respectively. The ratio of velocity between two numerical models is  $9.89/1.216$ , which is equal to  $8.13$ . This ratio is the same with the ratio of scale length of both models ( $8.13/1$ ). The relationship between two models resulted by numerical simulation follows the similarity of Reynolds, where the velocity ratio between physical model and prototype is equal to length scale. Velocity profile of asymmetrical flow in horizontal plane of a Y-bifurcator resulted by four numerical models are normalized with its maximum velocity and presented in Figure 100.

Figure 101 shows the comparison of velocity vector of asymmetrical flow between four numerical models in the horizontal section in the center of bifurcator. Velocity of four models in the main pipe, bifurcator, left and right branch have the same direction. The maximum velocity of four models occurs in the left branch. Swirl flow and reverse velocity can also be seen in the same location in the right branch of four models. Using the Reynolds similarity, the velocity magnitude produced by the realizable  $k-\epsilon$  in simulating flow through Y-bifurcator with different size can act as function of geometry scale.

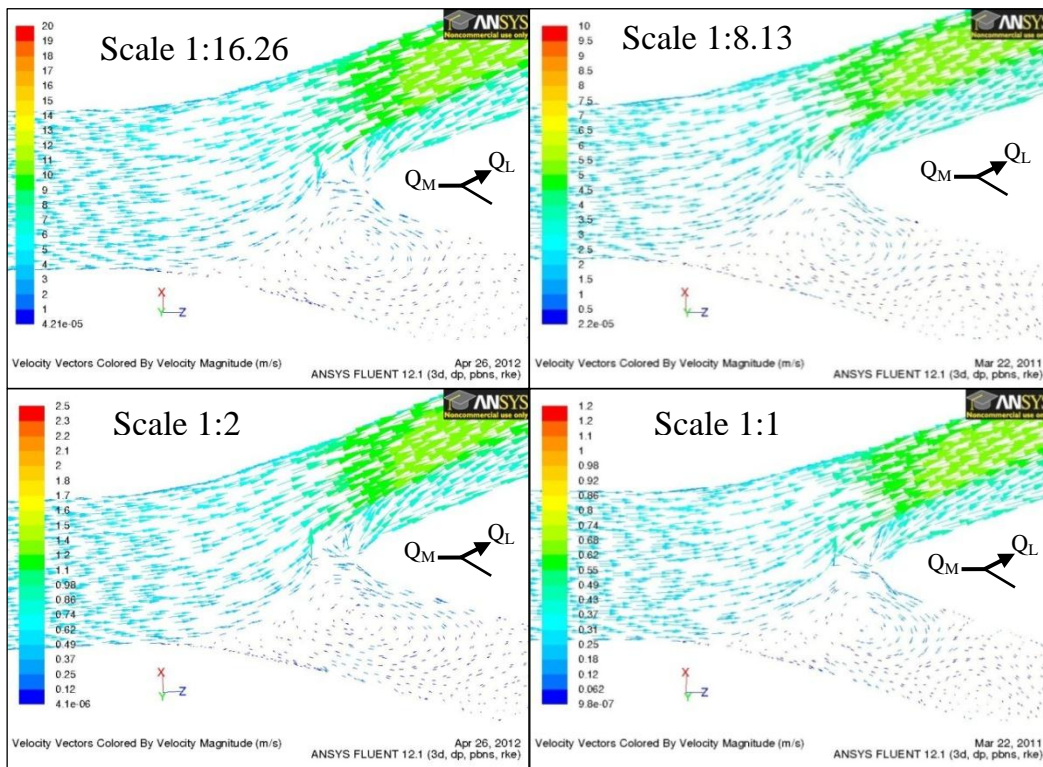


Figure 101: Velocity vector of numerical models with different scale

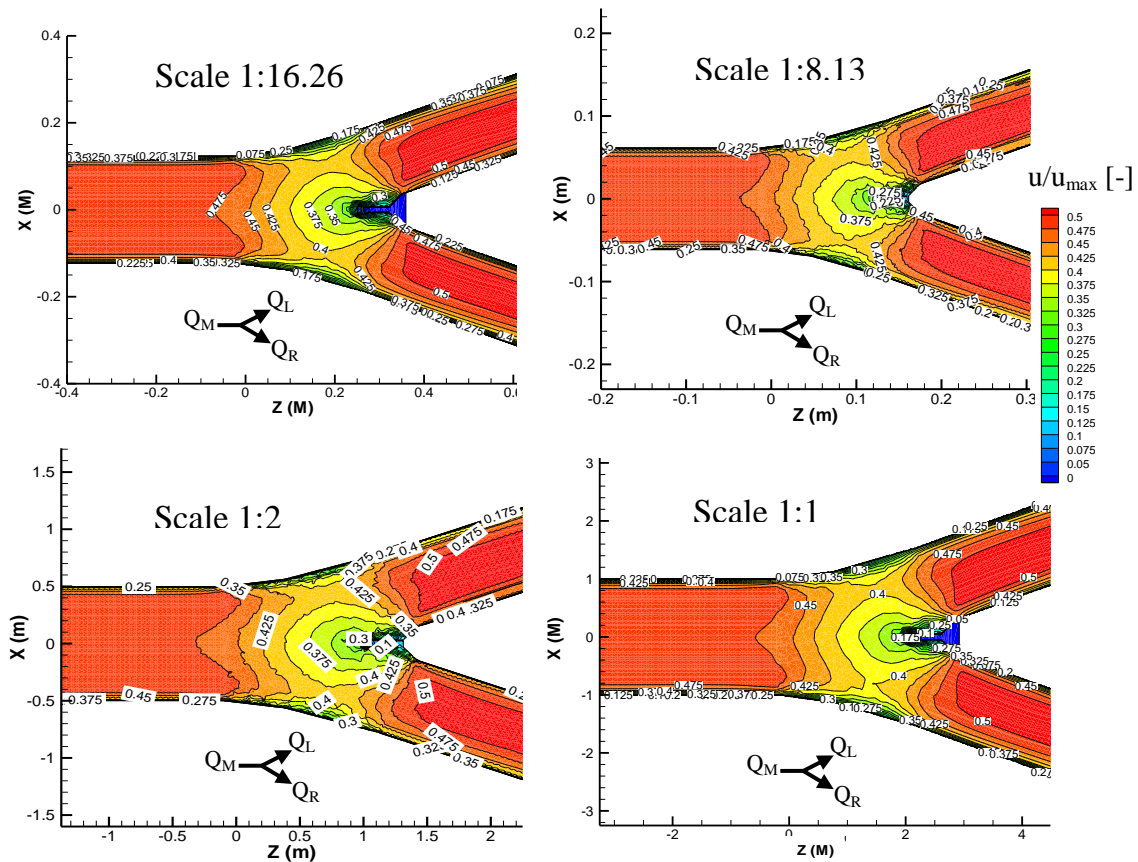


Figure 102: Normalized velocity contour in the center of pipe in symmetrical flow

A Reynolds number of  $1,08 \cdot 10^6$  is used in the simulation numerical model of symmetrical flow. Inflow for each model with scale of 1:1, 1:2, 1:8.13 and of 1:16.26 are  $1.706 \text{ m}^3/\text{s}$ ,  $0.853 \text{ m}^3/\text{s}$ ,  $0.21 \text{ m}^3/\text{s}$ , and  $0.105 \text{ m}^3/\text{s}$  respectively. They are calculated using the same Reynolds number. Figure 102 shows normalized velocity profile of symmetrical flow resulted by four numerical models. The four figures show similar velocity profile and magnitude.

## 4.3.6 Loss coefficient as function of velocity and pipe diameter

### 4.3.6.1 Loss coefficient as function of velocity

In this section, loss coefficients resulted by four numerical models with different scale factors are calculated using two sections that have low energy correction factor. Figure 103 shows comparison of normalized loss coefficient as function of velocity among four different scales of numerical models. In the low Reynolds number region, loss coefficient decreases steeply. In the middle region at certain Reynolds number, loss coefficient increases gradually approaching the high Reynolds number region. Increasing loss coefficient in the middle region of asymmetrical flow is higher than that in the symmetrical flow. Normalized coefficient variation over velocity of four different numerical models for some Reynolds number are presented in Figure 104. For the same Reynolds number, the difference of loss coefficient among four models with different scale are small.

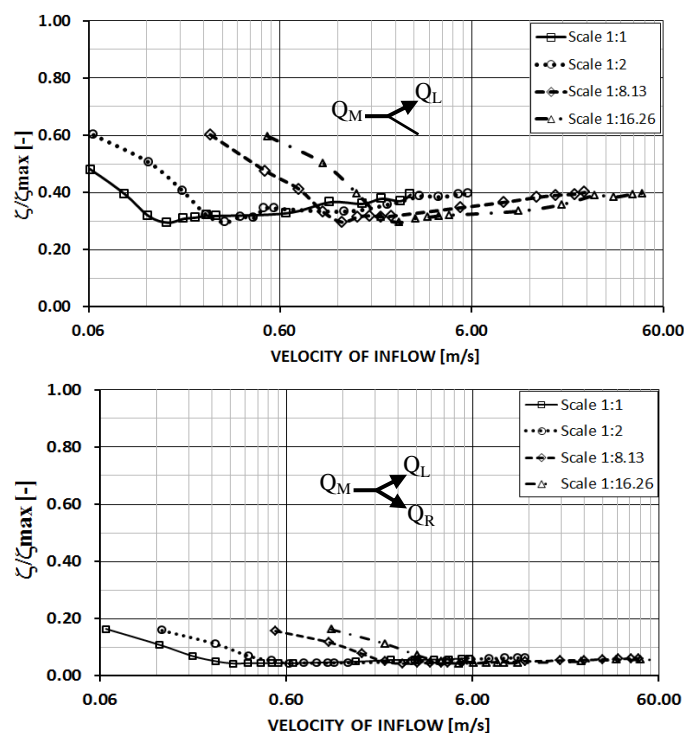


Figure 103: Normalized loss coefficient as function of velocity for different scale  
Top: asymmetrical flow and bottom: symmetrical flow

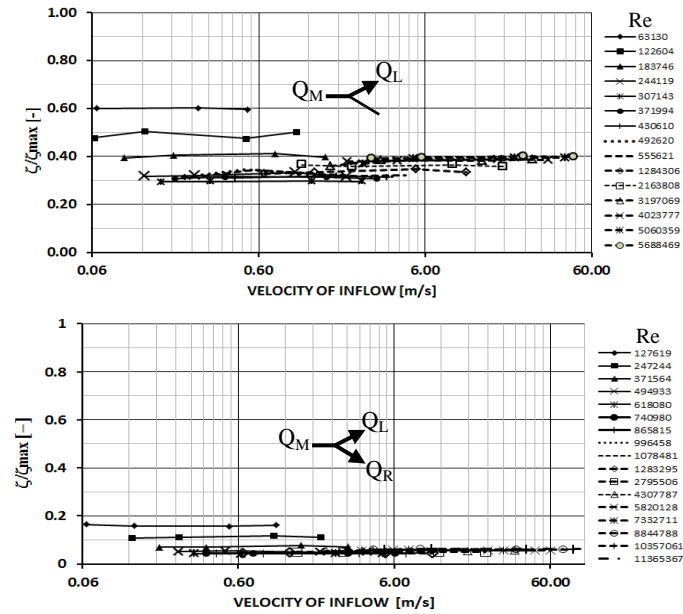


Figure 104: Normalized loss coefficient as function of velocity

### 4.3.6.2 Loss coefficient as function of pipe diameter

Using Reynolds similarity, normalized loss coefficient variations over main pipe diameter of four different numerical models for some Reynolds number are presented in Figure 105. For the same Reynolds number, loss coefficients resulted by numerical models with different diameter of pipe are almost the same. When the Reynolds number increases, the loss coefficient of models decreases. In the low Reynolds number region, loss coefficient of four models decrease steeply, but it doesn't happen in the high Reynolds number regions. The geometry size of numerical model (scale) does not affect the loss coefficient when the Reynolds similarity is applied.

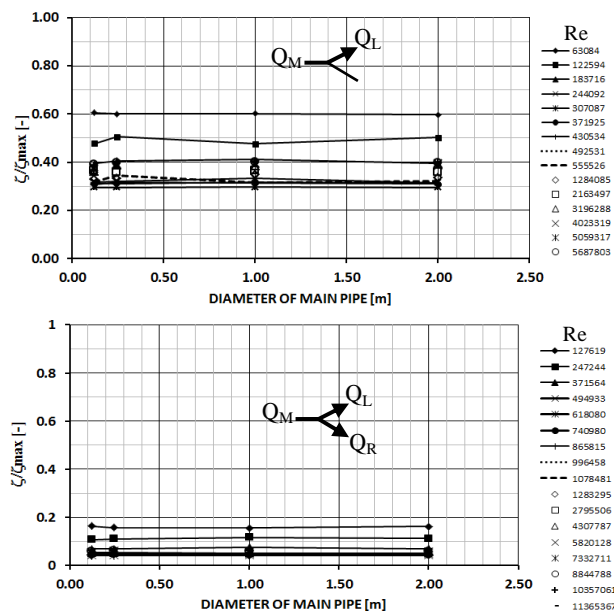


Figure 105: Normalized loss coefficient as function of main pipe diameter

### 4.3.7 Influence of roughness

As mention in the previous sub-chapter, the four different scale factor models have similarity in Reynolds number and relative roughness ( $k_s/D$ ). The purpose of using relative roughness similarity is to equate the roughness factor among the models. The physical model 1:8.13 has the roughness coefficient of 0.0187 mm, the main pipe diameter of 0.246 m, and the ratio of  $k_s/D$  is 0.000076. Using the similarity of  $k_s/D$ , the model with scale of 1:1 with the main pipe diameter of 2.0 m was simulated using roughness coefficient of 0.152 mm. This roughness is too high and it does not reflect to the roughness of the prototype pipe. For example, the GRP (Glass-fiber Reinforced Polyester) pipe that produced by Flowtite-Amiantit has roughness height of 0.029 mm. The steel commercial pipe approximately has roughness of 0.045 mm to 0.09 mm. By assuming the  $k_s/D$  of prototype pipe is one-fifth smaller than the  $k_s/D$  of physical model pipe, the  $k_s/D$  of prototype is  $0.000076/5 = 0.0000152$ . Thus, the roughness coefficient that will be used in the prototype simulation is  $0.0000152 \times 2000 \text{ mm} = 0.0304 \text{ mm}$ . One more roughness value of 0.0760 mm is also simulated to compare the loss coefficient.

Theoretically, using Reynolds similarity, all models with different roughness should produce the same value of loss coefficient. This happens because the friction loss has been subtracted from the total of energy loss in the loss coefficient calculation. Therefore, regardless of the roughness coefficient, the calculation will produce the same local loss. In order to find out the influence of friction loss calculation to the loss coefficient, numerical models were simulated using three different roughness heights of 0.0304 mm, 0.0760 mm, and 0.152 mm. The loss coefficients for each model were calculated and compared to the other model.

For the same Reynolds number, the normalized loss coefficient values generated by three numerical models are different as shown in Figure 106. Model with higher roughness produces loss coefficient smaller than the model with low roughness in the scale model Reynolds number are but in the prototype Reynolds number area, the highest roughness produces highest loss coefficient. Increasing  $k_s/D$  in the roughness of numerical model will affect to change in the loss coefficient.

The difference result of loss coefficient was investigated by comparing the friction loss calculation between result of numerical model and analytical calculation using Colebrook equation. Figure 107 shows comparison of friction loss of 1-meter length of straight pipe with diameter of 1.0 meter between numerical model (CFD) and analytical calculation using Darcy-Weisbach and Colebrook equations with Reynolds number in the range of scale model. The smallest roughness height produces small difference of friction loss between CFD and Colebrook equations. The largest roughness produces large difference of friction loss between CFD and analytical calculation. Because the local loss is obtained from total loss subtracted by friction

loss that calculated using Colebrook equation, then the large roughness model produces smaller local loss compared with small roughness model. Loss coefficient of large roughness model is smaller than that of small roughness model. When the relative roughness of model is small, the difference of friction loss calculated by CFD and analytical is small. The friction loss calculated using numerical model is different with the friction loss calculated analytically using Darcy-Weisbach and Colebrook equations. Allen et al. also investigated turbulent flow in smooth and rough pipes giving a conclusion that the friction factor behavior of a honed surface in the transitional regime does not follow the Colebrook relationship [91].

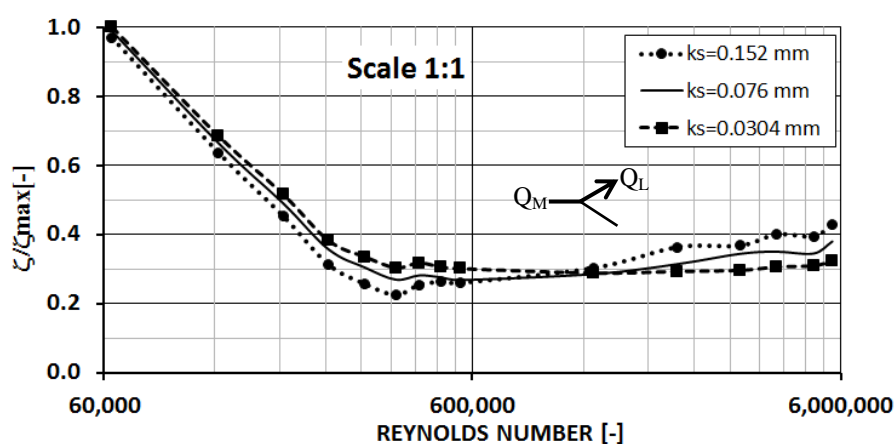


Figure 106: Comparison of normalized loss coefficients resulting by three model with different roughness coefficient

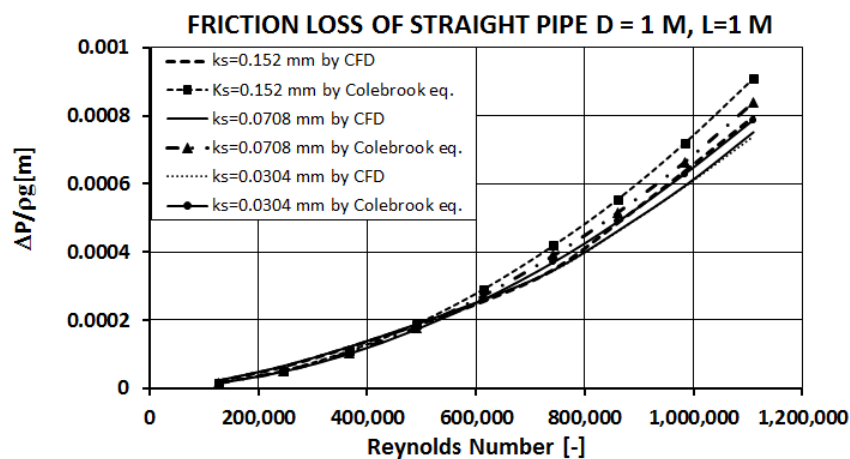


Figure 107: Comparison of friction losses between calculated by CFD and using Colebrook equation for different roughness coefficient

## 4.4 Conclusion

Conclusions of study on loss coefficient using scale and numerical models are:

- The flow meters and pressure sensors used in the discharge and differential pressure head measurement for experiment of low flow through a Y-bifurcator produce higher percentage of deviation than that in high flow. The percentage of deviation decreased with the increasing discharge measurements.
- The measurement on physical model gives the result that loss coefficient decreases and then tends to be near constant with increasing Reynolds number. There are different results of the pressure and loss coefficient between left and right branches of Y-bifurcator that was caused by not fully symmetric installation between both branches. Experiment using left branch produces loss coefficients with better trend and more consistent compared with experiment using right branch.
- Variations of loss coefficient resulted by calculations using several sections are not only caused by measurement accuracy but also caused by approximation in the calculation of friction loss.
- The experiments of flow through a Y-bifurcator in pumping mode produce variation of loss coefficient in Reynolds number and different sections smaller compared to those in the turbine mode.
- Numerical model with the smallest mesh interval produces the closest loss coefficient to physical model. Boundary layers size of mesh influence to the loss coefficient in the low Reynolds number region. In the high Reynolds number region, the influence is small so the loss coefficients resulted by five different models with different boundary layers size are almost the same.
- Comparison of loss coefficient between scale and numerical models gives specific result for each case, but in general, the deviation of loss coefficient in high Reynolds number flow is smaller compared with in low Reynolds number flow.
- Numerical simulation on steady and unsteady flow using the same geometry of Y-bifurcator and boundary conditions give the similar result of loss coefficient.
- Differential pressure head calculated by numerical model is different compared with that calculated using extrapolation method. Extrapolation of differential pressure head using second order polynomial produce loss coefficient closer to numerical model compared with others polynomials.
- Kinetic energy correction factor decreased with the increasing Reynolds number and the values close to one in the very high Reynolds number. Kinetic energy correction factor of a Y-bifurcator with high ratio of velocity between branch and main pipes has influence in the calculation of loss coefficient. Loss

coefficient calculated using kinetic energy correction factor is lower than loss coefficient calculated without using kinetic energy correction.

- Loss coefficients of flow through a Y-bifurcator are influenced by the flow magnitude, the shape, the pipe diameter ratio, the branching angle and the discharge ratio between outflow and inflow.
- Loss coefficients and velocity profiles produced by realizable k- $\epsilon$  model are closer to the result of the physical model than those are produced by other numerical models.

Conclusions of similarity study in loss coefficient using numerical models are:

- Friction loss calculated using equation of Darcy-Weisbach and Colebrook is different compared with friction loss calculated by numerical modeling using realizable k- $\epsilon$  turbulent model with standard wall function.
- The Reynolds similarity law is successfully applied to numerical models in the calculation of differential pressure head. The ratio of differential pressure head between two numerical models with different scale is close to the square of the length scale.
- With the Reynolds similarity, loss coefficients produced by four numerical models close each other for all ranges of inflows, and the loss coefficients decreased with the increasing inflow. The length scale of the model gives less influence to the loss coefficient. The normalized velocity of one model is similar to the other models in form of magnitude and direction.

## 5 Application of numerical modeling in the investigation of hydraulic problems

### 5.1. Numerical model of long elbow with different scale

#### 5.1.1. Introduction

Flow will turn when it runs through an elbow. In the elbow, pressure and velocity distribution change and secondary flows are generated. Secondary flow will re-energize the inner wall regions. Weak secondary flow causes separation flow in inside of elbow outlet.

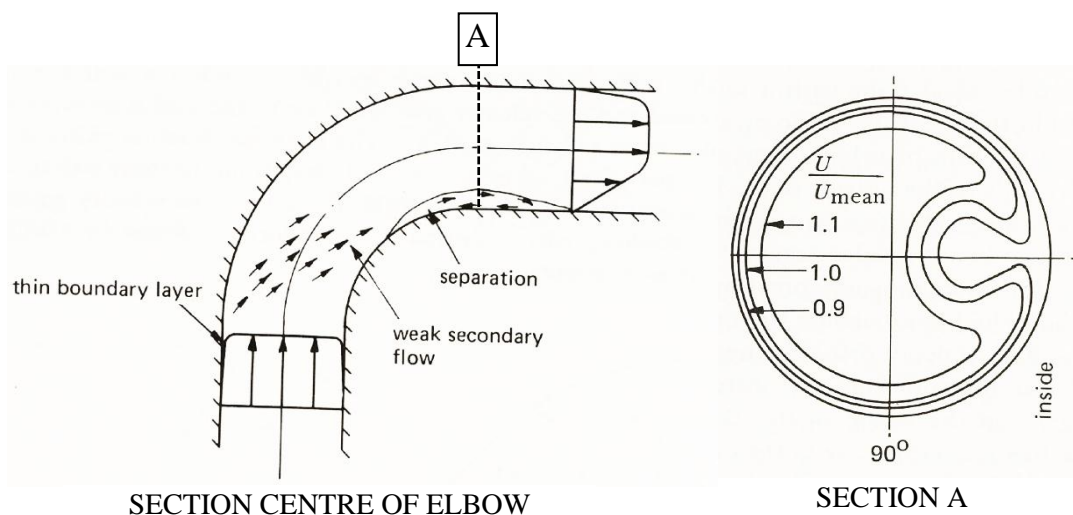


Figure 108: Flow separation (left) and bend outlet velocity contour (right)[68]

According to the experiment by Miller [68], for bend/elbow of centerline radius to diameter ratio between 0.8 and 1.5, loss occurs in the bend is about 80% and the rest occurs at two-pipe diameter after the bend. Secondary flow is weak when the flow at the inlet nearly one-dimensional. Reynolds number is proportional to the flow velocity. The pressure loss coefficient is inversely to flow velocity. When the Reynolds number increases, flow velocity also increases so the pressure loss coefficient becomes smaller. Pressure loss is affected by separation flow in the separation zone of bend. The greater flow velocity will increase pressure at high-pressure region (outer bend) and decreases pressure at low-pressure region (inner bend). This will cause separation area become smaller and the coefficient of pressure loss also become smaller.

## 5.1.2 Numerical model of flow through elbows

The objective of this study is to implement the numerical modeling to evaluate loss coefficient of long elbow with different diameter. Mesh of numerical model of long elbow of 12" was prepared using software Gambit. Mesh for elbows of 16", 20" and 24" are built using mesh 12" scaled by factors of 1.333, 1.667 and 2 respectively. Mesh interval of model elbow of 12" is 10 mm and the boundary layer size is 0.01 mm with is increased by factor of 1.5.

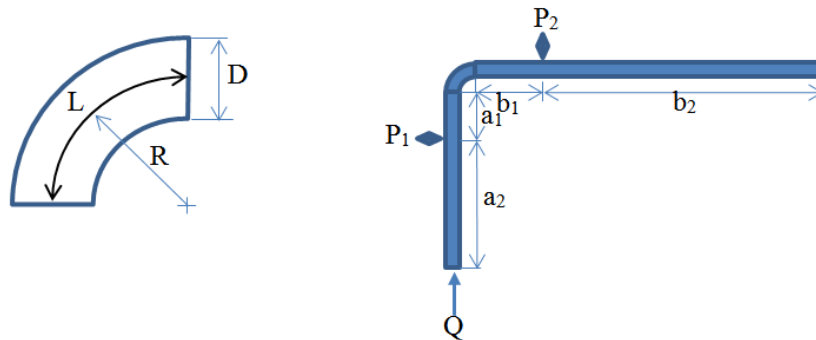


Figure 109: Scheme of numerical model of Long Elbow [46]

Table 20: Dimension properties of long elbow

Property	12"	16"	20"	24"
Scale	1:2	1:1.5	1:1.2	1:1
D (m)	0.3048	0.4064	0.508	0.6096
R/D	1.5	1.5	1.5	1.5
R (m)	0.457	0.610	0.762	0.914
Length (m)	0.718	0.957	1.196	1.436
a1 (m)	0.610	0.813	1.016	1.219
a2 (m)	5.390	7.187	8.984	10.781
b1 (m)	1.829	2.438	3.048	3.658
b2 (m)	8.171	10.895	13.619	16.342
Ks/D	0.003281			
Ks (m)	0.001	0.00133	0.00167	0.002

The four 3-dimension steady state numerical model simulations were done using commercial software of ANSYS FLUENT 12.1. The pressured-based was chosen as a solver and the absolute was used for velocity formulation. Density and viscosity of water is  $998.2 \text{ kg/m}^3$  and  $0.00122 \text{ kg/m.s}$  respectively. The inflow boundary condition is mass flow rate using turbulence specification method of intensity and hydraulic diameter. The mass flow rates are the inflow discharge in Table 21 multiplied by the water density. The outflow boundary conditions are the weighted factor equal to one. The wall boundary condition is static wall with the roughness coefficient as shown in Table 20. The equations of flow and turbulence were used for solution control. A

SIMPLE model was used as pressure velocity coupling. The discretization of momentum, turbulence kinetic energy, and turbulence dissipation rate used second order upwind. Inflow of four numerical models with different scale is calculated based on Reynolds similarity as shown in Table 21.

Table 21: Inflow of the four numerical models

Reynolds number	Discharge (m <sup>3</sup> /s)				Velocity (m/s)			
	12"	16"	20"	24"	12"	16"	20"	24"
319958	0.093	0.124	0.156	0.187	1.280	0.960	0.768	0.640
460892	0.134	0.179	0.224	0.269	1.844	1.383	1.106	0.922
757996	0.221	0.295	0.369	0.442	3.033	2.275	1.820	1.516
982728	0.287	0.382	0.478	0.574	3.932	2.949	2.359	1.966
1367440	0.399	0.532	0.665	0.798	5.471	4.103	3.283	2.736
1626454	0.475	0.633	0.791	0.949	6.507	4.881	3.904	3.254
1896894	0.553	0.738	0.922	1.107	7.590	5.692	4.554	3.795
2148290	0.627	0.836	1.045	1.254	8.595	6.447	5.157	4.298
2479675	0.724	0.965	1.206	1.447	9.921	7.441	5.953	4.961

Four numerical models are simulated using realizable k- $\epsilon$  turbulent model. Standard wall function is used for the model to link solution at near wall cell and corresponding value on the wall. Figure 110 shows increasing average  $y^*$  of numerical model with increasing Reynolds number.  $y^*$  is non-dimension wall distance that can be calculated using equation (84). Using similarity of Reynolds, the four numerical models with different sizes produces similar of  $y^*$ . In the range of  $y^*$  between 30 and 300, the logarithmic law for mean velocity is valid. FLUENT applies the log-law when  $y^* > 11.225$  and uses laminar stress-strain relationship for  $y^* < 11.225$ .

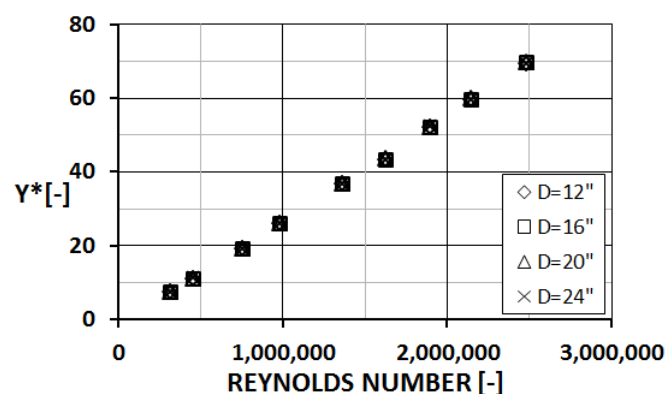


Figure 110: The non-dimension wall distance ( $y^*$ ) of four numerical models of elbow

Figure 111 shows comparison of velocity contour produced by numerical model of flow through an elbow of 24" between low and high Reynolds number of inflow. In the low Reynolds number, flow velocity is small, so that the secondary flow generated in the elbow is also small. The small secondary flow causes large flow separation in

inside of elbow outlet. Contrary to low Reynolds number flow, the high Reynolds number generates high secondary flow that affects to decrease separating flow. The separation flow region can be clearly seen in the cross section of elbow outlet.

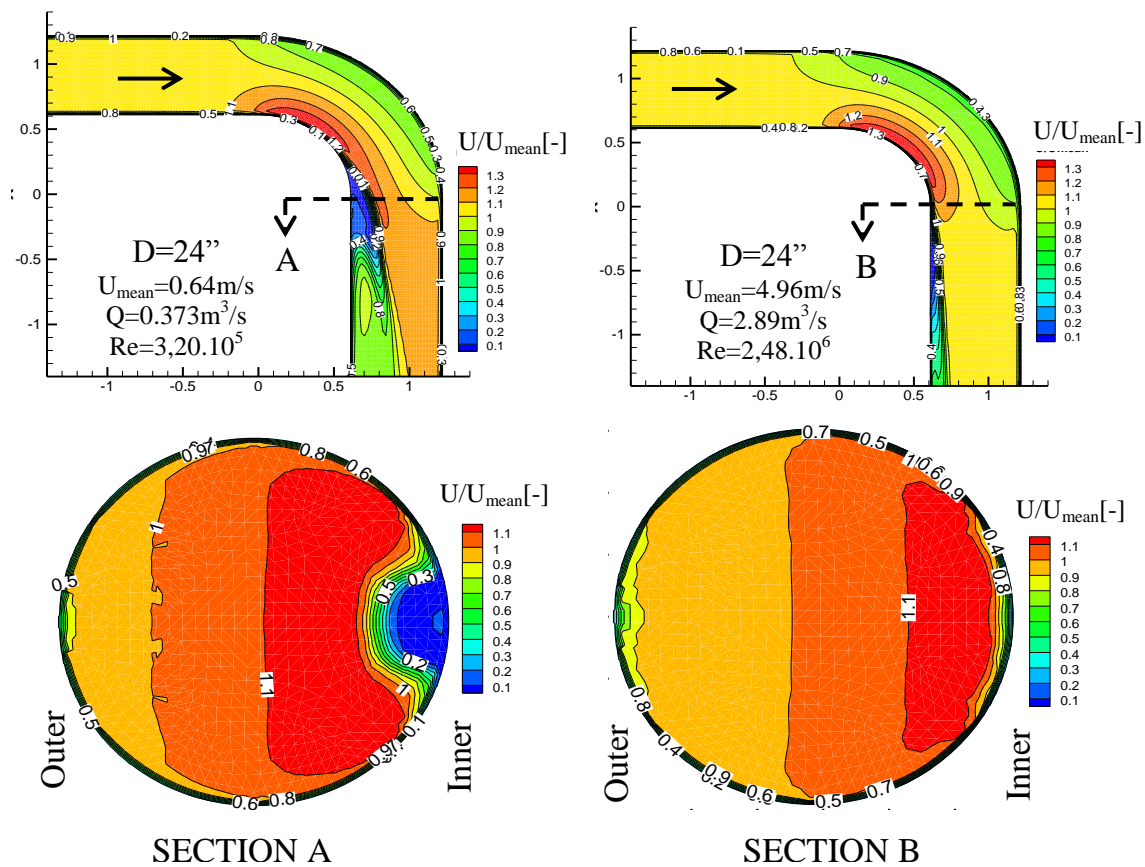


Figure 111: Comparison of velocity contours of elbow 24'' between low and high Reynolds number inflow

Using similarity of Reynolds, four numerical models of elbow with different sizes produce similar velocity distribution. Figure 112 shows comparison of relative velocity contour in the cross section of elbow outlet. The relative velocities in the cross sections of elbows with different size are similar. The separation region also appears similar in the four sections.

Figure 113 shows comparison of relative velocity contour in the center among four different size elbows. The velocities are resulted by numerical modeling of flow through elbows using inflow with similarity of Reynolds. Four elbows have similar relative velocity contour and separation flow region.

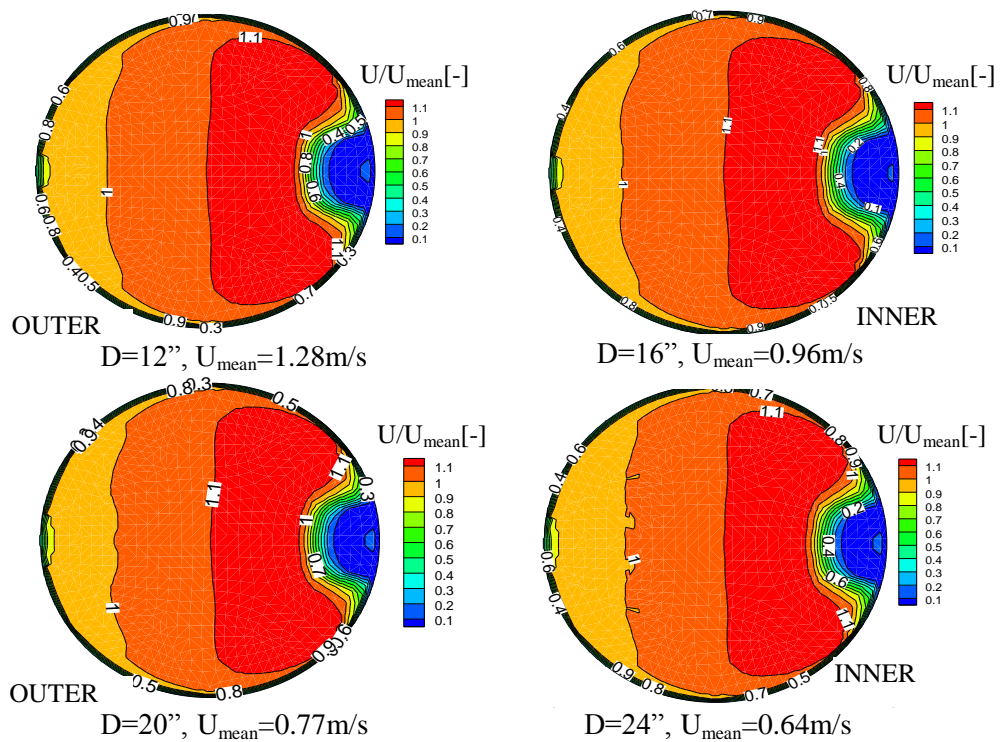


Figure 112: Velocity contours at outlet of elbow 12'', 16'', 20'' and 24''

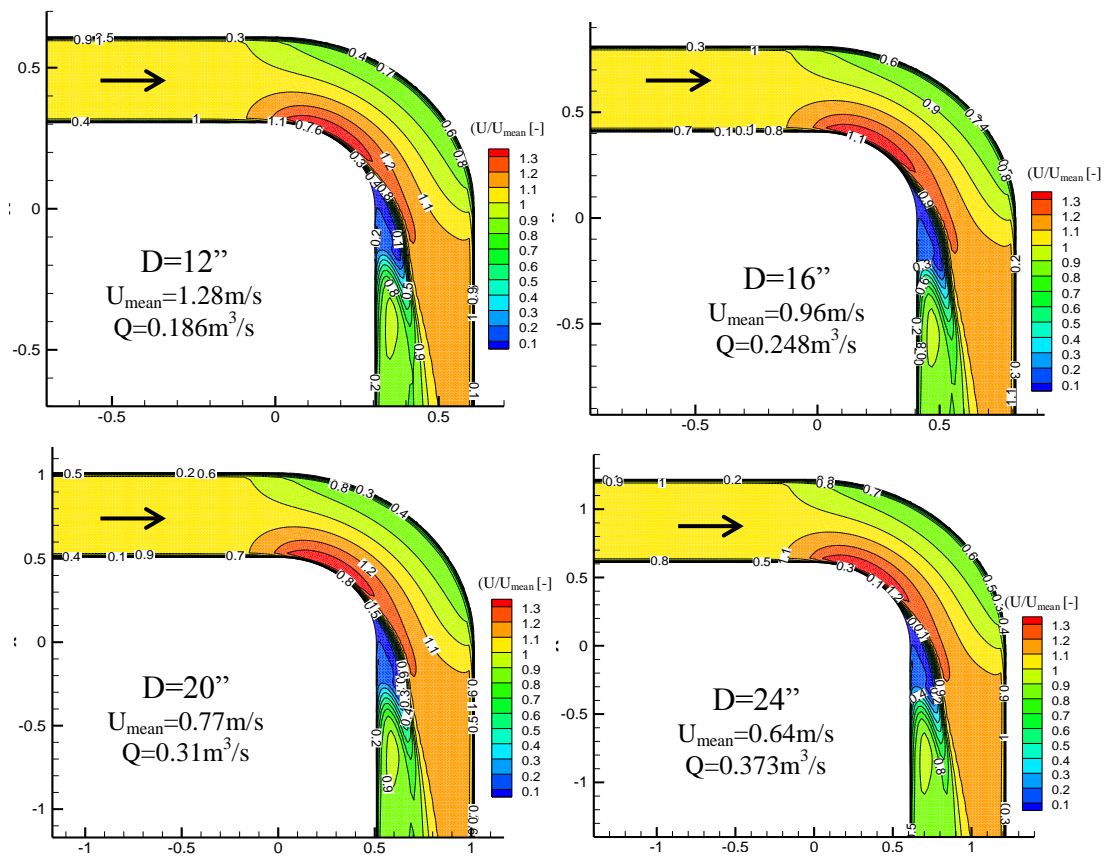


Figure 113: Velocity contours in several elbows for  $Re= 3,19.10^5$

Differential pressures head in the four elbows with similarity of Reynolds are plotted in the Figure 114. In the figures can be seen the high pressure occurs in outer and low pressure occurs in the inner of bend. The smallest elbow produces the largest differential pressure head because of flow the highest velocity (Reynolds similarity). Differential pressure head between outer and inner of the bend will increase with the increasing inflow velocity.

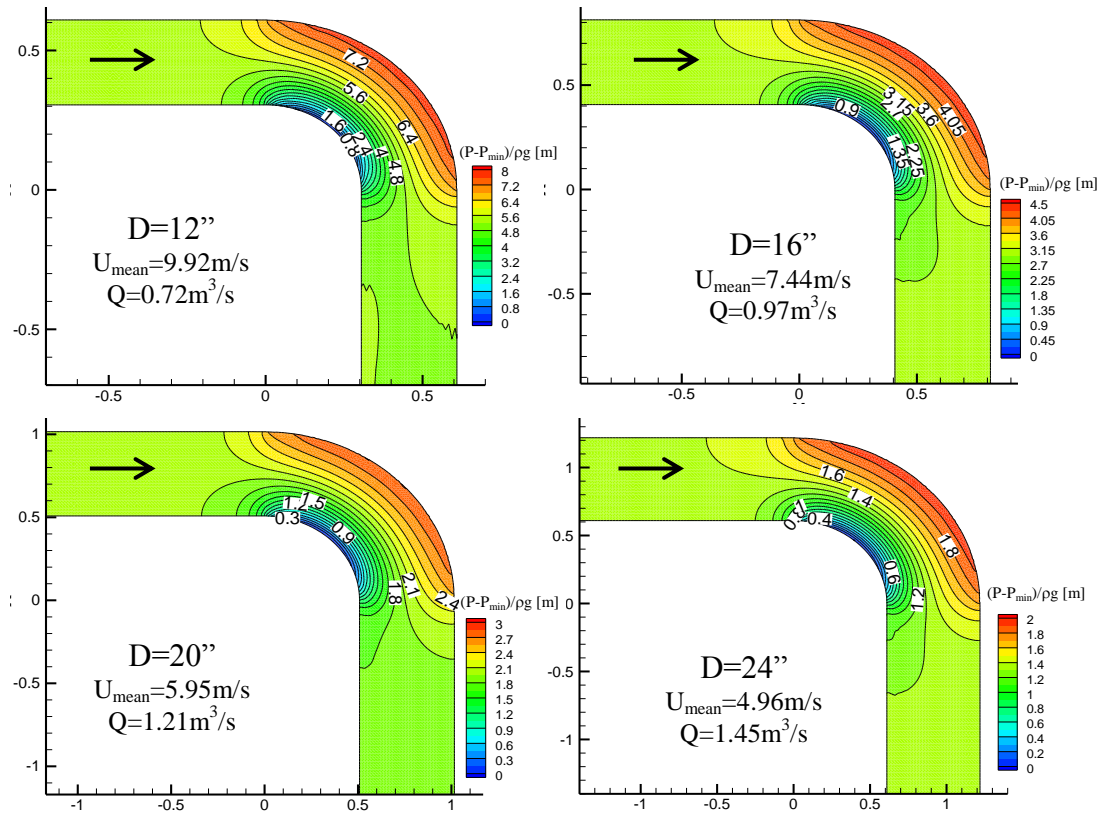


Figure 114: Pressure contours in several elbows for  $Re= 2,479.10^6$

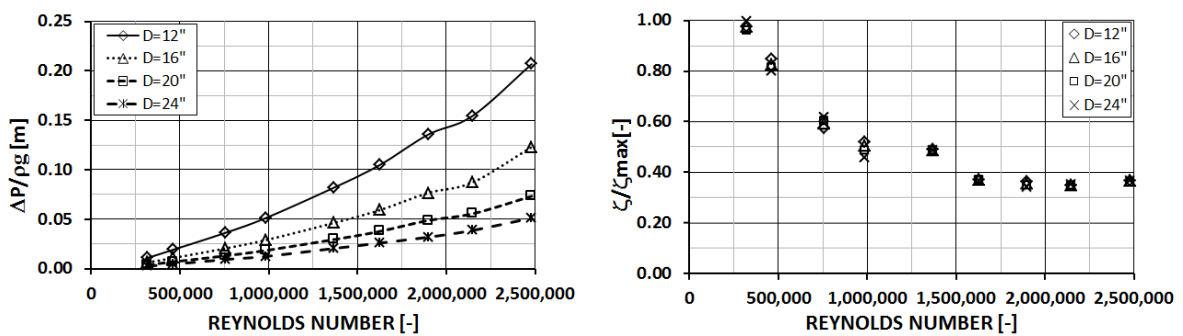


Figure 115: Comparison of differential pressure head (left) and normalized loss coefficients (right) among elbows with different scale

Differential pressure head between section at upstream and downstream of flow through an elbow increased with the increasing inflow discharge. In the Reynolds similarity, increasing elbow diameter will decrease differential pressure head caused by decreasing flow velocity (Figure 115-left). Using turbulent model, four numerical

models of elbow with different size but have similarities in geometry, Reynolds number and relative roughness produce almost the same loss coefficient (Figure 115-right).

## **5.2 Hydraulic problems in the development of pumped storage hydro plant**

Some important issues in the electricity markets in Europe are increase in tariffs, liberalization of energy sources, increasing consumption of electricity, network security systems, and decrease in energy supply. These encourage the development of various sources of electrical energy, such as nuclear, oil, renewable energy sources, etc. Nuclear energy tends to produce excess energy, especially at periods of low energy demand. Thermal power plants tend to produce an abundance of energy to optimize fuel usage. The growth in the construction of renewable energy sources has also been triggered by the agreement stipulated in the renewable energy technology road map, which targets are the use of renewable energy in 2020 at 20% [92].

Renewable energy supply depends on the weather, so it does not match on demand and it is not fully predictable [93]. For instance, wind power has unstable characteristics, i.e. the amount of energy produced fluctuates, and power can be cutoff due to high wind velocities. Furthermore, electric energy needs are not always stable either. These all lead to imbalances between energy production and demand. Therefore, balancing media are important so that they can store energy when production is greater than demand and those that can be used when the demand increase is needed.

The pumped storage scheme is the most widely used solution for storing energy [94]. PSPs can generate power 100 times greater than batteries and 10 times greater than compressed air/thermal solutions. PSPs also have storage capacity about 100 times greater than batteries and 10 times greater than compressed air/thermal solutions. Therefore, at present the PSP is the most economical technology for large-scale energy storage [95]. In the future, the increasing energy demand will be followed by the increasing supply of renewable energy that varies in time, such as from wind and solar. Pumped storage can compensate for these variations by storing and releasing energy. Energy generated by PSP in some central European countries such as Austria, Germany, Switzerland, France and Italy are predicted to increase in 2020. PSPs are also used for balancing the excess energy production from nuclear power plants or other plants in the network. PSPs pump water to the upper reservoir during periods of low electricity tariffs (low demand) and the pumped water is used in the turbines to produce electricity at high electricity prices (peak demand). The PSP can provide the fast and flexible balancing of production and demand that is needed by energy

suppliers. Other power plants may require significant time to change the system mode compared with the pumped storage hydro schemes.

Recent expansions of PSPs in Austria and Germany are response to the rising demand for readily available and flexible energy production. The current projects under construction are Kops II, Limberg II, Reisseck II in Austria, and Atdorf-Schluchseewerk in Germany. Most PSPs are equipped with pump-turbines enabling operation in either pumping or generating modes. In the construction of PSPs, some hydraulic problems arise, requiring investigations and studies to find solutions. The following investigation and study will discuss solutions to the hydraulic problems of PSP Kops II, Limberg II, Reisseck II and Atdorf-Schluchseewerk.

### **5.2.1 PSP Kops II**

The Hydropower Scheme Kops II is a PSP that can be used to regulate the grid in turbine mode as well as in pump mode. The Kops II power plant was built to generate electricity by using the head between upper Kops reservoir (1,800m) and lower Rifa Reservoir (1,000m). The installed turbine capacity can produce 450 MW of electricity [87]. The schematic of PSP Kops II is different in comparison to the others, in that it has separate pump and turbine equipment. The advantage of the PSP Kops II lies on permitting very rapid change-over between the two operation modes, within approximately 20 seconds. Other PSPs have response times ranging around one minute. The special construction feature of Kops II is the “hydraulic short-circuit” enabling simultaneous pumping into the upper reservoir and power generation at the turbine [96]. For example, the pump station can receive 150 MW of energy from the surplus of the network (100 MW) and generated by the turbine (50 MW). This energy is used by the pump station to move water from the lower reservoir to the upper reservoir for producing 100 MW of energy for the network during peak demand and the rest energy for powering the turbines.

A hydraulic study of PSP Kops II was made using physical modeling and numerical analysis. The physical model was used to investigate the upper surge tank and de-aeration of the tail water portion, while the numerical model was used to simulate the performance of the upper surge tank under unsteady hydraulic conditions. There are four objectives in the study [96]. The first is to investigate mass oscillation behavior caused by any desired switching sequence of turbines and pumps in the resonance frequency of the tail water in surge tank system (turbine-pump interaction in time). The second is to design and test an orifice nozzle (the “Gufel” throttle) in the branch to the chamber surge tank. The third was to assess quality of air entrainment under the Pelton turbines, or de-aeration in the pressure surge tank. The last is to test structures installed to reduce air entrainment or accelerate de-aeration, and to make a visual inspection of the general flow pattern and the performance of air-release domes at the entrance to the tailrace tunnel.

A physical model with scale 1:22.5 was built mainly of Plexiglas according to the dimensions of the tail water system, about 350m in length, and the local conditions at the laboratory (Figure 116). The Froude similarity was applied for the model, i.e. that the same relationship between inertial force and gravity applies both in the model and in the prototype. Several challenges in physical modeling under overpressure conditions arose due to the complexity and scope not being available or known, such as the scale effect and transferability of the result. Scale effects play an important role in the roughness and local head loss, and surface tension on suction vortices development. Other challenges are simulation of pressure surge tanks discharges of both turbines and pumps within the times converted according to the model laws, the main criterion being the repeated mode change between generation and pumping as well as uncontrolled load drop for the pumps as a special condition.

The time curves of the discharge of tailrace, pump, and turbine of the physical model as an example result of a measured pump and turbine. The curves illustrate the change in magnitude and direction of discharge in the tailrace tunnel generated by the turbines and pumps operated alternately. The results of this model will be transformed to the prototype based on the model scale used. Due to the requirements of the Kops II pump-storage scheme with the hydraulic short-circuit, air evacuation (degassing) needs to be completed before entering the branch tunnel and then the pumping devices. A supplementary study on a physical model is still needed for investigating the problem involved in the unsteady process and the air entrainment followed by the degassing process in the pressure surge tank [96].

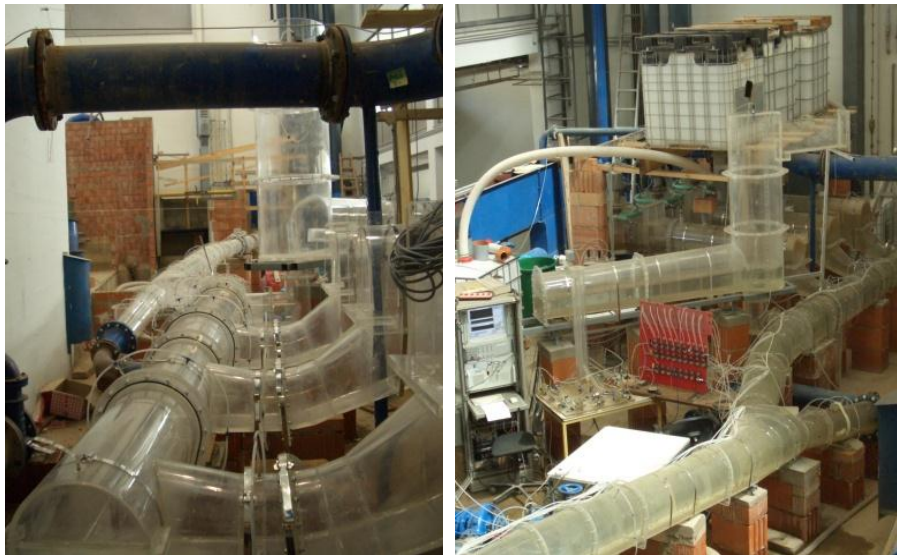


Figure 116: The Kops II physical model setup [96]

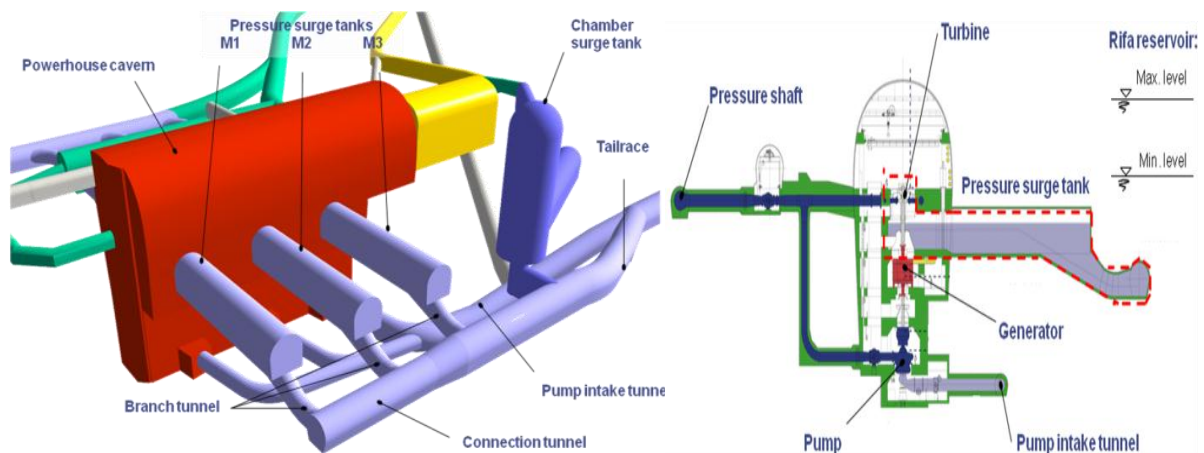


Figure 117: 3D view of powerhouse cavern with the pressure surge tanks (left) and schematic drawing showing system under investigation (right) [96].

### 5.2.2 PSP Limberg II

The new PSP Limberg II, which is being constructed by VERBUND-Austrian Hydro Power AG (AHP) as supplement to the existing Kaprun power plant group, is located at the rear of the Kaprun Valley. PSP Limberg II utilises water from lower reservoir of Wasserfallboden (live storage of 81.2 million m<sup>3</sup>) to the upper reservoir of Mooserboden (live storage of 81.2 million m<sup>3</sup>) through a 5.4 km-long power conduit with a diameter of 4.8–6.8 m. The capacity in generating and pumping modes is 2×240 MW. Optimising the difference in height between the upstream and downstream reservoirs, PSP Limberg II will increase the balance and backup Kaprun power plant group from 353 MW to 833 MW [97].

Some hydraulic problems exist in the development of PSP Limberg II. The physical model was used to investigate the head loss at a damper component of the upper surge tank. The model was also used to study the hydraulic conditions for mode changes between generation and pumping. The pipe junction with nozzle was analysed in the physical model (Figure 118, left). Besides using a physical model, numerical analysis was used to perform the upper surge tank of Limberg II. The conventional Reynolds Averaged Navier-Stokes equation system (RANS) in form of continuity equation, momentum equations, and k- $\epsilon$  turbulence model in the ANSYS–CFX software were applied for flow simulation [97]. Figure 118 (right) shows the comparison of pressure distribution resulting from the numerical model between model scale (top) and prototype (bottom) in the pipe junction with nozzle. The flow loss coefficient follows the experimental results at the area of lower Reynolds number values. The RANS model presents suitable tool for loss coefficient calculation in prediction of flow phenomena and as fast method for geometry optimization.

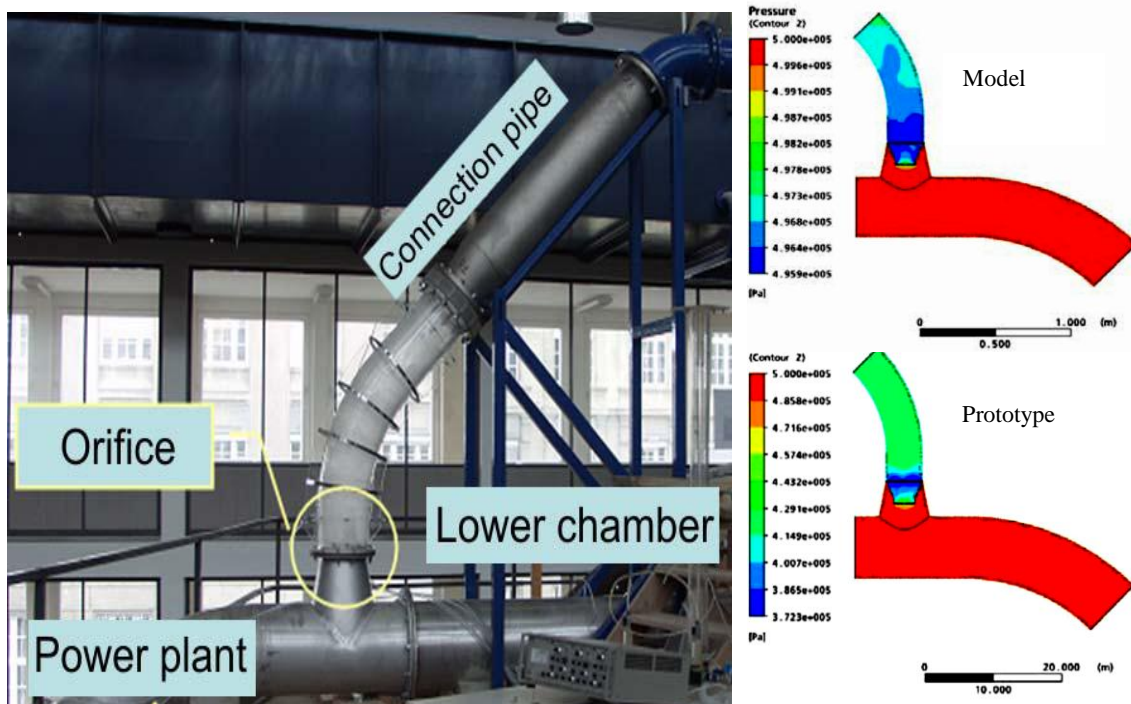


Figure 118 : Physical model of pipe junction (left) and numerical model of nozzle (right) [97]

### 5.2.3 PSP Reisseck II

The PSP Reisseck II, located in Upper Carinthia, was constructed by Verbund Hydro Power AG (VHP), which is part of Malta and Reisseck/Kreuzeck Power Station Group. With this project, the previous separate hydraulic system of Malta and Reisseck/Kreuzeck will be connected to increase the performance of the system. The objective of the PSP Reisseck II project is to supply the peak demand in electricity market by generating 430 MW of electricity. The output will be realized with the design of the nominal output of machine set in a generation/pumping operation of  $2 \times 215$  MW. The apparent power generator/motor is  $2 \times 240$  MVA, the upgraded water quantity in generation operation is  $2 \times 40$  m<sup>3</sup>/s, the upgraded water quantity in pumping operation is  $2 \times 35$  m<sup>3</sup>/s and the average structural fall height is 595 m. The total power of the power station group will increase from 425 to 855 MW in pumping operation [86]. The existing hydraulic system of Malta consists of two upper reservoirs (Galgenbichl and Gosskar) and one lower reservoir (Rottau). The Reisseck PSP II is planned to connect Großer Muhldorfer See as the upper reservoir and Galgenbichl and Gosskar as the lower reservoirs. A new surge tank in Burgstall will be built in addition to the existing surge tank in Hattelberg [98].

Investigations and studies were conducted on the PSP Reisseck II project's Burgstall surge tank. For these purpose, a 1:25 physical model was built in the laboratory. Studies on the physical model aim to examine the hydraulic performance of Burgstall surge tank. The complex combination of Malta and Reisseck hydraulic systems is the special feature of this project. The scale model was simulated under Reynolds similarity with the prototype. The design of nozzle and the head loss is calculated using a numerical model. The flow velocity in the part of surge tank is investigated using Particle Image Velocimetry (PIV) to obtain picture of velocity profile and distribution. Overall, the numerical model result has a good agreement with the physical model [99].



Figure 119: Burgstall surge tank, Left: Physical model, Right: 3D view [99]

## 5.2.4 PSP Atdorf-Schluchseewerk

PSP Atdorf-Schluchseewerk, the largest PSP in Germany, has been designed to produce 1400 MW of electricity. The PSP will utilise water from the lower reservoir of Hazelbeckel situated in Haselbachtal Valley to the upper artificial reservoir of Hornbergbecken II. Each reservoir has a capacity of 9 million  $\text{m}^3$ , corresponding to a storage capacity of more than 13 GWh. The upper reservoir will be connected to pump turbines with two vertical pressure pipes, while the connection between pump turbines and lower reservoir uses an 8.4 km-long tail water gallery [94]. The fall head between both reservoirs is about 600 m.

Some hydraulic problems in the development of pumped storage that were investigated and solved in the Hermann Grengg Laboratory in Institute of Hydraulic Engineering and Water Resources Management of the Graz University of Technology will be presented here. The surge tank for the new PSP Atdorf was studied and investigated in the laboratory. A 1:40 physical model made from Plexiglas was built (Figure 120, left). The model was designed using Froude similarity to investigate performance of the designed surge tank. The physical model was used to investigate the maximum oscillation in the upper and lower chamber, and the maximum discharge

flow through the surge tank. Figure 121 shows the example result of numerical model in drawing the velocity vector in the nozzle at the lower chamber. The pressure and velocity distributions in the upper chamber were investigated [100].



Figure 120: Physical model setup (left) and 3D view of surge tank (right) [100]

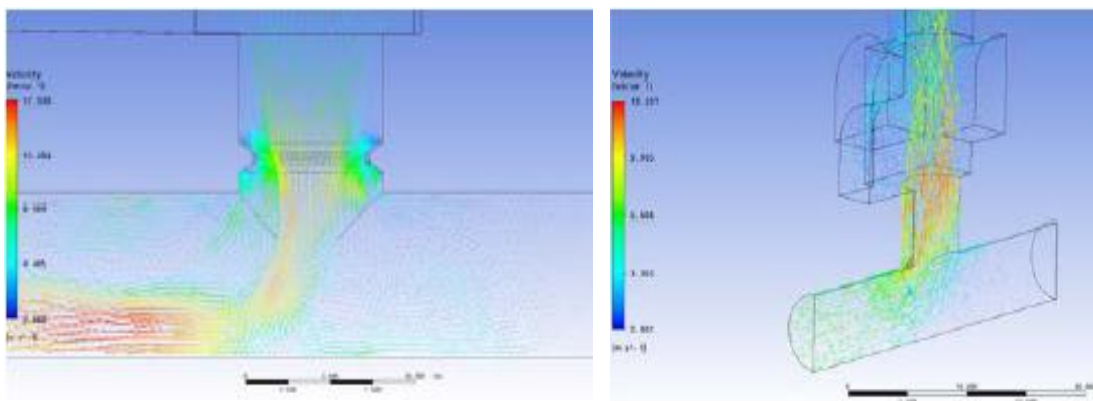


Figure 121: 2D and 3D view of velocity in the nozzle lower chamber [100]

### 5.3 Synthesis of the thesis result

This study has contributed to estimating loss coefficient of flow through a manifold in high Reynolds number. Estimating loss coefficient can be done by investigation in scale and numerical models. Phenomena of flow in the manifolds are studied by measurement in the scale model. Scale model is also used to estimate loss coefficient of low Reynolds number. Meanwhile, numerical model is used to investigate the flow phenomena that cannot be studied in scale model. The calibrated numerical model is used to predict loss coefficient of flow with high Reynolds number. Loss coefficient of a scale model is similar with the prototype for the same Reynolds number.

Realizable  $k$ - $\varepsilon$  numerical model with standard wall function is a good model to simulate flow through a manifold with high Reynolds number. Meanwhile, the near-wall treatment is needed in simulation flow with low Reynolds number. Near-wall treatment requires very fine mesh and boundary mesh size. Friction loss in a manifold is calculated by simplifying flow through an idealized straight pipe. Friction loss calculated using numerical model is better than calculated analytically using Darcy-Weisbach and Colebrook equations. Kinetic energy correction factor has influence to the loss coefficient of a manifold if the velocity ratio between flow in the branch and in the main pipes is high.

## 5.4 Conclusion

Conclusions of this study are:

- Realizable  $k$ - $\varepsilon$  turbulent model of has a good capability to describe flow phenomenon that occur in an elbow such as differential pressure, velocity distribution, secondary flow, and separation flow.
- Weak secondary flow configures separation zone in the inner of the elbow outlet. Increasing secondary flow will re-energizes the separation zone and gives impact to decreasing the loss coefficient.
- Calculation of friction loss of idealized pipe to obtain local loss of an elbow using numerical model produce better correlation between loss coefficient and Reynolds number compared with analytical calculation using Darcy-Weisbach and Colebrook equations.
- Using similarity of Reynolds, the four numerical models of long elbow with different diameter produce similar of relative velocity and proportional of differential pressure head in the elbow. Similarity of loss coefficient between elbows with different diameter is also achieved by numerical simulation.
- Pumped-storage hydropower offers the advantages of storage energy and grid balancing. The hydraulic problems that arise in the construction of PSPs can be investigated better using combination of scale and numerical models.
- Numerical modeling results have a good agreement with the results of physical model, so the use of combination of scale and numerical model provide benefits at the time and cost saving, as well as providing better pictures of flow processes.

## 6 Summary

The main problem investigated in this dissertation is how to transfer loss coefficient resulted by scale model to the prototype that have a high Reynolds number. To solve this problem, understanding the relationship between models with different size is required by investigations on the family model of manifolds.

This study begins by describing the background of the study. The problems were defined and the objectives to be achieved in these studies were determined. Some activities done are study in related literature, review to the result of previous research, review and analyse the weakness of existing method used to solve the problem. A new method has been proposed in hopes to obtain better results. The method was used in investigation of loss coefficient of some manifold with different size using measurement data in laboratory and numerical model. The results were presented, analysed, and discussed. The result of numerical model compared with the results of measurement. The method was also applied to others manifolds to prove the universality. Finally, to strengthen the result of this thesis, some future works were proposed.

Investigation on family model of fittings with different size shows good correlation of loss coefficient between fittings with different size, although there are some deviations results due to dissimilarity of the geometry and measurements accuracy. Estimation loss coefficient of flow through a Y-bifurcator in high Reynolds number using extrapolation of differential pressure head does not give satisfactory result. Similarity study on loss coefficient of a Y-bifurcator using numerical models family produces a good correlation of loss coefficients between models with different size. A good correlation of differential pressure, velocity and loss coefficient between manifolds with different size, the realizable  $k$ - $\epsilon$  turbulent model can be used in transferring result of scale model to the prototype. The method also applied to the elbow and a good result was also achieved.

Specific results of the study are summarized as follow:

- **Review of past investigation on loss coefficient of Y-bifurcator Alberschende**
  - Investigations on scale model of Y-bifurcator Alberschende done by several tests produce loss coefficients are close each other in the high Reynolds number. However, the trends of decreasing loss coefficients from low to high Reynolds number for each test are different. Extrapolation of different pressure

of scale models used to estimate the loss coefficients of flow with very high Reynolds number give varying results, depending on the trends and the number of data.

- Numerical model used to investigate velocity and loss coefficient of Y-bifurcator in flow with high Reynolds number produce results relatively close to the physical model. Numerical models of Y-bifurcator with scale model geometry and prototype geometry produce different loss coefficients for the same Reynolds number.
- **Similarity study on loss coefficient of fittings with different diameter**
  - Similarity study on loss coefficient of elbows and tees was done using manufactured fitting, so it was difficult to achieve the geometric similarity between an elbow/tee to another. Investigation on loss coefficients of elbows and tees with different diameter gave results that the loss coefficient decreased with the increasing Reynolds number and the increasing elbow/tees diameter.
  - The similarity study of a family model using manufactured elbows and tees shows that for the same Reynolds number, better proportional geometrical dimensions and measurement accuracy result in more similar loss coefficients.
- **Study on loss coefficient of a Y-bifurcator using scale and numerical models**
  - The discharge and pressure sensors used in measuring low flow produce higher percentage of deviation compared with high flow, but it decreased with increasing flow rate.
  - Loss coefficient of physical model of a Y-bifurcator decreased with the increasing Reynolds number of inflow. In the high Reynolds number, loss coefficient that calculated by different two pair sections at upstream and downstream of bifurcator was close each other.
  - Realizable k- $\epsilon$  model of a Y-bifurcator studied using various mesh and boundary layer sizes has fulfilled the criteria of stability, consistency, and convergence. The results of several flow scenarios of numerical model generally close to the results of physical model, especially for high Reynolds number flow.
  - Kinetic energy correction factor decreased with the increasing Reynolds number and it tended to close to one in the high Reynolds number. Loss coefficient of a Y-bifurcator that had a high velocity ratio between flow in the branch and the main pipes was mainly influenced by kinetic energy correction factor.
  - The method used to calculate friction loss influences to the result of local loss coefficient. The friction loss calculated by realizable k- $\epsilon$  numerical model is different from friction loss calculated analytically using Colebrook equation.

- Realizable k- $\epsilon$  model produces loss coefficient that was closer to the physical model compared with the result of other turbulent models.
- Loss coefficients of Y-bifurcator with constant inflow produced by steady and unsteady simulations are similar. Steady simulation produces more stable result and requires less computation time than unsteady simulation.
- **Similarity Study on loss coefficient of a Y-bifurcator using numerical models with different scale factor.**
  - Using similarity of Reynolds number, there is a correlation between differential pressure and geometry scale of numerical models of Y-bifurcator with different scale factor. The ratio of differential pressure between two numerical models with different scale is close to square root of the length scale.
  - The four numerical models with different scales produce similar loss coefficients in low and high Reynolds numbers. With a good correlation between numerical models with different scales, the realizable k- $\epsilon$  turbulent model meets expectation as a tool for solving problems in scale models especially in transferring the loss coefficient resulted by physical model to the loss coefficient of prototype.
- **Application of numerical model in investigation of hydraulic problem**
  - Realizable k- $\epsilon$  turbulent model had a good performance in the simulation of flow through a bend/elbow. The numerical models can describe the flow separation phenomenon in the inner of elbow outlet properly. Strong secondary flow was decreased the separating zone and it has an impact on loss coefficient reductions.
  - The model was successfully applied for similarity study of flow through elbows with different diameters. Scale effect to the loss coefficient produced by numerical models of elbow with different sizes is small. Loss coefficient of elbows in very high Reynolds numbers was near constant.
  - The hydraulic problems that arise in the construction of PSPs could be investigated and studied using a hydraulic model. The use of combination between scale and numerical models provided benefits at the time and cost saving, as well as providing better pictures of flow processes.

This page intentionally left blank

# References

- [1] G. K. Batchelor, "An introduction to fluid dynamics," *Cambridge University Press*, p. 211–215, 1967.
- [2] N. Rott, "Note on the history of the Reynolds number," *Annual Review of Fluid Mechanics* 22 (1), p. 1–11, 1990.
- [3] C. Colebrook and C. White, "Experiments with fluid friction roughened," in *Proc. R.Soc.(A)*, 1937.
- [4] L. Moody, "Friction factors for pipe flows," *Trans. ASME*, 66, p. 641, 1944.
- [5] D. Wood, "An Explicit friction factor relationship," *Civil Engineering*, pp. 60-61, 1966.
- [6] P. Swamee and A. Jain, "Explicit equation for pipe flow problems," *J. Hydr. Div., ASCE*, 102(5), pp. 657-664, 1976.
- [7] S. Churchill, "Friction factor equations spans all fluid-flow ranges," *Chemical Engineering*, 91, 1977.
- [8] N. Chen, "An explicit equation for friction factor in pipe," *Ind. Eng. Chem.Fundam.*, Vol. 18, No. 3, pp. 296-297, 1979.
- [9] G. Round, "An explicit approximation for the friction factor-Reynolds number relation for rough and smooth pipes," *Can. J. Chem. Eng.*, 58, pp. 122-123, 1980.
- [10] D. Barr, "Solutions of the Colebrook-White functions for resistance to uniform turbulent flows," *Proc. Inst. Civil. Engrs. Part 2* . 71, 1981.
- [11] D. Zigrang and N. Sylvester, "Explicit approximations to the Colebrook's friction factor," *AICHE J.* 28, 3, 514, 1982.
- [12] S. Haaland, "Simple and Explicit formulas for friction factor in turbulent pipe flow," *Trans. ASME, JFE*, 105, 1983.
- [13] G. Manadilli, "Replace implicit equations with sigmoidal functions," *Chem.Eng. Journal*, 104(8), 1997.
- [14] E. Romeo, C. Royo and A. Monzon, "Improved explicit equations for estimation of the friction factor in rough and smooth pipes," *Chem. Eng. J.*86, p. 369–374, 2002.
- [15] N. Olsen, Numerical Modelling and Hydraulic, Department of Hydraulic and Environmental Engineering The Norwegian University Science and Technology, 1st edition, 5 November 2007.
- [16] B. Launder and D. Spalding, Lectures in mathematical models of turbulence, London, England: Academic Press, 1972.
- [17] T. Shih, W. Liou, A. Shabbir, Z. Yang and J. Zhu, "A New k- $\epsilon$  Eddy-viscosity model for high Reynolds number turbulent flows - Model development and validation," *Computer Fluid*, pp. 23/3:227-238, 1995.
- [18] D. C. Wilcox, "Turbulence modeling for CFD, 1st edition," DCW Industries, La Canada CA, 1998.
- [19] F. R. Menter, "Two-equation Eddy-viscosity turbulence models for engineering applications," *AIAA Journal*,, vol. 32, no. 8, pp. 1598-1605., 1994.
- [20] B. E. Launder, G. J. Reece and W. Rodi, "Progress in the development of a Reynolds-stress turbulence closure," *Journal Fluid Mechanic*, vol. 68, no. 3, pp. 537-566, 1975.
- [21] I. FLUENT, "[http://202.118.250.111:8080/fluent/Fluent60\\_help/html/-ug/node429.htm](http://202.118.250.111:8080/fluent/Fluent60_help/html/-ug/node429.htm)," [Online].
- [22] M. Wolfstein, "The velocity and temperature distribution of one dimensional flow with

- turbulence augmentation and pressure gradient," *Int.J. Heat Mass Transfer*, vol. 12, pp. 301-318, 1969.
- [23] B. E. Launder and D. B. Spalding, "The numerical computation of turbulent flows," *Computer Methods in Applied Mechanics and Engineering*, vol. 3, pp. 269-289, 1974.
- [24] S.-E. Kim and D. Choudhury, "A near-wall treatment using wall functions sensitized to pressure gradient," *ASME FED, Separated and Complex Flows*, vol. 17, 1995.
- [25] R. Klasinc, "The measurement of dynamic pressures on hydraulic models," in *Proceeding IAHR Workshop on Instrumentation for Hydraulic Laboratory*, Burlington, Canada, 1989.
- [26] Institute of Hydraulic Engineering and Water Resources Management-Graz University of Technology, "Internal report of Hydraulic model test Pirris," Graz, 2010.
- [27] F. Hofman, "Fundamental of ultrasonic flow measurement for industrial applications," Krohne Messtechnik GmbH & Co.KG, Duisburg, 2000.
- [28] H. Knoblauch, R. Klasinc and T. Gleisler, "Application of an ultrasonic velocity profile monitor in a hydraulic laboratory," in *Hydraulic measurement and Experimental Method 2002*, Colorado, 2002.
- [29] C. Wang, T. H. H. Meng and L. Zhang, "Accuracy of the ultrasonic flow meter used in the hydroturbine intake penstock," *Flow Measurement and Instrumentation*, no. 25, pp. 32-39, 2012.
- [30] Y. Yeh and H. Cummins, "Localized fluid flow measurements with a He-Ne laser spectrometer," *Applied Physic Letters*, vol. 4, p. 176, 1964.
- [31] Dantec-Dynamic, "<http://www.dantecdynamic.com>," Nova Instrument, 2012. [Online]. [Accessed 17 April 2012].
- [32] T. Schluter and W. Merzkirch, "PIV measurements of the time-averaged flow velocity downstream of flow conditioners in a pipeline," *Flow Meas. Instrum.*, vol. 7, no. 3/4, pp. 173-179, 1996.
- [33] K. J. Hammad, V. Otugen and E. B. Arik, "A PIV study of the laminar axisymmetric sudden expansion flow," *Experiments in Fluids, Springer-Verlag*, vol. 26, pp. 266-272, 1999.
- [34] N. M. Nikolaidis and D. S. Mathioulakis, "Axial and secondary flow study in a 90-deg bifurcation under pulsating conditions using PIV," *Journal of Fluids Engineering*, vol. 124, pp. 505-511, 2002.
- [35] G. Pan and H. Meng, "Experimental study of turbulent mixing in a Tee mixer using PIV and PLIF," *AIChE Journal*, vol. 47, no. 12, pp. 2653-2665, 2001.
- [36] J. Woisetschlager, N. Mayrhofer, B. Hampel, H. Lang and W. Sanz, "Laser-optical investigation of turbine wake flow," *Experiments in Fluids*, vol. 34, pp. 371-378, 2003.
- [37] Z. Zhang and R. J. Hugo, "Stereo particle image velocimetry applied to a vortex pipe flow," *Experiments in Fluids*, vol. 40, pp. 333-346, 2006.
- [38] N. A. Ozturk, A. Akkoca and B. Sahin, "PIV measurements of flow past a confined cylinder," *Exp Fluids*, vol. 44, pp. 1001-1014, 2008.
- [39] R. Klasinc and H. Knoblauch, "Head loss in the manifold of pumped storage systems," in *International Symposium of pumped Storage Development*, Nanjing, 1994.
- [40] Institute of Hydraulic Engineering and Water Resources Management - Graz University of Technology, "Hydraulisch Modellversuch verteilrohrleitung KW Alberschwende," Graz, 1990.
- [41] R. Klasinc, H. Knoblauch and T. Dum, "Comparison of a numerical model with a

- physical model for a penstock bifurcator," in *IX International Conference on Computational method in Water Resources*, Denver, 1992.
- [42] H. Knoblauch, "Dissipationsvorgänge in Rohrleitungssystemen," TU Graz, Graz, 1995.
- [43] R. Klasinc and H. Knoblauch, "Numerical simulation in the manifold of hydro power schemes," in *XXVIth Congress of the International Association for Hydraulic Research*, London, 1995.
- [44] C. Ding, L. Carlson, C. Ellis and O. Mohseni, "Pressure loss coefficient of 6, 8 and 10 inch steel pipe fittings," ST. Anthony Falls Laboratory, University of Minnesota, Minneapolis, Minnesota, 2005.
- [45] W. Rahmeyer, "Final report on the ASHRAE Research Project 1034-RP:Develop design data of large pipe fitting," ASHRAE Inc., Atlanta.
- [46] W. Rahmeyer, "Pressure loss data of large pipe ells, reducers and expansions," *ASHRAE Trans.*, vol. 108, no. Part 1, Paper number 4533 (RP-1034), pp. 360-375, 2002.
- [47] W. Rahmeyer, "Pressure loss coefficient of threaded and forged weld pipe fitting for ells, reducing ells and pipe reducer," *ASHRAE Transaction research*, pp.105(2):334-354, Atlanta, 1999.
- [48] W. Rahmeyer, "Pressure loss data for large pipe tess," *ASHRAE Trans.*, Paper number 4534 (RP-1034), pp.376-389, 2002.
- [49] W. Rahmeyer, "Final report on Pressure loss data of PVC plastic pipe fittings, ASHRAE Research Project 1193-RP," ASHRAE Inc, Atlanta, 2005.
- [50] G. Vogel, "Untersuchung über den Verlust in rechtwinkligen Rohrverzweigungen," *Mitteilung des Hydr. Institutes der TH M'unchen.*, vol. 1, pp. 75-90, 1926.
- [51] F. Petermann, "Loss in oblique-angled pipe branches.," *Trans. Hydraul. Inst., Tech. Univ., Munich, Bull. 3.*, 1929.
- [52] E. Kinne, "Contribution to the knowledge of hydraulic losses in branches," Munchen, 1931.
- [53] F. W. Blaisdell and P. W. Manson, "Loss of energy at sharpedged pipe junctions in water conveyance systems," *US Department of Agriculture Technical Bulletin 1283*, August 1963.
- [54] F. W. Blaisdell and P. W. Manson, "Energy loss at pipe junctions.," *J. Irrig. and Drainage Div., ASCE, 93(IR3)*, pp. 59-78, 1967.
- [55] Y. M. T. Al-Naib, "Air flow losses in branching circular metal ducts," PhD thesis, University of Manchester Institute of Science and Technology, Manchester, 1978.
- [56] J. R. Nichols, "Techniques for the design of exhaust manifolds with pulse-converters," PhD thesis, University of Manchester Institute of Science and Technology, Manchester, 1984.
- [57] D. J. Wood, L. S. Reddy and J. E. Funk, "Modelling pipe networks dominated by junctions," *Journal of Hydraulic Engineering, ASCE 119(8)*, pp. 949-958, 1993.
- [58] A. Gardel, "Les pertes de charge dans les écoulements au travers de branchements en te," *Bull. Tech. Suisse Romande 83(9)*, p. 123±130., 1957.
- [59] A. Gardel, "Les pertes de charge dans les écoulements au travers de branchements en te," *Bull. Tech. Suisse Romande, 83(10)*, pp. 143-148, 1957.
- [60] H. Ito and K. Imai, "Energy losses at 90 pipe junctions," *Journal of Hydraulic Engineering, ASCE, 99(9)*, pp. 1353-1368, 1973.
- [61] M. Serre, A. J. Odgaard and R. A. Elder, "Energy losses at combining pipe junction," *J.*

- Hydraul. Engng, ASCE, 120(7)*, pp. 808-830, 1994.
- [62] K. Oka, T. Nozaki and H. Ito, "Energy losses due to combination flow at tees," *Jap. Soc. Mech. Engrs Int. J., Ser. B, 39(3)*, pp. 489-498., 1996.
- [63] J. F. Bingham and G. P. Blair, "An improved branched pipe model for multi-cylinder automotive engine calculations," *Journal of Automobile Engineering, 199(D1)*, p. 65±77, 1985.
- [64] M. D. Bassett, R. J. Pearson and D. E. Winterbone, "Estimation of steady flow loss coefficients for pulse converter junctions in exhaust manifolds," in *IMEchE International Conference on Turbocharging and Air Management Systems*, 1998.
- [65] P. Flamang, "Studie van de stroming in juncties van uitlaatsystemen van opgeladen dieselmotoren," PhD thesis, Rijksuniversiteit, Gent, 1989.
- [66] M. D. Bassett, D. Winterbone and R. Pearson, "Calculation of steady flow pressure loss coefficients for pipe junctions," in *Proc Instn Mech Engrs Vol 215 Part C*, 2001.
- [67] I. Idelchik, *Handbook of Hydraulic Resistance 3rd Edition*, Florida: CRC Press, Inc, 1994.
- [68] D. Miller, *Internal Flow Systems*, BHRH Fluid Engineering, 1978..
- [69] EDSU-73022, "Pressure losses in three-leg pipe junctions: dividing flows," Engineering Sciences Data Unit, London, 1973.
- [70] EDSU-73023, "Pressure losses in three-leg pipe junctions: combining flows," Engineering Sciences Data Unit, London, 1973.
- [71] W. Muller, "Pressure loss in the high pressure pipeline and distribution system of the Lucendro Power Station," Sulzer Technical Report No. 4, Switzerland, 1949.
- [72] F. Salvesen, "Hydraulic loss in branch pipes. Report No. VL121," Water Power Laboratory, The Technical University of Norway, Norway, 1962.
- [73] D. King, "Hydraulic model studies of Causey Dam Outlet Works. Report No. Hyd. 496," Hydraulic Laboratory-Bureau of Reclamation, Utah, USA, 1963.
- [74] E. Russ, "Head loss in Wyes and Manifolds," *Journal of the Hydraulic Division*, pp. 96: 593-608, 1970.
- [75] B. Lee, H. Coleman, J. Kim and H. Kwon, "Hydraulic model studies of Y-branch," *ASCE, New York*, 1993.
- [76] R. Klasinc, H. Knoblauch and T. Dum, "Power losses in distribution pipe," in *Fluid flow modelling*, Southampton, UK, 1992..
- [77] W. Dobler, H. Knoblauch and G. Zenz, "Hydraulic investigation of a Y-bifurcator," in *First IAHR European Division Congress*, Edinburg, UK, 2010.
- [78] W. Dobler, "Hydraulic Investigation of a Y-bifurcator," PhD Thesis, TU Graz, Graz, Austria, 2012.
- [79] F. Tuakia, *Dasar-dasar CFD menggunakan FLUENT*, Bandung: Informatika, 2008.
- [80] R. S. Benson, D. Woolatt and W. A. Woods, "Unsteady flow in simple branch systems," in *Proc. Instn Mech. Engrs, 178(3I(iii))*, 1963.
- [81] M. D. Bassett, R. J. Pearson, D. E. Winterbone and P. Batten, "Investigation of shock wave interaction with branched ducts," in *22nd International Symposium on Shock Waves*, London, 1999.
- [82] M. D. Bassett, D. E. Winterbone and R. J. Pearson, "Modelling engines with pulse converted exhaust manifolds using one-dimensional techniques," *SAE paper 2000-01-0290*, 2000.
- [83] T. W. Kuo and S. Chang, "Three dimensional steady flow computations in manifold-

- type junctions and a comparison with experiment," SAE paper 932511, 1993.
- [84] T. W. Kuo and B. Khalighi, "Numerical study on flow distribution in T-junctions and a comparison with experiment," in *Proceedings of ASME International Combustion Engines Division Spring Meeting*, Marietta, Ohio, 23-26 April 1995.
- [85] V. M. Klell, T. Sams and A. Wimmer, " Berechnung der Stroëmung in Rohrverzweigungen," *Motortechnische*, pp. 844-851, December 1998.
- [86] C. Dimitriadis, M. A. Leschziner, D. E. Winterbone, G. I. Alexander and R. Sierens, "Computation of three dimensional flow in manifold-type junctions," in *ASME Symposium on Flows and Related Phenomena in Reciprocating I.C. Engines*, Miami Beach, Florida, 1985.
- [87] P. Flamang and R. Sierens, " Experimental and theoretical analysis of the flow in exhaust pipe junctions," in *IMEchE Conference paper C382/082*, 1989.
- [88] V. Zmrha and J. Schwarzer, "Numerical simulation of local loss coefficients of ventilation duct fitting," in *Eleventh International IBPSA Conference*, Glasgow, Scotland, 2009.
- [89] R. Klasinc and I. Biluš, "Scale effects at form losses estimation in hydraulic components of hydro plants," in *33rd IAHR Congress: Water Engineering for a Sustainable Environment*, 2009.
- [90] J. V. Williamson and T. J. Rhone, "Dividing flow in branches and wyes," *Journal of the Hydraulic Division*, no. HY5, pp. 747-769, 1973.
- [91] J. Allen, M. Schockling and G. S. A. Kunkel, "Turbulent flow in smooth and rough pipes," *Phil. Trans. R. Soc.*, vol. 365, pp. 699-714, 2007.
- [92] E. European Renewable Energy Council, "Renewable energy technology roadmap 20% by 2020," 2007. [Online]. Available: <http://www.erec.org/media/publications/roadmap-2020.html>. [Accessed 17 August 2011].
- [93] P. Vannemann, L. Thiel and H. Funke, "Pumped storage plants in the future power supply system," *VGB PowerTech I/2*, pp. 44-48, 2010.
- [94] A. Cochran, D. Isles and I. Pope, "Development of pumped storage in a power system," *Proc. IEE Vol. 126, No. 5*, pp. 433-438, 1979.
- [95] P. Vannemann, K. Gruber, J. Haaheim and A. Kunsch, "Pumped storage plants-status and perspectives," *VGB PowerTech 4*, pp. 32-38, 2011.
- [96] R. Klasinc, M. Larcher, A. Predin and M. Kastrevc, "Simulation of fast pumped-storage schemes with the physical experiment," in *International Symposium on Hydraulic Structures*, Ciudad Guayana, Venezuela, 2006.
- [97] R. Klasinc and I. Bilus, "Experimental and numerical approach to surge tank improvements," in *International Symposium on Water Management and Hydraulic Engineering*, Ohrid, Macedonia, 2009.
- [98] M. Freitag, M. Larcher and A. Blauhut, "The Reißbeck II pumped storage power station," *Geomechanic and Tunnelling 4 No.2*, pp. 119-128, 2011.
- [99] Institute of Hydraulic Engineering and Water Resources Management-Graz University of Technology, "Internal Report PSKW Reisseck 2 Wasserschloss Burgstall," Graz, 2011.
- [100] Institute of Hydraulic Engineering and Water Resources Management-Graz University of Technology, "Internal report Hydraulic model of Atdorf-Schluchseewerk," Graz, 2011.

# List of tables

<i>Number</i>	<i>Page</i>
Table 1: Variable size ratios of long elbow diameter 6, 8 and 10 inches [44].....	44
Table 2: Ratio of size variables of tees 6, 8 and 10 inches [44].....	47
Table 3: Ratios of size among long elbow 12, 16, 20 and 24 inches [48].....	50
Table 4: Ratio of size variables between tees 12 and 16 inches [48].....	52
Table 5: Size ratio of PVC Elbows diameter 2, 4, 6, and 8 inches [49].....	55
Table 6: Size ratios among PVC Tees diameter of 2, 4, 6 and 8 inches [49].....	57
Table 7: Scenario of discharge weighted factor for physical model simulation ....	63
Table 8: List of diameter and length of idealized pipe.....	68
Table 9: Mesh size of the boundary layer (in mm) .....	79
Table 10: Absolut deviation of differential pressure head between section M2 and L6 for asymmetrical turbine flow .....	80
Table 11: Absolut deviation of differential pressure head between physical and numerical models for symmetrical turbine flow.....	81
Table 12: Comparison of normalized loss coefficient between physical and numerical models for asymmetrical turbine flow .....	81
Table 13: Number of iteration and Root Mean Square Deviation .....	88
Table 14: Discharge and velocity inflow for turbine mode simulation.....	94
Table 15: Property of Y-bifurcator for numerical modeling with different scales .....	105
Table 16: Discharge and velocity inflow of models in asymmetrical flow.....	106
Table 17: Discharge and velocity inflow of models in symmetrical flow .....	107
Table 18: Differential pressure head of models in asymmetrical flow .....	108
Table 19: Differential pressure head of models in symmetrical flow .....	109
Table 20: Dimension properties of long elbow .....	120
Table 21: Inflow of the four numerical models.....	121

# List of figures

<i>Number</i>	<i>Page</i>
Figure 1: Components of the forces action on a fluid particle in the flow direction	7
Figure 2: Energy Conservation.....	9
Figure 3: Moody diagram.....	10
Figure 4: Mass balance.....	11
Figure 5: Momentum balance.....	12
Figure 6: Turbulent model in FLUENT [21].....	16
Figure 7: Sub-division of near wall region [21].....	22
Figure 8: Near Wall treatment in FLUENT [21].....	22
Figure 9: 3-D drawing of pressure sensor [25].....	26
Figure 10: Control section and the pressure hole, Top: example of pressure hole, Bottom: picture of the ring line [26].....	26
Figure 11: Pressure head calibration tool [26].....	27
Figure 12: Principle of inductive flow measurement [26].....	29
Figure 13: Basic principle of ultrasonic flow meter.....	30
Figure 14: Basic principle of the Laser Doppler Anemometry [31].....	31
Figure 15: Basic principle of the PIV technique [31].....	33
Figure 16: Geometry of physical model (top) and nature (bottom) [42].....	36
Figure 17: Location installation of pressure transducer [39].....	37
Figure 18: Idealized pipe sections for calculation friction loss [42].....	37
Figure 19: Comparison of net differential pressure head among several tests on physical model of bifurcator for symmetrical flow [40]. ....	38
Figure 20: Normalized loss coefficient of physical model of bifurcator symmetrical flow. ....	39
Figure 21: Normalized loss coefficients of physical model of bifurcator for symmetrical flow resulted by extrapolation of differential pressure head .....	39
Figure 22: Comparison of net differential pressure head among several tests on physical model of bifurcator for asymmetrical flow [40].....	40

Figure 23: Normalized loss coefficients of physical model of bifurcator for asymmetrical flow.....	40
Figure 24: Normalized loss coefficients of physical model of bifurcator for asymmetrical flow resulted by extrapolation of differential pressure head .....	40
Figure 25: Geometry and generated mesh for numerical model [42] .....	41
Figure 26: Normalized loss coefficients resulted by numerical model of bifurcator Alberschwende in physical model and nature sizes. ....	42
Figure 27: Comparison of normalized loss coefficients between results of physical model and numerical model for symmetrical flow.....	42
Figure 28: Comparison of normalized loss coefficient between results of physical model and numerical model for asymmetrical flow. ....	43
Figure 29: Normalized minor loss coefficients of long radius elbow 6, 8 and 10 inches .....	45
Figure 30: Normalized local loss coefficients of long elbow 6, 8 and 10 inches using Reynolds similarity (left) and Froude similarity (right).....	45
Figure 31: Normalized local loss coefficients of long elbow as function of diameter for several Reynolds number (left) and Froude number (right) .....	46
Figure 32: Schematic of flow for branching (left) and mixing tees (right) [44] ....	47
Figure 33: Normalized loss coefficient of branching tees for several discharge ratios.....	47
Figure 34: Normalized loss coefficients of mixing tees for several discharge ratios .....	48
Figure 35: Normalized loss coefficients of branching tees over Reynolds number	48
Figure 36: Normalized loss coefficients of mixing tees over Reynolds number ...	49
Figure 37: Configuration of test elbow [48].....	50
Figure 38: Normalized loss coefficients of long elbow 12, 16, 20 and 24 inches from four vendors [48].....	51
Figure 39: Normalized loss coefficients of long elbows with similarity of Reynolds .....	51
Figure 40: Pipe configuration for branching and mixing tees [48] .....	52

Figure 41: Normalized loss coefficients of branching tee over discharge ratio .....	52
Figure 42: Normalized loss coefficients of inline flow branching tee .....	53
Figure 43: Normalized loss coefficients of perpendicular flow of branching tees	53
Figure 44: Normalized loss coefficients of inline flow of mixing tees .....	54
Figure 45: Normalized loss coefficients of perpendicular flow mixing tees .....	54
Figure 46: Normalized loss coefficients of PVC elbows as function of velocity, Reynolds number, and pipe diameter .....	56
Figure 47: Normalized loss coefficients of tees for several discharge ratios in branching flow (top) and mixing flow (bottom).....	57
Figure 48: Installation of physical model Y-bifurcator in the laboratory [26].....	62
Figure 49: Measurement sections of differential pressure head [26] .....	63
Figure 50: Discharge measurement and standard deviation of the main pipe (left) and the branch pipe (right).....	64
Figure 51: Differential pressure head (top) and the standard deviation (bottom)..	65
Figure 52: Differential pressure head of asymmetrical (top) and symmetrical flows (bottom).....	66
Figure 53: Idealized pipe sections of Pirris Y-bifurcator [26] .....	67
Figure 54: Normalized loss coefficients of Case 1, RUN1 to RUN4, $Q_{out}/Q_{in}=1$ .	68
Figure 55: Normalized loss coefficients (average value) of Case 1 .....	69
Figure 56: Normalized loss coefficients of Case 2, RUN1 to RUN4, $Q_{out}/Q_{in}=0.67$ .....	70
Figure 57: Normalized loss coefficients of Case 2, RUN1 to RUN4, $Q_{out}/Q_{in}=0.33$ .....	70
Figure 58: Normalized loss coefficients (average value) of Case 2, $Q_{out}/Q_{in}=0.67$ (left) and $Q_{out}/Q_{in}=0.33$ (right) .....	71
Figure 59: Normalized loss coefficients of Case 3, RUN1 to RUN4, $Q_{out}/Q_{in}=0.57$ .....	72
Figure 60: Normalized loss coefficients of Case 3, RUN1 to RUN4, $Q_{out}/Q_{in}=0.43$ .....	72
Figure 61: Normalized loss coefficients (average value) of Case 3, $Q_{out}/Q_{in}=0.57$ (left) and $Q_{out}/Q_{in}=0.43$ (right) .....	73

Figure 62: Normalized loss coefficients of Case 4-L, RUN1 to RUN4, $Q_{out}/Q_{in}=0.5$ .....	74
Figure 63: Normalized loss coefficients of Case 4-R, RUN1 to RUN4, $Q_{out}/Q_{in}=0.5$ .....	74
Figure 64: Normalized loss coefficients (average value) of Case 4, $Q_{out}/Q_{in}=0.5$ using left branch (left) and right branch (right) .....	75
Figure 65: Normalized loss coefficients of Case 5 ( $Q_L/Q_M=1.0$ ) pumping mode..	75
Figure 66: Normalized loss coefficients of Case 6, $Q_L/Q_M=0.50$ (left) and $Q_L/Q_M=0.50$ (right) in pumping mode .....	76
Figure 67: Geometry and mesh of Y bifurcator .....	78
Figure 68: Normalized loss coefficients of numerical models Y-bifurcator with different mesh interval .....	78
Figure 69: Comparison of differential pressure head (M2 to L6) between measurement and numerical models in asymmetrical (top) and symmetrical (bottom) flow .....	80
Figure 70: Comparison of normalized loss coefficients between scale and numerical models for asymmetrical (left) and symmetrical (right) turbine mode .....	82
Figure 71: Comparison of normalized velocity contour between result of PIV measurement (left) and Realizable k- $\epsilon$ (right). .....	83
Figure 72: Comparison of velocity (m/s) between result of physical model and numerical models of asymmetrical flow in diagonal right plane .....	84
Figure 73 : Comparison of differential pressure head (section M2 and L6/R6) between physical and numerical models for various ratios of discharge. .....	85
Figure 74: Differential pressure head for asymmetrical flow (top) and symmetrical flow (bottom) for several discharges .....	85
Figure 75: Differential pressure head (refer to M1) for asymmetrical flow (top) and symmetrical flow (bottom) .....	86
Figure 76: Differential energy head (refer to M1) for asymmetrical flow (top) and symmetrical flow (bottom) .....	87

Figure 77: Comparison of normalized loss coefficients among several turbulent models in asymmetrical flow in turbine mode.....	89
Figure 78: Comparison of normalized loss coefficient between measurement and numerical models for asymmetrical (left) and symmetrical (right) flow .....	89
Figure 79: Normalized loss coefficients of realizable k- $\epsilon$ numerical model for Case 1 to Case 4 (turbine mode).....	90
Figure 80: Normalized loss coefficients of realizable k- $\epsilon$ numerical model for Case 5 and Case 6 (pumping mode) .....	91
Figure 81: Comparison of normalized coefficient loss for Case 1 to 4.....	92
Figure 82: Comparison of normalized loss coefficient for Case 5 and 6.....	92
Figure 83: Normalized loss coefficient of steady and unsteady simulation.....	93
Figure 84: Comparison of normalized losses coefficient among several bifurcator with different shape, size and angle.....	93
Figure 85: Differential pressure head of asymmetrical and symmetrical turbine mode.....	95
Figure 86: Comparison differential pressure head between numerical model and extrapolation of physical model in turbine mode. ....	96
Figure 87: Normalized loss coefficient of asymmetrical (top) and symmetrical (bottom) flow turbine mode.....	97
Figure 88: Normalized loss coefficient of asymmetrical (top) & symmetrical (bottom) flow in pumping mode .....	97
Figure 89: Comparison of normalized loss coefficient between numerical model and extrapolation of physical model.....	98
Figure 90: Friction loss and differential velocity head normalized by differential pressure head.....	99
Figure 91: Illustration of velocity and average velocity of flow in the pipe .....	99
Figure 92: Mesh of pipe cross section.....	100
Figure 93: Velocity profile in the main pipe cross sections of asymmetrical flow-turbine mode .....	101

Figure 94: Velocity profile in the left branch cross sections of asymmetrical flow-turbine mode .....	102
Figure 95: Kinetic energy correction factor for each section .....	103
Figure 96: Comparison normalized loss coefficient resulted by realizable k- $\epsilon$ between calculated $\alpha$ and $\alpha=1$ in the energy equation .....	104
Figure 97: Comparison of differential pressure head among different scales models .....	108
Figure 98: Comparison of normalized loss coefficients among four different models .....	110
Figure 99: Comparison of normalized loss coefficients between two different scale models for symmetrical flow in pumping mode simulation .....	110
Figure 100: Normalized velocity contour in the center of pipe in asymmetrical flow .....	111
Figure 101: Velocity vector of numerical models with different scale .....	112
Figure 102: Normalized velocity contour in the center of pipe in symmetrical flow .....	112
Figure 103: Normalized loss coefficient as function of velocity for different scale .....	113
Figure 104: Normalized loss coefficient as function of velocity .....	114
Figure 105: Normalized loss coefficient as function of main pipe diameter .....	114
Figure 106: Comparison of normalized loss coefficients resulted by three model with different roughness coefficient .....	116
Figure 107: Comparison of friction losses between calculated by CFD and using Colebrook equation for different roughness coefficient .....	116
Figure 108: Flow separation (left) and bend outlet velocity contour (right)[68] .	119
Figure 109: Scheme of numerical model of Long Elbow [46].....	120
Figure 110: The non-dimension wall distance ( $y^*$ ) of four numerical models of elbow.....	121
Figure 111: Comparison of velocity contours of elbow 24” between low and high Reynolds number inflow.....	122
Figure 112: Velocity contours at outlet of elbow 12”, 16”, 20” and 24” .....	123

---

Figure 113: Velocity contours in several elbows for $Re= 3,19.10^5$ .....	123
Figure 114: Pressure contours in several elbows for $Re= 2,479.10^6$ .....	124
Figure 115: Comparison of differential pressure head (left) and normalized loss coefficients (right) among elbows with different scale .....	124
Figure 116: The Kops II physical model setup [96].....	127
Figure 117: 3D view of powerhouse cavern with the pressure surge tanks (left) and schematic drawing showing system under investigation (right) [96]. .....	128
Figure 118 : Physical model of pipe junction (left) and numerical model of nozzle (right) [97].....	129
Figure 119: Burgstall surge tank, Left: Physical model, Right: 3D view [99] ....	130
Figure 120: Physical model setup (left) and 3D view of surge tank (right) [100]	131
Figure 121: 2D and 3D view of velocity in the nozzle lower chamber [100].....	131

# List of symbols and abbreviations

## Small letters

$a$	speed of sound	[m/s]
$a_s$	acceleration	[m/s <sup>2</sup> ]
$k$	turbulent kinetic energy	[m <sup>2</sup> /s <sup>2</sup> ]
$k_s$	roughness height	[m]
$k_p$	kinetic energy at point P	[m <sup>2</sup> /s <sup>2</sup> ]
$g$	acceleration of gravity	[m/s <sup>2</sup> ]
$p$	Pressure	[N/m <sup>2</sup> ]
$q$	Heat flux	[W/m <sup>2</sup> ]
$s$	distance	[m]
$t$	time	[s]
$\bar{u}$	Average velocity	[m/s]
$u_m$	Velocity of model	[m/s]
$u_p$	Velocity of prototype	[m/s]
$u$	Velocity at x direction	[m/s]
$v$	Velocity at y direction	[m/s]
$w$	Velocity at z direction	[m/s]
$y_p$	Distance from point p to the wall	[m]
$y_v$	physical viscous sub layer thickness	[m]
$y_n$	height of the cell	[m]
$y^*$	dimensionless distance from the wall	[-]
$x, y, z$	Coordinate direction	[m]

## Capital letters

$A$	Area	[m <sup>2</sup> ]
$A_m$	Cross section area of model	[m <sup>2</sup> ]
$A_p$	Cross section area of prototype	[m <sup>2</sup> ]
$C_{i\varepsilon}$	constant value of k- $\varepsilon$ model	[-]
$C_\mu$	Eddy viscosity	[-]
$D$	Pipe diameter	[m]
$D_m$	Diameter of pipe model	[m]
$D_p$	Diameter of pipe prototype	[m]
$E$	Empirical constant	[-]
$F_r$	Froude number	[-]
$F_s$	Force	[N]
$F_x$	Force in x direction	[N]

$F_y$	Force in y direction	[N]
$F_z$	Force in z direction	[N]
$G$	Gravitational force	[N]
$G_k$	Generation of turbulence kinetic energy due to the mean velocity gradient	$[m^2/s^2]$
$\overline{G_k}$	Cell-averaged production	$[m^2/s^2]$
$\bar{\varepsilon}$	Cell-averaged dissipation rate	$[m^2/s^3]$
$G_b$	Generation of turbulence kinetic energy due to buoyancy	$[m^2/s^2]$
$G_i$	Component of the gravitational vector in i direction	$[m/s^2]$
$H$	Energy Head	[m]
$K$	Loss coefficient of fittings (including friction loss)	[-]
$L_i$	Length of pipe	[m]
$L_m$	Length of model	[m]
$L_p$	Length of prototype	[m]
$M_t$	Turbulent match number	[-]
$Pr$	Prandtl number	[-]
$Q$	Discharge	$[m^3/s]$
$Q_m$	Discharge of model	$[m^3/s]$
$Q_p$	Discharge of prototype	$[m^3/s]$
$Re$	Reynolds number	[-]
$Re_y$	Turbulent Reynolds number	[-]
$S$	modulus of the mean rate-of-strain sensor	[-]
$S_{ij}$	Mean rate-of-strain tensor	$[s^{-1}]$
$S_k$	User defined sources term for k- $\varepsilon$ model	$[kg/m^3.s]$
$S_\varepsilon$	User defined sources term for k- $\varepsilon$ model	$[kg/m^3.s]$
$S_\omega$	User defined sources term for k- $\omega$ model	$[kg/m^3.s]$
$U_p$	average velocity of fluid at point P	[m/s]
$Y_M$	the contribution of the fluctuating dilatation in compressible turbulence to the overall dissipation rate	$[m^2/s^3]$
$Y_k$	dissipation of k due to turbulence	$[m^2/s^3]$
$Y_\omega$	dissipation of $\omega$ due to turbulence	$[m^2/s^3]$
$Z$	Position head	[m]

### Small Greek letters

$\alpha$	Kinetic energy correction factor	[-]
$\alpha_k$	Inverse effective Prandtl number for k	[-]
$\alpha_\varepsilon$	Inverse effective Prandtl number for $\varepsilon$	[-]
$\alpha_s$	Swirl constant	[-]
$\beta$	Coefficient of thermal expansion	[-]
$\delta_{ij}$	Kronecker delta	[-]
$\varepsilon$	Rate dissipation of turbulence kinetic energy	$[m^2/s^3]$
$\zeta$	Coefficient of local loss	[-]

$\eta$	Length scale	[-]
$\theta$	Angle	[°]
$\vartheta$	Kinematic viscosity	[m <sup>2</sup> /s]
$\vartheta_t$	Eddy viscosity	[kg/m.s]
$\kappa$	Von Karman constant	[-]
$\lambda$	Friction factor	[-]
$\mu$	Dynamic viscosity	[kg/m.s]
$\mu_t$	turbulent viscosity	[kg/m.s]
$\mu_{t0}$	turbulent viscosity calculated without swirl	[kg/m.s]
$\pi$	Phi number (3.14...)	[-]
$\omega$	Rate dissipation of k- $\omega$ model	[m <sup>2</sup> /s <sup>3</sup> ]
$\rho$	Fluid density	[kg/m <sup>3</sup> ]
$\sigma_{ij}$	Stress tensor due to molecular viscosity	[kg/m.s]
$\sigma_k$	Turbulent Prandtl number for k	[-]
$\sigma_\varepsilon$	Turbulent Prandtl number for $\varepsilon$	[-]
$\tau_{ij}$	Sub grid-scale stress	[N/m <sup>2</sup> ]

### Capital Greek letters

$\Delta h$	Differential energy head/total loss	[m]
$\Gamma_\omega$	effective diffusivity of $\omega$	[kg/m.s]
$\Gamma_k$	effective diffusivity of k	[kg/m.s]
$\nabla$	Del operator	[-]
$\Omega$	Characteristic swirl number	[-]

### Abbreviation:

CFD	Computational Fluid Dynamic
DES	Detached Eddy Simulation
DNS	Direct Numerical Simulation
GRP	Glass-fiber Reinforced Polyester
LDA	Laser Doppler Anemometer
LES	Large Eddy Simulation
PIV	Particle Image Velocimetry
RANS	Reynolds Average Numerical Simulation
RNG	Re-Normalization Group
RSM	Reynolds Stress Model
RMSE	Root Mean Square Deviation
SM	Scale Model
SST	Shear Stress Transport
UFM	Ultrasonic Flow Meter

# Appendixes

## PHYSICAL MODEL OF Y-BIFURCATOR ALBERSCHWENDE

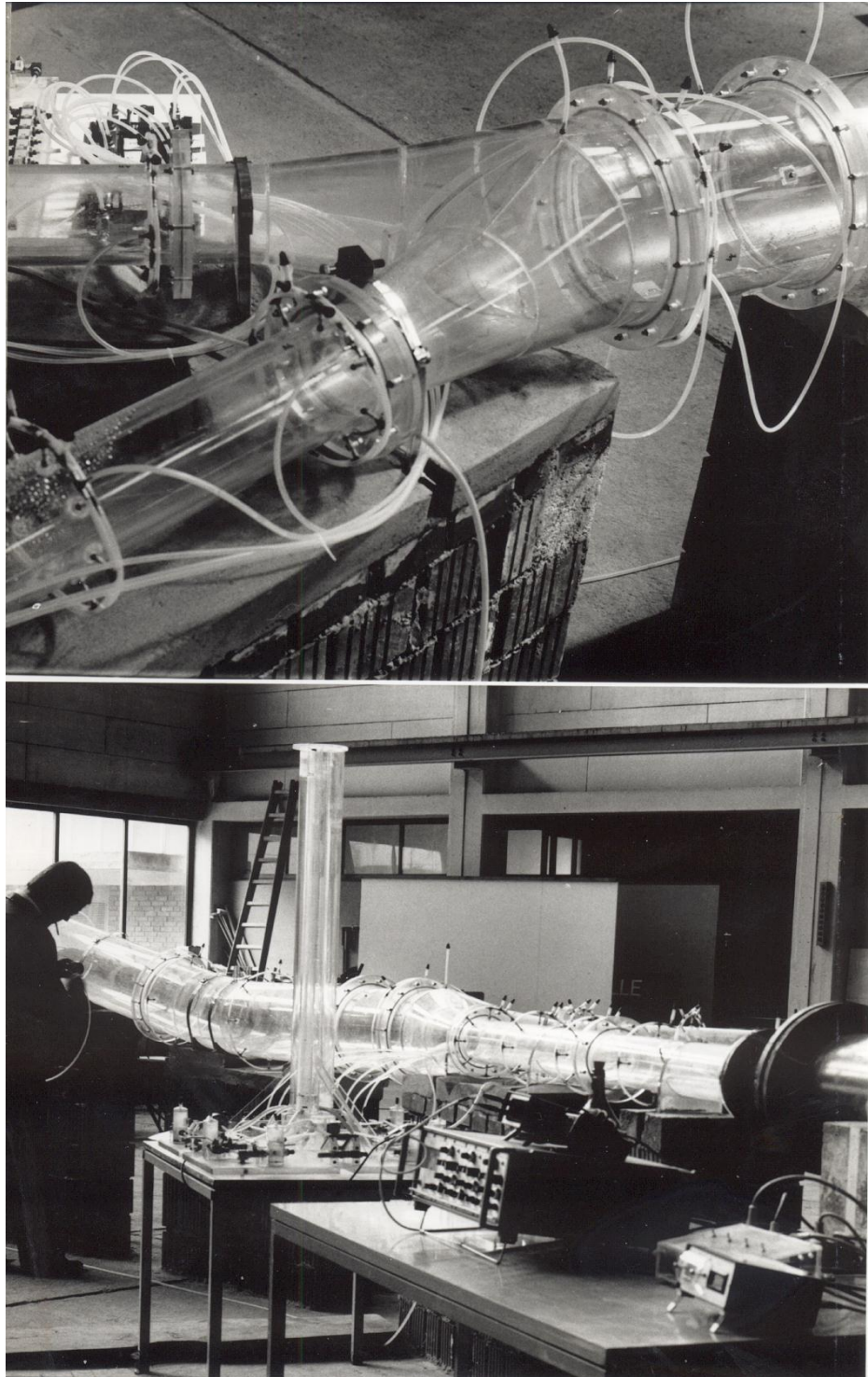


Figure A1: Installation of pressure transducer [40]



Figure A2: Installation of Y-bifurcator Alberschwende [40]



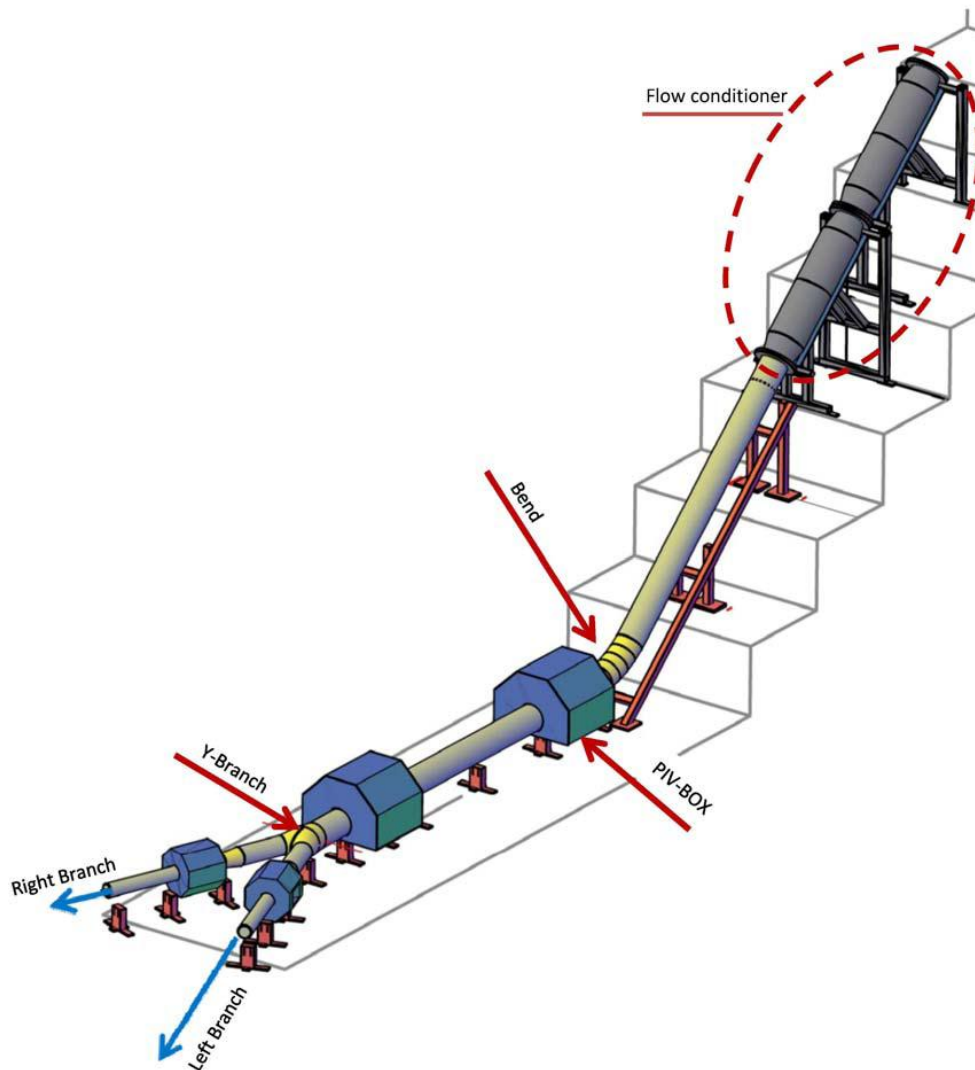
**PHYSICAL MODEL OF PIRRIS BIFURCATOR**

Figure A4: Installation of the model test Pirris – General view [26]